Transmission Electron Microscopy Imaging Alkali Ion (De)intercalation in van der Waals Crystals

A thesis submitted to the University of Manchester for the degree of Doctor of Philosophy in the Faculty of Science and Engineering

Shouqi Shao

Department of Materials

2022

[Blank page]

Contents

Word Count: 39548

List of Figures

List of Abbreviations

2D: Two-dimensional

4DSTEM: Four-dimensional scanning transmission electron microscope

ADF: Annular dark field

BF: Bright field

BFP: Back focal plane

CBED: Convergent beam electron diffraction

CCD: Charge coupled device

CTEM: Conventional transmission electron microscopy

DI water: Deionised water

ED: Electron diffraction

EDS: Energy dispersive X-ray spectroscopy

EELS: Electron energy loss spectroscopy

FEG: Field emission gun

FFTs: Fast Fourier transforms

FLG: Few-layer graphene

HAADF: High-angle annular dark field

hBN: Hexagonal born nitride

HOPG: Highly oriented pyrolytic graphite

IPA: Isopropyl alcohol

LaB_6: Lanthanum hexaboride

OTF: Optical transfer function

SAED: Selected area electron diffraction

STEM: Scanning transmission electron microscopy

TEM: Transmission electron microscope

TMDCs: Transition metal dichalcogenides

XRD: X-ray diffraction

Abstract

Layered van der Waals crystals have been extensively studied because of their attractive physical and chemical properties. Alkali ion intercalation as a unique avenue for tuning the fundamental properties of these layered materials is a rapidly expanding field of research to develop the novel materials applied in the next generation nanoelectronics, catalyst, and energy storage device. Understanding the atomic structures of the intercalated materials and the (de)intercalation process are prerequisites to produce the desirable materials with expected properties. *In-situ* scanning/ transmission electron microscopy (S/TEM) allows researchers to dynamically observe structural and chemical variations of the specimen under external stimuli at very high resolution, providing an ideal platform to study intercalation process and intercalated materials. This thesis details the application of *in-situ* S/TEM combined with energy dispersive X-ray spectroscopy (EDS) spectral imaging and four-dimensional (4D) STEM to directly image the structural evolution and chemical variation within the intercalated van der Waals crystal under heating and biasing.

The first work discusses structural and chemical variations of the K-doped MoS_2 flake heated at different temperatures using *in-situ* TEM. Studying the dynamics of the K deintercalation in a van der Waals crystal is applied in order to understand the intercalation process and the accompanying phase and compositional changes. Selected area electron diffraction (SAED) confirms the change of local K ordering supported by structural modelling and diffraction simulation, and STEM-EDS suggests K deintercalation in the flake follows first-order kinetics. The second work introduces the 4DSTEM imaging technique and the principle of the 4DSTEM dataset processing methods through which the superstructures appearing in the K-intercalated MoS_2 were first characterized at the nanoscale, supporting the hypothesis purposed in the first work. The third work provides insight into Eu intercalation into bilayer graphene. The intercalation process was imaged by STEM in real time and we observed the morphologic changes of the suspended bilayer graphene membrane induced by intercalation. Both intercalation of Eu and ionic liquid cations have been achieved at low applied bias (-4V) and high applied bias (-8V) respectively, as evidenced using SAED and STEM-EDS.

Declaration

No portion of the work referred to in the thesis has been submitted in support of an application of another degree or qualification of this or any other university or other institute of learning.

Copyright Statement

i. The author of this thesis (including any appendices and/or schedules to thisthesis) owns certain copyright or related rights in it (the "Copyright") and s/he has given The University of Manchester certain rights to use such Copyright, including for administrative purposes.

ii. Copies of this thesis, either in full or in extracts and whether in hard or electronic copy, may be made only in accordance with the Copyright, Designs and Patents Act 1988 (as amended) and regulations issued under it or, where appropriate, in accordance with licensing agreements which the University has from time to time. This page must form part of any such copies made.

iii. The ownership of certain Copyright, patents, designs, trademarks and other intellectual property (the "Intellectual Property") and any reproductions of copyright works in the thesis, for example graphs and tables ("Reproductions"), which may be described in this thesis, may not be owned by the author and may be owned by third parties. Such Intellectual Property and Reproductions cannot and must not be made available for use without the prior written permission of the owner(s) of the relevant Intellectual Property and/or Reproductions.

iv. Further information on the conditions under which disclosure, publication and commercialisation of this thesis, the Copyright and any Intellectual Property and/or Reproductions described in it may take place is available in the University IP Policy (see http://documents.manchester.ac.uk/DocuInfo.aspx?DocID=24420), in any relevant Thesis restriction declarations deposited in the University Library, the University Library's regulations (see http://www.library.manchester.ac.uk/about/regulations/) and in the Uni-versity's policy on Presentation of Theses.

Acknowledgement

Firstly, I would like to thank my main supervisor Prof Sarah Haigh and co-supervisor Prof Irina Grigorieva for their continuing support, patience, and expert guidance during the period of my PhD journey. Their inspiring suggestions and enthusiastic encouragement always lit the path of my research studies and motivated me to look ahead, which will absolutely impact my life for a long time. Without their helps, the research I carried out over the past four years would have been far less fruitful. I must also thank two professional technicians in the EM centre, Matt Smith and Dr Duc-The Ngo. They offered explicit trainings and invaluable assistance to me on using TEM, which resulted in the micrographs existing in this thesis.

I would also like to thank the colleagues in our group and who I worked with. Dr Dan Kelly provided a great number of inspiring ideas in my first first-author scientific paper, and he patiently offered me guidance in processing and presenting data by using python. Drs Rongsheng Cai, Yichao Zou, David Hopkinson, Yi-Chi Wang I must thank for my skill-up in performing TEM, image simulation and EDS analysis. Dr Wenjun Kuang, Mengjie and Dr Rui Zhang I have to thank for the sample preparation and efforts for the results in this thesis. Additionally, I also must thank the rest of the Haigh group, past and present, as well as many collaborators.

Lastly, I would like to thank my parents and girlfriend. Not only for sponsoring my four-year study, but also for special cares to my life during the pandemic lock down in UK. They encouraged and supported me to finish the PhD study in the tough time. None of this would have ever happened without them.

List of Publications

1 **Shao, S.**, Kelly, D.J., Kuang, W.J., Grigorieva, I.V. and Haigh, S.J., Thermal deintercalation of K-doped MoS_2 analysed via *in situ* TEM (2022) In submission.

2 **Shao, S.**, Feng, M., Cai, R., Mishchenko, A., Haigh, S.J., Imaging Eu intercalation in bilayer graphene via TEM *in situ* biasing (2022) In progress.

3 Yu, J., Nelo, M., Liu, X., **Shao, S.**, Wang, B., Haigh, S.J., Jantunen, H. and Freer, R., Enhancing the Thermoelectric Performance of Cold Sintered Calcium Cobaltite Ceramics Through Optimized Heat-Treatment. *Available at SSRN 3962653*.

4 Maughan, P.A., Bouscarrat, L., Seymour, V.R., **Shao, S.**, Haigh, S.J., Dawson, R., Tapia-Ruiz, N. and Bimbo, N., 2021. Pillared Mo_2TiC_2 MXene for high-power and long-life lithium and sodium-ion batteries. *Nanoscale advances*, *3*(11), pp.3145-3158.

5 Maughan, P.A., Seymour, V.R., Bernardo-Gavito, R., Kelly, D.J., **Shao, S.**, Tantisriyanurak, S., Dawson, R., Haigh, S.J., Young, R.J., Tapia-Ruiz, N. and Bimbo, N., 2020. Porous silica-pillared MXenes with controllable interlayer distances for long-life Na-Ion batteries. *Langmuir*, *36*(16), pp.4370-4382.

6 Synnatschke, K., **Shao, S.**, Van Dinter, J., Hofstetter, Y.J., Kelly, D.J., Grieger, S., Haigh, S.J., Vaynzof, Y., Bensch, W. and Backes, C., 2019. Liquid Exfoliation of $Ni_2P_2S_6$: Structural Characterization, Size-Dependent Properties, and Degradation. *Chemistry of Materials*, *31*(21), pp.9127-9139.

7 Yu, W., Batchelor-McAuley, C., Wang, Y.C., **Shao, S.**, Fairclough, S.M., Haigh, S.J., Young, N.P. and Compton, R.G., 2019. Characterising porosity in platinum nanoparticles. *Nanoscale*, *11*(38), pp.17791-17799.

Chapter 1

Introduction

1.1 Project Objectives

Akali ion (de)intercalation can play a key role in tuning the behaviour of van der Waals materials, for instance modifying the band structure to realise superconductivity and engineer stable structural phases for superior catalysts. It is also important as part of many intercalation assisted synthesis routes for yielding atomically thin flakes and used in the charging/discharging cycle of some designs of alkali ion batteries/supercapacitors. Due to the complexity of the (de)intercalation process, significant open questions remain around the details of (de)intercalation induced superstructural evolution, phase transition and chemical variation, hindering the further development of these van der Waals materials and their applications. *In-situ* scanning/ transmission electron microscopy (S/TEM) provides an effective platform to directly image the (de)intercalation process in real time and to provide a wealth of structural and physicochemical information through the employment of advance analytical techniques, such as the energy dispersive X-ray spectroscopy (EDS), electron energy loss spectroscopy (EELS), four-dimensional (4D) STEM.

The primary aim of this project was to study the structural variation of intercalation compounds during the (de)intercalation processes,

correlating these to high spatial resolution elemental analysis to demonstrate (de)intercalation dynamics. These objectives were accomplished through performing *in-situ* S/TEM imaging and correlative analysis of the deintercalation process in the K-intercalated MoS_2 system and the electrochemical intercalation process of Eu intercalation into bilayer graphene. Both systems were comprehensively characterized from structural and chemical perspectives through electron diffraction (ED) in TEM, high resolution (HR) S/TEM, 4DSTEM and EDS elemental analysis, supported by multislice ED simulation and STEM image simulation. A parallel aim of the project was to fabricate an electrochemical nano-device based on a commercial *in-situ* TEM chip which was achieved through modifying the previously published fabrication process and extensive *in-situ* intercalation testing.

1.2 Thesis Structure

The work demonstrated in this thesis was carried out as part of the Graphene NowNano Centre for Doctoral Training in the Department of Materials at the University of Manchester from April 2018 – December 2021 funded by the Engineering and Physical Sciences Research Council (EPSRC).

This thesis begins with an overview of TEM in the Chapter 2, including the principles of TEM imaging, ED, EDS and EELS, being essential to the project and its execution. Chapter 3 demonstrates the crystallography of two-dimensional (2D) materials and their derived superstructures. Chapter 4 presents a literature review introducing the

kinetics of alkali ion intercalation in the van der Waals materials including charge transfer and ion diffusion, followed by discussion of the published work concerning the structural characterisation of layered intercalation compounds. Chapter 5-7 presents the results of this project in three draft journal papers. These focus on the investigation of structural and chemical variations in K ion (de)intercalation in MoS_2 (Chapter 5-6) and Eu intercalation in bilayer graphene (Chapter 7) via advanced *in-situ* S/TEM.

The first paper, "Thermal deintercalation of K-doped MoS_2 analysis via *in-situ* TEM", presented in Chapter 5, showcases structural and chemical variations of the K-doped MoS_2 flake heated at different temperatures by using *in-situ* TEM. We demonstrate the formation of the superstructures, measure local K concentrations, and map the K distributions in the fresh K-doped MoS_2 flakes before heating by using various analytical techniques. Comprehensive characterisations of the specimen are performed during *in-situ* heating at four different temperatures (room temperature, 150 ˚C, 200 ˚C, 300 ˚C) to study mechanisms and kinetics of K deintercalation from MoS_2.

The second paper, "4D-STEM imaging local nanostructures of K-intercalated MoS_2", presented as Chapter 6 which extends the structural diffraction investigation of the K-doped MoS_2 to the nanoscale by using the 4DSTEM technique. We demonstrate the theory and principle of the 4DSTEM dataset acquisition and data processing methods. Taking advantage of the flexibility of the 4DSTEM dataset we manipulate the stack of diffraction patterns and reconstruct images by employing virtual objective apertures and virtual selected area apertures to reveal the

distribution of superstructures in the specimen.

The third paper, “Imaging the intercalation process in bilayer graphene via TEM *in-situ* biasing”, presented in Chapter 7 showcases the workflow of manufacturing an electrochemical nanodevice based on a commercial *in-situ* TEM E-chip for Eu intercalation experimented under different biasing conditions. At -8V, the *in-situ* STEM imaging illustrates the formation of bubbles in the suspended bilayer graphene membrane induced by the ionic liquid intercalation. Eu intercalation is observed at -4V. STEM-EDS spectrum illustrates the Eu peak and HR-STEM images the formation of Eu clusters in the bilayer graphene membrane, accompanied with the stacking order change of the graphene layer from AB (before intercalation) to AA (after intercalation).

The final chapter summarizes results of the project and provides an outlook for future work.

Chapter 2

Transmission Electron Microscopy

Since it was invented and first used in 1932 by Knoll and Ruska[1], the transmission electron microscope (TEM) has become one of the most widely applied analytical instruments in materials sciences, physics, chemistry and life sciences - enabling researchers to directly "see" a specimen from the micrometre down to the sub-ångstrom scale. In recognition of remarkable achievement in electron optics and the design of the first electron microscope, Ernst Ruska was awarded the Nobel Prize in Physics in 1986. Since then, the further development of TEM instrumentalism and techniques has continued. More recently, the 2017 Nobel Prize in chemistry was awarded jointly to Jacques Dubochet, Joachim Frank and Richard Henderson for developing cryo-electron microscopy for biological applications[2]. Additionally, thanks to significant technological advancements, new techniques have been developed to push TEM performance and applications to new levels, such as aberration-corrected TEM[3,4], *in-situ* TEM[5,6] and four-dimensional scanning transmission electron microscopy (4DSTEM)[7].

This chapter starts with an introduction to the configuration of the TEM including electron sources, electromagnetic lenses and apertures in section 2.1, followed by the demonstration of basic principles and applications of the electron diffraction in TEM in section 2.2. Image contrast mechanisms are discussed in section 2.3, followed by an

explanation of inelastic scattering behaviours, that form the basis of two powerful analytic tools: energy dispersive X-ray spectroscopy (EDS) and electron energy loss spectroscopy (EELS), in section 2.4. *In-situ* TEM capabilities, including a specially designed TEM holders and micro-electromechanical systems (MEMS)-chips are presented in section 2.5. Finally, beam damage mechanisms are discussed in the section 2.6.

2.1 Configuration of Microscope

Fig. 2.1 shows a schematic of the configuration of a TEM that consists of an electron gun, distinct lenses, apertures, beam deflectors, stigmators, detectors and a sample holder in general.

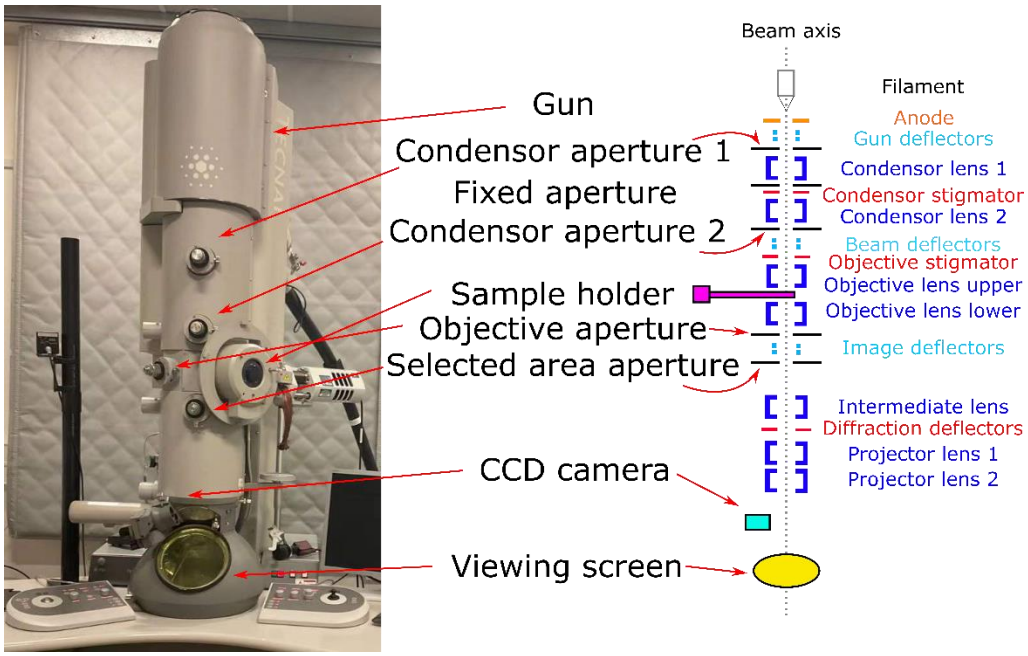

Figure 2.1 A schematic of the detailed internal structure of a TEM (right) with an example of a modern instrument (left).

2.1.1 Electron Sources

An electron beam illuminating a sample of interest is generated from an electron source as shown on the top of the left image in Fig. 2.1. It is also known as the electron gun or filament, and is analogous to the light source of an optical light microscope. The electrons are emitted from the cathodic electron gun and accelerated toward an anode to produce the electron beam. The common electron sources in TEM are thermionic-emission electron gun and the field emission electron gun (FEG), made by a lanthanum hexaboride (LaB_6) crystal tip (or a tungsten filament) and a sharpened tungsten needle, respectively[8]. The former source, emitting thermoelectrons by heating the material, is cheaper and requires a lower vacuum condition, but the latter produces the electrons with higher stability, brightness and coherence, although it requires an ultra-high vacuum[9,10].

There are two types of FEG: the Schottky-type FEG and the cold (cathode) FEG. In the Schottky-type FEG, a tungsten tip is heated to a lower temperature than the temperature at which the tip can effectively emit thermoelectrons, and a strong electric field is applied to the tip. This reduces the work function, causing emission of electrons from the tungsten tip (also known as the Schottky effect). Similarly, the cold FEG emits the electrons due to a strong electric field, but at room temperature, producing an electron beam with a narrower energy spread, higher coherency and smaller size, facilitating high contrast/signal-to-noise imaging and analytical spectroscopy[11]. However, high-quality vacuum conditions are necessary for operation of a cold FEG, since it is likely to be contaminated

by residual gases and other contaminants in the TEM column, which leads to the fluctuation of the emission current[12]. The Schottky-type FEG, taking advantage of constant heating, does not adsorb contaminates and consequently, is much more stable than the cold FEG.

2.1.2 Lenses

Electromagnetic lenses employed by the TEM are equivalent to the glass lenses in an optical microscope. They play two roles: 1) gathering all electron rays generated from a point in an object and recreating a point in an image, and 2) focusing the parallel rays to a point in the focal plane of the lens[13]. Usually, the electromagnetic lens consists of copper coils, polepieces and a water-cooled surface as shown in Fig. 2.2a. The gap and bore between the polepieces control the characteristics of the magnetic field that comprises the lens itself[13]. As current passes through the copper coils, the magnetic field is created in the bore. The water-cooled surface is to remove the resistive heat in the coils by a water recirculating system[13].

2.1.2.1 Ideal perfect lenses

Understanding the trajectory of an electron beam passing through an electromagnetic lens is of importance to understand the formation of the electron diffraction pattern and the image. Fig. 2.2b illustrates a ray diagram of an object lying above the electromagnetic lens and the image of this object lies below the lens. For a perfect lens, the rays leaving a point in the object plane are brought to the correspond ding point in the image plane. The back focal plane (BFP) of the lens is the plane in which the

parallel rays are brought to a focus point as shown in Fig. 2.2b, and the information about crystal structures present in this plane as the diffraction pattern. Diffraction and imaging modes of conventional transmission electron microscopy (CTEM) are detailed in sections 2.2 and 2.3, respectively. The magnetic field is inhomogeneous along the horizonal direction, i.e. the magnetic field is weakest on axis and strongest close to the polepieces, thereby the outer rays deflect more than the rays close to the axis to ensure that they can focus at the same point. Due to the cylindrical shape of the electromagnetic lens, the magnetic field is axially symmetric for an ideal lens.

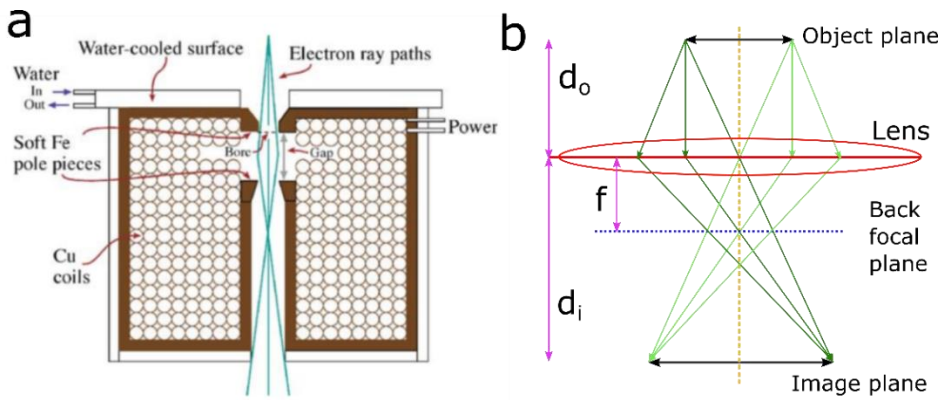

Figure 2.2 Schematics of an electromagnetic lens and a ray diagram for imaging an object. (a) Cross-sectional schematic diagram of an electromagnetic lens. There is a channel in the middle of the cylindrical lens for electron beam to pass through, where a pair of conical polepieces sit. The central hole of each polepiece is called the bore and the distance between two polepieces is called the gap. Polepieces are surrounded by the copper coils through which the current runs to magnetize the polepieces and to focus the electron beam. Adapted with permission from[13]. Copyright 1996 Springer Science Business Media New York. (b) A ray diagram of a perfect lens, where d_o and d_i stand for the distances from the object and image to the lens, respectively. f stands for the distance from the BFP to the lens.

Fig. 2.2b denotes three significant distances namely: the object distance d_o, the image distance d_i and the focal length f. Newton's lens equation shown below presents the relation between them[13]:

$$\frac{1}{f} = \frac{1}{d_o} + \frac{1}{d_i} \tag{2.1}$$

By using the lens equation, the magnification (M) of a convex lens can be defined as:

$$M = \frac{d_i}{d_o} \tag{2.2}$$

Consequently, to magnify the image of the specimen, the only way is to increase d_i by weakening the strength of the magnetic field in the lens, since d_o is fixed in TEM. Furthermore, building a series of lenses in which the image plane of the first lens coincides with the object plane of the second lens and so on enables further magnification of the image, which is the basis of the intermediate and projector lenses in the TEM.

2.1.2.2 Aberrations in Real Lenses

Real lenses used in the TEM is far from perfect, despite the best efforts of improving the design of the lens in the past decades.[14] There are many kinds of unavoidable defects in the real lens which distort the image and limit the TEM performance. Among them, chromatic aberration, spherical aberration and astigmatism are three major impediments to improve the point resolution for imaging and spectroscopy[15]. Fig. 2.3 shows the comparison of the ray diagrams for different lens aberrations and their corresponding beam shapes produced.

Chromatic aberration is related to the energy (or frequency,

wavelength) of the electron beam, which usually originates from either the energy spread of the electron source, which can vary from 0.3 eV (cold FEG) to 1.0 eV (LaB_6)[13], or the interaction between the electron beam and a thick specimen leading to a wide energy spread emerging. The objective lens focuses the electrons of higher (lower) energy more weakly (strongly) as shown in the blue (red) rays in Fig. 2.3b and thus a blurred disk forms in the Gaussian image plane. The radius r_{chr} of this disk is related to the collection semi-angle (α) and calculated by:

$$r_{chr} = C_c \frac{\Delta E}{E_0} \alpha \tag{2.3}$$

where C_c is the chromatic aberration coefficient of the lens, ΔE is the energy loss of the electrons, E_0 is the initial beam energy.

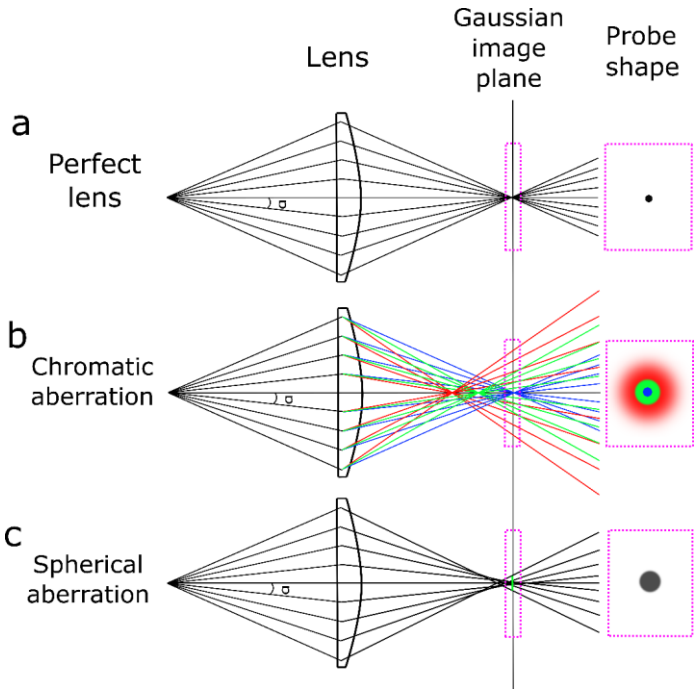

Figure 2.3 Comparison of the ray diagrams for the perfect lens and the imperfect lens with the different aberrations. (a) shows a perfect lens producing a bright and sharp probe shown in the dotted box. α stands for the collection semi-angle. (b) is a schematic of the chromatic aberration. Red, green and blue rays depict the focused electron beams with different energies ($E_{blue} > E_{green} > E_{red}$), resulting in different rays focusing on the distinct image planes. The probe produced by green and red rays are blurring causing loss in information in an image. (c) illustrates the spherical aberration effect of which the rays at the outside of the lens deflects more than those close to the optical axis. The diameters of the disks in the Gaussian image plane can be calculated by equation (2.4).

Spherical aberration originates from an intrinsic defect of the objective lens: the strength of magnetic field is inhomogeneous (intensity decreasing from the lens to the optical axis) inside the polepiece, resulting in rays focusing into distinct positions as shown in Fig. 2.3c. Thus a point from the object forms a disk in the Gaussian image plane with the diameter (d_{sph}) related to the spherical aberration coefficient C_s:

$$d_{sph} = C_s \alpha^3 \tag{2.4}$$

Therefore, the spherical aberration degrades the details of the object and the point resolution in the image.

Astigmatism usually arises from the imperfect soft iron polepiece. The inhomogeneous microstructures or symmetrical issues generated while polepiece is machined cause a non-uniform magnetic field down the bore. Additionally, the misalignment of the condenser lens aperture and contamination charging effects can also deflect the beam and thus contribute to the astigmatism. As a result, the distorted image is formed.

2.1.2.3 Aberration Corrections

As we discussed in the previous section, the achievable resolution of a CTEM is limited by the aberrations of the objective lens and thus imaging at higher spatial resolution can be achieved by reducing the effect of the aberrations through aberration corrections. For chromatic aberration, the common methods include monochromating the electron source by using chromatic aberration correctors to focus electron beams with energy difference to the same point on the specimen, or installing an energy filter underneath the sample. The former approach is required for high special resolution electron energy loss spectroscopy (EELS)[16] and low voltage imaging[17], but is restricted by high cost, while the latter one is used in the energy filtered TEM (EFTEM)[13].

The method for compensating spherical aberrations can be described by considering a concave lens which spreads out the off-axis beams so that they can be converged to a point instead of a disk in the Gaussian plane (Fig. 2.3c). The spherical-aberration corrector is composed of hexapoles[18] or quadrupole-octupole lenses[19] rather than the round magnetic lenses, and they are placed underneath the condenser or objective lens system to

correct spherical aberrations by varying the polarity distributed radially around the optic axis.

Two-fold astigmatism can be corrected by stigmators which are octupoles for compensating the inhomogeneous magnetic field generated in both the condenser and objective lenses in which stigmators are mounted.

2.1.3 Apertures

Apertures are as significant as the electromagnetic lenses in the TEM. They are usually circular holes with different diameters in a metallic disk made of either Pt or Mo and can be placed above, in or below the plane of the lens. Using the aperture enables the operator to reduce the collection angles (α) of the lens and the convergence angle of the beam. In the plane of the image and the BFP, a selected area aperture and an objective aperture can be used to select the region of interest in real space and the diffraction spot with given diffraction angles, respectively. Additionally, use of an aperture can protect the specimen from electron radiation by controlling the fluence of the electron beam.

2.2 Electron Diffraction

Electron diffraction (ED) is a consequence of the wave nature of the electrons interacting with matter. It is a special form of elastic scattering and ED patterns have been widely used to analyse the crystal structure of the specimen. In this section, the origin of ED is introduced and then two approaches to electron diffraction are discussed: selected area electron diffraction (SAED) in CTEM and 4DSTEM in STEM.

2.2.1 Elastic Scattering and the Bragg Condition

Elastic scattering is caused by incident electrons interacting with electrostatic field of atomic nuclei without any experimentally detectable energy loss, due to the fact that the mass of an electron is thousands of times less than that of a nucleus[20]. It is a significant process in creating the intensity in diffraction patterns (DPs) (section 2.2) and the crystalline contrast in TEM imaging (section 2.3).

Elastic scattering can be considered in two principal forms: high and low angle scatterings. The former process results in electrons scattering through high angles (up to 180°) and is related to the particle nature of the electrons, being analogous to the backscattered α particles by a thin gold foil observed by Ernest Rutherford[21]. Thus, the high angle scattering is primarily quantified by the Rutherford differential cross section, $d\sigma/d\Omega$[20]:

$$\frac{d\sigma}{d\Omega} = \frac{4\gamma^2 Z^2}{a_0^2 q^4} \tag{2.5}$$

where Z is the atomic number, $a_0 = 0.529 \times 10^{-10}$ m is the first Bohr radius, q is the magnitude of the scattering vector for the momentum transferring to the specimen and γ:

$$\gamma = \frac{1}{\sqrt{1-\frac{v^2}{c^2}}} \tag{2.6}$$

is a relativistic factor where v is the velocity of the incident electron and c is the speed of light in vacuum[20]. However, for scattering angles lower than ~ 3°, the nuclear screening and relativistic effects modify the Rutherford differential cross section into other expressions[13] that are not significantly relevant to the work presented in this thesis.

On the other hand, electron diffraction effects become dominant at the low scattering angle (< 3°) where the CTEM electron beam can be treated as a plane wave. In this case, the atomic-scattering factor, $f(\theta)$, being a measure of the amplitude of an electron wave scattered from an isolated atom, is introduced to complement the Rutherford model and is related to the scattering cross section $d\sigma(\theta)/d\Omega$ as:

$$|f(\theta)|^2 = \frac{d\sigma(\theta)}{d\Omega} \tag{2.7}$$

where θ is the semi-angle of scattering and $|f(\theta)|^2$ is proportional to the scattered intensity. In a crystalline material, a sum of $f(\theta)$ for *i* atoms in a unit cell is termed the structure factor $F(\theta)$ with atomic coordinates x_i, y_i and z_i:

$$F(\theta) = \sum_i^{\infty} f_i e^{2\pi i(hx_i + ky_i + lz_i)} \tag{2.8}$$

in which *h*, *k* and *l* are Miller indices from the given atomic planes and thus for certain planes, the amplitude of scattering is zero according to the structure factor equation, due to the destructive interference.

The most straightforward and simplified method for interpretation of diffraction patterns is using the Bragg condition. This theory was proposed by the Braggs, who suggested the wave-like behaviour of electrons, where incident waves are reflected by parallel atomic planes. Those contributing to the maximum constructive interference must have a path difference equal to an integral number of illumination wavelengths shown as[22]:

$$2d \sin \theta_B = n\lambda \tag{2.9}$$

where *d* is the interplanar spacing of atomic plane, θ_B is Bragg angle of the incident beam, λ stands for the wavelength of the electron beam and

n is an integer.

2.2.2 Reciprocal Lattice and Ewald Sphere

The reciprocal lattice is an array of points in reciprocal space which represents a particular set of planes (hkl) in the crystal instead of the arrangement of atoms in the real space lattice, and the distance between a single point to the lattice origin is $1/d_{hkl}$. We can rewrite the Bragg equation with the scattering vector $\boldsymbol{K}$ as shown in Fig. 2.4:

$$\frac{2\sin\theta_B}{\lambda} = \frac{n}{d} = |\boldsymbol{K}| \tag{2.10}$$

where the scattering vector $|\boldsymbol{K}|$ is reciprocally related to d.

The mathematical definition of the reciprocal lattice and its relationship to the real space lattice will now be discussed. The real space, the lattice vector $\boldsymbol{r}_n$ can be defined by the equation[13]:

$$\boldsymbol{r}_n = n_1\boldsymbol{a} + n_2\boldsymbol{b} + n_3\boldsymbol{c} \tag{2.11}$$

where the vectors $\boldsymbol{a}$, $\boldsymbol{b}$ and $\boldsymbol{c}$ are the unit cell vectors in real space and n_1, n_2 and n_3 are all integers. Similarly, the reciprocal lattice vector is defined as:

$$\boldsymbol{r}^* = m_1\boldsymbol{a}^* + m_2\boldsymbol{b}^* + m_3\boldsymbol{c}^* \tag{2.12}$$

where $\boldsymbol{a}^*$, $\boldsymbol{b}^*$ and $\boldsymbol{c}^*$ are the unit cell vectors in reciprocal space and m_1, m_2 and m_3 are all integers. The direction relations between the unit cell vectors in the real and reciprocal space are:

$$\boldsymbol{a}^* \cdot \boldsymbol{b} = \boldsymbol{a}^* \cdot \boldsymbol{c} = \boldsymbol{b}^* \cdot \boldsymbol{c} = \boldsymbol{b}^* \cdot \boldsymbol{a} = \boldsymbol{c}^* \cdot \boldsymbol{a} = \boldsymbol{c}^* \cdot \boldsymbol{b} = 0 \tag{2.13}$$

i.e. $\boldsymbol{a}^*$ is normal to both $\boldsymbol{b}$ and $\boldsymbol{c}$. The length relations between the vectors are:

$$\boldsymbol{a}^* \cdot \boldsymbol{a} = 1;\ \boldsymbol{b}^* \cdot \boldsymbol{b} = 1; \boldsymbol{c}^* \cdot \boldsymbol{c} = \mathbf{1} \tag{2.14}$$

In a crystal consisting of repeat, three dimensional unit cells in the real space, a crystal plane can be defined by (*h,k,l*) which are plane intersections with $\boldsymbol{a}, \boldsymbol{b}, \boldsymbol{c}$ axes, giving rise to a specific reciprocal lattice vector $\mathbf{g}_{hkl}$ for the plane:

$$\mathbf{g}_{hkl} = h\boldsymbol{a}^* + k\boldsymbol{b}^* + l\boldsymbol{c}^* \tag{2.14}$$

and the interplanar distance d_{hkl} is inversely related to $\mathbf{g}_{hkl}$:

$$d_{hkl} = \frac{1}{|\mathbf{g}_{hkl}|} \tag{2.15}$$

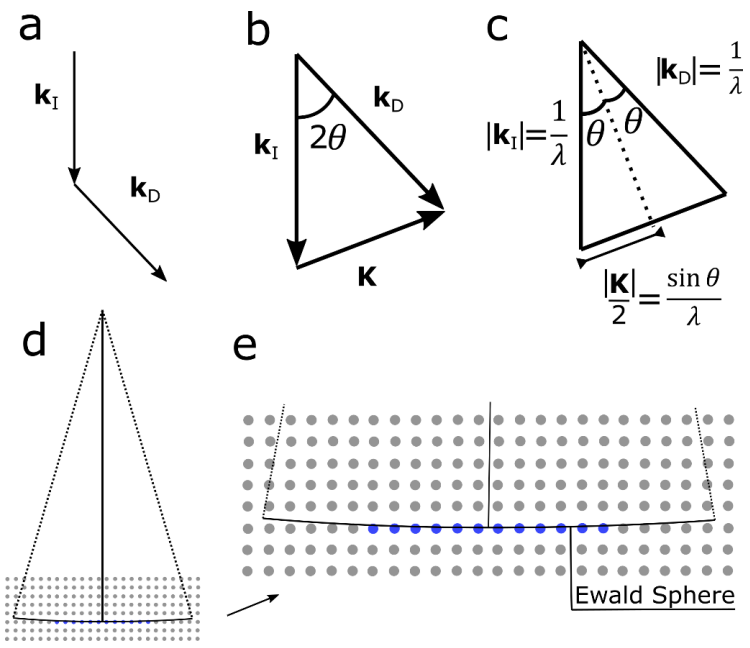

Figure 2.4 Illustration of the scattering vector and the Ewald sphere. (a-c) $\mathbf{k}_I$ and $\mathbf{k}_D$ are the incident and diffracted wavefront normal. $\mathbf{K}$ is the difference vector of $\mathbf{k}_D$ - $\mathbf{k}_I$. θ is incident angle of the plane wave to the atomic planes of spacing *d*. (d-e) illustrate the Ewald sphere intersecting a cubic array of reciprocal lattice points (blue dots).

The Ewald sphere is a sphere with the radius defined as the reciprocal of the wavelength of the incident wave, $1/\lambda$, and is constructed in the three-dimensional reciprocal space[23]. The central point of the sphere is at a certain point along the direction of the incident wave to the specimen crystal. The Ewald sphere illustrates the condition under which the Bragg diffraction occurs using the relation between the incident wave vector and the reciprocal lattice points, i.e. all the reciprocal lattice points cut by the Ewald sphere satisfy the Bragg condition[13]. Considering a high energy electron source (200 kV corresponding to approximately λ =0.002508 nm) as the illumination condition, the Ewald sphere surface can be approximated as a flat plane and intersects many points because the radius is much larger than the distance between the reciprocal lattice points as shown in Fig. 2.4d, e.

2.2.3 Selected Area Electron Diffraction in TEM

The incident electrons, acting as waves, interact with the periodic structures in the crystal and are diffracted to form a diffraction pattern (DP). This pattern can be used to extract and analyze the structural information of the crystal. For instance, distinguishing different crystal phases and studying the grain structure of polycrystalline materials[24]. However, to reduce the intensity of the electron beam which may damage the camera sensor, selected area electron diffraction (SAED) is often performed via inserting a selected area (SA) aperture in the image plane of the objective lens or equivalent conjugate plane in the diffraction mode. This SA aperture results in creating a virtual aperture in the plane of the specimen, which ensures only the electrons incident on specific region of the specimen are transmitted, as shown in Fig. 2.5a. Hence a sharp SAED pattern of the interested area is formed in the BFP, magnified by intermediate lenses and ultimately captured by the scintillator coupled camera. One SAED example from a $NiPS_3$ flake is shown in Fig. 2.5b, c. In this case, we can conclude that this is a single crystal flake and measure the interplanar distances of the representative crystal planes.

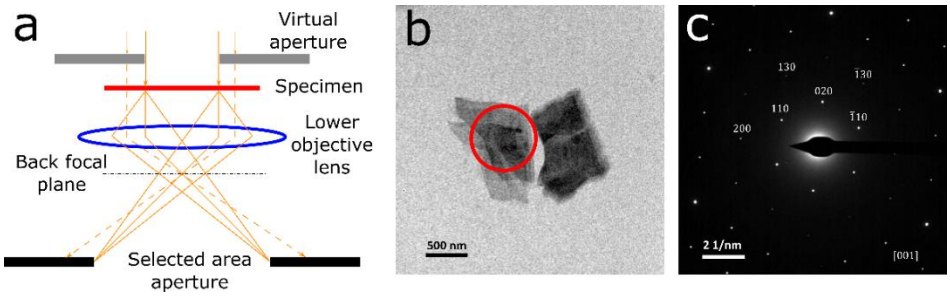

Figure 2.5 Ray diagrams for SAED and a SAED example from $NiPS_3$ single flakes. (a) is a ray diagram illustrating the formation of a SAED pattern. (b) is a bright field image of the $NiPS_3$ flakes and the red circle illustrates the selected area resulting in a SAED as shown in (c). To protect the CCD camera, a beam-stop shown as the shadow in the centre of the pattern is often used to block the intense direct beam. (b) and (c) adapted from my work and adapted with permission from[25]. Copyright 2019 American Chemical Society.

2.2.4 Diffraction Spot Splitting

Diffraction spot splitting describes the separation of a single reflection into a few spots in the diffraction pattern due to the structural variation in the region of interest and it is a significant phenomenon to demonstrate the formation of the new phases in van der Waals crystals which are induced by alkali ion intercalation, of particular significance to results presented in Chapter 5. Therefore, the spot-splitting effect is introduced and reviewed in this section as a primer.

The split spots can be attributed to phase transition resulting in changes of lattice parameters. Chrissafis K. et al. reported the splitting of the primary diffraction reflection of MoS_2 induced by Li intercalation as shown in Fig. 2.6a viewing along [001][26]. The outer split $(10\bar{1}0)$ spot has the same d-spacing with the pristine MoS_2 in the basal plane. The inner spot appearing in the middle of $(10\bar{1}0)$ and (0000) spots, but close to $(10\bar{1}0)$, corresponds to the new phase, with a lattice constant in the basal

plane 6% larger than MoS_2 caused by intercalated Li. Another TEM investigation of $K_{0.5}Bi_{0.5}TiO_3$ perovskite ceramics exhibited a phase transition from the paraelectric cubic to the ferroelectric tetragonal structure at about 270°C, resulting in the formation of twins and the split reflections along the characteristic crystallographic directions, depending on the viewing direction and the orientation of the twins[27]. The diffraction pattern viewed along [100] explicitly showed the spot splitting along [011], accompanied by an 'unsplit' row of reflections (USR) normal to the $(02\bar{2})$ twin plane (Fig. 2.6b-c). This USR contained one of the characteristic twin boundaries, (011) plane, in the perovskites and it was parallel to the split spots. The distance between two split spots increased with the distance from the USR. Such twining induced spot splitting was also observed in other materials[28-30]. Furthermore, several domains concurrently existing in the electron beam illuminated area can cause the splitting of the reflection spots (Fig. 2.6d-e), because the domains scattered the electron into different ways[31].

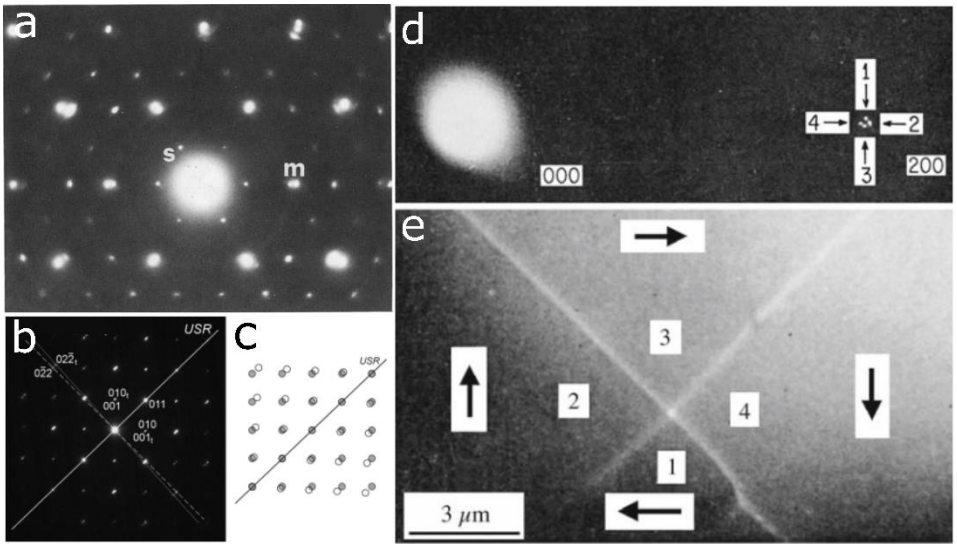

Figure 2.6 TEM images of the electron diffraction splitting. (a) electron diffraction pattern of Li intercalated MoS_2. The superlattice spots and splitting spots are denoted by the letter s and m, respectively. Adapted with permission from[26]. Copyright 1989 Published by Elsevier B.V. (b-c) selected area electron diffraction pattern viewing along [100] and the schematic representation of an identical pattern. Adapted with permission from[27]. Copyright 2010 The American Ceramic Society. (d) splitting [200] reflections from Ni_3Mn due to four magnetic domains shown in (e). Adapted with permission from[31]. Copyright 1963 Taylor & Francis.

2.2.5 Four-dimensional STEM

The previous section introduced the mechanism of producing SAED patterns with a parallel electron beam in CTEM mode, while STEM mode is also widely used for imaging and spectroscopy of the materials in the TEM. Diffraction patterns produced by a convergent beam of electrons has been shown to give further insights into local structural characteristics of materials at the atomic scale[7]. Techniques utilising this method are four-dimensional STEM (4DSTEM)[32], convergent beam electron diffraction (CBED)[33] and scanning precession electron diffraction (SPED)[34]. CBED and SPED will not be discussed in this thesis since they are not relevant to this project.

4DSTEM refers to recording two-dimensional (2D) diffraction patterns using a converged electron beam, over a 2D grid of beam positions, resulting 4D (2D+2D) datasets as shown in Fig. 2.7. Interestingly, 4DSTEM data not only can be processed to produce the bright field (BF) and dark field (DF) STEM image contrasts, but also the diffraction pattern at each scanned probe position, providing a greater flexibility of image contrast. The development of 4DSTEM as a characterization method has been made possible by high speed and efficient direct electron detectors, and the widespread availability of computational power[7].

As an increasing popular technique, 4DSTEM has played a crucial role in various studies of the materials science, such as virtual diffraction imaging[35], phase distinguishing[36], crystal orientation[37] and strain mapping[38], measurements of medium-range thickness[39], differential phase contrast imaging[40] and ptychography[41].

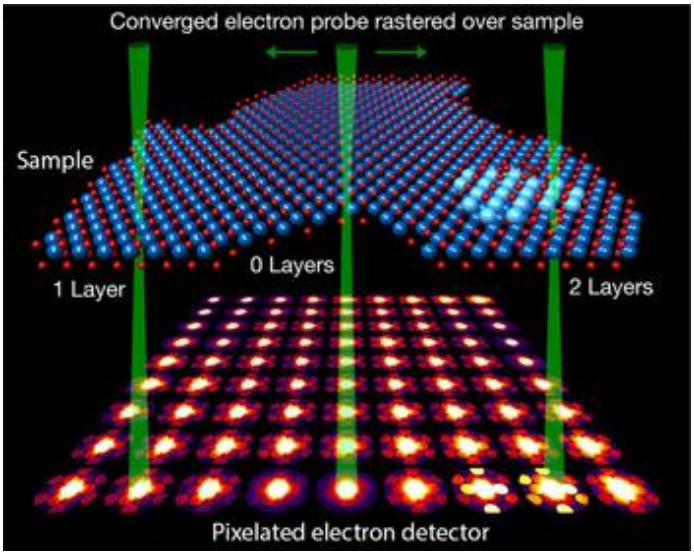

Figure 2.7 Illustration of experimental 4DSTEM of a 2D dichalcogenide flake. Green cones represent electron beam scanning across 1 layer, vacuum and 2 layers regions. Adapted with permission from[7]. Copyright 2019 Microscopy Society of American.

2.3 Imaging

Apart from electron diffraction, imaging morphological and atomic structures at low and high magnification, respectively, are fundamental functions for TEM.

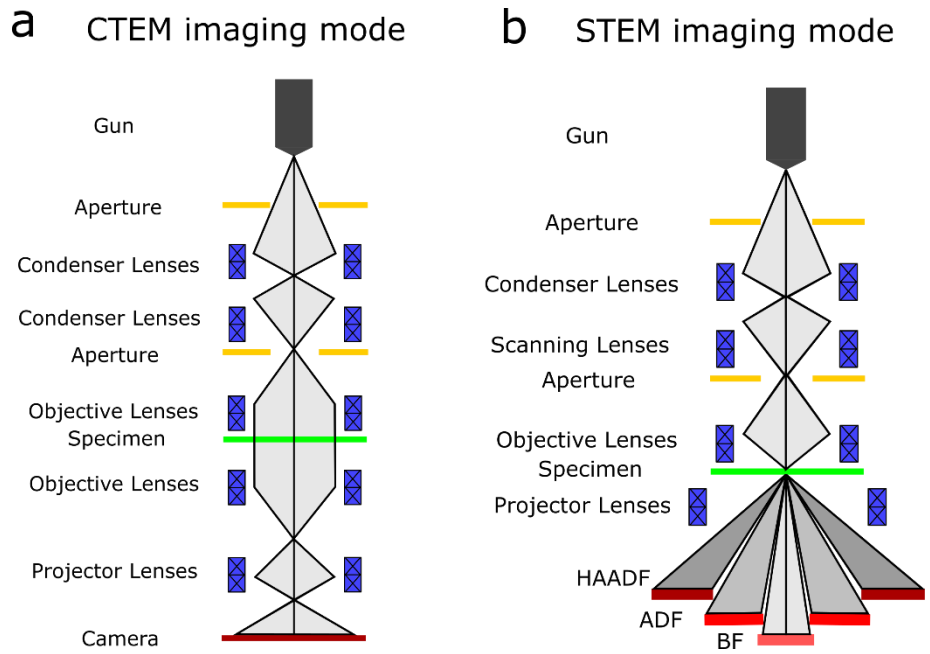

Figure 2.8 Schematics of (a) CTEM and (b) STEM imaging methods.

2.3.1 Conventional Transmission Electron Microscopy

Image contrast can be produced by various methods, such as amplitude contrast and phase contrast, to show the distinct specimen details on the image. In this section, we will discus the different mechanisms contributing to the images produced by the TEM in the CTEM mode in which the lens system casts a parallel beam onto the sample and then images can be recorded by the camera, typically a CCD as shown in Fig. 2.8a.

2.3.1.1 Bright Field and Dark Field TEM

Once the SAED pattern is acquired, we can use the objective aperture to select the transmitted spot or the diffraction spots on the back focal plane of the objective lens to produce a BF or a DF image, respectively, related to the amplitude contrast. In the BF image, a location where diffraction takes place appears dark, whereas a location where diffraction does not take place appears bright. In contrast with this, high (low) electron scattering regions of the specimen exhibit bright (dark) contrast in the DF image, and can be used to localise the specific specimen orientation, with the precise contrast behaviour dependent on chosen reflection $\boldsymbol{g}_{hkl}$. Combining BF and DF images is useful for analysis of lattice defects and crystal orientations. Fig. 2.9 b,c shows an example of BF and DF images of the $NiPS_3$ flakes.

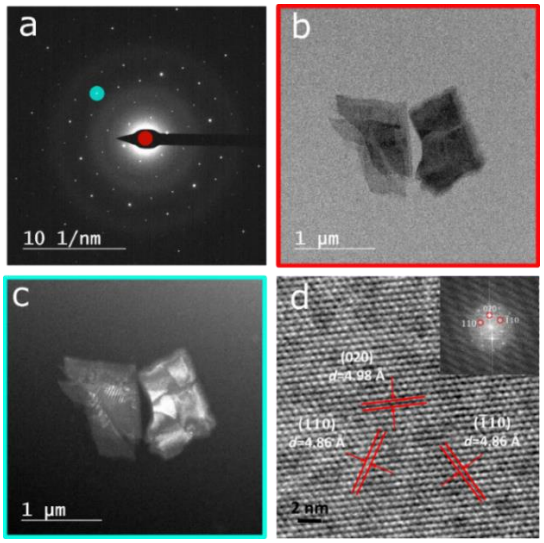

Figure 2.9 Bright field and dark field images of a $NiPS_3$ flake. The SAED pattern of the specimen is shown in (a) where red and cyan circles represent the positions of the objective aperture to produce the corresponding (b) bright field and (c) dark field images. (d) is a high-resolution TEM image showing the interplanar spacings of (110), $(1\bar{1}0)$ and (020) lattice planes and corresponding fast Fourier transforms (FFTs) in the inset. Adapted with permission from[25]. Copyright 2019 American Chemical Society.

2.3.1.2 High-Resolution TEM

The essence of forming high resolution (HR) TEM image is phase contrast, that originates from the differences in the phases of the scattered waves exiting from a very thin specimen which does not affect the amplitude of scattered electron wave, a condition known as the weak phase object approximation. To create phase contrast, multiple beams should be collected by the objective aperture, which is the main distinction to the amplitude contrast imaging. In general, more beams being collected is the requirement for acquiring high resolution images. The objective lens ,with a small spherical aberration, causes the interference between the transmitted and diffracted waves and the phase change of the diffracted waves is converted into the change of amplitude, producing the phase contrast that enables imaging of the crystal lattice at an appropriate defocus of the objective lens. However, interpreting HRTEM image is complex, since it is sensitive to the thickness, orientation, the scattering factor of the specimen and various imaging conditions. The exception is when the lattice image (shown in Fig. 2.9d, an HRTEM example of a $NiPS_3$ flake) is acquired at a specific defocus condition: Scherzer focus (Δf_{Sch}) is defocus value optimal for HR-TEM image contrast and is determined by the spherical aberration of the objective lens (C_s) and the accelerating voltage of the incident beam (λ)[8]:

$$\Delta f_{Sch} = -1.2(C_s\lambda)^{1/2} \tag{2.15}$$

Under this defocus condition, all the beams have nearly constant phase causing a long flat negative region in the phase contrast transfer function

(PCTF) extending to a higher spatial frequency where phase oscillations occur[42]. More details of the PCTF are discussed in section 2.3.2.1.

2.3.2 Scanning Transmission Electron Microscopy

In the STEM mode, the electron beam is converged by a series of lenses before arrives at the sample, as shown in Fig. 2.8b. With improvements in the design of electromagnetic lenses and the implementation of aberration correctors, the focused probe size on the order of ångstoms has become possible, even as low as 47 pm for the finest probe[43]. It directly determines the resolution of the STEM image. This converged beam is controlled by the scanning coils, and raster scans over an area on the specimen, so the scanned area is divided into rows of probe positions where the probe interacts with the specimen atoms. This produces scattered electrons at each position on the specimen, which are collected by electron detectors (typically BF, annular dark field (ADF) and high-angle annular dark field (HAADF) detectors) depending on the scattering angles of the scattered electrons.

The mechanism of image formation in STEM mode is discussed mathematically in this section. In order to simplify this description, a very thin crystal with a stationary crystal lattice is considered as the specimen interacting with the converged STEM electron probe, thus avoiding multiple scattering effects and thermal lattice vibrations.

Based on these assumptions, the wavefunction of a scattered electron recorded by any STEM detectors is a function of the illuminating probe position, $\mathbf{R}_p$, and is written as[44]:

$$\Psi_{\mathrm{f}}(\mathbf{K}_{\mathrm{f}},\mathbf{R}_{\mathrm{p}}) = \sum_{\mathbf{g}} \phi_{\mathbf{g}} A(\mathbf{K}_{\mathrm{f}} - \mathbf{g}) \exp\left[-i(\mathbf{K}_{\mathrm{f}} - \mathbf{g}) \cdot \mathbf{R}_{\mathrm{p}}\right] \quad (2.16)$$

where $\mathbf{K}_{\mathrm{f}}$ stands for the transverse component of the scattering vector $\mathbf{K}$, $\phi_{\mathbf{g}}$ represents the complex amplitude of the beam scattered to $\mathbf{g}$, $A(\mathbf{K})$ is the aperture function and $\exp(i\mathbf{K}_{\mathrm{f}} \cdot \mathbf{R}_{\mathrm{p}})$ represents a linear phase ramp due to the shift of the probe to $\mathbf{R}_{\mathrm{p}}$. This equation (2.16) generates a series of diffracted discs as shown in Fig. 2.10a and the intensities on different STEM detectors can be derived from it as is discussed in the following sections.

2.3.2.1 Bright Field STEM

Similar to the process of acquiring BF image in CTEM where an aperture is placed in the BFP, allowing only the direct beam through it into the imaging system, for BF STEM imaging we insert an electron detector onto the optical axis (Fig. 2.8b) to capture the directly transmitted electron beam at each scanned position on the specimen. The intensity of the scattering on the BF detector plane, I_{BF} can be simply written for a given $\mathbf{R}_{\mathrm{p}}$ as[44]:

$$I_{\mathrm{BF}}(\mathbf{R}_{\mathrm{p}}) = \left|\psi_{\mathrm{p}}(\mathbf{R}_{\mathrm{p}}) \otimes \phi(\mathbf{R}_{\mathrm{p}})\right|^2 \quad (2.17)$$

where $\otimes$ denotes a convolution operation. $\psi_{\mathrm{p}}(\mathbf{R}_{\mathrm{p}})$ is the complex amplitude of the STEM probe at the $\mathbf{R}_{\mathrm{p}}$ position and $\phi(\mathbf{R}_{\mathrm{p}})$ stands for a transmission function by assuming the sample is a weak phase object which operates a small phase shift, σV:

$$\phi(\mathbf{R}_{\mathrm{p}}) = 1 + i\sigma V(\mathbf{R}_{\mathrm{p}}) \quad (2.18)$$

where σ is the scattering interaction constant between specimen potential

and electron wave and $V(\mathbf{R}_\mathrm{p})$ is the electrostatic potential at the $\mathbf{R}_\mathrm{p}$ position[44]. Equation (2.17) is known as the coherent imaging model.

Considering the case shown in Fig. 2.10a where only the interference between the direct beam and the diffracted beams at +**g** and -**g** occurs at the detector, the wave (equation 2.16) arriving on the BF detector can be rewritten:

$$\Psi_\mathrm{f}(\mathbf{K}_\mathrm{f}=0,\mathbf{R}_\mathrm{p}) = 1 + \phi_\mathbf{g} \exp i\left[-\chi(-\mathbf{g}) + \mathbf{g}\cdot\mathbf{R}_\mathrm{p}\right] + \phi_{-\mathbf{g}} \exp\, i[-\chi(\mathbf{g}) - \mathbf{g}\cdot\mathbf{R}_\mathrm{p}] \quad (2.19)$$

Given the projected potential, V_g, being real, the intensity function on the detector is the modulus-squared of equation (2.19) and written as:

$$I_\mathrm{BF}(\mathbf{R}_\mathrm{p}) = 1 + 2\left|\sigma V_\mathbf{g}\right| \cos(\mathbf{g}\cdot\mathbf{R}_\mathrm{p} + \angle V_\mathbf{g}) \sin\chi(\mathbf{g}) \quad (2.20)$$

This equation results in a set of fringes due to the phase variation. $\angle V_\mathbf{g}$ is a phase of the potential at **g** controlling the position of the fringes, and a component $\sin\chi(\mathbf{g})$ determines the strength of the phase contribution. $\chi(\mathbf{g})$ is a wave aberration function, dominated by influences of the spherical aberration (C_s) and defocus (Δf) for an uncorrected STEM:[44]

$$\chi(\mathbf{g}) = \tfrac{1}{2}\Delta f \lambda \mathbf{g}^2 + \tfrac{1}{4}C_s\lambda^3\mathbf{g}^4 \quad (2.21)$$

where λ is the wavelength of the incident beam.

$\sin\chi(\mathbf{g})$ is known as the PCTF shown in Fig. 2.10b, relevant to the phase contrast both in the BF STEM and HRTEM imaging methods. The positive regions of the PCTF contribute to the bright contrast for the atomic sites while the negative PCTF values lead to the atomic site imaged dark. The first intersection between the function and the horizontal axis is called

First Zero, with its position determined by the C_s, λ and Δf. The inverse of the frequency at First Zero is the best possible interpretable resolution of the structural image. In order to optimise the imaging condition, an extended negative region of PCTF is preferred for a given amount of C_s and λ, and thus Scherzer defocus is preferred as mentioned in section 2.3.1.2.

2.3.2.2 Annular Dark Field STEM

In the STEM mode we often use annular dark field (ADF) detectors concentric to the optical axis to collect the diffracted electrons on the diffraction plane, while unscattered or weakly scattered electrons are excluded. In general, there are two predominant types of annular detectors collecting electrons at different angles: low angle annular dark field (LAADF) and high angle annular dark field (HAADF) detectors, each operating via different contrast formation mechanisms.

Compared to the BF detector, which is sensitive to the phase change due to its small detector size, an ADF detector usually averages data from a wide range of the interference fringes as shown in Fig. 2.10c and thus the coherent phase information is suppressed. The intensity of the ADF image can be calculated by convoluting the squared modulus of the probe wave function, $\left|\psi_{\mathrm{p}}(\mathbf{R}_{\mathrm{p}})\right|^2$, with an object function, O($\mathbf{R}$), and hence can be written as[45]:

$$I_{\mathrm{ADF}}(\mathbf{R}_{\mathrm{p}}) = \left|\psi_{\mathrm{p}}(\mathbf{R}_{\mathrm{p}})\right|^2 \otimes \mathrm{O}(\mathbf{R}_{\mathrm{p}}) \tag{2.22}$$

The object function represents the fraction of intensity from the scattering

centre that reaches the detector and this equation is known as the incoherent imaging model. Fig. 2.10b shows the optical transfer function (OTF) that represents the intensity strength monotonically decaying as the spatial frequency increasing, hence an ADF image does not show the contrast reversal that occur in HRTEM imaging. Additionally, because it only involves the intensities and is independent of the interference between scatterings, the ADF image is more directly interpretable than the BF image.

LAADF detector receives inelastically scattered and diffracted electrons at a range of 20 to 60 mrad (approximately) to produce a LAADF STEM image. An image is generated from the integrated intensities of the electrons at each incident beam position, exhibiting diffraction contrast from the Bragg diffraction beams. This mechanism enables us to obtain high-resolution images of the light elements and the strain field[41] in the species with high signal-to-noise ratio, attributed to strong elastically and inelastically scattered electrons collected at low angles.

In terms of the electrons scattered to high angle (60 - 200 mrad) collected by the HAADF detector, they can be considered particles in nature, and their scattering behaviours can described by the Rutherford model mentioned in equation (2.5), where the differential cross section is highly dependent on Z (being proportional to about $Z^{1.6}$- $Z^{1.8}$)[8]. This yields another contrast mechanism sensitive to the atomic number, and thus chemical composition, of the specimen. Hence it is often termed 'Z contrast' and allows a degree of chemical identification of atomic species via the HAADF STEM image intensity, shown for a copper sulfide (CuS) nanoparticle in Fig. 2.10e, f.

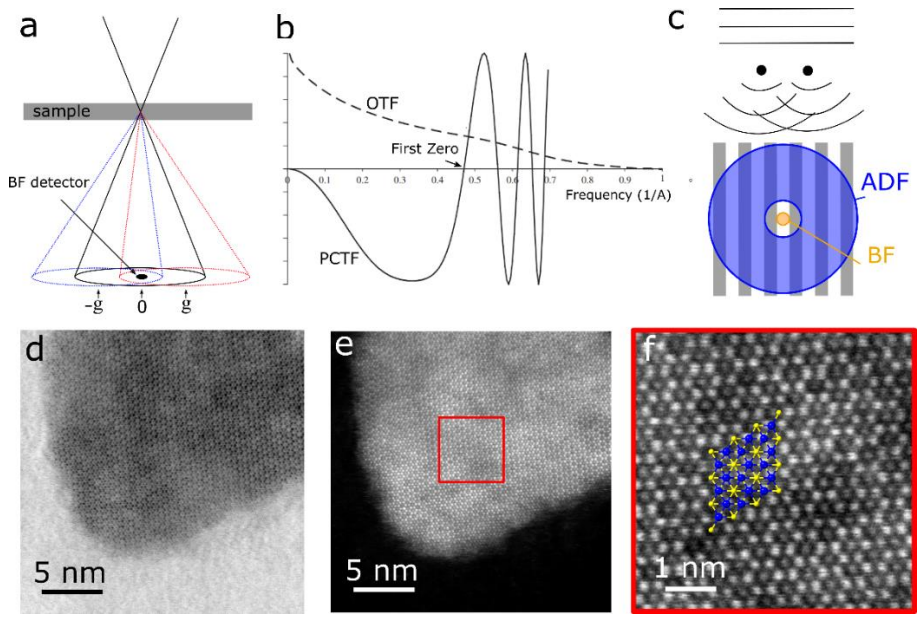

Figure 2.10 Schematics of STEM imaging theory and example images. (a) shows diffraction of the coherent STEM electron probe by a specimen resulting in three overlapping diffraction discs collected by a BF detector. (b) compares the incoherent OTF and coherent PCTF for identical imaging conditions (V = 300kV, C_s = 1mm, Δf = -40nm). (c) illustrates interference fringes produced by two illuminated atoms and the covered regions by BF and ADF detectors. (a-c) Adapted with permission from[44]. Copyright 2011 John Wiley and Sons. (d,e) show the BF and HAADF STEM images of an identical area of a CuS nanoparticle and a magnified area in (e) enclosed by a red square is shown in (f) overlaid with a CuS atomic model. In (f), Cu has higher atomic number than S, and thus Cu atomic columns are brighter than S in the image due to the Z contrast imaging mechanism.

2.3.3 STEM Image and Electron Diffraction Simulation

It has been demonstrated that a wealth of structural information can be acquired from the specimen by using STEM imaging. However, verification of this STEM findings requires additional analytical methods such as image simulation. As the speed of computational data progressing boosted in a rapid pace over the past decades, electron micrographs can be computed from first principles. Briefly, the wave function of the imaging

electrons may be computed based on the quantum mechanical description of the interaction between incident electrons and the atoms in the specimen. The two-dimensional intensity distribution in the final simulated image can be obtained with the known optical properties of the lenses in the microscope[46]. One of the major purposes for the image simulation in this work is to compare the simulated and experimental STEM images in order to describe the origin of anomalous features produced by lens aberrations or due to specimen artifacts. Multislice STEM image simulation is an efficient method to achieve this and is based on fast Fourier transform (FFTs) algorithm, significantly reducing computeation time, although the periodic potential of the specimen and electron wave function in the *xy* plane are needed.

The process of multislice STEM image simulation consists of the following steps[46]:

1. Divide the atomic model of the specimen into thin (n) slices along z axis.
2. Calculate the projected atomic potential ($v_{zn}(x)$) for each slice. Each slice must be thin enough to be a weak phase object and is typically one atomic layer of the specimen.
3. Calculate the transmission functions (2.23) which are different for each slice and derived from the atomic potential,

$$t_n(\boldsymbol{x}) = \exp\left[i\sigma v_{zn}(x)\right] \tag{2.23}$$

   where σ is the interaction parameter.
4. At a given probe position the electron wave function is $\psi_p(x, x_p)$.

5. Recursively transmit and propagate the probe wave function through each slice using FFTs by equation (2.24),

$$\psi_{n+1}(x,y) = p_n(x,y,\Delta z_n) \otimes [t_n(x,y) \times \psi_n(x,y)] \qquad (2.24)$$

where $\times$ denotes multiplication of the second expression by the first. $p_n(x,y,\Delta z_n)$ is a propagator function and Δz_n is the thickness of the slice. Repeat this process through all the slices until the wave function of the exit surface is acquired.

6. Fourier transform the ultimate transmitted wave function to get the wave function in the diffraction plane where the detector integrates the intensity of the wave function to generate a pixel intensity at the given probe position. The entire simulated image can be produced by iterating the calculation of the intensity of exit wave function in the diffraction plane for all probe positions on the specimen.
7. Repeat step 4 to step 7 for every beam position on the image grid.

The simulation process of electron diffraction is similar to the STEM image simulation and listed below[46]:

1. Divide the specimen into thin slice.
2. Calculate the projected atomic potential ($v_{zn}(x)$) for each slice.
3. Calculate the transmission function $t_n(\boldsymbol{x})$ for each slice.
4. Set the incident wave function $\psi_0(x,y) = 1$, due to the plane wave applied on the specimen in TEM mode.
5. Recursively transmit and propagate the incident wave function through each slice using FFTs by equation (2.24),

6. Fourier transform the wave function at the exit surface of the specimen $\Psi_n(k_x, k_y) = FT[\psi_n(x, y)]$.
7. The transformed wave function goes through the objective lens, thus multiples by the transfer function of the lens, $H_0(\boldsymbol{k})$ to acquire the wave function in the BFP $\Psi_i(k) = H_0(\boldsymbol{k})\Psi_n(k)$.
8. Calculate the square modulus of the wave function $\Psi_i(k)$ and the final electron diffraction intensity will be obtained $g(x) = |\Psi_i(k)|^2$.

2.4 Spectroscopy

Spectroscopic equipment for chemical analysis, such as energy dispersive X-ray spectroscopy (EDS, discussed in section 2.4.1) and electron energy loss spectroscopy (EELS, discussed in section 2.4.2), are commonly integrated in a modern TEM instrument for quantitative chemical or elemental analysis. These are usually performed in the STEM mode due to the higher spatial resolution that provides for spectroscopic analysis. These analytical techniques provide insight into the local chemical species, stoichiometry, electronic states within the specimen, based on the characteristic signals from the sample under electron illumination. These signals are produced by inelastic scattering between the incident electron beam and the electrons in the specimen. Contrary to the elastic scattering discussed in section 2.2.1, energy dissipation occurs in the inelastic interaction because of the Coulomb repulsion between the incident electrons and the core or outer shell valence electrons of the atoms in the specimen.

2.4.1 Energy Dispersive X-ray Spectroscopy

EDS provides the localized chemical information of the specimen by using the emitted X-ray signals from the interaction between sample atoms and the focused electron beam. Almost all element can be detected in principle excluding atomic number less than 4 (Be) because Li has very low energy of characteristic radiation that is not easily detected. H and He do not produce characteristic radiation at all. Qualitative analysis allows identification the elemental peaks present in the spectrum and quantitative analysis involves measuring the intensity of the peaks to know the composition of the specimen. In this thesis, EDS will exclusively refer STEM-EDS unless stated otherwise.

2.4.1.1 X-ray Emission

A solid sample bombarded by the incident electron beam produce two types of X-rays: characteristic X-rays and bremsstrahlung X-rays. The former signals are widely used for the chemical analysis, but the latter are usually considered as the nuisance needed to be filtered out for materials science purposes.

To produce a characteristic X-ray signal from a sample, a high energy beam electron interacts with a core-shell electron in the specimen and transfers a critical amount of energy to the core-shell electron. The core electron can then escape the attractive electrical field of the nucleus and leaves a vacancy in the core shell. This energy is called critical ionization energy (E_c) which must be significantly less than the beam energy (E_0) to

produce X-rays. For an isolated atom, the process will cause the atom to be excited to a higher energy state than before the interaction, known as ionized. Because this state is unstable, the ionized atom readily returns back to the ground state by filling the vacant site with an outer-shell electron accompanied by the emission of a characteristic X-ray as illustrated in Fig. 2.11a. The X-ray energy is equal to the energy difference between the core and outer shell and can be recorded by an EDS detector placed as close to the sample as possible. The emitted X-ray energy is characteristic of the electronic transition and this energy difference is unique to the atom, hence EDS is a powerful tool to identify elements. Fig. 2.11b shows the potential electronic transitions from the outer to inner shell and the conventional rule for naming them[13]. For instance, if a K-shell hole is filled by an electron from L-shell, the characteristic X-ray is called K_α X-ray. α_1 and α_2 are used to differentiate the subshells from which the L-shell electrons fall to the K-shell. Note that the atomic ionization may not occur in low-voltage SEMs due to the E_0 is close to E_c. But the very high ratio of E_0 (> 100 keV) to E_c (generally <20 keV) facilitates constant X-ray generation from the specimen under the electron beam.

Some incident electrons can penetrate through the electron cloud and interact with the Coulomb field of the nucleus of the atom, which induces a substantial change in the momentum and in the energy loss, resulting in the bremsstrahlung X-rays. Unlike the characteristic X-rays which show discrete peaks in the spectrum, the bremsstrahlung X-rays are distributed in a wide range of energies. They form a continuous spectrum which limits the detection of some weak (low signal-to-noise) characteristic X-ray peaks,

owing to the presence of 'background'.

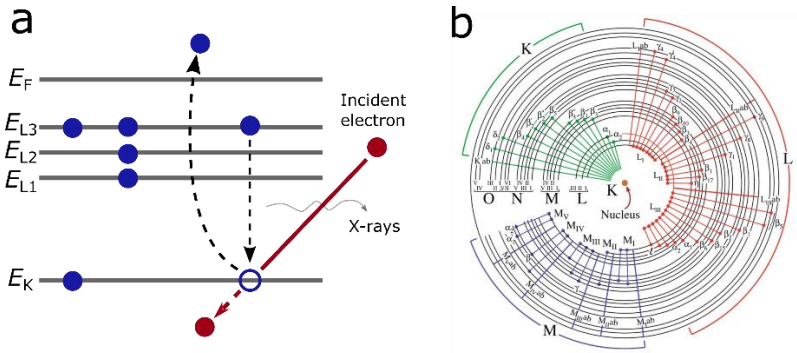

Figure 2.11 Energy dispersive X-ray spectroscopy in TEM. (a) shows the ionization process. An electron in the inner (K) shell is ejected to the vacuum by an incident electron and the left hole is occupied by the outer (L3) shell electron accompanied by emitting X-rays. (b) shows the possible electronic transitions and their names. Adapted with permission from[13]. Copyright 1996 Springer Science Business Media New York.

2.4.1.2 EDS Detectors

There are two types of detector commonly used for EDS: Si(Li) detector and silicon drift detector (SDD). The Si(Li) semiconducting detector (Fig. 2.12a) consists of Si doped by Li to generate an intrinsic Si region where any electron-hole pairs attributed to incoming X-rays are separated under an external bias. Electrons are attracted by a positive bias and accumulate on an ohmic contact. The detector then generates charge pulses proportional to the X-ray energy for further digitizing the signal and displaying in the computer. However, incomplete Li doping and additional coatings can form dead layers at the front and back side of the Si detector, leading reduced detection efficiency. The large anode also suffers from thermal noise unless liquid nitrogen cooling is supplied, but this may also cause the formation of ice or hydrocarbon contaminations in front of the detector.

The SDD detector consists of concentric p-doped Si rings implanted on n-type Si with a small anode in the centre of p-type Si rings for charge collection as shown in (Fig. 2.12b). This design benefits the detector in multiple aspects compared to Si(Li) detector with a large anode: the primary advantage is high throughput of X-ray counts due to the smaller anode of the SDD having lower capacitance than that of Si(Li). The other merits of the SDD design include low thermal noises and liquid nitrogen cooling being unnecessary.

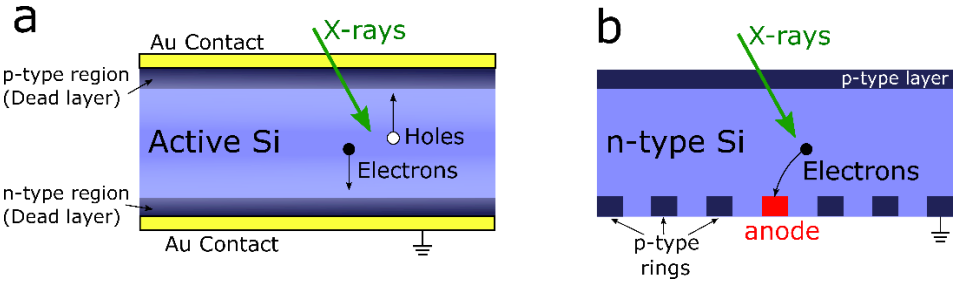

Figure 2.12 Schematic cross section images of (a) Si(Li) EDS detector and (b) silicon drift detector.

2.4.1.3 Artefacts in Qualitative EDS analysis

Currently, the EDS analytical software enable us to rapidly identify the peaks and their corresponding elements in the spectrum. However, a few artefacts raised by the EDS system cannot be neglected, since they may cause misidentification of peaks. Therefore, their principles are described in this section.

These artefacts are divided into two groups. The first is signal-detection artefacts, comprising escape peaks and the internal fluorescence peaks. The escape peak results from the imperfection of the detector: if the incoming X-ray energy (E) is higher than the ionisation energy of the Si as the major material of the detector, the intrinsic Si can be excited and

generate secondary Si Kα X-rays (1.74 kev). Therefore, the detector has to register an actual X-ray energy equal to (*E*-1.74) keV. The issue of the escape peak can be addressed by using the modern EDS analysis system which finds the escape peak and re-register it back to its characteristic peak. The internal fluorescence peak is attributed to the fluorescence of the Si in the dead layers by the incoming high energy X-ray, which results in the secondary Si Kα X-rays detected although there is no Si in the specimen. The thicker dead layers in the Si(Li) detector are chiefly responsible for this issue, which is not frequently observed in SDD, where dead layers are very thin.

The second type of artefact is related to signal-processing, for example sum peaks. This issue can be attributed imperfections in the intrinsic design and the electronics set up of the detector. During the EDS data collection, once a photon is collected by the detector, it will reject any other incoming photons as the signal-processing electronics digitise the photon until it assigned to the correct energy. This processing time is known as 'dead time'. However, it is possible to collect two photons at exactly same time and the processing electronics consequently register the doubled energy, giving a sum peak appearing at twice the energy of the characteristic peak.

2.4.1.4 Quantitative EDS analysis

The spectrum records the characteristic X-ray intensities, measured by counting photons for the elements in the specimen. In order to increase the accuracy, sufficient counts should be acquired for the qualitative and

quantitative analysis and the overall analytical accuracy of EDS is ±3-5%[13]. But the element may not be detected if concentration is lower than detection limits typically about 1000 ppm.

Background subtraction is the first step for EDS quantification. The background manifests as counts under the characteristic peaks in the spectrum, arising from the bremsstrahlung process as incident beam interacts with the coulomb field of the nuclei. Two methods can be performed to remove the background: 1. selecting appropriate windows on both sides of the peak to define the real peak regime and then estimating the total counts of the peak, and 2. modeling the bremsstrahlung distribution on the spectrum based on the expression developed by Kramers[47], which has benefits to spectra containing many adjacent peaks where the window selection technique is difficult.

The Cliff-Lorimer ratio technique was the first method introduced for quantitative EDS elemental analysis in 1975[48]. Considering a binary system consisting of two compositions C_A and C_B in a thin sample, their characteristic X-ray intensities (I_A and I_B) can be acquired by EDS detector. The relation between the compositions and intensities can be written as:

$$\frac{C_A}{C_B} = k_{AB}\frac{I_A}{I_B} \tag{2.25}$$

where k_{AB} is the k-factor (or Cliff-Lorimer factor). Acquiring an accurate k-factor is essential for the accurate elemental quantification. Theoretical calculation from first principles is a straightforward method for estimating k-factors, but is also associated with relatively high systematic errors (±15-20%), affecting the quantitative result, due to the combination of uncertainties in Q and in the detector parameters (ε) in the k-factor

expression (2.26) that cannot be measured accurately[49,50]:

$$k_{AB} = \frac{(Q\omega a)_A}{(Q\omega a)_B} \frac{A_B}{A_A} \frac{\varepsilon_A}{\varepsilon_B} \tag{2.26}$$

Where the subscripts denote elements A and B. A is the atomic weight of element, Q stands for the ionization cross sections which is strongly affected by accelerating voltage, a is relative transition probability, and ω and ε represent fluorescence yield and detector efficiency, respectively. The quantities a, ω and ε are also dependent on atomic number. k-factors also can be determined experimentally with the relative errors of approximately $\pm 1\%$ for more accurate quantification[51,52]. We usually compute the k-factors for different elements by comparing them to a standard such as silicon (k_{Si}).

However, the previous Cliff-Lorimer equation (2.25) is not perfect to quantify the chemical compositions in the specimen due to the absorption of X-rays by the materials themselves (especially for thick TEM specimens) during EDS acquisition is neglected, resulting in the detected X-ray signals being less than the generated X-ray signals and thus C_A is not proportional to I_A. To address this an absorption correction factor (ACF) is built in to the k-factor equation[13]:

$$\frac{C_A}{C_B} = k_{AB}(\mathrm{ACF})\frac{I_A}{I_B} \tag{2.27}$$

The Zeta (ζ) factor method is a newer method for EDS quantification developed in 1996[53]. It assumes that the mass-thickness ρt (ρ and t are the density and thickness of the specimen, respectively) is proportional to various factors including the X-ray intensity, I_A, normalised by the composition, C_A, and the total electron dose illuminating on the specimen,

D_e, and thus ρt is written as[54]:

$$\rho t = \zeta_A \frac{I_A}{C_A D_e} \tag{2.28}$$

where

$$\zeta = \frac{M_A}{N_0 Q \omega a [\Omega / 4\pi] \varepsilon} \tag{2.29}$$

where M_A is atomic weight, N_0 is Avogadro's number, Q is the ionization cross-section, ω is the fluorescence yield, a is the relative transition probability, Ω is the detector solid angle, ε is the detector efficiency. The advantage of this method is ζ-factor can be determined from a pure element standard with given thickness, rather than a multi-element standard used in the k-factor method. Additionally, if the ζ-factor is known, the sample thickness can be calculated by equation (2.28).

2.4.1.3 STEM-EDS Spectrum Imaging

EDS signal can be acquired simultaneously while STEM imaging with the high spatial resolution, thus it is very useful not only in elemental identification, but also in visualizing the local elemental distribution. At present, it has been widely implemented to demonstrate elemental variation for complex materials such as core-shell nanoparticles[55], elemental segregation[56] and precipitates[57], known as EDS spectrum imaging. It is an advanced technique where the whole EDS spectral information is collected from each pixel of a STEM-EDS spectral image (i.e. STEM and EDS have the same resolution), resulting in a three-dimensional data set consisting of two dimensional compositional maps and a one dimensional EDS spectrum at each beam position point[58]. Compared to the conventional EDS analysis,

this spectrum image has a wealth of data allowing flexible data processing, and avoids interpretation mistakes due to the completeness of data[59].

Fig. 2.13a-c shows examples of EDS spectrum images acquired from a potassium doped molybdenum disulphide (K_xMoS_2) flake sample, where the different elemental distributions are obvious from the individual maps. The intensity in the map originates from the number of X-ray counts at a specific energy detected in the pixel positions, and thus the brighter pixels indicate regions rich in a specific element. Note that in order to show the continuous elemental distribution and increase the signal to noise ratio in the specimen, the raw maps with the size of 1024 × 1024 pixels were binned down to 53 × 53 pixels maps with pixel size of 34.2 nm as shown in Fig. 2.13a-c, and then the background surrounding the flake was subtracted by a masking algorithm. More details of image and data processing are discussed in Chapter 5. The EDS spectrum (Fig. 2.13d) comes from integrating intensities over all the pixels of the flake in Fig. 2.13a-c. It confirms the presence of Mo, S and K in the sample, but also unwanted species of Si and C from sputtering of the ceramic heater of the heating chip, and O from hydroxide contaminations. Other common elements present in the spectrum including Cu or Au from the TEM support grid, Fe or Co in the pole-piece, Si or Pb from the EDS detector[60].

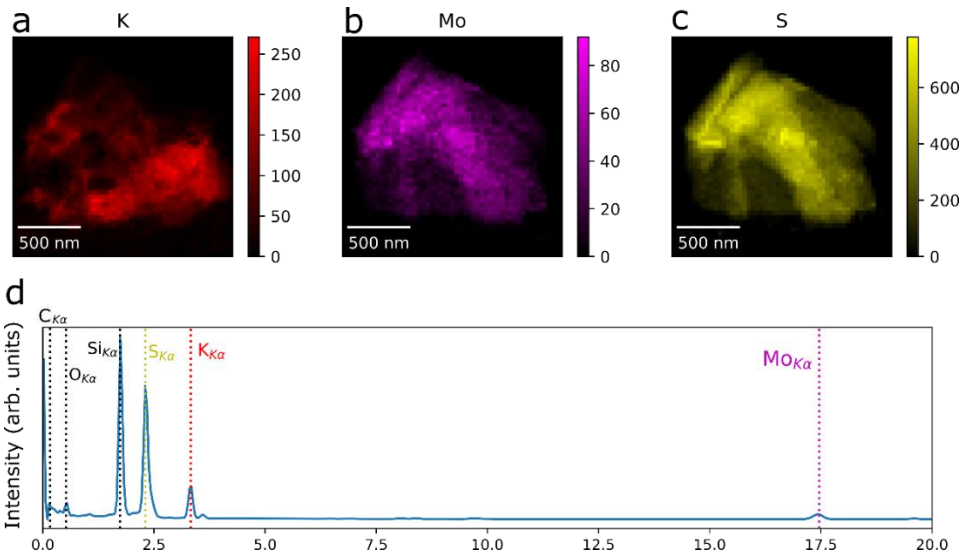

Figure 2.13 EDS spectrum images of a K_xMoS_2 flake. (a-c) shows the EDS element distribution of K, Mo and S in the specimen, and an integrated EDS spectrum of X-ray signals in all pixels is presented in (d)

2.4.2 Electron Energy Loss Spectroscopy

EELS is another important chemical analysis technique that measures the energy distribution of the inelastically scattered primary electrons after they have undergone energy loss events and their deflections during interactions with the specimen atoms. An electron spectrometer, placed on the exit side of the sample and along the optic axis, collects the transmitted inelastic electrons. The energy loss provides a tremendous amount of information about the local environment of atoms and electrons in the sample, revealing their bonding state, nearest-neighbor information, dielectric response, free electron density, bandgap structure, as well as the thickness of a specimen[13]. However, consequently EELS acquisition and analysis requires more expertise than EDS acquisition in most cases.

Generally EEL spectra are divided into two regimes based on the electron energy: low-loss spectra (< 50eV) and core-loss spectra (> 50eV),

each of which provides different information about the specimen. Fig. 2.14 shows two partial spectra recorded at low energy loss and from 600 to 800 electron volts extracted from a single region of interest.

The most intense peak in the low-loss spectrum (Fig. 2.14a) is the zero-loss peak, occurring at 0 eV, which shows the integrated intensity of the unscattered electrons (transmitted beam) and the elastically scattered electrons. It can be used to calibrate the energy offset of the whole spectrum if there is significant energy drift. At a slightly higher energy loss range there is a broad peak representing a plasma resonance of the valence atoms. The chemical information provided in this region is related to the dielectric properties of a material, such as the band gap and the surface plasmon response.

In the higher energy loss region (core-loss spectrum, Fig. 2.14b), the spectrum exhibits characteristic features termed ionization edges. These edges originate from the same process that is mentioned in the X-ray emission in section 2.4.1.1 where core shell electrons are ejected by incident electrons and the atom is ionized. However, instead of considering the emitted X-ray, we now consider the inelastically scattered incident electron which loses a characteristic amount of energy for different elements, forming the ionization edges in the EELS spectrum (Fig. 2.14b). This can be used for analysis of many chemical elements and is particularly useful for the lighter elements such as Li[61,62] that are not detectable in EDS because the weak X-rays of Li are absorbed by the materials or the window of the EDS detector. Quantitative analysis is also available, since the edge intensities are proportional to the concentration of the corresponding

elements, but there are some challenges for EELS quantification such as the accurate background fitting, the variation of specimen thickness and the edge overlaps[20].

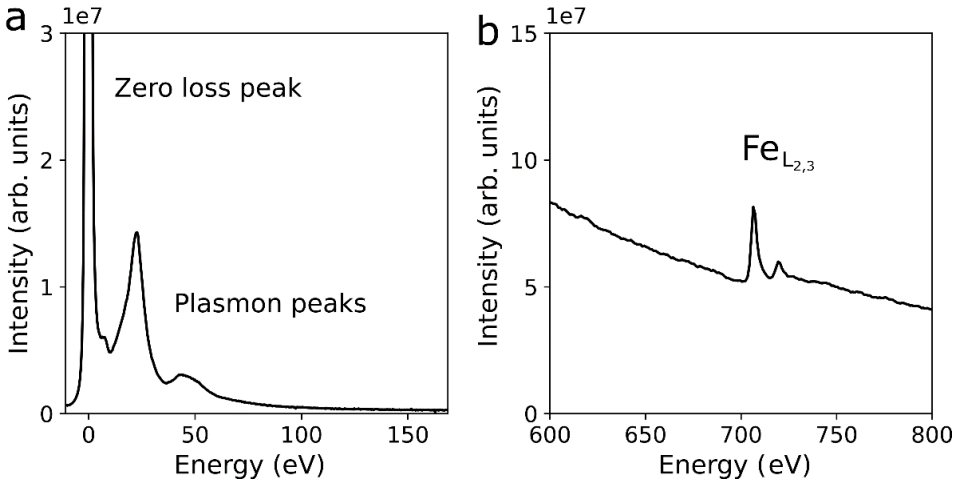

Figure 2.14 EELS spectrum of a $FePS_3$ nanoflake. (a,b) show low-loss EELS and core-loss EELS, respectively. Note that S and P edges are not present in (b), since their major edges ($L_{2,3}$) local at 165 and 132eV. respectively.

2.5 *In-situ* TEM E-chips and Holder

In-situ TEM is an advanced technique that allows researchers to study materials in real time and under real-world conditions. It provides dynamic observations of physical behaviours of the materials in response to external stimuli such as biasing or heating, atmospheric pressure and liquid suspension[63]. Thus information regarding the structural and chemical changes that occur under these conditions can be extracted by *in-situ* TEM, providing insight into dynamic process associated with phase transition[64], catalysis[65] and crystal growth[66] at the nanoscale, which cannot be easily accessed by the traditional TEM. In my research, I employed a commercial *in-situ* TEM holder (Fusion, Protochips) equipped with heating/biasing E-

chips to study K-intercalated MoS_2 samples at elevated temperatures and Eu intercalation in bilayer graphene under applied voltage. This section demonstrates the basis of the *in-situ* TEM holder and the E-chip.

2.5.1 Thermal E-chip

The thermal E-chip, as shown in Fig. 2.15a, provides a platform for precise temperature control, low drift, heating up to 1200°C with the rate up to 1000°C/ms[67] while TEM imaging. It consists of a silicon carbide (SiC) membrane supported over an etched Si window 300-500μm^2 in a silicon substrate. Nine holes with the diameter of 8μm located in the centre of the SiC window provide an electron transparent region for optimal imaging conditions. To support specimens with smaller sizes, a holey carbon film with 2μm holes is coated on the membrane. Resistive heating can be induced when electrical current is passed through the membrane and a uniform heating area is created in the membrane as illustrated in Fig. 2.15b[68,69]. Each thermal E-chip is individually calibrated before the experiment to correlate the measured resistance to the measured heater temperature. The key difference between the SiC and conventional metal heating technology is that the cold resistance of the metal heater is only a few hundred ohms or less and changes only a few hundred ohms during heating, and thus a 4-point resistance measurement is required to accurately measure the temperature variation. The SiC heater is 10× more sensitive to local temperature changes than a metal heater, since it has much higher cold resistance, therefore only a 2-point resistance measurement is need to monitor the temperature. Additionally, the SiC heater is very stable at high

temperature and it will not react with the specimen, undergo electromigration or melt.

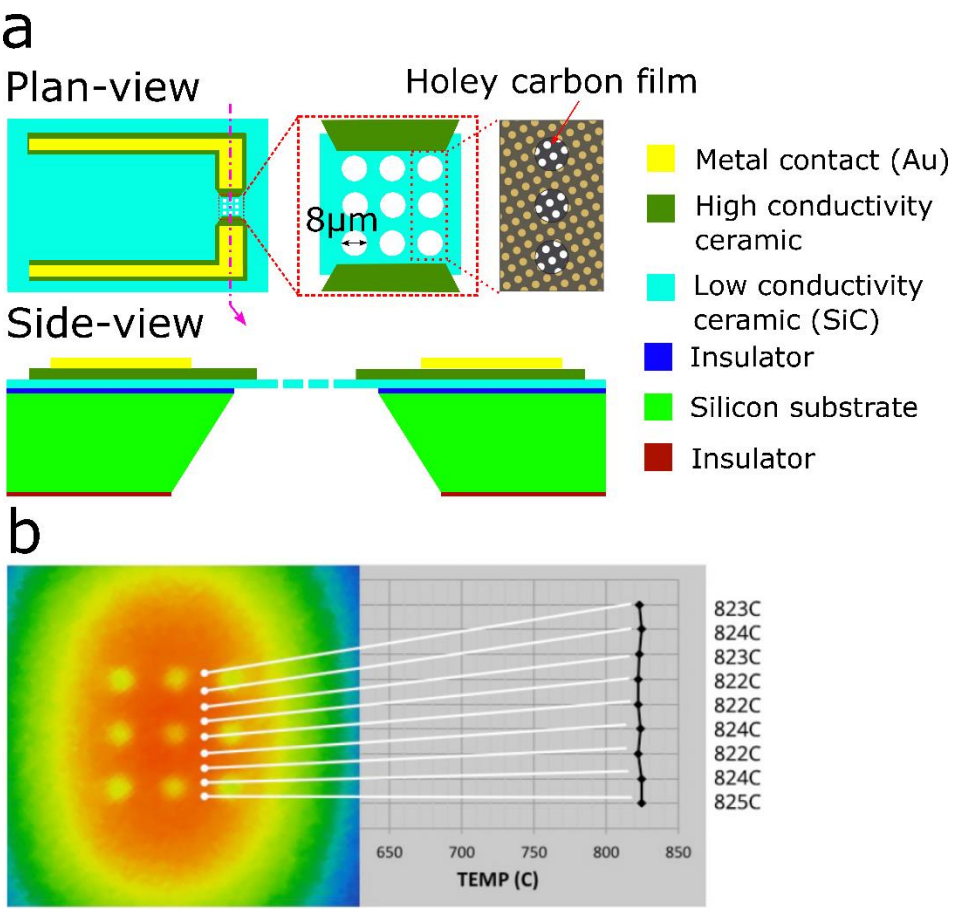

Figure 2.15 Schematics of thermal E-chip. (a) shows the plan-view and side-view of the thermal E-chip and the magnified inspection area containing nine holes covered by holey carbon film. (b) shows the thermal image demonstrating uniformity of SiC heater (Courtesy of Protochips Inc.).

2.5.2 Electrical E-chip

The electrical E-chip used in this project has the configuration shown in Fig. 2.16a which is comprised of a silicon nitride membrane on an etched silicon substrate and four gold contacts, through which electrical stimulation can be delivered to the sample. There are nine holes in the centre of the inspection window without coating of the carbon film which would affect the flatness and attachment of the bilayer graphene for this

project. The electrical E-chip can be employed for various specimens such as nanowires, carbon nanotubes and layered materials.

2.5.3 *In-situ* TEM Holder

The *in-situ* TEM holder (Fig. 2.16b) has a special tip (Fig. 2.16c) compared to standard TEM holder. There is a spring-loaded module with six pins to provide the electrical connection and to securely fix the E-chip on the holder. This module is also wire linked to the connection port at the end of the holder which is used to link the holder to an external power supply.

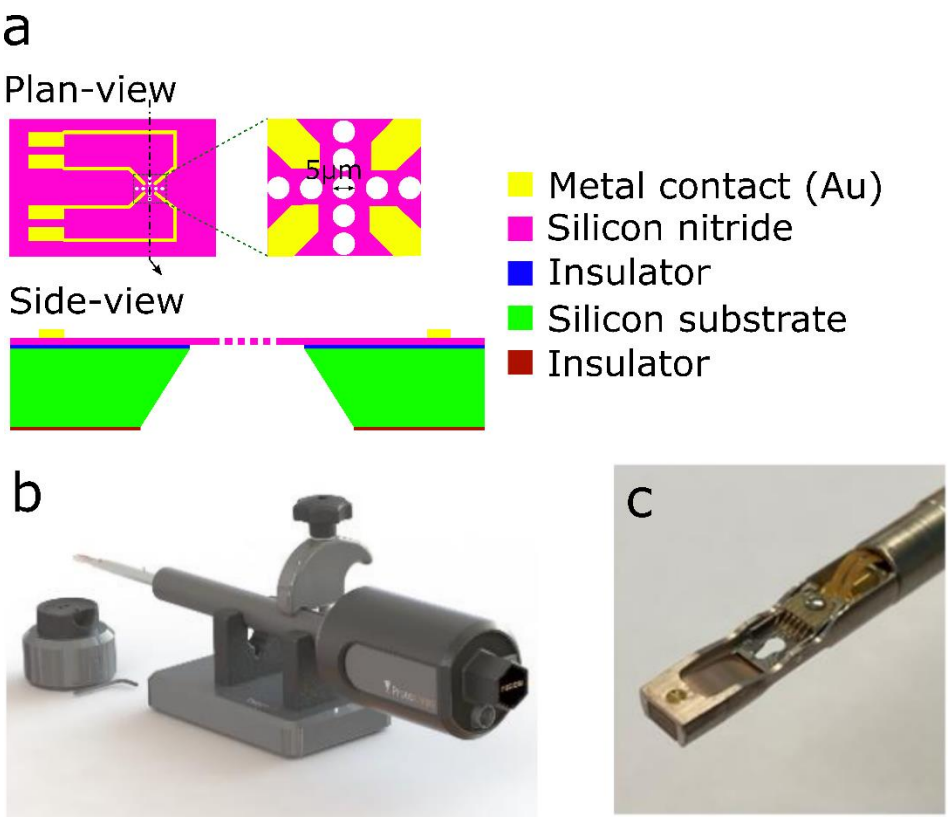

Figure 2.16 (a) Schematic of the electrical E-chip and (b-c) images of *in-situ* TEM holder.

2.6 Beam Damage Mechanism

In order to acquire images or spectra with the high signal to noise ratio, high electron fluence is often required to generate enough scattering between the incident beam and the specimen. However, it may also change the structure and chemistry of susceptible materials so that the examined material differs from the intended specimen[70]. Radiation damage of materials by the high energy electron irradiation cannot be neglected for TEM imaging and spectroscopy. In particular, the aberration corrected S/TEM allows even more electron current to be focused into a smaller beam. There are two predominant means by which the beam damage occurs, the first is knock-on damage, and the second is radiolysis[71,72]. Note that beam damage can be deliberately used to manipulate the structural or chemical of materials, such as localized oxidation[73] and to induced phase transition of two dimensional materials[74]. This section discusses the mechanisms of these two forms of the beam damage, accompanied by the discussion of potential strategies for reducing the effects of beam damage.

Knock-on damage refers to the atomic displacement resulting from elastic scattering. There is no energy loss in elastic scattering so that the incident electron transfers an amount of energy to the atomic nucleus based on conservation of energy and momentum. Those transferred energy is positively correlated to the angle of elastic scattering and negatively correlated to the atomic weight. Therefore, for high angle elastic scattering, especially where the species has low atomic weight, the transferred energy

may exceed the displacement energy of the atom, which depends on the bond strength, the crystal lattice and the atomic weight[71]. This atom is ejected from its lattice site forming an interstitial atom or adatom, which a complementary atomic vacancy at the corresponding lattice site. If the displaced atom is entirely ejected from the material in particular for atoms at the surface, this displacement is known as the electron beam sputtering. Knock-on damage can be avoided by reducing the accelerating voltage of the electron source below the threshold energy of the material for the atomic displacement. Single layer two-dimensional materials are typically imaged under 80kV accelerating voltage to reduce knock-on damage. For example, the threshold sputtering energy for graphene and carbon nanotube perfect crystal are 80kV[75] and 86kV[76], respectively. The knock-on threshold for the S atom in MoS_2 is 77kV[77].

Radiolysis occurs during inelastic scattering where the electron beam ionizes an atom and breaks the chemical bonds with neighbouring atoms, resulting in phase changes and bond scission. Radiolysis is not a very severe issue for the conductive materials (e.g. metals and graphite) because the empty vacancy left by an ejected electron in the valence band can be filled very rapidly by the conduction electrons before deterioration happens[72]. However, for insulating or semiconducting materials, for example polymers, radiolysis-induced bond breakage rapidly leads to a loss of short- or long-range order, crystalline decomposition and shrinkage or distortion of the specimen[71]. Reducing the specimen temperature is an ideal approach to overcome the radiolytic damage in organic materials by using cryo-protection[78] to reduce the atomic mobility and thus the

structural damage and mass loss[78,79]. In addition radiolysis is generally effective less at high accelerating voltage, due to the damage cross section inversely varies with the accelerating voltage[79].

Chapter 3

Crystallography of van der Waals Materials and Superstructures

Few-layer van der Waals materials have attracted enormous academic and industrial attention since the first isolation and characterisation of graphene in 2004[80]. These layered crystals consist of the robust in-plane bonds and the weak van der Waals interaction between adjacent layers. Therefore, various thinning approaches, such as the mechanical exfoliation[80] and the liquid-phase exfoliation[81] can be employed to break weak interlayer bonds and to produce the single or few-layer crystal having a typical thickness of a few ångstoms and lateral dimension of tens of microns, leading to these materials also being known as two dimensional (2D) materials[80,82-84]. There is a wide variety of 2D materials other than graphene for instance hexagonal born nitride (hBN), transition metal dichalcogenides (TMDCs) and Mxenes which exhibit unusual physical and chemical properties compared with their counterpart bulk crystals[85-89] and hence 2D materials possess a promising potential of applications in various fields, such as the miniaturized electronic and optoelectronic[90-92], high energy storage device[93,94] and chemical nanoreactor or catalyst[95].

3.1 Graphene

Graphene, a one atom thick layer of graphite, was presumed not to exist in nature, since it was believed to be thermodynamically unstable and tended

to form curved carbon (C) allotropies for example fullerenes and nanotubes or to decompose due to the melting point rapidly deceasing as the thickness[87]. However, the theory was defeated by Novoselov et al. in 2004 who isolated and characterised graphene mechanically exfoliated from the high ordered pyrolytic graphite (HOPG) by a Scotch tape[80]. It presents unique physical properties compared to its bulk counterpart and the investigation of the 2D materials still vigorously flourished until now.

Graphene consists of C atoms packed into a 2D honeycomb lattice (Fig. 3.1a-b), where each C atom is sp^2 hybridised to three equivalent orbitals, 2s, $2p_x$ and $2p_y$, orienting in three directions 120˚ with respect to each other. Thus each C atom can form in-plane covalent σ-bonds with three adjacent others corresponding to the C-C bond with the length of 1.42Å, giving graphene superior strength-to-weight ratio and an incredible high Young's modulus (~1TPa)[96]. A free p-orbital, $2p_z$, forms the out-of-plane π-bond which produces the weak van der Waals interaction between layers in graphite and contributes to the extraordinary electronic properties of graphene.

In the electronic band structure of graphene, the valence (π) and conductive (π*) bands coincide at six corners (**K** and **K**' points) of the hexagonal Brillouin zone and form a conical Fermi surface near the **K**/**K**' points (Fig. 3.1c-d). This intersection points are known as the Dirac points and the conical structures near the points are named the Dirac cones[97,98]. The linear dispersion near the Dirac point results in the charge carriers (holes and electrons) behaving as massless Dirac Fermions, leading to numerous unusual phenomena such as ultra-fast mobility of the charge

carriers independent of the temperature[80,98], quantum Hall effect and Berry's phase in graphene[99].

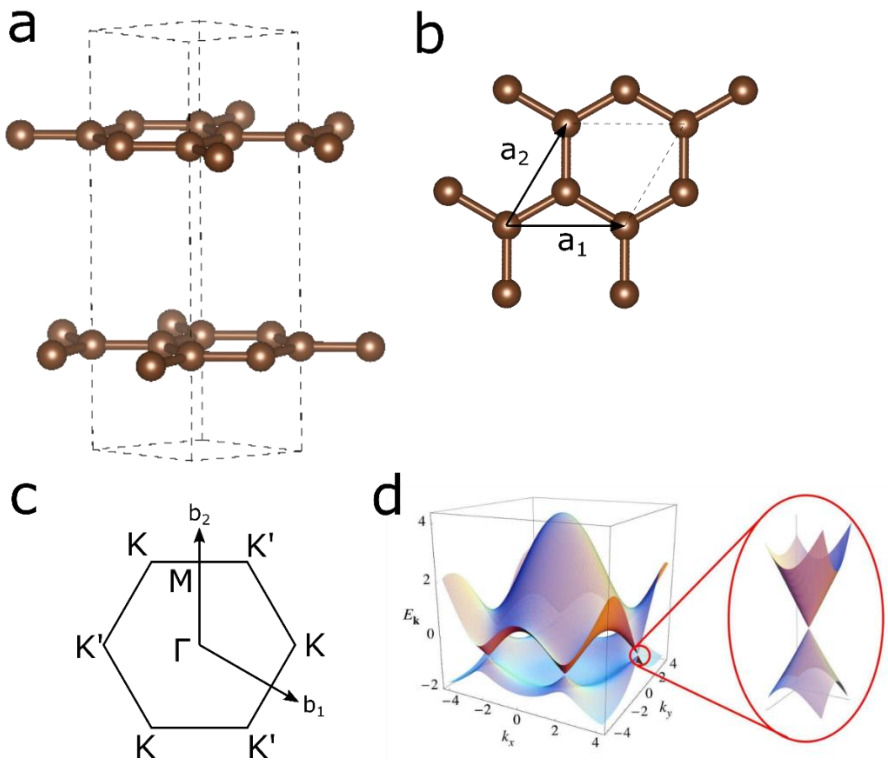

Figure 3.1 Structure and dispersion relationship of graphene. (a) shows the side view of Bernal stacked bilayer graphene and the plane view of one graphene layer is illustrated in (b). The dashed lines depict the unit cell of graphene with the atomic lattice vectors, $\mathbf{a}_1$ and $\mathbf{a}_2$ shown in (b). First Brillouin zone of graphene is shown in (c) where the reciprocal lattice vectors are $\mathbf{b}_1$ and $\mathbf{b}_2$. (d) illustrates the meeting point of conduction and valence bands of graphene with zero bandgap at the Dirac point. The inset shows a magnified the Dirac cone with the linear gradient. (c, d) are adapted with permission from[97]. Copyright 2009, American Physical Society.

3.2 MoS_2

Similar to the graphite, molybdenum disulfide (MoS_2) is also one of the family members of the van der Waals layered crystal and composed by parallel stacked few atomic-thick layers with the weak van der Waals interaction between them. Each layer of MoS_2 consists of a thin sheet of

Mo sandwiched by two layers of S atomic sheets, with covalent bonds connecting atoms within the layer[100]. According to the arrangement of the chalcogen to the transition metal atoms, MoS_2 is defined to different polytypes or phases. The most stable one in nature is 2H (hexagonal) MoS_2 where sulfur atoms triagonal prismatic coordinate around the Mo atoms giving a space group: $P6_3/mmc$ [194] as shown in Fig. 3.2a, having stacking order of AbA, BaB, AbA… where the upper and lower cases stand for relative position of S and Mo atoms, respectively[90,101]. The number 2 in the name stands for the number of layers in a unit cell. The lattice parameters of 2H phase is a=3.15Å, c= 12.30Å[102] and it is a semiconductor[103,104], but the nature of its band gap tends to transit from indirect (1.29 eV) to direct (1.9 eV) as the thickness of MoS_2 down to monolayer[105,106], raising the interests in the electronic and optoelectronic device development[90]. 3R (rhombohedral, shown in Fig. 3.2b) polytype has the same trigonal prismatic coordination of Mo atoms like the 2H phase but has different stacking order of AbA, BcB, CaC, AbA… resulting in a unit cell consisting of three layers. Additionally, it also has the similar crystallographic parameters[107] and electronic properties (semiconductor with indirect bandgap 1.29eV) with 2H polytype[108].

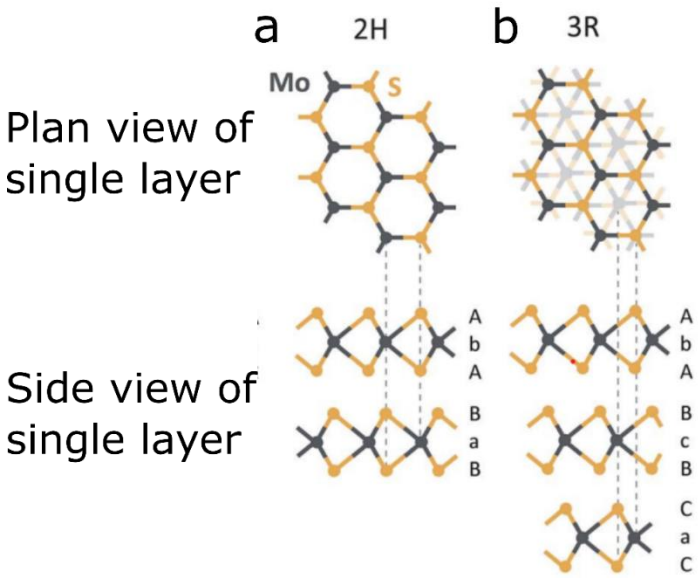

Figure 3.2 Schematic crystal structures of (a) 2H and (b) 3R MoS_2 polytypes. Adapted with permission from[109]. Copyright 2015, The Royal Society of Chemistry.

3.3 Superstructures in Layered Materials

These intriguing properties of graphene and MoS_2 have been summarized in comprehensive reviews. One of the most promising strategies to tailor the properties even further is to fabricate the superstructures comprised either by two dissimilar layered materials or by a layered material subject to a periodic perturbation and each component in the superstructure contributes their characteristics to the entire system[110]. There are various approaches to build the superstructure such as vertical assembling the different layered materials[111,112], twisting layers to form Moiré pattern[113], strain-engineered layers[114] and synthetic layered superstructures by the intercalation process[115]. Note that only the crystallography of the alkali ion intercalation compounds is introduced in this section, since the others are not relative to this project. More structural variations occurring in intercalation process are also discussed in Chapter 4.

3.3.1 Graphite Superstructures

Intercalated alkali ions regularly stayed over the centres of carbon hexagons to minimized the free energy of the system, and depending on the alkali metal there are two types of stacking correlation between the graphene layer to the ordering intercalant shown in Fig. 3.3[116]. The superstructure of K intercalated graphite intercalation compound (GIC) and Rb-GIC shown in Fig. 3.3a has four equivalent origins (α, β, γ and δ) of the GIC unit cell, being notated as $p(2\times2)$R 0° superstructure with the in-plane lattice constant of $2a_0$ (a_0=2.46 Å is the graphite in-plane lattice constant), and p and R 0° denote the primitive unit cell rotating 0° with respect to the graphite unit cell. In the Li-GIC and Cs-GIC a different superstructure was found as shown in Fig. 3.3b where the primitive unit cell only has three equivalent origins (α, β and γ) and rotates 30° with respect to the graphite unit cell so that it is notated as $p(\sqrt{3}\times\sqrt{3})$R 30°.

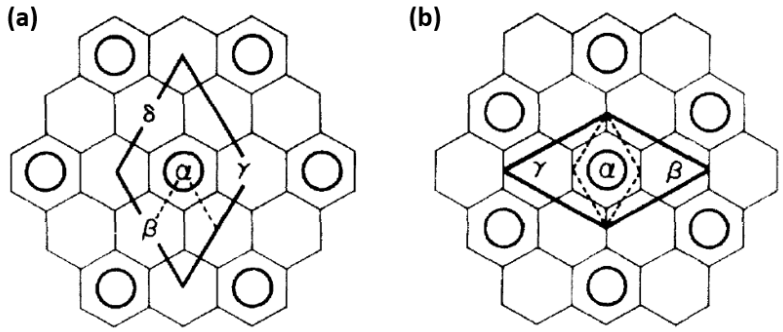

Figure 3.3 Schematic in-plane superstructures of alkali ion intercalated graphite. (a) $p(2\times2)R\,0°$ for K-, Cs- and Rb-GICs and (b) $p(\sqrt{3}\times\sqrt{3})$R 30° for Li- GICs. C atoms occupy the corners of each hexagonal position in the graphite layer, and open circles show the projected α intercalant layer onto the graphite layer. Dark lines denote a unit cell of the superlattice structure, while the dashed lines denote a graphite unit cell. Adapted with permission from[116]. Copyright 1980, American Physical Society.

For the GICs with stoichiometries of C_6Li and C_8X (X=K, Rb and Cs) i.e. each interlayer spacing of the graphite is occupied by a layer of intercalant, the same pattern as the pristine graphite (Fig. 3.4a) can be acquired from the alkali intercalated graphite, if the graphite layers are commensurate with intercalant layers which are ordering in the specific $\alpha, \beta, \gamma, \delta$ (or α, β, γ) sequence (Fig. 3.4) for K and Rb (or Li and Cs) at a relative low temperature (about 110 K)[116-118]. The missing of the superlattice reflections is because the calculation of the structure factor demonstrates the cancellation of the superlattice spots in the diffraction pattern[116,117]. Additionally, some alkali GICs, e.g. Rb[116], need to be annealed following the intercalation procedure to achieve a sufficient homogeneity of the desired intercalant sequence in the graphite crystal at the low temperature so as to produce the graphite pattern in the Rb-GIC. On the other hand, increasing the temperature of the GIC can break the characteristic ordering to form a random stacking sequence of the intercalant layers or incommensurate intercalant structures in the graphite crystal, resulting in the superlattice spots (Fig. 3.4b) or rings (Fig. 3.4c) superimposing on the graphite pattern, respectively[116,117].

Some complex diffraction patterns of the superstructures were acquired from K-, Rb- and Cs- GICs at specific temperatures[116,119]. At 170 K, two groups of hexagonal superlattice reflections emerged around the graphite diffraction spots and rotated $\pm 19.1°$ with respect to the graphite reciprocal lattice spot (Fig. 3.4d). Its corresponding superstructure in real space was deduced to have 14 C atoms and 1 alkali ion in a unit cell with the lattice constant of $\sqrt{7}a_0$ and hence is notated as $p(\sqrt{7} \times \sqrt{7})R\ 19.1°$

shown in Fig. 3.4e[116,119]. As the temperature increased over 170 K a more complex diffraction pattern was observed as shown in Fig. 3.4f, indicating structural transition to a new superstructure which consisted of the superposition of $h(\sqrt{12}\times\sqrt{12})R\ 30°$ (Fig. 3.4g)[120] and $o(\sqrt{39}\times\sqrt{39})\ R\ (16.1°, 43.9°)$ (Fig. 3.4h)[116]. However, some reflections of this pattern were not interpreted by authors due to the complexity.[116] Further increasing the temperature of TEM examination induced the formation of the ring patterns for the higher stage GICs resulted from the coexistence of multiple phases incommensurate with the graphite crystal[121,122].

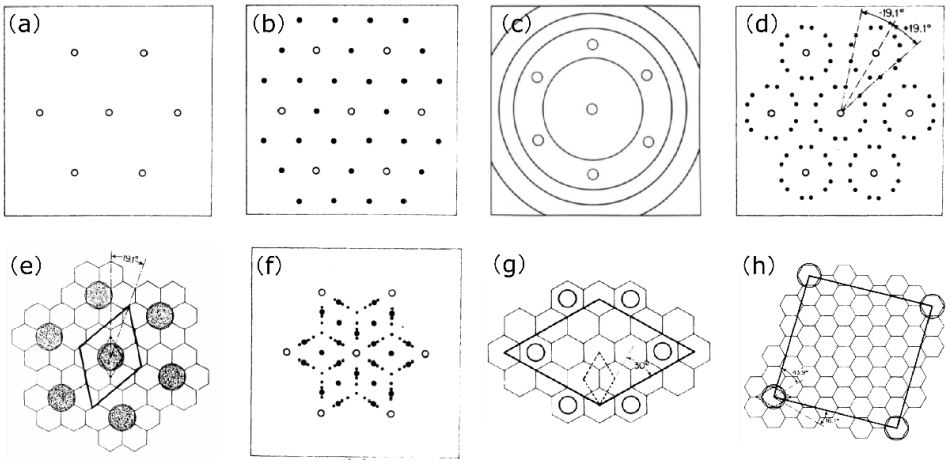

Figure 3.4 In-plane electron diffraction schematics of alkali GICs. (a) stage 1 alkali GICs where intercalant layers are strictly in sequence. (b) stage 1 alkali GICs with the random intercalant sequence. (c) a ring pattern superimposes on the pristine graphite pattern resulting from multiple incommensurate phases coexisting in the host interlayer spaces. (d) complex electron diffraction patterns observed in $C_{24}Rb$ at low temperature (T<170K). (e) a real space superlattice reflecting the electron diffractions of (d) where hexagons are graphite lattice and shadow circles stand for the Rb ions. (f) a schematic representation of the diffraction pattern for the stage-2 Rb-graphite sample heated at T (170 < T < 620 K). (g) and (h) show two known superstructures ($h(\sqrt{12}\times\sqrt{12})R\ 30°$ and $o(\sqrt{39}\times\sqrt{39})R\ (16.1°, 43.9°)$) that contribute to the diffraction pattern in (f). (a-b, d-h) Adapted with permission from[116]. Copyright 1980, American Physical Society. (c) Adapted with permission from[117]. Copyright 1979, Elsevier B.V.

3.3.2 MoS_2 Superstructures

Intercalated alkali metal prefer to occupy the octahedral sites of the MoS_2 and donates an electron to the host[123], resulting in the S atomic layer gliding along one direction[74,124] and the phase transition from 2H to 1T (tetragonal)[125,126], and hence the arrangement of S atoms becomes to an octahedral coordination around the Mo atoms with the space group of: $P\bar{3}m1$ [164] shown in Fig. 3.5b,g and l. Note that 1T polytype has stacking order of AbC, AbC… and it has almost the same lattice parameters with 2H and it was first synthesised by Wypych F. et al. in 1992[127]. The 1T phase can be retained even after alkali ion deintercalation[128,129], which is the primary approach to prepare the 1T phase MoS_2. However, 1T phase is not stable and simultaneously tends to form the 1T' because of clustering of the transition metal atoms within a layer[130,131]. In 1T' phase shown in Fig. 3.2c,h and m the adjacent Mo atomic rows form zig-zag chains across the layer resulting in the superstructure with lattice parameters of $2a \times a$ in ab plane of a hexagonal system (or a $\sqrt{3}a \times a$ superstructure in an orthorhombic system) which doubles the lattice constant of the 1T (a) in one direction[74,132,133], Mo atoms also can tetramerize to diamond-shape clusters to form another distorted 1T phase (1T") which has the lattice parameter of $2a \times 2a$ in ab plane shown in Fig. 3.5d,i and n[132]. 1T"' is a new distorted phase harvested in a recent work where this new distorted structure is a $\sqrt{3}a \times \sqrt{3}a$ superstructure of 1T MoS_2 composed by the trimerized Mo atoms and the neighbouring two trimers share one Mo atom as illustrated in Fig. 3.5e, j and o[134]. Distorted Mo lattice causing

distinguished superstructures of 1T', 1T'' and 1T''' results in the appearance of superlattice reflections in the electron diffraction pattern[135] and there is no doubt that these distinct structures of 1T lead to different electronic properties compared to 2H. The experimental studies and first-principal calculations suggested 1T, 1T' and 1T'' are metallic,[128,136,137] while 1T''' is a semiconductor with a band gap of 0.65 eV[134]. More details of the structural transitions between the MoS_2 superstructures induced by alkali ion intercalation are reviewed in Chapter 4.

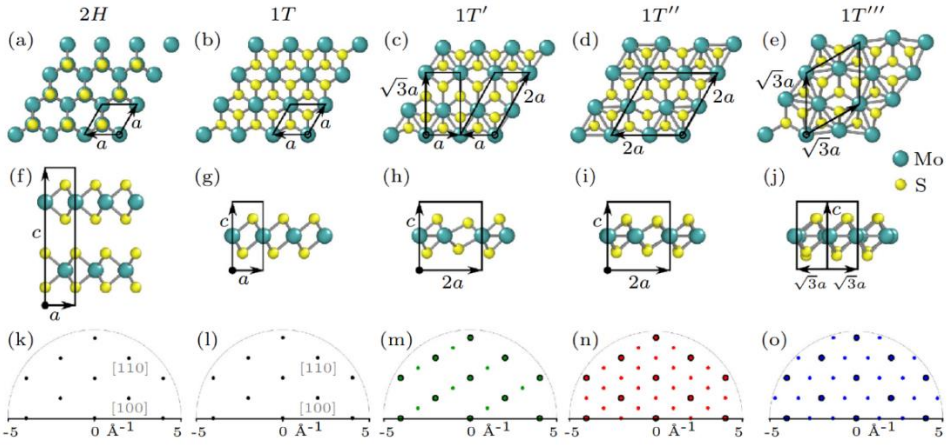

Figure 3.5 Crystal structures of MoS_2 polytypes and their corresponding electron diffraction patterns. (a-e) and (f-j) shows the plan views and side views of the unit cell for 2H, 1T, 1T', 1T'' and 1T''' MoS_2, respectively. Solid lines illustrate the regimes of the unit cell and arrows exhibit the lattice vectors of the unit cells. (k-o) are the simulated diffraction patterns of the polytypes of MoS_2. The superlattice reflections originated from the distorted structures are highlighted by green, red and blue dots in (m-o), respectively. Adapted with permission from[135]. Copyright 2020, American Physical Society.

Chapter 4

Alkali Ion Intercalation in van der Waals Materials

Despite the unique intrinsic properties of 2D materials, numerous tuning approaches are employed to yield more attractive outcomes. Some common modification methods include heterostructure building[138], intercalation or doping[139], twisting stacks[140] and dimensional sizing[141]. Among these modification methods, intercalation is a process where foreign species intercalate in the interlayer galleries of the host material and is a unique avenue for changing the properties of the pristine 2D materials, because:

1. Intercalation-induced structural changes or superior properties are usually reversible[62,142]

2. The degree of intercalation can be easily controlled by chemical reaction time or electrochemical voltage[143,144]

3. The intercalation process can be monitored by various *in-situ* techniques to unveil the associated dynamics[64,145]

4. Intercalation-induced structural or electronic variations drastically influence the applications of 2D materials[146,147]

Alkali metals are one of the most common intercalants for applications involving layered materials for multiple reasons. They provide a valence electron, allowing tuning of the band structure and induction of

a phase change in the host, a property that has been widely investigated for production of the charge density wave and applications in superconductivity and catalysis[101,147-152]. Additionally, the alkali ion intercalation process promotes structural changes, which can aid in the performance of high energy density batteries[153-155] and to facilitate high-yield liquid phase exfoliation of 2D materials[156-158].

However, many fundamental questions regarding the intercalation phenomenon in van der Waals materials remain unanswered, and explorations with new approaches are required for further development of intercalated systems for future applications. Over the past few decades, intense research has been directed toward comprehensive understanding of the intercalation of layered materials in their bulk form. This has produced new insights into existing structural variations, for instance the staging transition in carbon isotopes[41,159,160], the phase transition of TMDCs[127,134,137] and the formation of new superstructures. Such information is vital in enabling further improvement of advanced functional materials with the superior properties. In this literature review, we introduce two types of host materials in the intercalation studies of layered materials: graphite/few-layer graphene and MoS_2, and summarize the basis of alkali metal intercalation theories based on the experimental and theoretical results. Finally, we report recently significant progresses in the structural characterisation of the intercalation process in the layered materials using various techniques, such as transmission electron microscopy (TEM) and X-ray diffraction (XRD).

4.1 Alkali Ion Intercalation Approaches

4.1.1 Gaseous Intercalation Method

The gaseous intercalation method, also known as the two-zone vapour transport method, is the most common method to prepare the intercalated graphite[161,162] and MoS_2[163] through vaporization of the alkali metal. This intercalation process can effectively be controlled by changing the temperature, regulating the vapour pressure of the intercalant and thus controlling the thermodynamics of intercalation[161]. Fig. 4.1a shows a schematic of the experimental setup where the graphite and the intercalant are separately heated at T_g and T_i, respectively. The amount of intercalant uptake is determined by the temperature difference (T_g - T_i) between two chambers[161]. The smaller value of the temperature difference corresponds to the lower stage intercalation compound i.e. higher intercalation degree as shown in the bottom of Fig. 4.1a. Note that T_g in general should be kept higher than T_i to prevent the intercalant condensation on the sample and this intercalation method must be conducted in vacuum or inert gas to avoid the oxidation and contamination of the alkali metal[161].

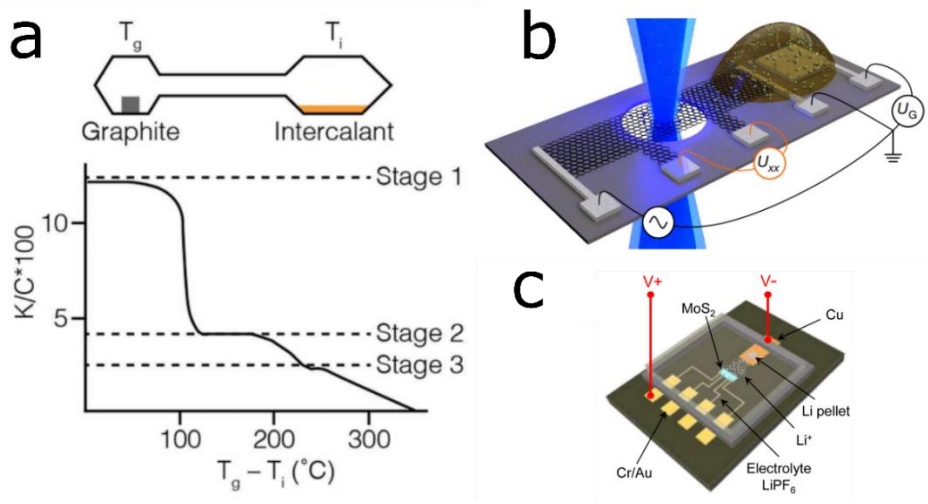

Figure 4.1 Schematics of gaseous and electrochemical intercalation methods. (a) Schematic of the gaseous intercalation method where T_g and T_i indicate the temperature of the graphite and intercalant, respectively. Bottom panel: staging phenomenon of K-intercalated graphite versus temperature difference (T_g-T_i). Adapted with permission from[161]. Copyright 2002, Taylor & Francis. (b) Electrochemical nanodevice applied in the *in-situ* TEM characterisation. The blue cones stand for the electron beam. Adapted with permission from[62]. Copyright 2018, Springer Nature Limited (c) Electrochemical cell fabricated for *in-situ* study for the optical property. Adapted with permission from[164]. Copyright 2015, American Chemical Society.

4.1.2 Electrochemical Intercalation Method

Electrochemical intercalation is an alternative technique for achieving reversible intercalation in the layered materials, where an external voltage or current drives the intercalation or deintercalation process. There are two types of electrochemical intercalation: 1. alkali cations from the electrolyte migrate to the cathode during intercalation driven by the external electric field, and 2. ionization of the alkali metal at the cathode and subsequent intercalation of said ions into the cathode structure[165]. The degree of intercalation is controlled by an external source and the amount of intercalant can be estimated by calculating the amount of charges

transferred between the foreign species and the host[166].

The electrochemical method benefits from *in-situ* intercalation studies and Fig. 4.1b,c show two examples of nanodevices designed for investigating the Li intercalation behaviours in bilayer graphene[62] and the optical properties of Li intercalated MoS_2[164], respectively. In the former, the authors used a bilayer graphene flake etched into a Hall bar shape which was supported by a Si_3N_4-coated Si substrate shown in Fig 4.1b. One end of the bilayer graphene was connected to an electrolyte containing the Li salt, which allows Li ions to migrate towards or away from the flake based on the applied voltage (U_G) - giving control over the reversible intercalation process. A thin layer of SiO_x encapsulated the solid-state electrolyte of the cell to prevent from outgassing and oxidation. Two electrodes extending from the tips of the hall bar were used to measure the resistance of the system during lithiation and delithiation. In the latter case (Fig 4.1c), the design and working principles of the electrochemical device are similar, but with different components, and so will not be described any further.

4.1.3 Liquid Phase Intercalation Method

Liquid phase is the simplest intercalation method, where the host is immersed in a solution containing the guest species, for example intercalated graphite prepared in liquid ammonia containing the alkali metal (Li, Na, K, Rb, Cs), where the alkali ions can gradually intercalate into the layered material.[161] The intercalation degree is controlled by the immersion time and the concentration of alkali ions in solution[166]. However,

this process is time-consuming (about a few days)[165]. Further details of the synthesis of intercalation compounds through the liquid ammonia is introduced in the Chapter 5.

4.2 Intercalation Kinetics

4.2.1 Charge Transfer

Charge transfer, referring to the exchange of electrons between the host and the intercalant, is a crucial driving force for the donor- or acceptor- type of guest intercalation in van der Waals materials[166]. Hence, a deeper understanding of the charge transfer is needed to rationalize the electrical, thermal and chemical properties of intercalated materials[167]. For donor-type compounds, such as alkali metal-graphite intercalation compounds (GICs), the mechanisms of charge transfer have been established via experiment or density functional theory (DFT) studies. Semi-metallic pristine graphite with a narrow band gap has a low density of states (DOS) near the Fermi energy level, shown in Fig. 4.2a[168]. Once an alkali metal intercalates into the interlayer spacing, the graphite π-bands overlap with the bands of the intercalant, and one electron in the *s*-valence band of the alkali metal transfers to the graphite so called 'donors'. This substantially affects the electronic band structure and increases DOS around the Fermi energy (E_F) of the graphite to accommodate the additional charge, illustrated in Fig. 4.2b-c. The computed electronic structures of K-GICs and Li-GIC indicate that their E_F shifts due to the contribution of electrons from the K and Li metals. However, the effect of charge transfer on the

electronic structure of the host differs for distinct intercalant elements[169]. In the projected DOS of K intercalated GICs, both the 2*p* orbital of carbon atoms and the 3*p* orbital of K ions are localized at the valence band, pushing the E_F of the graphite to a higher level as in Fig. 4.2b. On the contrary, the 2*s* orbital of Li appears at a low energy level in the conduction band, inducing a blue shift of E_F shown in Fig. 4.2c. These computational outcomes indicate the primary interaction between the K and C are entirely ionic, but there is a relatively weak covalent binding between Li and C[168,170]. By employing a different DFT calculation approach, Wang et al. demonstrated that K and Li are both entirely ionized in the host without the covalent bonding character, which is attributed to the similar DOS distribution near the Fermi energy in their study[171]. Experimental X-ray Raman spectroscopic results also demonstrate a substantial charge transfer from Li to the graphite and the ionization of Li in GICs[172,173]. Furthermore, electrochemical intercalation has been used as method to quantify the charge transfer, based on the assumption that the number of the charges donated to the host are equal to the charges flowing in the circuit[166]. Intercalants also can also acquire electrons from the host known as 'acceptor-type' compounds. Examples of this include PF_6^-, $TFSI^-$, ClO_4^-, etc. in intercalated graphite[174], but they are not demonstrated in this thesis and thus not reviewed here.

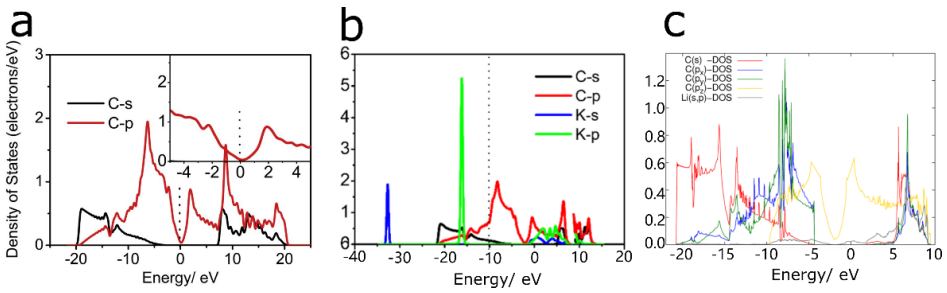

Figure 4.2 Electronic structure of pristine graphite and alkali ion intercalated graphite. Projected density of states (PDOS) of (a) graphite (Inset: a window of ±5 eV around the Fermi level of (a)), (b) KC_8. Adapted with permission from[168]. Copyright 2014, American Chemical Society. (c) LiC_8, respectively, with Fermi energy set to zero. Adapted with permission from[170]. Copyright 2016, Elsevier Ltd.

In the case of MoS_2, the intercalation scenario is different in which only the donor intercalants can be taken up by the host, due to the repulsion between the negative charges on the chalcogen layers and on the acceptors[175]. Considering alkali ion intercalation, donated electrons from *s*-valence bands of the guest are primarily added in the *d*-bands of the transition metal upon intercalation, since the empty or partial filled *d*-bands are the lowest unoccupied energy levels[175]. A large fraction of alkali valence electrons transfer to the host MoS_2, resulting in several effects on the intercalation compound, including the stabilization of certain phases over others and the strengthening of weak interlayer bonding to Coulombic forces from van der Waals forces, and hence increasing the coupling between layers[175].

Intercalation-induced superconductivity and structural phase transition are explicit proofs of the charge transfer from the alkali intercalants to the host TMDCs. The band structure of MoS_2 is demonstrated in Fig. 4.3a where the valence band of MoS_2 is based primarily on the *s* and *p* orbitals of the S anion, the conduction band is made up of the Mo cation's *s* and *p* orbitals, and the transition metal *d* and

p orbitals are indicated by the non-bonding bands. The Fermi level lies in the gap between the filled d_{z^2} and the *d/p* bands. Once an alkali metal intercalates into MoS_2, the conduction band of the intercalant overlaps with the unfilled *d/p* bands of MoS_2, resulting in the charge transfer to the host and forming a metallic species shown in Fig. 4.3b, with a drastic increase of the free electron charge density[163]. This shifting Fermi level into a region with the high density of states is thought to be the primary reason for superconductivity in the intercalated MoS_2[163]. Additionally, the phase transition of MoS_2 induced by the charge transfer is demonstrated by crystal field theory, illustrated in Fig. 4.3c-e, where the donated electrons from alkali metals transfer to the host and occupy the Mo $4d_{xz}$ and $4d_{x^2-y^2}$ orbitals, leading to an unstable crystal lattice which has a metallic character. Then a phase transition from hexagonal (H) to tetragonal (T) occurs in order to increase the stability of the structure, so that 2H phase transforms to 1T as a result of alkali ion intercalation of MoS_2[126].

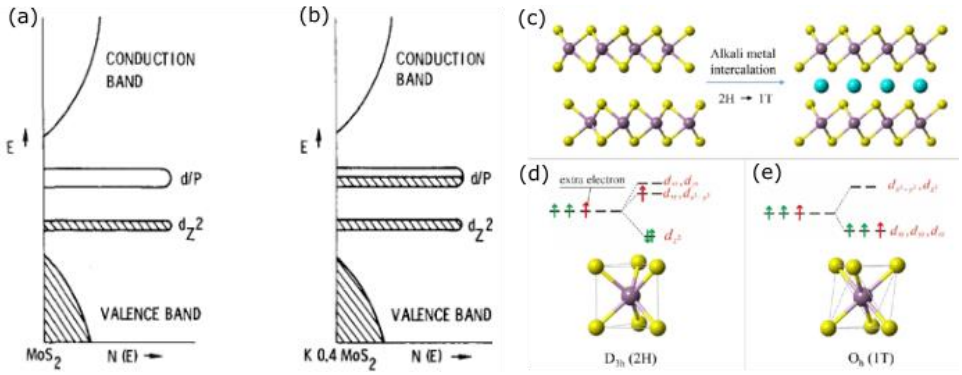

Figure 4.3 Schematic of intercalation-induced changes of the MoS_2 band structure and phase transitions. (a) and (b) illustrate the band structure of MoS_2 before and after alkali metal intercalation. (c) illustrates the intercalation resulting in the phase transition, and (d, e) show a demonstration of the phase transition mechanism based on the crystal field theory. (d) Mo 4*d* orbitals of 2H phase split into 3 groups whereas only d_{z2} is fully occupied. The red arrows show the donated electron from the alkali intercalant. (e) Mo 4*d* orbitals of 1T phase split into 2 groups where Mo $4d_{xy,yz,xz}$ orbitals are occupied part of their orbitals such that the incoming electron can fill the Mo $4d_{xy,yz,xz}$ orbitals to stabilize the 1T phase. (a-b) adapted with permission from[163]. Copyright 1973, AIP Publishing. and (c-e) adapted with permission from[126]. Copyright 2011, American Chemical Society

4.2.2 Alkali Ion Diffusion in Layered Materials

4.2.2.1 Diffusivity Estimation via Fick's Law

Alkali ion diffusion into the interlayer spacing of the layered host has been identified as the rate-controlling step for the intercalation processes[169]. The ideal rate of alkali ion diffusion in a few-layer flake with a finite lateral size can be estimated by Fick's first law (equation 4.1) for an electrochemical system:

$$\Delta r^2 = 4D\Delta t \tag{4.1}$$

where r is the lateral size in polar coordinates, D is the diffusion constant and t is charge and discharge time[166]. Based on the assumptions of ions entering the layered materials only at edges and no grain-boundary

transport occurring, Stark M. et al. found the dependency of the diffusion time (charge and discharge time) to the lateral size of the layered materials (2.5 nm to 100 μm) by calculating the different diffusion coefficients of ions within the electrode[166]. Intercalation time dramatically decreases with materials size, with a diffusion constant illustrated in Fig. 4.4a. However, this diagram is an estimation, as it regards the solid-state host and electrolyte as the primary contributors to the charge/discharge rates but neglects the existence of the solid electrolyte interface, which is known to be a rate-limiting step within the electrochemical system[166]. The diffusion coefficients of K and Li in graphite were estimated using a theoretical hopping model calculation, indicating that K has a higher diffusion constant (2.0×10^{-10} m^2 s^{-1}) than that of Li (1.5×10^{-15} m^2 s^{-1}) in graphite, so that K-GIC may be a better selection for the anode[176]. However, experimental studies of K intercalation in graphite have drawn opposing conclusions, since some issues were neglected in the DFT simulations, such as interactions at surface sites and interfaces of GICs, which may hinder the K kinetics in graphite[177,178].

Achieving high diffusion coefficients for alkali ions in graphite at room temperature is one of the key goals for accelerating charging/discharging rates of commercial Li-ion battery electrodes. Ultrafast Li diffusion was discovered in bilayer graphene with the chemical diffusion coefficient (D) of up to 7×10^{-9} m^2 s^{-1}, calculated by Fick's second law (equation 4.2) with the charge-carrier density (n) and the diffusion distance (x):

$$\frac{\partial n_{\mathrm{Li}}}{\partial t} = D \frac{\partial^2 n_{\mathrm{Li}}}{\partial x^2} \qquad (4.2),$$

This quantity is multiple orders of magnitude higher than that in graphite at room temperature (Fig. 4.4b)[179]. The authors also experimentally demonstrated that Li only intercalates in between bilayer graphene instead of residing on the intact surface (i.e. absence of defects)[179]in agreement with the *ab initio* calculations[180], since intercalation in between graphene is energetically favourable[181]. Nonetheless, Li diffusion on the graphite surface is possible with a relative high diffusion rate (5×10^{-10} m^2 s^{-1}) at room temperature[181].

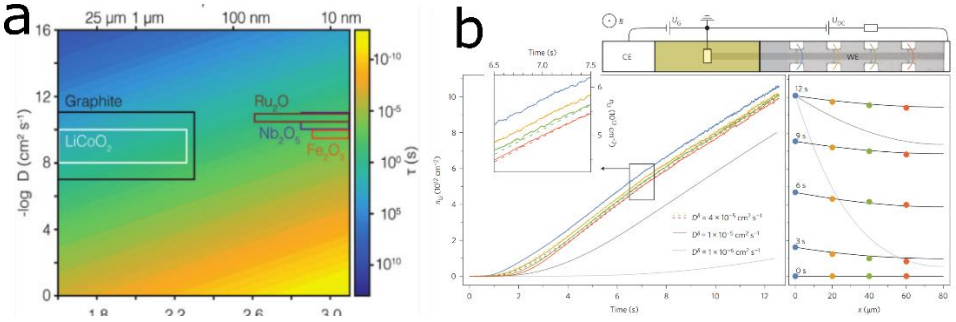

Figure 4.4 Alkali ion diffusion in graphite. (a) A log-log-log plot of the relationship between lateral size *r*, diffusion constant *D*, and the diffusion time *t* for intercalation of layered materials, with references to existing and potential materials for the energy storage. Adapted with permission from[166]. Copyright 2019, WILEY-VCH Verlag GmbH & Co. KGaA, Weinheim. (b) The schematic electrochemical cell for the measurement of Li diffusion coefficient between bilayer graphene. Left panel: Li concentration n_{Li} calculated from Hall measurements at B=10 T and T=300K versus intercalation time at four different positions shown in the schematic. The inset is the magnified result at 7s. Right panel: Li concentrations along the bilayer graphene device at different times. Adapted with permission from[179]. Copyright 2017, Nature Publishing Group.

4.2.2.2 Diffusivity Estimation via Randles-Sevcik Equation

The Randles-Sevcik equation is an alternative method for calculating ion diffusion in the solid state[182]:

$$I_p = 0.4463 n^{3/2} F^{3/2} C S R^{-1/2} T^{-1/2} {D_{Li}}^{-1/2} v^{-1/2} \qquad (4.3)$$

where I_p is the peak current (A), n is the number of electrons transferred for the redox couple, F is the Faraday constant (96485.4 C mol^{-1}), C is the ion concentration in graphite (mol cm^{-3}), S is the electrode area (cm^2), R is the gas constant (8.314J mol^{-1} K^{-1}), I_p is the temperature, D stands for the diffusion coefficient (cm^2 s^{-1}) and v is the scanning rate (V s^{-1}). Note that this equation is often used to calculate the ion diffusion in the electrochemical measurement of coin cell batteries. The K^+ diffusion coefficient computed by this equation is 6.1 × 10^{-14} m^2 s^{-1} for a graphite host[183]. The diffusion coefficients of Li^+ and Na^+ in MoS_2 calculated by the Randles-Sevcik equation (4.3) were 5.4 m^{-16} s^{-1} and 3.5 m^{-17} s^{-1}, respectively[184]. The difference between the estimated diffusivity of the ions from *in-situ* TEM experiments and the calculated results by the equation is attributed to ions diffusion across the solid-electrolyte in the former, while the latter estimation only reflects the ion migration in the interior of the van der Waals crystals[184].

4.2.2.3 Diffusivity Estimation via *In-situ* TEM

TEM imaging is another viable method for determining the alkali-ion diffusivity in layered materials, since the movement of the intercalation reaction front can be directly captured via *in-situ* TEM. The diffusion front is a noticeable boundary splitting the intercalated and non-intercalated regions in both lithiation[62,185] and sodiation studies[186]. The dotted yellow lines shown in Fig. 4.5a marks a Na diffusion front, which propagates across the pristine MoS_2 along the directions indicated by yellow arrows, and the fast Fourier transforms (FFTs) pattern obtained at 4s indicates a

2×2 superstructure[186]. The diffusivity of the Li^+ and Na^+ can be estimated from the movement of the reaction front shown in the *in-situ* TEM images, based on the equation $D=d^2/2t$, where D is the diffusivity, t is the diffusion time, and d is the diffusion distance. The diffusivity of the Na^+ (1-2 $m^{-17}s^{-1}$) in MoS_2 is much lower than that of lithium (0.9-4.9 $m^{-15}s^{-1}$)[186]. The difference of diffusivity for two ions results from the distinct energy barriers for diffusion in MoS_2, revealed by the theoretical calculations. The energy barrier for Li^+ diffusion between the adjacent octahedral sites in MoS_2 is ~0.49eV[187], compared to ~0.7eV for Na^+ diffusion[188]. Fig. 4.5b shows a filtered high resolution phase contrast TEM image of the 2H- and 1T-MoS_2 phase boundary, approximately 2 nm in width, where the intermediate phase distorting the lattice[74] results in a large strain gradient across the boundary and thus the contrast of the boundary is different in the image[186].

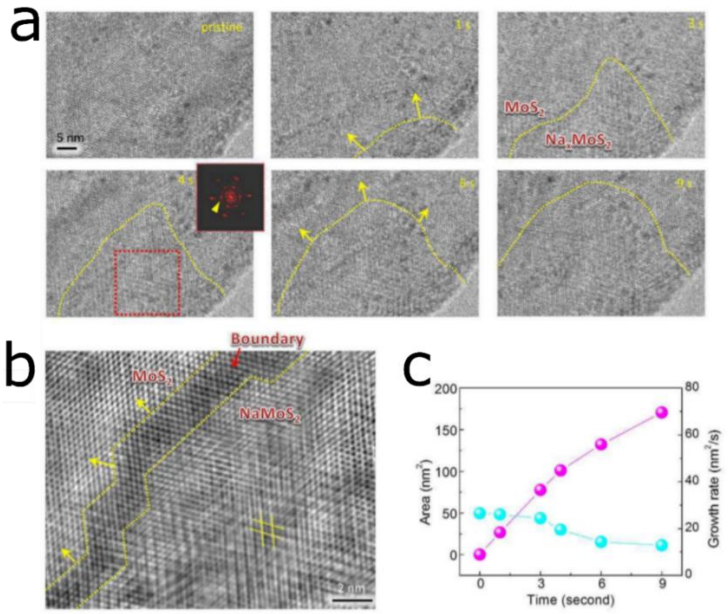

Figure 4.5 High resolution TEM images of Na^+ diffusion in MoS_2. (a) *in-situ* high resolution TEM image series showing the propagation of the phase boundary of Na_xMoS_2/MoS_2. The inset shows a fast Fourier transform pattern of a Na intercalated area. (b) Filtered high resolution image of the Na_xMoS_2/MoS_2 boundary acquired at 4s. (c) A plot of the size of the Na-intercalated domain (magenta) and growth rate (cyan) as a function of time. Adapted with permission from[186]. Copyright 2015, American Chemical Society.

4.2.2.4 Temperature Effect on Diffusion and Arrhenius Equation

The temperature dependence of the chemical reaction constant can be demonstrated by the Arrhenius equation, proposed by a Dutch chemist in 1889, and justified and interpreted by the Swedish chemist Svante Arrhenius. Regarded as an empirical relationship, this equation is used to model the temperature (T) variance of diffusion, permeability and other chemical process[189]. The most common form of the Arrhenius equation is:

$$k = k_0 e^{-\frac{E_a}{RT}} \tag{4.4}$$

where k and k_0 are the kinetic reaction rate and rate constant,

respectively. E_a (kJ/mol) denotes the activation energy of the reaction and R stands for the universal gas constant. There is a similar Arrhenius equation that demonstrates the diffusion coefficient (D):

$$D = D_0 e^{-\frac{E_d}{RT}} \tag{4.5}$$

where E_d denotes the activation energy of diffusion and D_0 stands for the pre-exponential factor, which is characteristic of a particular material.[189] A more useful form of the equation (4.5) is acquired by taking the logarithm of both sides of the equation is:

$$\ln(D) = \ln(D_0) - E_d/RT \tag{4.6}$$

Equation (4.6) describes a negative linear relation between ln(D) and 1/T, plotted in a Arrhenius plot (Fig. 4.6) through which the values of E_d/R and D_0 can be experimentally calculated by measuring the slope of the line and the y-intercept, respectively. It has been reported that Li diffusion coefficient increases as temperature increasing in the graphite and MoS_2.

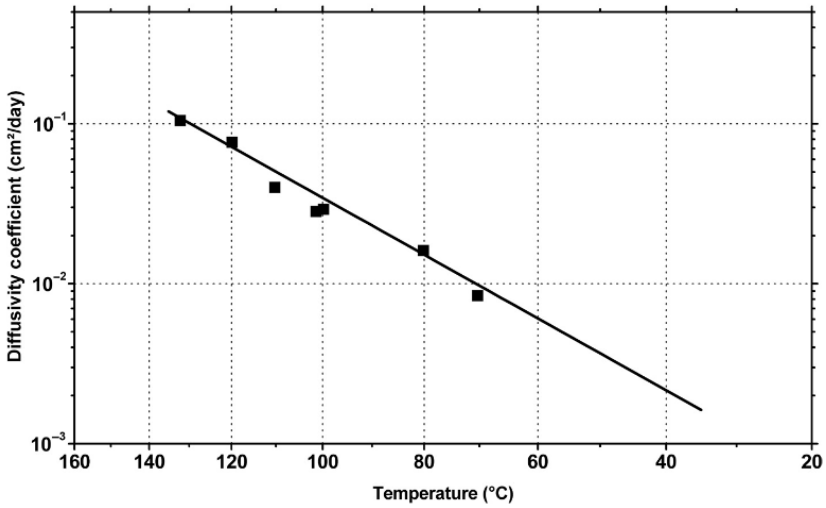

Figure 4.6 Arrhenius plot of the diffusion coefficient against temperature for carbon dioxide through polyvinylidene fluoride. Adapted with permission from[189]. Copyright 2017, Elsevier Inc.

4.2.2.5 Defect Effect on Diffusion

Intrinsic defects always exist in the solid-state materials, often affecting rates of ionic diffusion[168] and electronic conduction[190]. By using dispersion-corrected DFT methods, two typical defects affecting ion migration were studied in Li- and K-based systems: the Schottky defect, i.e. cation and anion vacancies, and the Frenkel defect, i.e. a cation vacancy and a cation interstitial[168,170]. These two defects contribute to different diffusion mechanisms. In the case of graphite, Li cannot transport via the interlayer migration (along crystallographic *c* direction) through the hollow site of graphene plane, due to the extremely high energetic barrier[168]. The calculated activation energy of Li migrating on the crystallographic *AB* plane via the Frenkel mechanism (~0.52 eV) is slightly preferred compared to the vacancy mechanism (~0.56 eV)[168]. On the other hand, DFT simulation of K diffusion has indicated that K migration in the *ab* plane via the vacancy mechanism (0.11 - 1.58 eV) is energetically preferable to the Frenkel mechanism (2.42 - 7.92 eV)[170]. The proposed favorable migration paths of Li and K are shown in Fig 4.7a and c, respectively.

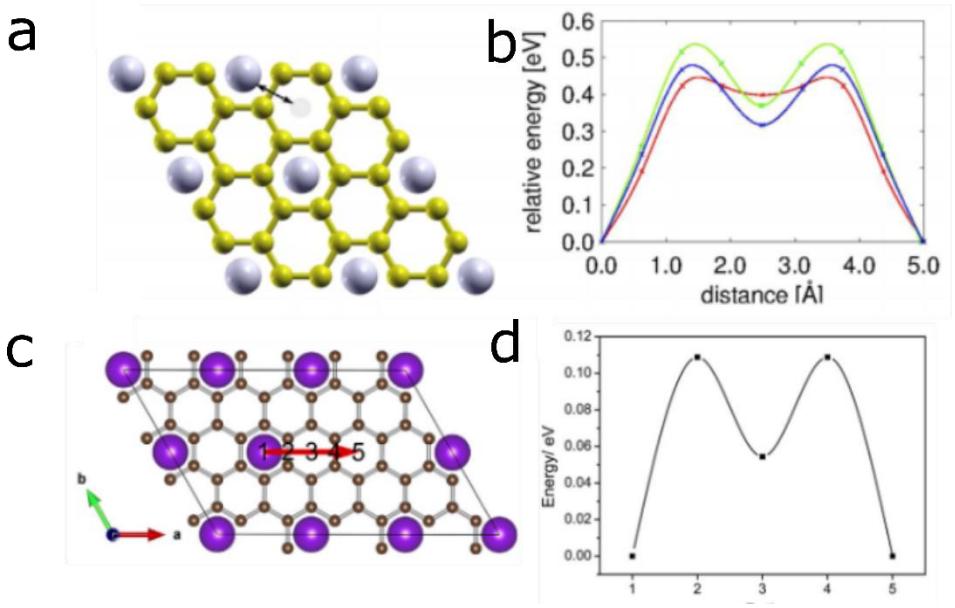

Figure 4.7 Frenkel and vacancy diffusion mechanisms of alkali ion migration in graphite. (a, b) Illustration of the bridge-migration pathway of Li via the Frenkel mechanism and the energy profile curves for LiC_6, st-LiC_6 and LiC_{12} are shown in red, blue and green. Note that LiC_6 and st-LiC_6 are allotropes and form at high (220 K ~ room temperature) and low temperatures (100 K ~ 220 K), respectively. Adapted from[168]. Copyright 2014, American Chemical Society. (c, d) A schematic of K migration path *via* the vacancy mechanism of KC_8 and the energy profile. Adapted with permission from[170]. Copyright 2016, Elsevier Ltd.

4.3 Intercalation-induced Structural Changes in Graphitic Materials

4.3.1 Staging Phenomenon

Due to the structural simplicity and stability of graphite, it is one of earliest host materials used for intercalation studies, with derived intercalation compounds such as Li-GIC and K-GIC being consistently studied since 1950s. Rudorff and Schultze first used XRD to investigate the K arrangement in the interlayer galleries of the graphite, and found K to periodically appear between the graphite layers. Based on their findings, they proposed a staging model to describe the rules of intercalant distribution in the K-graphite lamellar compound along the vertical axis[120]. The order of the stage n (where n ≥ 1) is a measure of the number of graphene layers sandwiched by adjacent intercalant layers, for example stage 1 indicates that the graphite is entirely intercalated with the highest intercalant concentration. GICs in various staging orders can be synthesised by the vapour transport method introduced in section 4.1.1. *Ex-situ* XRD can be used to extract the stacking information of the intercalated graphite, according to the measurement of the intensity of reflections along the $[10\bar{1}l]$ direction. The stacking sequences of the first order staging K(Rb)-GIC[116,162] and Li(Cs)-GIC[117,191] are:

(K, Rb) Stage 1 A α A β A γ A δ A,

(Li, Cs) Stage 1 A α A β A γ A,

Where capital letters denote the stacking sequences of graphite layers, and

The Greek alphabet letters denote the ordering of alkali intercalant layers shown in Fig. 3.3. At room temperature, this ordering intercalant may change to disordering when the alkali ion concentration reduces (i.e. the stage increased) giving the vertical stacking sequence as:

Stage 2 A B | B C | C A | A,

Stage 3 A B A | A C A | A,

Stage 4 A B A B | B C B C | C A C A | A,

where vertical bars denote disordered intercalant layers. This phenomenon is generally observed either in the freshly prepared samples in higher-order staging or in the transition from stage 1 to higher staging[162]. However, in some cases the disorder of intercalants in stage 2 GIC can transform to an ordered state when the species is cooled down to an order-disorder transition temperature, reported in various XRD studies for the different alkali ion GICs[118,191-193]. For instance in the K-GIC system, the X-ray diffraction pattern showed a change from a streak pattern at room temperature, to a pattern with discrete reflections as the temperature was reduced down to 98 K due to the formation of an ordered intercalant stacking sequence (A B α B C β C A γ A B)[116]. The order-disorder transition temperatures for Rb- and Cs-GICs are 159 K and 163 K, respectively[194]. This transformation does not affect the structure of the graphite layer, since there is no obvious variation in the intensity of graphite reflections[116].

In terms of continuously investigating intercalation (reduction in stage number) or deintercalation (increase in stage number), electro-chemical characterisation is one of the best methods for recognizing stage transitions in GICs and providing insights into the staging phenomenon,

since the intercalation is amenable to be reversibly controlled in the electrochemical system. Charge/discharge profiles of Li and K ion intercalation/deintercalation in a graphite anode, shown in Fig. 4.8a,c give sequential information about staging transitions involved (stage III to stage II to stage I)[195]. Although this transition sequence has been widely recorded for Li/K intercalation, variation in the compositions of the electrolyte can lead to a higher stage, e.g. stage IV[178,195,196]. Fig. 4.8b,d shows the cyclic voltammograms (CVs) of such processes, where sharp redox peaks can be correlated to staging transitions occurring at specific voltages[178]. CV curves also confirm that the average intercalation potential of K ions is higher than that of Li ions, which demonstrates K intercalation in graphite easier than Li[178], agreeing with theoretical calculations for the formation energy of K-GIC being more negative than that of Li-GIC[171]. *In operando* XRD is another popular structural characterisation approach to continuously monitor the staging behaviour, throughout which the appearance and disappearance of the characteristic peaks corresponding to the distinct phases in the different stages can be observed in a cycle of intercalation/ deintercalation process, shown in Fig. 4.8e, that can also be correlated to electrochemical measurements[197,198].

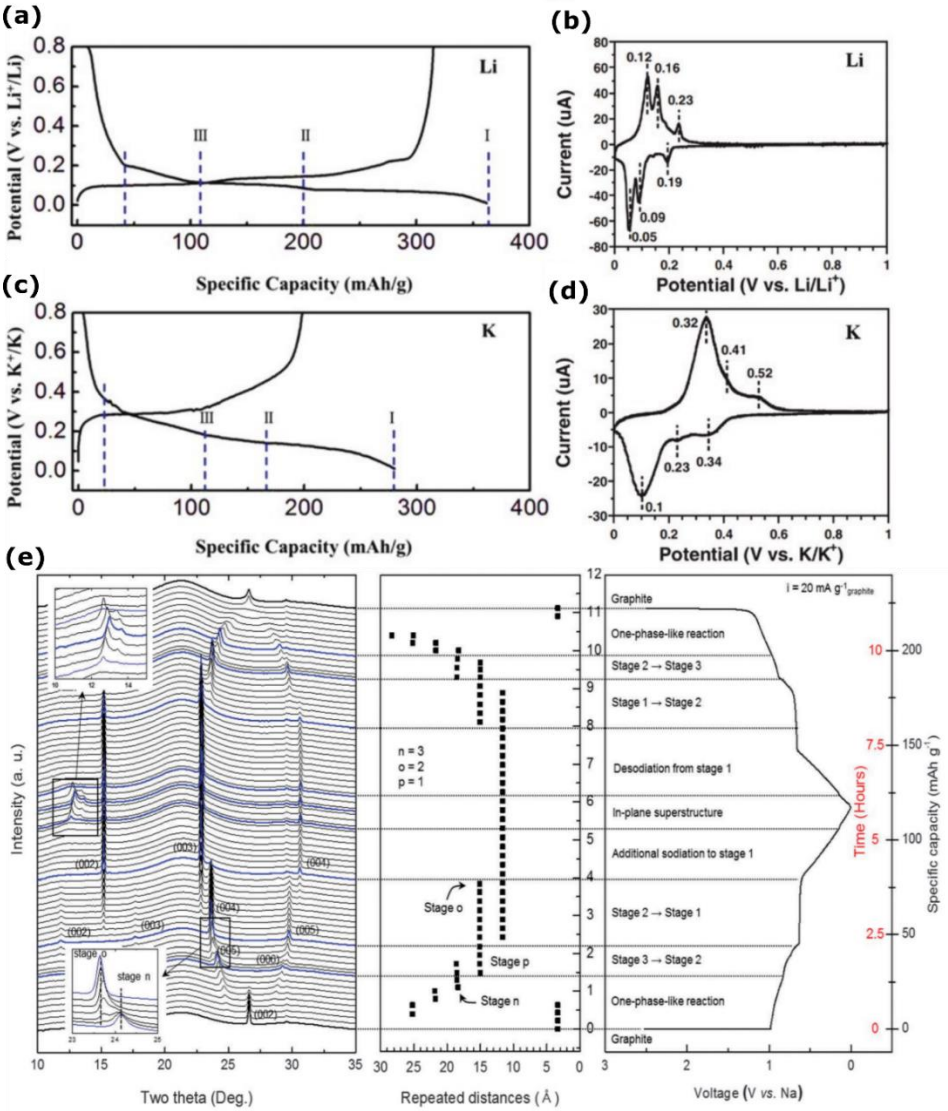

Figure 4.8 Electrochemical results of Li and K intercalation in graphite. (a, c) discharge/charge profiles versus Li and K at 5 mA/g for a graphite anode. Adapted with permission from[195]. (b, d) CV curves of graphite anodes in Li-based and K-based system at a scan rate of 0.01 mV s^{-1} between 0 and 1.0 V. Adapted with permission from[178]. Copyright 2016 WILEY-VCH Verlag GmbH & Co. KGaA, Weinheim. (e) *In operando* synchrotron X-ray diffraction analysis of the structural evolution of the sodiated graphite system observed during electrochemical intercalation and deintercalation into/out of graphite in a sodium-graphite cell. Adapted with permission from[198]. Copyright 2015, Royal Society of Chemistry.

Despite these revelations, uncertainties about the exact nature of structural changes that occur during stage transitions still exact, as it is still a great challenge to directly image the dynamic changes at atomic scale. There are numerous theoretical models that have been proposed to

demonstrate the stage transition process, but no one can reproduce every aspect of intercalation phenomenon. The Daumas-Hérold (DH) model shown in Fig. 4.9a provides a reasonable explanation for the structural transformation, considering the mechanically induced strain in the graphene layer[199]. The strain is generated from the distortion of the host material due to accepting the guest species with different atomic size[145,199,200]. In the DH model, the graphene layers are flexible and deform around the intercalant, differing to the earlier reported RH model[201] which indicates that alternating graphene interlayer spaces are sequentially occupied by the guest without mechanical strain. The staging transformation proceeds via rearrangements of the guests inside the interlayer galleries. For example, Nishitani, R., et al. suggested a subtle intermediate phase existing in a narrow phase boundary region, regarding it as a locally rearranged region existing between the remaining well-staged regions[41]. Besides the mechanical aspect, the DH model can also explain the slow rate of (de)intercalation, which can be confirmed by kinetic Monte Carlo simulations[202]. However, the increased exchange current density in the electrochemical system and the use of ultra-small graphite flakes would suppress the appearance of DH structures[202]. Drüe, M., et al. prepared a sample (Fig. 4.9c) containing a lithium concentration gradient to investigate the mechanism of the stage 2 to 1 transition. They observed a number of intermediate phases, including superdense, dilute or pseudo-stage structures forming when $C_{12}Li$ took up extra Li as it transformed to to C_6Li as illustrated in Fig. 4.9b[203]. Based on the DH model, Liu, J., et al. suggested the complex kinetics of the staging transition (Fig. 4.9d)

involves dislocation and sliding of the graphite and K ion intercalation into the host through the edges (step I), which facilitates insertion of the intercalant. In the host, the structural variations include intrastage intercalation (step III), which involves transportation of the alkali ions between two regions with the same stage, as well as interstage intercalation (step II and IV) that describes the intercalant diffusion between two regions with different staging[204].

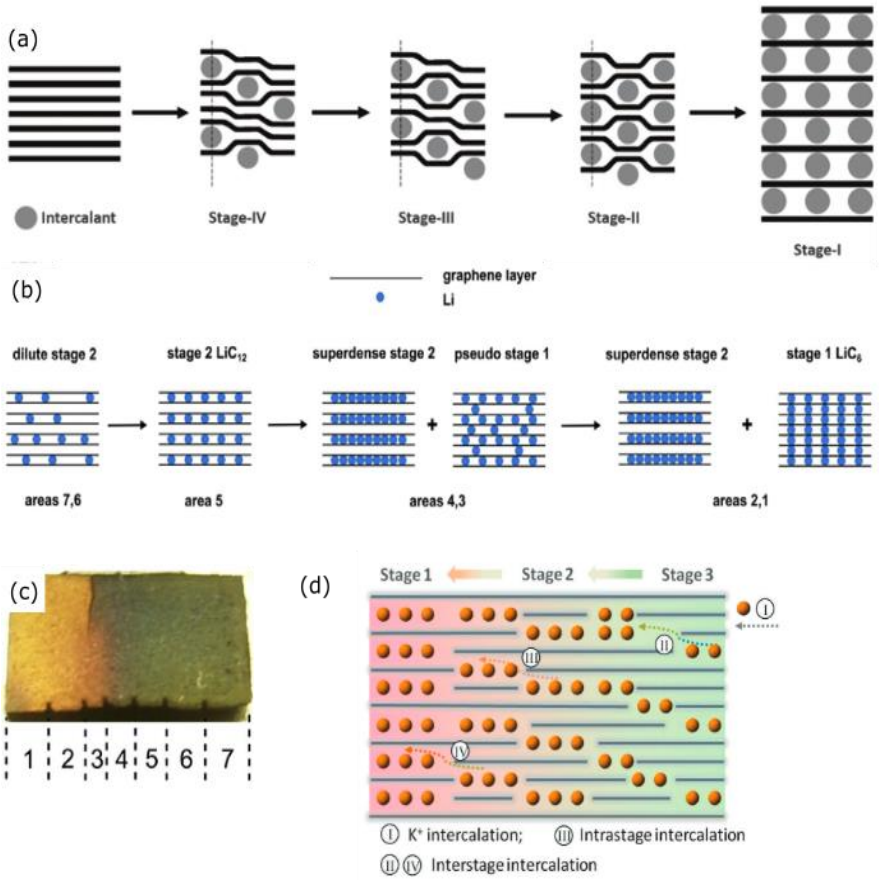

Figure 4.9 Comparisons of intercalation behaviours of alkali ions. (a) a schematic of the Daumas-Hérold model of alkali metal intercalation into graphite. Adapted with permission from[145]. Copyright 2014, Royal Society of Chemistry. (b) a schematic illustration of the staging transition mechanism of Li-GICs where area 1-7 correspond to the tested regions in (c). (c) sample with Li gradient. Seven areas have distinct Li concentration and area 1 has the highest Li content while area 7 has lowest. Adapted with permission from[203]. Copyright 2017, Elsevier B.V. (d) stage transition model proposed for K-GICs. Adapted with permission from[204]. Copyright 2019, WILEY-VCH Verlag GmbH & Co. KGaA, Weinheim.

4.3.2 Domain Formation and Host Lattice Expansion

TEM imaging can provide information about the homogeneity of GICs, including variations in intercalant domain size and interlayer spacing of the host, which are typical structural evolutions that accompany phase transitions induced by intercalation[186,205,206]. TEM bright field (BF) images exhibit the dependency of the cluster size to the heating temperature. Small Rb clusters with ~40 Å diameter at 110K grew to ~180 Å with an increase in temperature to 223 K. The size of the clusters also reduced when the species was cooled down back to 110 K again, shown in Fig. 4.10a, b. This reversible change of the cluster in the intercalated graphite was also observed in the further investigation of a stage 2 K-GIC system in which the orientation and structure of the cluster were studied using electron diffraction at different temperatures. In the range 86 - 130 K, the clusters in the specimen with a size of 33 Å were formed as the dark features in the Fig. 4.10c, d, surrounded by the disordered phase (grey) of the K-intercalated graphite which gave rise to the ring pattern in the electron diffraction as shown in Fig. 4.10e,f.[205] As the temperature increased above 130 K, new diffraction spots emerged on the pattern which exactly overlapped with the rings shown in Fig. 4.10e, f, due to the precipitous clusters growing and tending to lock orientation with the host.

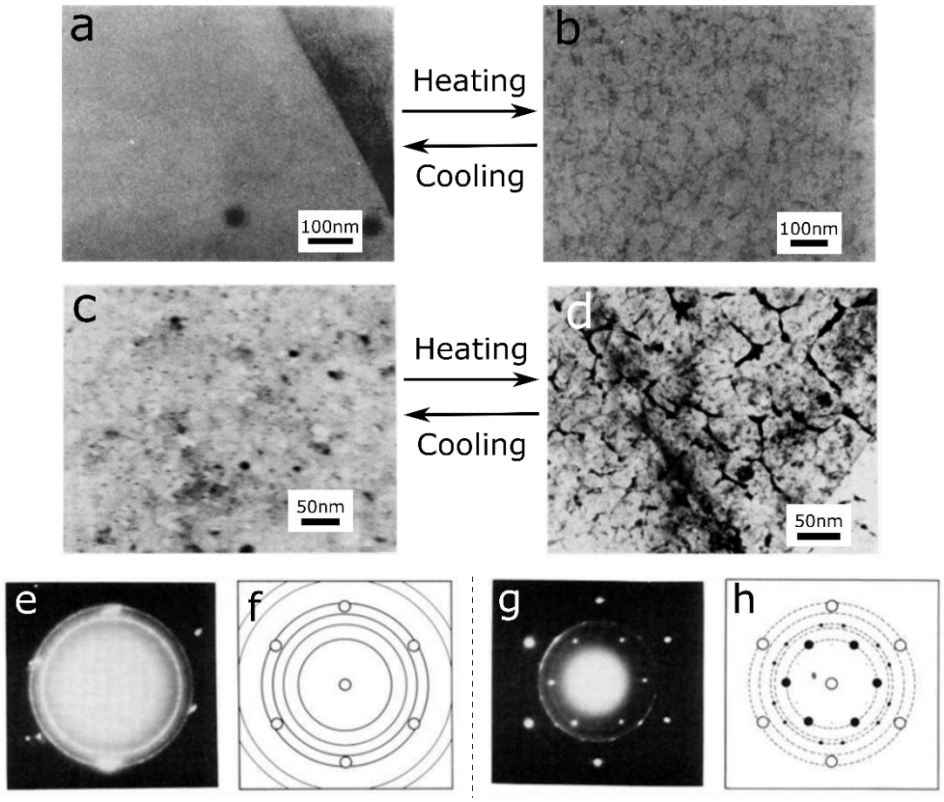

Figure 4.10 Intercalant cluster variations as the temperature. (a, b) show reversible changes of Rb clusters in the bright field images of a stage 2 GIC obtained at 110 and 223 K. Adapted with permission from[116]. Copyright 1980, American Physical Society. (c, d) show similar reversible morphological variation of the K clusters in $C_{21}K$ sample obtained at 118 and 293 K. The dark areas were identified as the clusters. In-plane electron diffraction patterns for $C_{21}K$ at (e) 118 K and at (g) 305 K. (f) and (h) are schematic illustrations of (e) and (g), respectively. Adapted with permission from[205]. Copyright 1980, American Physical Society.

Since the discovery and isolation of single layer graphene, there has been some shift in interests from intercalation in the graphite bulk to its 2D counterpart. It has been predicted that graphene has double the theoretical capability of storing alkali ions (e.g. Li_2C_6) than graphite, which has the potential to enhance the energy storage performance of rechargeable alkali ion batteries[207-209]. However, the expected performance graphene anode has still yet to be reached, despite considerable experimental efforts. This is due to the adsorption of alkali metals on to the surface of pristine

monolayer graphene being an energetically unfavourable process[210], and the fact that alkali metal can only intercalate into the spacing of layer materials through intrinsic edges or high-order defects, which a monolayer does not possess. However, it was found that there is not a great difference between bulk and few-layer graphene in terms of their ability to store Li, based to the similar results from analysis of electrochemical kinetics and structural characterisation[211,212]. Recently *in-situ* TEM revealed a multilayer close-packed arrangement of Li atoms in bilayer graphene, which far exceeded the previous reported formation of LiC_6[62]. Fig. 4.11a presents a schematic of Li intercalation and Fig 4.11c-e shows a series of HRTEM images captured during lithiation, where a clear reaction front appeared (denoted by white dashed lines) and propagated throughout the entire flake after 288 s biasing. It should be noted that an additional three sets of hexagonal ordered diffraction spots (Fig 4.11f) appear in the fast Fourier transformation of Fig 4.11d, corresponding to three grains with different orientations shown in Fig 4.11g. They correspond to a crystalline phase with an in-plane constant of 3.1 Å, which matches that of a superdense Li crystal[213]. This superdense Li crystal was only previously reported to be form under special conditions. For instance, Li crystallizes in a body-centred cubic (bcc) structure at room temperature and extremely high pressure (~7 GPa), and bcc Li crystal transforms into a close-packed structure when cooled down below 77 K at 0 GPa pressure[214]. The encapsulated Li crystals can be directly viewed by excluding graphene signals in von Hann filtered Fourier transformation, with the inverse fast Fourier transformation shown in Fig 4.11i-k, where the observed contrast

of this crystal in Fig 4.11j indicates regions of different thickness. In order to confirm that the multilayer close-packed Li could be formed in the bilayer graphene, first-principle simulations were carried out. Two possible structures of the superdense Li crystal are bilayer and trilayer Li intercalants, with a hexagonal closed packed lattice sandwiched by two graphene layers. This coincides with experimental data in terms of the lattice constant of close-packed Li crystal, and the free energy of the systems that where shown to be close to that of the C_6LiC_6 configuration observed under the standard conditions. Therefore these multilayer close-packed Li configurations can form in bilayer graphene under non-extreme reaction conditions[62].

In-plane and out-of-plane lattice expansions that arise from intercalation of foreign ions are also non-negligible structural variations in the host materials structure that can be characterised by *in-situ* TEM and *in operando* XRD. Depending on the intercalant species, the *d*-spacing of graphite layer increases from 0.335 nm (pristine) to 0.370 nm and to 0.535 nm measured at the end of lithiation and potassiation processes, respectively. This results in a volume expansion of the lithiated and potassiated graphite of about 13% and 60%, respectively[178,196,197] which is related to the atomic sizes of K and Li.

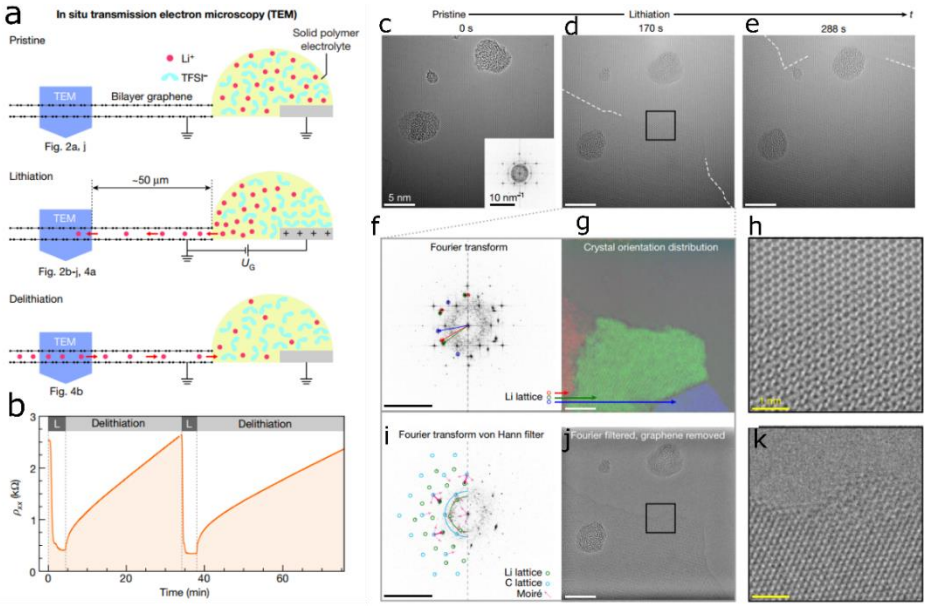

Figure 4.11 Reversible Li intercalation in bilayer graphene. (a) Schematic side views of the pristine device (top), the device during lithiation (middle) and delithiation (bottom). (b) Resistivity measurement of bilayer graphene as a function to the intercalation time. (c-e) TEM images show the lithiation reaction front propagating throughout the flake, obtained on the same area at consecutive times, and the inset in (c) is the Fourier transformation. Hydrocarbon contaminations appear on these images showing as the bulb features. (f) is the Fourier transformation of (d). Three sets of spots in (f), red, blue and green correspond to the grains shown in (g). (h) Magnified details of the boxed area in (d). (i) von Hann-filtered Fourier transform of (d), Li and graphene spots are denoted in green and blue circles respectively, and the origins of Moiré pattern are highlighted in bold magenta. Half circles are representative of the periodicities for graphene and Li. (j) Fourier-filtered image of (d) where onlsy Li grains are left. (k) Magnified details of the boxed area in (j). Scale bars of equal size are coloured identically but labelled only once in (c-k). Adapted with permission from[62]. Copyright 2018, Springer Nature Limited.

4.5 Intercalation-induced Structural Changes in TMDCs

4.5.1 Structural Evolution of Intercalated MoS_2

In-situ TEM can monitor the intercalation process and structural changes in real time without missing reaction details or degrading the sample through exposure to ambient which usually happens in the traditional TEM study. Electrochemical intercalation is the only approach that can be used in TEM at present, but two configurations have been shown to be capable of *in-situ* intercalation. One involves employing a tungsten electrode with alkali metal attached to the tip as the intercalant provider, and a MoS_2 flake as the working electrode to accept the intercalant. A piezo controller is used to manipulate the tungsten tip and bring it into contact with the MoS_2 flake[64,125,185]. The other configuration consists of two Au (or Ti) electrodes which are connected by the host flake, and solid-state electrolyte composed of an alkali ion salt and polymer matrix[164].

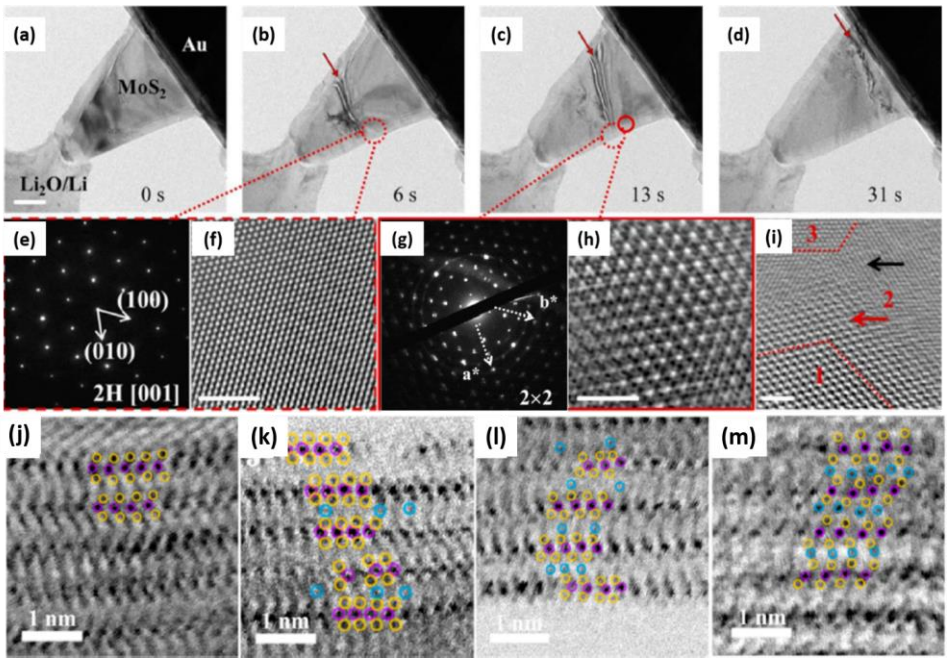

Figure 4.12 *In-situ* TEM and *ex-situ* STEM images of lithiation and sodiation in MoS_2. (a-d) *In-situ* TEM images of the morphological evolution of a MoS_2 sheet during lithiation. Red arrows show the reaction front. Scale bar, 0.2 μm. (e) and (f) are a selected area electron diffraction (SAED) pattern and a HRTEM image of a region ahead of reaction front in unlithiated MoS_2 section, respectively. Scale bar, 2 nm. (g) and (h) are SAED and HRTEM image of the same region corresponding (e) and (f) after lithiation. Scale bar, 2 nm. (i) HRTEM image of the phase boundary where region 1 is the intercalated phase, region 3 is the unreacted phase and region 2 is dominated by dislocations. Red and black arrows indicate the wavy-distorted structure and slip dislocations respectively. Scale bar, 2 nm. Adapted with permission from[185]. Copyright 2014, American Chemical Society. (j-m) Side views of MoS_2 nanosheets along [100] zone axis. (j) The pristine 2H-MoS_2 and sodiated by applying 1.0 V (k), 0.8 V (l), and 0.2 V (m) potential. Higher sodiation potential results in lower Na capacity of MoS_2 nanosheets. The yellow, purple and blue circles represent S, Mo and Na atoms respectively. Adapted with permission from[129]. Copyright 2014, American Chemical Society.

Using *in-situ* TEM, Wang et al.[129] reported a morphological transition during the lithiation of a MoS_2 nanosheet in which the lithiated and unlithiated regions were separated by a wavy boundary during intercalation (indicated by a red arrow), and this boundary moved across the flake after 31 seconds (Fig. 4.12a-d). The electron diffraction pattern of a local region varied from a pristine MoS_2 pattern to a superlattice pattern after the

reaction front had passed (Fig. 4.12e-h). The superstructure reflections appeared along a*(100) and b* (010) directions with a 2-fold periodicity in the selected area electron diffraction (SAED) pattern, thus the pattern is referred to as a 2a×2a superstructure, which has similarly been reported in the Na tuned MoS_2 study[186]. The change in lattice parameters of the host MoS_2 was also monitored by SAED, which revealed a subtle expansion along *c*-axis from 1.23 nm to 1.4nm[185]. HRTEM demonstrated that the buffer zone between lithiated and unlithiated MoS_2 regions consisted of wavy periodic structures near the lithiated side, and a distorted area with slip dislocations close to the unlithiated side shown in Fig. 4.13i. Additionally, a variety of superlattices were found in the lithiated areas by HRTEM, including $\sqrt{3}a \times \sqrt{3}a$, $2a \times 2a$, $2a \times a$, $a \times a$ and $\sqrt{3}a \times a$[64,185]. Similar superlattices were observed in sodiated MoS_2, but a new intermediate superlattice assigned to the $2a \times \sqrt{3}a$ superstructure was formed when the stoichiometric ratio of Na to Mo was 0.25[64,125]. This new superstructure is composed by three identical $2a \times \sqrt{3}a$ superlattices having equivalent orientational relations with the host MoS_2 through atomic modelling and diffraction simulation shown in Fig. 4.13a,b. Further Na intercalation caused a variation in the intensity profile across {11-20} and {10-10} spots of MoS_2 in the SAED, where the {11-20} spots became more intense than {10-10} once the atomic ratio of Na to Mo reached 0.5, suggesting the phase transition of MoS_2 from 2H to 1T shown in Fig. 4.13c-h[125].

Cross-sectional annular bright field (ABF) images reveal the distribution of intercalants in the interlayer spacing, as well as the

intercalation mechanism, shown in Fig. 4.12j-m, where Na ions primarily appeared within every other interlayer of the 2H MoS_2 while the other interlayers remained empty in Fig. 4.12k[129]. When more Na ions were intercalated, the other empty spacings began to be filled until total occupation (Fig. 4.12l). Meanwhile, one of the sulfur planes in each MoS_2 layer glided along an atomic plane to generate 1T-MoS_2 phase where S-Mo-S arrangement becomes a straight chain (Fig. 4.12m).

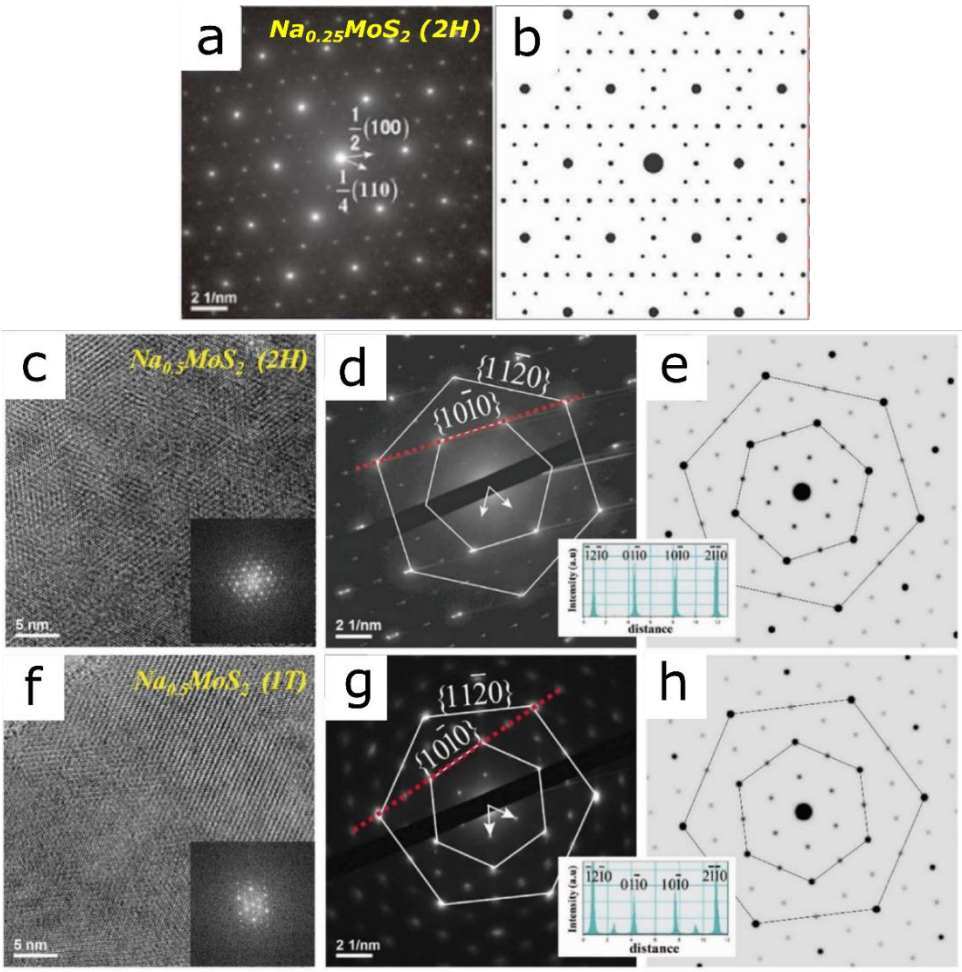

Figure 4.13 TEM characterisation of Na-intercalated MoS_2. (a,b) Experimental and simulated SAED patterns of the new intermediate phase in $Na_{0.25}MoS_2$. (c-e) HRTEM image, experimental and simulated SAED patterns of the 2H $Na_{0.5}MoS_2$, compared to (f-h) the 1T $Na_{0.5}MoS_2$. Note that the intensity profiles of 2H and 1T phases are in the insets. Adapted with permission from[125]. Copyright 2017, WILEY-VCH Verlag GmbH & Co. KGaA, Weinheim.

4.5.1 Alkali Ion Intercalation into Other TMDCs

Apart from the phase transition of the host material for TMDCs being induced by intercalation, lattice expansion due to the insertion of foreign species as also been imaged by TEM. Xu et al. reported a 16.6% volume expansion of layered WS_2 after lithiation, shown in Fig. 4.14a,d[215]. The structure changed from a uniform contrast flake (Fig. 4.14c) to that with

numerous bright and dark features (Fig. 4.14f). Additionally, the diffraction pattern of the lithiated WS_2 displays a polycrystalline ring pattern (Fig. 4.14e) rather than a single crystal pattern (Fig. 4.14b), due to over-lithiation inducing decomposition of the WS_2 and formation of Li_2S[215]. This volume expansion originated from the weak van der Waals force which accommodated the interplanar distance during the lithiation. Measurements of the intercalation-induced expansion of the basal plane (00*l*) were conducted by Kim[216] and Li[217] during lithiation of $SnSe_2$ and $TiSe_2$, respectively. Fig. 4.14g shows cross-sectional views of the $SnSe_2$ during lithiation, where the spacing changed from 0.61 to 0.67 nm, imaged using *in-situ* HRTEM.

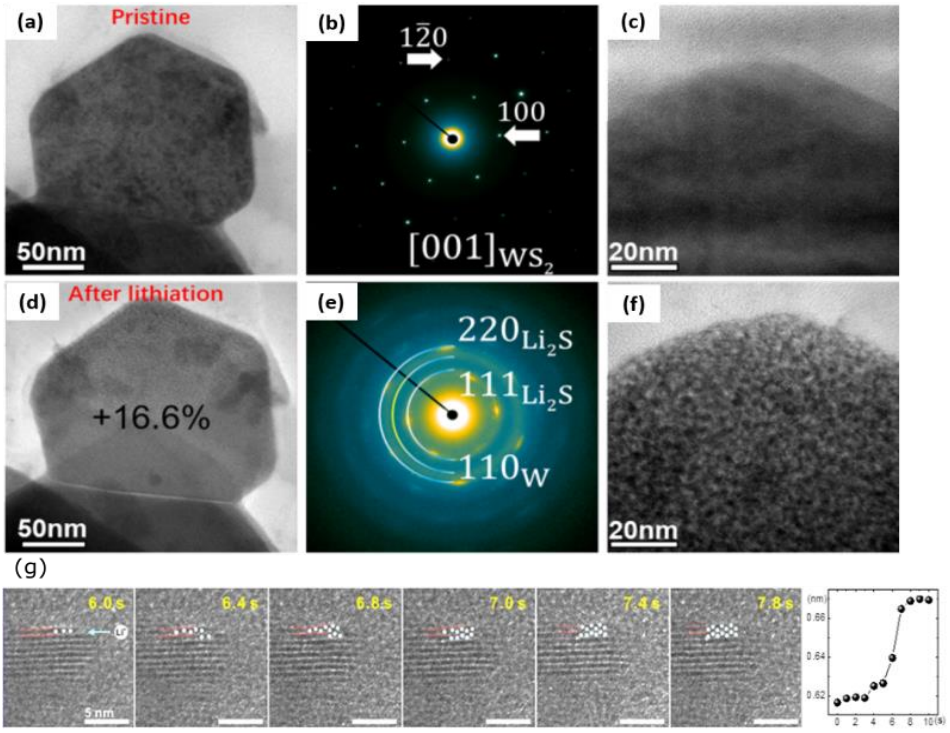

Figure 4.14 Lattice expansion induced by alkali ion intercalation. (a-c) Pristine state of WS_2 nanosheet. (d-f) Lithiated WS_2. Adapted with permission from[215]. Copyright Microscopy Society of America 2018. (g) *In-situ* HRTEM images show interlayer distance changing during lithiation of $SnSe_2$. Adapted with permission from[216]. Copyright Microscopy Society of America 2018.

As the concentration of the alkali ion in the host increased over the limit, distinct structural decompositions were witnessed in the intercalated TMDCs[218,219]. These can be classified into two mechanisms: displacement reactions and conversion reactions[219-223]. For the displacement reaction, Li ions break the interlayer chalcogen bonds of the host material, but keep the overall anion framework intact. Further Li ions intercalation triggers microscopic phase separation and the precipitation of transition metals[220,224]. Compared to the displacement reaction, the conversion reaction involves the host structure being entirely destroyed, leading to nanoscopic phase separation and metal nano-precipitation[222,225-227]. These differences affect the ion storage and charge/discharge properties of electrodes to be used in the next generation of alkali ion batteries[225,226]. The displacement reaction was reported in the studies of lithiated CuS[221-223]. Using *in-situ* STEM, He et al. suggested that the lithiation of CuS nanoflakes contains planar lithiation channels, visualized with side-view ADF-STEM in Fig. 4.15d, that appear as dark lines extending from the surface to the inner regions[222]. Fig. 4.15f, g show that the contrast of CuS nanoflakes varies from bright to dark, indicating that intercalation of Li into the interlayer spacing has occurred. In time-lapse STEM, plan view (Fig. 4.15h) and side view (Fig. 4.15i) images of the sample, the reaction fronts are marked by Roman numerals. They propagated towards the edge of the nanoflakes, meanwhile, Cu nanoparticles precipitated on the surface and agglomerated to form large particles (>50nm)[222]. The similar formation of the Cu particles on the host matrix was imaged by McDowell et al.[221], who also performed HRTEM to investigate lithiated Co_3S_4 and FeS_2,

shown in Fig. 4.16a-d. However, they did not observe precipitation of the Co and Fe nanoparticles. HRTEM images illustrate that both Co_3S_4 and FeS_2 crystals transformed into polycrystalline mixtures of Li_2S and the finely dispersed Co or Fe domains, consistent with the results of the conversion reaction[221]. It is suggested that the displacement reaction likely depends on the metallic ion conductivity of the host materials and the structural similarity of the S lattice in the initial and final phases[220]. A schematic (Fig. 4.16e) illustrates the difference between the conversion reaction of Co_3S_4 and the displacement reaction of CuS in principle.

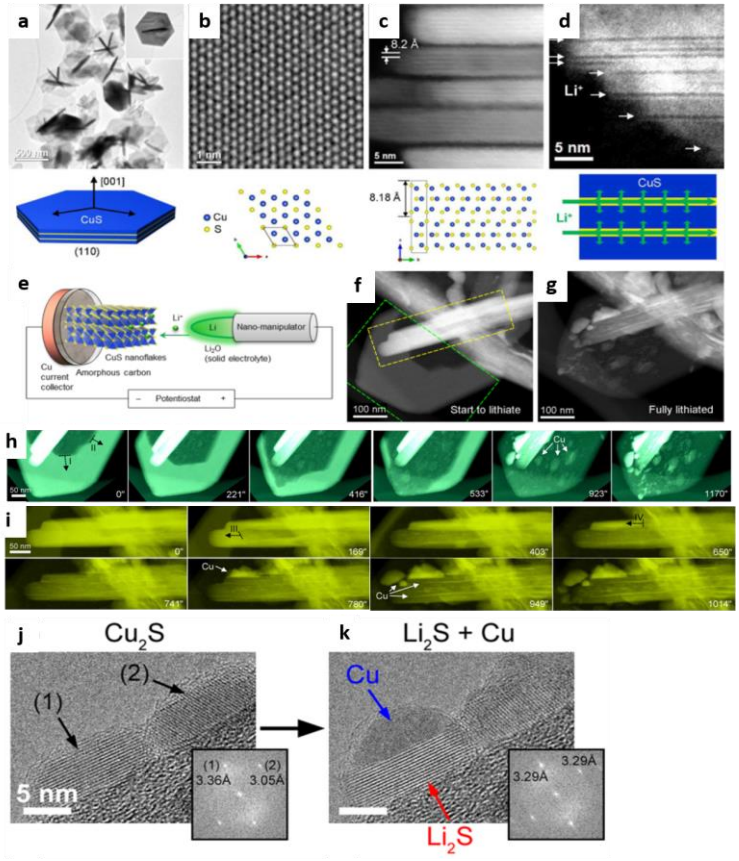

Figure 4.15 TEM and STEM images of Li intercalation into CuS. (a) TEM image of synthesized CuS nanoflakes with hexagonal geometry and a schematic of one nanoflake shown below. (b) HRTEM and (c) ADF-STEM images of the plan-view and side-view of CuS crystal structure along [001] and [100] directions. Corresponding atomic models are shown below. (d) ADF-STEM image of partial lithiated CuS crystal where white arrows show the channels for Li intercalation. (e) A battery setup for *in-situ* STEM observation employed in K. He et al.'s study. STEM images of CuS nanoflakes before (f) and after (g) lithiation. Time sequential STEM images of Li intercalation process showing the plane-view (h) and side-view (i) of CuS nanoflakes which correspond to the area of green and yellow dashed boxes in (f). (j) HRTEM image of CuS nanoparticles (1) and (2) attaching on the host matrix. The (002) plane of the nanoparticle 1 and (101) planes of the nanoparticle 2 with 3.36 Å and 3.05 Å interlayer spacing respectively determined by fast Fourier transformation (FFT) pattern. (k) The same nanoparticles after reaction with lithium. The initial CuS crystal transform to Li_2S while maintaining the original shape, and Cu metal extruded out and formed nanoparticles. A new Li_2S $(11\bar{1})$ plane was visible with 3.29 Å interlayer spacing, while the (002) spacing decreased (~2%) in the Li_2S crystal. (a-i) Adapted with permission from[222]. Copyright 2017, American Chemical Society. (j,k) Adapted with permission from[221]. Copyright 2015, American Chemical Society.

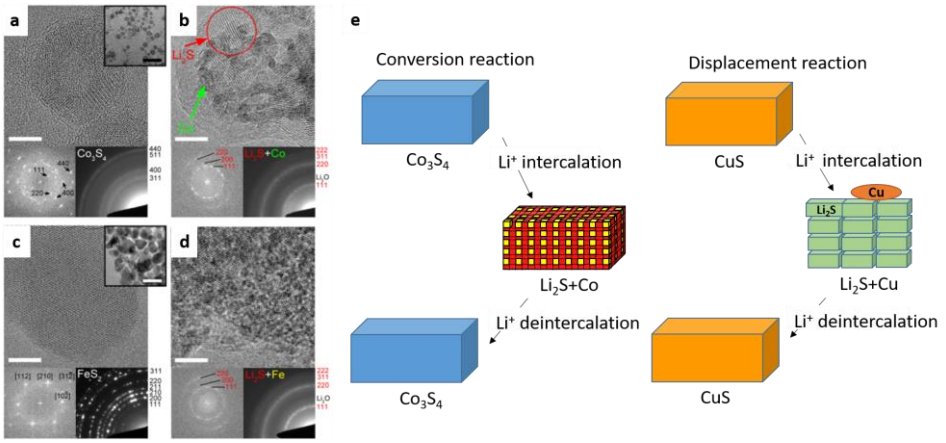

Figure 4.16 TEM characterisation of Li intercalation into Co_3S_4. HRTEM images of unlithiated Co_3S_4 nanocrystal (a) and lithiated nanocrystal (b). After reaction, a polycrystalline mixture of many Li_2S and Co metal domains highlighted by red and green arrows respectively. The diffraction rings of Co metal are not discernible due to the small size of the Co nanoparticles. (c) TEM characterisation of single crystal FeS_2 indicated by FFT. (d) The same single crystal FeS_2 became the mixture polycrystalline of Li_2S and Fe metal similar to the Co_3S_4. Co metal diffraction rings were also discernible due to the tiny crystalline. Scale bar, 5nm. Adapted with permission from[221]. Copyright 2015, American Chemical Society. (e) Schematic illustration of the conversion reaction and the displacement reaction. In the conversion reaction, yellow cubes represent the nanosized Co which are dispersed into Li_2S matrix (red cubes). In the displacement reaction, Cu nanoparticles precipitate on the surface of Li_2S matrix during lithiation.

Bibliography

1 Knoll, M. & Ruska, E. Das elektronenmikroskop. *Zeitschrift für physik* **78**, 318-339 (1932).

2 Dubochet, J., Frank, J. & Henderson, R. *The Nobel Prize in Chemistry 2017*, <https://www.nobelprize.org/prizes/chemistry/2017/prize-announcement/> (2017).

3 Smith, D. J. Development of aberration-corrected electron microscopy. *Microscopy and Microanalysis* **14**, 2-15 (2008).

4 Batson, P. E., Dellby, N. & Krivanek, O. L. Sub-ångstrom resolution using aberration corrected electron optics. *Nature* **418**, 617-620 (2002).

5 Ferreira, P., Mitsuishi, K. & Stach, E. In situ transmission electron microscopy. *MRS bulletin* **33**, 83-90 (2008).

6 Taheri, M. L. *et al.* Current status and future directions for in situ transmission electron microscopy. *Ultramicroscopy* **170**, 86-95 (2016).

7 Ophus, C. Four-dimensional scanning transmission electron microscopy (4D-STEM): From scanning nanodiffraction to ptychography and beyond. *Microscopy and Microanalysis* **25**, 563-582 (2019).

8 Hawkes, P. W. & Spence, J. C. *Springer Handbook of Microscopy*. (Springer Nature, 2019).

9 Orloff, J. Survey of electron sources for high-resolution microscopy. *Ultramicroscopy* **28**, 88-97 (1989).

10 Otten, M. T. & Coene, W. M. High-resolution imaging on a field emission TEM. *Ultramicroscopy* **48**, 77-91 (1993).

11 Ross, I. & Walther, T. in *Journal of Physics: Conference Series.* 012012 (IOP Publishing).

12 Konings, S. & Bischoff, M. A Cold Field Emission Gun Optimized for Cryo-EM Applications. *Microscopy and Microanalysis* **26**, 566-567 (2020).

13 Williams, D. B. & Carter, C. B. in *Transmission electron microscopy* 3-17 (Springer, 1996).

14 Hetherington, C. Aberration correction for TEM. *Materials Today* **7**, 50-55 (2004).

15 Scherzer, O. The theoretical resolution limit of the electron microscope. *Journal of Applied Physics* **20**, 20-29 (1949).

16 Brydson, R. & Hondow, N. Electron energy loss spectrometry and energy dispersive X-ray analysis. *Aberration-Corrected Analytical Transmission Electron Microscopy*, 163-210 (2011).

17 Rose, H. H. Future trends in aberration-corrected electron

microscopy. *Philosophical Transactions of the Royal Society A: Mathematical, Physical and Engineering Sciences* **367**, 3809-3823 (2009).

18 Haider, M., Hartel, P., Müller, H., Uhlemann, S. & Zach, J. Current and future aberration correctors for the improvement of resolution in electron microscopy. *Philosophical Transactions of the Royal Society A: Mathematical, Physical and Engineering Sciences* **367**, 3665-3682 (2009).

19 Krivanek, O., Dellby, N. & Lupini, A. Towards sub-Å electron beams. *Ultramicroscopy* **78**, 1-11 (1999).

20 Egerton, R. F. *Electron energy-loss spectroscopy in the electron microscope*. (Springer Science & Business Media, 2011).

21 Rutherford, E. LXXIX. The scattering of α and β particles by matter and the structure of the atom. *The London, Edinburgh, and Dublin Philosophical Magazine and Journal of Science* **21**, 669-688 (1911).

22 Bragg, W. H. & Bragg, W. L. The reflection of X-rays by crystals. *Proceedings of the Royal Society of London. Series A, Containing Papers of a Mathematical and Physical Character* **88**, 428-438 (1913).

23 Ewald, P. Zur theorie der interferenzen der röntgenstrahlen in kristallen. *Physikalische Zeitschrift* **14**, 465-472 (1913).

24 Cowley, J. M. *Electron diffraction techniques*. Vol. 2 (Oxford University Press, 1992).

25 Synnatschke, K. *et al.* Liquid Exfoliation of Ni2P2S6: Structural Characterization, Size-Dependent Properties, and Degradation. *Chemistry of Materials* **31**, 9127-9139 (2019).

26 Chrissafis, K. *et al.* Structural studies of MoS2 intercalated by lithium. *Materials Science and Engineering: B* **3**, 145-151 (1989).

27 Otoničar, M., Škapin, S. D., Jančar, B., Ubic, R. & Suvorov, D. Analysis of the phase transition and the domain structure in K0. 5Bi0. 5TiO3 perovskite ceramics by in situ XRD and TEM. *Journal of the American Ceramic Society* **93**, 4168-4173 (2010).

28 Marshall, A. *et al.* Lorentz transmission electron microscope study of ferromagnetic domain walls in SrRuO 3: statics, dynamics, and crystal structure correlation. *Journal of applied physics* **85**, 4131-4140 (1999).

29 Zhu, Y. *et al.* Microstructural evolution of [PbZr x Ti1–x O3/PbZr y Ti1–y O3] n epitaxial multilayers (x/y= 0.2/0.4, 0.4/0.6)–dependence on layer thickness. *Philosophical Magazine* **90**, 1359-1372 (2010).

30 Ma, C. *et al.* Structural features and tetragonal-orthorhombic phase transition in SrFe2As2 and CaFe2As2. *arXiv preprint arXiv:0811.3270* (2008).

31 Marcinkowski, M. J. & Poliak, R. M. Variation of magnetic structure with order in the Ni3Mn superlattice. *Philosophical Magazine* **8**,

1023-1050, doi:10.1080/14786436308214462 (1963).
32 Ophus, C., Ercius, P., Sarahan, M., Czarnik, C. & Ciston, J. Recording and using 4D-STEM datasets in materials science. *Microscopy and Microanalysis* **20**, 62-63 (2014).
33 Tanaka, M. Convergent-beam electron diffraction. *Acta Crystallographica Section A: Foundations of Crystallography* **50**, 261-286 (1994).
34 Midgley, P. A. & Eggeman, A. S. Precession electron diffraction–a topical review. *IUCrJ* **2**, 126-136 (2015).
35 Gammer, C., Ozdol, V. B., Liebscher, C. H. & Minor, A. M. Diffraction contrast imaging using virtual apertures. *Ultramicroscopy* **155**, 1-10 (2015).
36 Tao, J. *et al.* Direct imaging of nanoscale phase separation in La 0.55 Ca 0.45 MnO 3: relationship to colossal magnetoresistance. *Physical Review Letters* **103**, 097202 (2009).
37 Caswell, T. A. *et al.* A high-speed area detector for novel imaging techniques in a scanning transmission electron microscope. *Ultramicroscopy* **109**, 304-311 (2009).
38 Ozdol, V. *et al.* Strain mapping at nanometer resolution using advanced nano-beam electron diffraction. *Applied Physics Letters* **106**, 253107 (2015).
39 LeBeau, J. M., Findlay, S. D., Allen, L. J. & Stemmer, S. Position averaged convergent beam electron diffraction: Theory and applications. *Ultramicroscopy* **110**, 118-125 (2010).
40 Kimoto, K. & Ishizuka, K. Spatially resolved diffractometry with atomic-column resolution. *Ultramicroscopy* **111**, 1111-1116 (2011).
41 Nishitani, R., Uno, Y. & Suematsu, H. In situ observation of staging in potassium-graphite intercalation compounds. *Physical Review B* **27**, 6572 (1983).
42 Egerton, R. F. *Physical principles of electron microscopy*. Vol. 56 (Springer, 2005).
43 Erni, R., Rossell, M. D., Kisielowski, C. & Dahmen, U. Atomic-resolution imaging with a sub-50-pm electron probe. *Physical review letters* **102**, 096101 (2009).
44 Brydson, R. *Aberration-corrected analytical transmission electron microscopy*. Vol. 3 (John Wiley & Sons, 2011).
45 Pennycook, S. J. & Nellist, P. D. *Scanning transmission electron microscopy: imaging and analysis*. (Springer Science & Business Media, 2011).
46 Kirkland, E. J. *Advanced computing in electron microscopy*. Vol. 12 (Springer, 1998).
47 Kramers, H. A. XCIII. On the theory of X-ray absorption and of the continuous X-ray spectrum. *The London, Edinburgh, and Dublin Philosophical Magazine and Journal of Science* **46**, 836-871 (1923).

48 Cliff, G. & Lorimer, G. W. The quantitative analysis of thin specimens. *Journal of Microscopy* **103**, 203-207 (1975).
49 Maher, D., Joy, D., Ellington, M., Zaluzec, N. & Mochel, P. Relative accuracy of k-factor calculations for thin-film X-ray analysis. *Analytical Electron Microscopy*, 33-38 (1981).
50 Newbury, D., Williams, D., Goldstein, J. & Fiori, C. Observation on the calculation of kAB factors for analytical electron microscopy. *Anal Electron Microsc* **2**, 276-278 (1984).
51 Wood, J., Williams, D. & Goldstein, J. Experimental and theoretical determination of kAFe factors for quantitative X-ray microanalysis in the analytical electron microscope. *Journal of Microscopy* **133**, 255-274 (1984).
52 Sheridan, P. J. Determination of experimental and theoretical kASi factors for a 200-kV analytical electron microscope. *Journal of electron microscopy technique* **11**, 41-61 (1989).
53 Watanabe, M., Horita, Z. & Nemoto, M. Absorption correction and thickness determination using the ζ factor in quantitative X-ray microanalysis. *Ultramicroscopy* **65**, 187-198 (1996).
54 Watanabe, M. & Williams, D. The quantitative analysis of thin specimens: a review of progress from the Cliff-Lorimer to the new ζ-factor methods. *Journal of microscopy* **221**, 89-109 (2006).
55 Slater, T. J., Lewis, E. A. & Haigh, S. J. Energy dispersive X-ray tomography for 3D elemental mapping of individual nanoparticles. *JoVE (Journal of Visualized Experiments)*, e52815 (2016).
56 Wang, Y.-C. *et al.* Imaging three-dimensional elemental inhomogeneity in Pt–Ni nanoparticles using spectroscopic single particle reconstruction. *Nano letters* **19**, 732-738 (2019).
57 Nakamichi, H., Yamada, K. & Sato, K. Sub-nanometre elemental analysis of Cu cluster in Fe–Cu–Ni alloy using aberration corrected STEM-EDS. *Journal of microscopy* **242**, 55-61 (2011).
58 Jeanguillaume, C. & Colliex, C. Spectrum-image: the next step in EELS digital acquisition and processing. *Ultramicroscopy* **28**, 252-257 (1989).
59 Hofer, F., Schmidt, F.-P., Grogger, W. & Kothleitner, G. in *IOP conference series: Materials science and engineering.* 012007 (IOP Publishing).
60 Li, Y., Chen, Z. & Loretto, M. Spurious contributions from scattered electrons in thin-film X-ray microanalysis. *Journal of Microscopy* **170**, 259-264 (1993).
61 Wang, Z. *et al.* In situ STEM-EELS observation of nanoscale interfacial phenomena in all-solid-state batteries. *Nano letters* **16**, 3760-3767 (2016).
62 Kühne, M. *et al.* Reversible superdense ordering of lithium between two graphene sheets. *Nature* **564**, 234-239 (2018).

63 Ross, F. M. & Minor, A. M. in *Springer Handbook of Microscopy* (eds Peter W. Hawkes & John C. H. Spence) 101-187 (Springer International Publishing, 2019).
64 Huang, Q., Wang, L., Xu, Z., Wang, W. & Bai, X. In-situ TEM investigation of MoS 2 upon alkali metal intercalation. *Science China Chemistry* **61**, 222-227 (2018).
65 Xin, H. L., Niu, K., Alsem, D. H. & Zheng, H. In situ TEM study of catalytic nanoparticle reactions in atmospheric pressure gas environment. *Microscopy and Microanalysis* **19**, 1558-1568 (2013).
66 Kelly, D. J. *et al.* In Situ TEM Imaging of Solution-Phase Chemical Reactions Using 2D-Heterostructure Mixing Cells. *Advanced Materials*, 2100668 (2021).
67 Lu, N., Wang, J., Xie, S., Xia, Y. & Kim, M. J. Enhanced shape stability of Pd–Rh core–frame nanocubes at elevated temperature: In situ heating transmission electron microscopy. *Chemical Communications* **49**, 11806-11808 (2013).
68 van Huis, M. A. *et al.* Atomic imaging of phase transitions and morphology transformations in nanocrystals. *Advanced materials* **21**, 4992-4995 (2009).
69 Asoro, M. A., Kovar, D. & Ferreira, P. J. In situ transmission electron microscopy observations of sublimation in silver nanoparticles. *ACS nano* **7**, 7844-7852 (2013).
70 Zhang, D. *et al.* Atomic-resolution transmission electron microscopy of electron beam–sensitive crystalline materials. *Science* **359**, 675-679 (2018).
71 Egerton, R., Li, P. & Malac, M. Radiation damage in the TEM and SEM. *Micron* **35**, 399-409 (2004).
72 Egerton, R. Mechanisms of radiation damage in beam-sensitive specimens, for TEM accelerating voltages between 10 and 300 kV. *Microscopy research and technique* **75**, 1550-1556 (2012).
73 Clark, N. *et al.* Scalable patterning of encapsulated black phosphorus. *Nano letters* **18**, 5373-5381 (2018).
74 Lin, Y.-C., Dumcenco, D. O., Huang, Y.-S. & Suenaga, K. Atomic mechanism of the semiconducting-to-metallic phase transition in single-layered MoS 2. *Nature nanotechnology* **9**, 391-396 (2014).
75 Meyer, J. C. *et al.* Accurate measurement of electron beam induced displacement cross sections for single-layer graphene. *Physical review letters* **108**, 196102 (2012).
76 Smith, B. W. & Luzzi, D. E. Electron irradiation effects in single wall carbon nanotubes. *Journal of Applied Physics* **90**, 3509-3515 (2001).
77 Komsa, H.-P. *et al.* Two-dimensional transition metal dichalcogenides under electron irradiation: defect production and doping. *Physical review letters* **109**, 035503 (2012).
78 Henderson, R. Cryo-protection of protein crystals against radiation

damage in electron and X-ray diffraction. *Proceedings of the Royal Society of London. Series B: Biological Sciences* **241**, 6-8 (1990).
79 Egerton, R. Control of radiation damage in the TEM. *Ultramicroscopy* **127**, 100-108 (2013).
80 Novoselov, K. S. *et al.* Electric field effect in atomically thin carbon films. *science* **306**, 666-669 (2004).
81 Ciesielski, A. & Samori, P. Graphene via sonication assisted liquid-phase exfoliation. *Chemical Society Reviews* **43**, 381-398 (2014).
82 Naguib, M., Mochalin, V. N., Barsoum, M. W. & Gogotsi, Y. 25th anniversary article: MXenes: a new family of two-dimensional materials. *Advanced materials* **26**, 992-1005 (2014).
83 Coleman, J. N. *et al.* Two-dimensional nanosheets produced by liquid exfoliation of layered materials. *Science* **331**, 568-571 (2011).
84 Nicolosi, V., Chhowalla, M., Kanatzidis, M. G., Strano, M. S. & Coleman, J. N. Liquid exfoliation of layered materials. *Science* **340** (2013).
85 Lin, Y.-M. *et al.* 100-GHz transistors from wafer-scale epitaxial graphene. *Science* **327**, 662-662 (2010).
86 Novoselov, K. S. *et al.* A roadmap for graphene. *nature* **490**, 192-200 (2012).
87 Geim, A. K. Graphene: status and prospects. *science* **324**, 1530-1534 (2009).
88 Chakraborty, P., Das, T. & Saha-Dasgupta, T. 1.15 MXene: A New Trend in 2D Materials Science. *Comprehensive Nanoscience and Nanotechnology* **319** (2019).
89 Manzeli, S., Ovchinnikov, D., Pasquier, D., Yazyev, O. V. & Kis, A. 2D transition metal dichalcogenides. *Nature Reviews Materials* **2**, 1-15 (2017).
90 Wang, Q. H., Kalantar-Zadeh, K., Kis, A., Coleman, J. N. & Strano, M. S. Electronics and optoelectronics of two-dimensional transition metal dichalcogenides. *Nature nanotechnology* **7**, 699-712 (2012).
91 Levendorf, M. P. *et al.* Graphene and boron nitride lateral heterostructures for atomically thin circuitry. *Nature* **488**, 627-632 (2012).
92 Schaibley, J. R. *et al.* Valleytronics in 2D materials. *Nature Reviews Materials* **1**, 1-15 (2016).
93 Sahoo, R., Pal, A. & Pal, T. 2D materials for renewable energy storage devices: outlook and challenges. *Chemical Communications* **52**, 13528-13542 (2016).
94 Zhang, X., Hou, L., Ciesielski, A. & Samorì, P. 2D materials beyond graphene for high-performance energy storage applications. *Advanced Energy Materials* **6**, 1600671 (2016).
95 Fu, Q. & Bao, X. Surface chemistry and catalysis confined under two-dimensional materials. *Chemical Society Reviews* **46**, 1842-1874

(2017).
96 Lee, C., Wei, X., Kysar, J. W. & Hone, J. Measurement of the elastic properties and intrinsic strength of monolayer graphene. *science* **321**, 385-388 (2008).
97 Castro Neto, A. H., Guinea, F., Peres, N. M. R., Novoselov, K. S. & Geim, A. K. The electronic properties of graphene. *Reviews of modern physics* **81**, 109-162 (2009).
98 Novoselov, K. S. *et al.* Two-dimensional gas of massless Dirac fermions in graphene. *nature* **438**, 197-200 (2005).
99 Zhang, Y., Tan, Y.-W., Stormer, H. L. & Kim, P. Experimental observation of the quantum Hall effect and Berry's phase in graphene. *nature* **438**, 201-204 (2005).
100 Novoselov, K. S. *et al.* Two-dimensional atomic crystals. *Proceedings of the National Academy of Sciences* **102**, 10451-10453 (2005).
101 Chou, S. S. *et al.* Understanding catalysis in a multiphasic two-dimensional transition metal dichalcogenide. *Nature communications* **6**, 1-8 (2015).
102 Dickinson, R. G. & Pauling, L. The crystal structure of molybdenite. *Journal of the American Chemical Society* **45**, 1466-1471 (1923).
103 Mattheiss, L. Band structures of transition-metal-dichalcogenide layer compounds. *Physical Review B* **8**, 3719 (1973).
104 Kasowski, R. Band Structure of Mo S 2 and Nb S 2. *Physical review letters* **30**, 1175 (1973).
105 Mak, K. F., Lee, C., Hone, J., Shan, J. & Heinz, T. F. Atomically thin MoS 2: a new direct-gap semiconductor. *Physical review letters* **105**, 136805 (2010).
106 Böker, T. *et al.* Band structure of MoS 2, MoSe 2, and α− MoTe 2: Angle-resolved photoelectron spectroscopy and ab initio calculations. *Physical Review B* **64**, 235305 (2001).
107 Jellinek, F., Brauer, G. & Müller, H. Molybdenum and niobium sulphides. *Nature* **185**, 376-377 (1960).
108 Wilson, J. A. & Yoffe, A. The transition metal dichalcogenides discussion and interpretation of the observed optical, electrical and structural properties. *Advances in Physics* **18**, 193-335 (1969).
109 Song, I., Park, C. & Choi, H. C. Synthesis and properties of molybdenum disulphide: from bulk to atomic layers. *Rsc Advances* **5**, 7495-7514 (2015).
110 Ryu, Y. K., Frisenda, R. & Castellanos-Gomez, A. Superlattices based on van der Waals 2D materials. *Chemical Communications* **55**, 11498-11510 (2019).
111 Kang, K. *et al.* Layer-by-layer assembly of two-dimensional materials into wafer-scale heterostructures. *Nature* **550**, 229-233 (2017).

112 Masubuchi, S. *et al.* Autonomous robotic searching and assembly of two-dimensional crystals to build van der Waals superlattices. *Nature communications* **9**, 1-12 (2018).
113 Schmidt, H., Rode, J. C., Smirnov, D. & Haug, R. J. Superlattice structures in twisted bilayers of folded graphene. *Nature communications* **5**, 1-7 (2014).
114 Kalikka, J. *et al.* Strain-engineered diffusive atomic switching in two-dimensional crystals. *Nature communications* **7**, 1-8 (2016).
115 Yao, J. *et al.* Optical transmission enhacement through chemically tuned two-dimensional bismuth chalcogenide nanoplates. *Nature Communications* **5**, 1-7 (2014).
116 Kambe, N., Dresselhaus, G. & Dresselhaus, M. Electron diffraction from superlattices in graphite-rubidium intercalation compounds. *Physical Review B* **21**, 3491 (1980).
117 Kambe, N. *et al.* Intercalate ordering in first stage graphite-lithium. *Materials Science and Engineering* **40**, 1-4 (1979).
118 Hastings, J., Ellenson, W. & Fischer, J. Phase Transitions in Potassium-Intercalated Graphite: K C 24. *Physical Review Letters* **42**, 1552 (1979).
119 Parry, G. Structural ordering in intercalation compounds. *Materials Science and Engineering* **31**, 99-106 (1977).
120 Rüdorff, W. & Schulze, E. Über Alkaligraphitverbindungen. *Zeitschrift für anorganische und allgemeine Chemie* **277**, 156-171 (1954).
121 Onn, D. G., Foley, G. & Fischer, J. Electronic properties, resistive anomalies, and phase transitions in the graphite intercalation compounds with K, Rb, and Cs. *Physical Review B* **19**, 6474 (1979).
122 Kambe, N., Mazurek, H., Dresselhaus, M. & Dresselhaus, G. Multi-phase superlattices and phase transitions in graphite intercalation compounds with Rb, Cs, K, Li. *Physica B+ C* **105**, 272-276 (1981).
123 Andersen, A. *et al.* First-principles characterization of potassium intercalation in hexagonal 2H-MoS2. *The Journal of Physical Chemistry C* **116**, 1826-1832 (2012).
124 Eda, G. *et al.* Coherent atomic and electronic heterostructures of single-layer MoS2. *ACS nano* **6**, 7311-7317 (2012).
125 Huang, Q. *et al.* The mechanistic insights into the 2H-1T phase transition of MoS2 upon alkali metal intercalation: from the study of dynamic sodiation processes of MoS2 nanosheets. *Advanced Materials Interfaces* **4**, 1700171 (2017).
126 Enyashin, A. N. *et al.* New route for stabilization of 1T-WS2 and MoS2 phases. *The Journal of Physical Chemistry C* **115**, 24586-24591 (2011).
127 Wypych, F. & Schöllhorn, R. 1T-MoS 2, a new metallic modification of molybdenum disulfide. *Journal of the Chemical Society, Chemical*

Communications, 1386-1388 (1992).
128 Kappera, R. *et al.* Phase-engineered low-resistance contacts for ultrathin MoS 2 transistors. *Nature materials* **13**, 1128-1134 (2014).
129 Wang, X., Shen, X., Wang, Z., Yu, R. & Chen, L. Atomic-scale clarification of structural transition of MoS2 upon sodium intercalation. *ACS nano* **8**, 11394-11400 (2014).
130 Kan, M. *et al.* Structures and phase transition of a MoS2 monolayer. *The Journal of Physical Chemistry C* **118**, 1515-1522 (2014).
131 Eda, G. *et al.* Photoluminescence from chemically exfoliated MoS2. *Nano letters* **11**, 5111-5116 (2011).
132 Calandra, M. Chemically exfoliated single-layer MoS 2: Stability, lattice dynamics, and catalytic adsorption from first principles. *Physical Review B* **88**, 245428 (2013).
133 Guo, C. *et al.* Observation of superconductivity in 1T′-MoS 2 nanosheets. *Journal of Materials Chemistry C* **5**, 10855-10860 (2017).
134 Fang, Y. *et al.* Structural determination and nonlinear optical properties of new 1T‴-type MoS2 compound. *Journal of the American Chemical Society* **141**, 790-793 (2019).
135 Habenicht, C., Lubk, A., Schuster, R., Knupfer, M. & Büchner, B. Investigation of potassium-intercalated bulk MoS 2 using transmission electron energy-loss spectroscopy. *Physical Review B* **101**, 155429 (2020).
136 Pal, B. *et al.* Chemically exfoliated Mo S 2 layers: Spectroscopic evidence for the semiconducting nature of the dominant trigonal metastable phase. *Physical Review B* **96**, 195426 (2017).
137 Singh, A., Shirodkar, S. N. & Waghmare, U. V. 1H and 1T polymorphs, structural transitions and anomalous properties of (Mo, W)(S, Se) 2 monolayers: first-principles analysis. *2D Materials* **2**, 035013 (2015).
138 Novoselov, K., Mishchenko, o. A., Carvalho, o. A. & Neto, A. C. 2D materials and van der Waals heterostructures. *Science* **353** (2016).
139 Wan, J. *et al.* Tuning two-dimensional nanomaterials by intercalation: materials, properties and applications. *Chemical Society Reviews* **45**, 6742-6765 (2016).
140 Cao, Y. *et al.* Unconventional superconductivity in magic-angle graphene superlattices. *Nature* **556**, 43-50 (2018).
141 Li, X., Wang, X., Zhang, L., Lee, S. & Dai, H. Chemically derived, ultrasmooth graphene nanoribbon semiconductors. *science* **319**, 1229-1232 (2008).
142 Zhang, J. *et al.* Reversible and selective ion intercalation through the top surface of few-layer MoS 2. *Nature communications* **9**, 1-9 (2018).
143 Zhang, R. *et al.* Superconductivity in potassium-doped metallic

polymorphs of MoS2. *Nano letters* **16**, 629-636 (2016).
144 Shu, Z., McMillan, R. & Murray, J. Electrochemical intercalation of lithium into graphite. *Journal of The Electrochemical Society* **140**, 922 (1993).
145 Sole, C., Drewett, N. E. & Hardwick, L. J. In situ Raman study of lithium-ion intercalation into microcrystalline graphite. *Faraday Discussions* **172**, 223-237 (2014).
146 Zeng, F. *et al.* Synthesis of mixed alcohols with enhanced C3+ alcohol production by CO hydrogenation over potassium promoted molybdenum sulfide. *Applied Catalysis B: Environmental* **246**, 232-241 (2019).
147 Yang, X. *et al.* Preparation and characterization of a new metal-intercalated graphite superconductor. *Materials Research Express* **6**, 016003 (2018).
148 Somoano, R. & Rembaum, A. Superconductivity in intercalated molybdenum disulfide. *Physical Review Letters* **27**, 402 (1971).
149 Xue, M. *et al.* Superconductivity in potassium-doped few-layer graphene. *Journal of the American Chemical Society* **134**, 6536-6539 (2012).
150 Attanayake, N. H. *et al.* Effect of intercalated metals on the electrocatalytic activity of 1T-MoS2 for the hydrogen evolution reaction. *ACS Energy Letters* **3**, 7-13 (2017).
151 Ambrosi, A., Sofer, Z. & Pumera, M. Lithium intercalation compound dramatically influences the electrochemical properties of exfoliated MoS2. *Small* **11**, 605-612 (2015).
152 Yu, Y. *et al.* High phase-purity 1T′-MoS 2-and 1T′-MoSe 2-layered crystals. *Nature chemistry* **10**, 638-643 (2018).
153 Sun, J. *et al.* A phosphorene–graphene hybrid material as a high-capacity anode for sodium-ion batteries. *Nature nanotechnology* **10**, 980-985 (2015).
154 Xu, Z.-L. *et al.* Tailoring sodium intercalation in graphite for high energy and power sodium ion batteries. *Nature communications* **10**, 1-10 (2019).
155 Rehman, J., Fan, X., Laref, A., Dinh, V. A. & Zheng, W. Potential anodic applications of 2D MoS2 for K-ion batteries. *Journal of Alloys and Compounds* **865**, 158782 (2021).
156 Fan, X. *et al.* Fast and efficient preparation of exfoliated 2H MoS2 nanosheets by sonication-assisted lithium intercalation and infrared laser-induced 1T to 2H phase reversion. *Nano letters* **15**, 5956-5960 (2015).
157 Jawaid, A. *et al.* Mechanism for liquid phase exfoliation of MoS2. *Chemistry of Materials* **28**, 337-348 (2016).
158 Bang, G. S. *et al.* Effective liquid-phase exfoliation and sodium ion battery application of MoS2 nanosheets. *ACS applied materials &*

interfaces **6**, 7084-7089 (2014).
159 He, H., Huang, C., Luo, C.-W., Liu, J.-J. & Chao, Z.-S. Dynamic study of Li intercalation into graphite by in situ high energy synchrotron XRD. *Electrochimica Acta* **92**, 148-152 (2013).
160 Kim, H., Yoon, G., Lim, K. & Kang, K. A comparative study of graphite electrodes using the co-intercalation phenomenon for rechargeable Li, Na and K batteries. *Chemical Communications* **52**, 12618-12621 (2016).
161 Dresselhaus, M. S. & Dresselhaus, G. Intercalation compounds of graphite. *Advances in physics* **51**, 1-186 (2002).
162 Nixon, D. & Parry, G. Formation and structure of the potassium graphites. *Journal of Physics D: Applied Physics* **1**, 291 (1968).
163 Somoano, R., Hadek, V. & Rembaum, A. Alkali metal intercalates of molybdenum disulfide. *The Journal of Chemical Physics* **58**, 697-701 (1973).
164 Xiong, F. *et al.* Li intercalation in MoS2: in situ observation of its dynamics and tuning optical and electrical properties. *Nano letters* **15**, 6777-6784 (2015).
165 Zhou, X. *et al.* Intercalation of two-dimensional layered materials. *Chemical Research in Chinese Universities*, 1-13 (2020).
166 Stark, M. S., Kuntz, K. L., Martens, S. J. & Warren, S. C. Intercalation of layered materials from bulk to 2D. *Advanced Materials* **31**, 1808213 (2019).
167 DiVincenzo, D. & Rabii, S. Theoretical investigation of the electronic properties of potassium graphite. *Physical Review B* **25**, 4110 (1982).
168 Thinius, S., Islam, M. M., Heitjans, P. & Bredow, T. Theoretical study of Li migration in lithium–graphite intercalation compounds with dispersion-corrected DFT methods. *The Journal of Physical Chemistry C* **118**, 2273-2280 (2014).
169 Li, Y., Lu, Y., Adelhelm, P., Titirici, M.-M. & Hu, Y.-S. Intercalation chemistry of graphite: alkali metal ions and beyond. *Chemical Society Reviews* **48**, 4655-4687 (2019).
170 Xu, Z. *et al.* Dispersion-corrected DFT investigation on defect chemistry and potassium migration in potassium-graphite intercalation compounds for potassium ion batteries anode materials. *Carbon* **107**, 885-894 (2016).
171 Wang, Z., Selbach, S. M. & Grande, T. Van der Waals density functional study of the energetics of alkali metal intercalation in graphite. *Rsc Advances* **4**, 4069-4079 (2014).
172 Boesenberg, U. *et al.* Electronic structure changes upon lithium intercalation into graphite–Insights from ex situ and operando x-ray Raman spectroscopy. *Carbon* **143**, 371-377 (2019).
173 Stutz, G. E. *et al.* Intercalation stage dependence of core electronic

excitations in Li-intercalated graphite from inelastic X-ray scattering. *Applied Physics Letters* **110**, 253901 (2017).

174 Xu, J. *et al.* Recent progress in graphite intercalation compounds for rechargeable metal (Li, Na, K, Al)-ion batteries. *Advanced Science* **4**, 1700146 (2017).

175 Friend, R. & Yoffe, A. Electronic properties of intercalation complexes of the transition metal dichalcogenides. *Advances in Physics* **36**, 1-94 (1987).

176 Wang, Z., Ratvik, A. P., Grande, T. & Selbach, S. M. Diffusion of alkali metals in the first stage graphite intercalation compounds by vdW-DFT calculations. *Rsc Advances* **5**, 15985-15992 (2015).

177 Kim, H. *et al.* Recent progress and perspective in electrode materials for K-ion batteries. *Advanced Energy Materials* **8**, 1702384 (2018).

178 Zhao, J., Zou, X., Zhu, Y., Xu, Y. & Wang, C. Electrochemical intercalation of potassium into graphite. *Advanced Functional Materials* **26**, 8103-8110 (2016).

179 Kuhne, M. *et al.* Ultrafast lithium diffusion in bilayer graphene. *Nat Nanotechnol* **12**, 895-900, doi:10.1038/nnano.2017.108 (2017).

180 Lee, E. & Persson, K. A. Li absorption and intercalation in single layer graphene and few layer graphene by first principles. *Nano Lett* **12**, 4624-4628, doi:10.1021/nl3019164 (2012).

181 Mandeltort, L. & Yates, J. T. Rapid Atomic Li Surface Diffusion and Intercalation on Graphite: A Surface Science Study. *The Journal of Physical Chemistry C* **116**, 24962-24967, doi:10.1021/jp308101c (2012).

182 Wang, L. *et al.* A better understanding of the capacity fading mechanisms of Li 3 V 2 (PO 4) 3. *RSC Advances* **5**, 71684-71691 (2015).

183 Wang, L. *et al.* Graphite as a potassium ion battery anode in carbonate-based electrolyte and ether-based electrolyte. *Journal of Power Sources* **409**, 24-30 (2019).

184 Chen, S. *et al.* Atomic structure and migration dynamics of MoS2/LixMoS2 interface. *Nano energy* **48**, 560-568 (2018).

185 Wang, L., Xu, Z., Wang, W. & Bai, X. Atomic mechanism of dynamic electrochemical lithiation processes of MoS2 nanosheets. *Journal of the American Chemical Society* **136**, 6693-6697 (2014).

186 Gao, P., Wang, L., Zhang, Y., Huang, Y. & Liu, K. Atomic-scale probing of the dynamics of sodium transport and intercalation-induced phase transformations in MoS2. *ACS nano* **9**, 11296-11301 (2015).

187 Li, Y., Wu, D., Zhou, Z., Cabrera, C. R. & Chen, Z. Enhanced Li Adsorption and Diffusion on MoS2 Zigzag Nanoribbons by Edge Effects: A Computational Study. *J Phys Chem Lett* **3**, 2221-2227, doi:10.1021/jz300792n (2012).

188 Su, J., Pei, Y., Yang, Z. & Wang, X. Ab initio study of graphene-like monolayer molybdenum disulfide as a promising anode material for rechargeable sodium ion batteries. *RSC Adv.* **4**, 43183-43188, doi:10.1039/c4ra06557c (2014).
189 McKeen, L. W. Introduction to permeation of plastics and elastomers. *Permeability Properties of Plastics and Elastomers*, 1-12 (2012).
190 Park, M., Zhang, X., Chung, M., Less, G. B. & Sastry, A. M. A review of conduction phenomena in Li-ion batteries. *Journal of power sources* **195**, 7904-7929 (2010).
191 Chung, D., Dresselhaus, G. & Dresselhaus, M. Intralayer crystal structure and order-disorder transformations of graphite intercalation compounds using electron diffraction techniques. *Materials Science and Engineering* **31**, 107-114 (1977).
192 Parry, G. & Nixon, D. Order–Disorder Transformation in Potassium Graphite. *Nature* **216**, 909-910 (1967).
193 Zabel, H., Moss, S., Caswell, N. & Solin, S. X-ray Study of Intercalate Order-Disorder Transition in C 24 K. *Physical Review Letters* **43**, 2022 (1979).
194 Parry, G. S., Nixon, D., Lester, K. & Levene, B. Order-disorder transformations in rubidium and caesium graphites. *Journal of Physics C: Solid State Physics* **2**, 2156 (1969).
195 Luo, W. *et al.* Potassium ion batteries with graphitic materials. *Nano letters* **15**, 7671-7677 (2015).
196 Jian, Z., Luo, W. & Ji, X. Carbon electrodes for K-ion batteries. *Journal of the American chemical society* **137**, 11566-11569 (2015).
197 Schweidler, S. *et al.* Volume changes of graphite anodes revisited: a combined operando X-ray diffraction and in situ pressure analysis study. *The Journal of Physical Chemistry C* **122**, 8829-8835 (2018).
198 Kim, H. *et al.* Sodium intercalation chemistry in graphite. *Energy & Environmental Science* **8**, 2963-2969 (2015).
199 Daumas, N. & Herold, A. Relations between phase concept and reaction mechanics in graphite insertion compounds. *Comptes Rendus Hebdomadaires Des Seances De L Academie Des Sciences Serie C* **268**, 373-& (1969).
200 Sethuraman, V. A., Hardwick, L. J., Srinivasan, V. & Kostecki, R. Surface structural disordering in graphite upon lithium intercalation/deintercalation. *Journal of Power Sources* **195**, 3655-3660 (2010).
201 Rüdorff, W. & Hofmann, U. Über graphitsalze. *Zeitschrift für anorganische und allgemeine Chemie* **238**, 1-50 (1938).
202 Gavilán-Arriazu, E. M. *et al.* The kinetic origin of the Daumas-Hérold model for the Li-ion/graphite intercalation system. *Electrochemistry Communications* **93**, 133-137 (2018).
203 Drüe, M., Seyring, M. & Rettenmayr, M. Phase formation and

microstructure in lithium-carbon intercalation compounds during lithium uptake and release. *Journal of Power Sources* **353**, 58-66 (2017).

204 Liu, J. *et al.* Unraveling the potassium storage mechanism in graphite foam. *Advanced Energy Materials* **9**, 1900579 (2019).

205 Berker, A., Kambe, N., Dresselhaus, G. & Dresselhaus, M. Island Growth and Orientational Locking of Potassium Intercalated in Graphite. *Physical Review Letters* **45**, 1452 (1980).

206 Oshida, K. *et al.* Image analysis of TEM pictures of fluorine-intercalated graphite fibers. *Journal of materials research* **8**, 512-522 (1993).

207 Pollak, E. *et al.* The interaction of Li+ with single-layer and few-layer graphene. *Nano letters* **10**, 3386-3388 (2010).

208 Bonaccorso, F. *et al.* Graphene, related two-dimensional crystals, and hybrid systems for energy conversion and storage. *Science* **347** (2015).

209 Raccichini, R., Varzi, A., Wei, D. & Passerini, S. Critical insight into the relentless progression toward graphene and graphene-containing materials for lithium-ion battery anodes. *Advanced materials* **29**, 1603421 (2017).

210 Lee, E. & Persson, K. A. Li absorption and intercalation in single layer graphene and few layer graphene by first principles. *Nano letters* **12**, 4624-4628 (2012).

211 Ji, K. *et al.* Lithium intercalation into bilayer graphene. *Nature communications* **10**, 1-10 (2019).

212 Sugawara, K., Kanetani, K., Sato, T. & Takahashi, T. Fabrication of Li-intercalated bilayer graphene. *AIP Advances* **1**, 022103 (2011).

213 Wyckoff, R. W. G. & Wyckoff, R. W. *Crystal structures*. Vol. 1 (Interscience publishers New York, 1963).

214 Barrett, C. S. A low temperature transformation in lithium. *Physical Review* **72**, 245 (1947).

215 Xu, Y., Kang, J., Hersam, M. C., Wu, J. & Dravid, V. P. Lithium electrochemistry of WS2 nanoflakes studied by in-situ TEM. *Microscopy and Microanalysis* **24**, 1860-1861 (2018).

216 Kim, S., Dravid, V. P. & He, K. In Situ Atomic-Scale TEM Observation of Phase Transformation in Two-Dimensional SnSe2 Single Crystals. *Microscopy and Microanalysis* **24**, 1862-1863 (2018).

217 Li, P. *et al.* Electrochemical potassium/lithium-ion intercalation into TiSe2: kinetics and mechanism. *Energy Storage Materials* **16**, 512-518 (2019).

218 Hwang, S. *et al.* Multistep lithiation of tin sulfide: an investigation using in situ electron microscopy. *ACS nano* **12**, 3638-3645 (2018).

219 Li, Q. *et al.* Intermediate phases in sodium intercalation into MoS2

nanosheets and their implications for sodium-ion batteries. *Nano Energy* **38**, 342-349 (2017).

220 Débart, A., Dupont, L., Patrice, R. & Tarascon, J.-M. Reactivity of transition metal (Co, Ni, Cu) sulphides versus lithium: The intriguing case of the copper sulphide. *Solid state sciences* **8**, 640-651 (2006).

221 McDowell, M. T. *et al.* In situ observation of divergent phase transformations in individual sulfide nanocrystals. *Nano letters* **15**, 1264-1271 (2015).

222 He, K. *et al.* Kinetically-driven phase transformation during lithiation in copper sulfide nanoflakes. *Nano letters* **17**, 5726-5733 (2017).

223 Chen, G.-Y. *et al.* Conversion and displacement reaction types of transition metal compounds for sodium ion battery. *Journal of Power Sources* **284**, 115-121 (2015).

224 Jache, B., Mogwitz, B., Klein, F. & Adelhelm, P. Copper sulfides for rechargeable lithium batteries: Linking cycling stability to electrolyte composition. *Journal of Power Sources* **247**, 703-711 (2014).

225 Chung, J.-S. & Sohn, H.-J. Electrochemical behaviors of CuS as a cathode material for lithium secondary batteries. *Journal of power sources* **108**, 226-231 (2002).

226 Wang, Y., Zhang, X., Chen, P., Liao, H. & Cheng, S. In situ preparation of CuS cathode with unique stability and high rate performance for lithium ion batteries. *Electrochimica acta* **80**, 264-268 (2012).

227 Ren, Y., Wei, H., Yang, B., Wang, J. & Ding, J. "Double-Sandwich-Like" CuS@ reduced graphene oxide as an anode in lithium ion batteries with enhanced electrochemical performance. *Electrochimica Acta* **145**, 193-200 (2014).

Chapter 5

Thermal Deintercalation of K-doped MoS_2 Analysed via *In-situ* TEM

This chapter discusses structural and chemical variations of the K-doped MoS_2 flake heated at different temperatures using *in-situ* TEM. Studying the dynamics of the K deintercalation in the van der Waal crystal, as a reverse process of intercalation, is applied in order to understand the intercalation process and the accompanying phase and compositional changes. In addition, studying deintercalation also can support numerous researches of two-dimensional materials such as yield promotion for intercalation-assisted liquid exfoliation, preparation of the specific MoS_2 phase for optoelectronic and catalytic applications. However, K-doped MoS_2 is the very air-sensitive material where intercalated K ions readily deintercalate from the interlayer gallery spacings. *In-situ* TEM heating of the specimen allows a controlled environment to study the degradation, enables the identical flake to be imaged at different time points and prevents the structural changes that might be induced by the air exposure when transferring the sample after the *ex-situ* heat treatment.

In this manuscript, we analyse the prepared K-doped MoS_2 flakes using the TEM electron diffraction and STEM with EDS to determine the superstructures formed in the fresh specimen as well as the quantitative K content and elemental distribution. We perform comprehensive characterisations of the specimen after heating at three different

temperatures (from room temperature to 300 °C) to characterise the structural and chemical variations of the material. Selected area electron diffraction (SAED) confirms the change of local K ordering and the relaxation of host MoS_2 lattice, and STEM-EDS suggests K deintercalation in the flake following first-order kinetics.

Author Contributions

S. Shao performed all S/TEM and SAED imaging, STEM-EDS data collection, STEM and SAED simulation and image analysis and STEM-EDS spectral image analysis. W. J. Kuang prepared K intercalated MoS_2 sample. This manuscript was drafted by S. Shao, with contributions and edits from D. Kelly, S.J. Haigh and I. V. Grigorieva and it has not been submitted.

Thermal Deintercalation of K-doped MoS_2 Analysed via *In-situ* TEM

Shouqi Shao[1,2], Daniel J. Kelly[1,2,4†], W. J. Kuang[3] , Irina V. Grigorieva[2,3ϕ] and Sarah J. Haigh[1,2*]

[1] *Department of Materials, University of Manchester, Oxford Road, Manchester M13 9PL, United Kingdom*

[2] *National Graphene Institute, University of Manchester, Oxford Road, Manchester M13 9PL, United Kingdom*

[3] *Department of Physics and Astronomy, University of Manchester, Oxford Road, Manchester M13 9PL, United Kingdom*

[4] *DTU Nanolab, Technical University of Denmark, DK-2800, Kgs. Lyngby, Denmark*

Corresponding author email: *sarah.haigh@manchester.ac.uk; †dankel@dtu.dk; ϕirina.grigorieva@manchester.ac.uk;

Keywords: *In-situ* S/TEM, SAED, EDS spectrum imaging, alkali metal intercalation, first order kinetics, $KMoS_2$

Abstract

Understanding intercalation and deintercalation is vital for the development of nanoelectronics, solid-state batteries and catalysts, yet the structural changes associated particularly with deintercalation remain poorly understood. Here, we present a quantitative study of deintercalation dynamics in K-intercalated MoS_2 as a function of temperature, using *in-situ* atomic resolution scanning transmission electron microscopy (STEM)

imaging, selected area electron diffraction (SAED) and energy dispersive X-ray spectroscopy (EDS). These methods reveal the presence of previously unknown intermediate superstructures, supporting a layer-by-layer deintercalation mechanism of the intercalant which maintains local K ordering within the interlayer space. Systematic time-temperature measurements during deintercalation demonstrate first order kinetics, allowing compositional and superstructural changes to be predicted for practical operating temperatures (room temperature to 300 °C). Furthermore, we expect that this *in-situ* correlative STEM-EDS/SAED methodology can be further extended to determine optimal synthesis, processing and working conditions for a variety of intercalated or pillared materials.

5.1 Introduction

Intercalation of layered van der Waals crystals such as graphite, transition metal dichalcogenides (TMDCs) and MXenes with dopant atoms is an established method for tuning the material's chemical, electronic and optical properties[1-9]. Among the diverse family of intercalated 2D materials and possible dopant atom species, alkali metal intercalated MoS_2 has potential applications in nanoelectronics and optoelectronics, as well as supercapacitors and batteries.[6,10-12] According to the relative arrangement of Mo and S atoms within the hexagonal layers, MoS_2 can exist in three different phases: trigonal prismatic (2H)[13], octahedral (1T)[14,15], and distorted octahedral with Mo-Mo zigzag chains (1T'), tetramerized Mo atoms in diamondlike cluster (1T'') or corner-sharing Mo_3 triangular trimers (1T''')[10,16-18]. Intercalation of alkali metals, such as Li, Na and K, between the MoS_2 layers induces a phase transition from the most stable 2H phase to the rarer 1T or disordered 1T octahedral phases[8]. This process is driven by charge transfer, where the alkali intercalants donate an electron from the valence *s* orbital of the alkali metal to the *d* orbital of the transition

metal closing the material's bandgap and leading to a change in the electronic structure from semiconducting (2H) to metallic (1T/1T'/1T'') or semiconducting (1T''')[8,18,19]. The induced 1T or disordered 1T phase persists in the host even after the intercalant is removed although the semiconducting 2H phase can be restored via annealing[13,17,18,20]. Consequently intercalation-driven phase transformations can be exploited to prepare exfoliated sheets of MoS_2 in different 1T phases, which are difficult to synthesize directly in bulk form[21,22]. The resulting change in electronic structure can be harnessed in nanoelectronic applications, for example, leading to a change in the critical temperature for superconductivity (T_c)[11,12] and reduced contact resistance[6]. The metallic 1T phase of MoS_2 is also desirable in catalytic applications; in particular having been shown to enhance the efficiency of the hydrogen evolution reaction[22]. Nonetheless, optimal deintercalation conditions that preserve the phase transformation in the host lattice, whilst removing deleterious effects from remanent alkali elements are laborious and would benefit from better understanding of the deintercalation mechanisms. Significant interest in the deintercalation behaviour of MoS_2 also stems from the materials potential applications in solid-state batteries and supercapacitor systems, which exploit the great efficiency and reversibility whereby large K^+ and Na^+ ions can be inserted and withdrawn from the lattice[23-25]. The lifetimes and cyclabilities of these energy storage devices are highly dependent on the kinetics of alkali metal intercalation and deintercalation during charge/discharge processes[26], motivating further research efforts to understand the underlying mechanisms so as to optimize long term

performance.

Structure-property relationships in intercalated/deintercalated materials are thus of wide scientific interest. Electrochemical intercalation of alkali-metal (Li and Na) intercalated MoS_2 has been effectively studied using *in-situ* electrical biasing in the transmission electron microscope (TEM)[27-29]. The insights gleaned from the combination of high-resolution imaging and controlled electrical stimulus have been used to gain mechanistic knowledge of the process, including demonstration of local superstructure evolution, phase transition and diffusion kinetics[27-29]. Additionally, the majority of the TEM characterisation to date has focused on intercalation, while deintercalation, the reverse process, has not been subject to the same level of characterisation. Indeed, it is unknown whether deintercalation involves similar structural transitions, and no studies have focused on the kinetics governing local compositional changes during deintercalation. Deintercalation occurs spontaneously in alkali-metal intercalated MoS_2 materials, with the intercalated alkali ions escaping from the host lattice on exposure to heat[30], air[12] and moisture[31]. This has been shown, for example, to influence the system's superconducting properties[12,31] and catalytic activity[2]. Despite the importance of the deintercalation process for energy storage applications, as well as a need to control its effects in nanoelectronics applications, currently there is a lack of detailed mechanistic knowledge in the area. Hence, a better understanding of the structural and chemical changes occurring during the loss of alkali metal ions from MoS_2 crystals is highly desirable. Here we use *in-situ* TEM to characterize the structural and chemical changes that

occur when annealing K-intercalated MoS_2 as a function of temperature. We combine multiple *in-situ* electron microscopy methods (electron diffraction (ED), high-resolution TEM (HR-TEM), and scanning transmission electron microscopy (STEM) with quantitative energy dispersive X-ray spectroscopy (EDS) spectrum imaging) to provide new understanding of the dynamics of thermally induced alkali ion deintercalation in intercalated MoS_2, including new superstructures and direct correlation of local crystal structure and composition.

5.2 Structural Characterisation of Intercalated MoS_2

The well-known liquid-ammonia method was used to achieve K intercalation into MoS_2[32]. In brief, MoS_2 powder is immersed in a liquid ammonia solution containing K at -78 °C for 24 hours. Dissolved K atoms dissociate into solvated cations (K^+) and solvated electrons (e^-) in the ammonia solution[33]. Solvated electrons are provided to the empty Mo *d*-bands of 2H-MoS_2 as K^+ ions intercalate into the interlayer gallery of the layered crystal to balance the charges[12]. Following intercalation, the dried powder was stored under argon before transferring a thin layer of intercalated crystals onto TEM heating E-chips and rapidly loading these into the TEM to minimize exposure to oxygen (see Methods for further details).

STEM-EDS elemental analysis of twenty-five individual K-doped MoS_2 flakes in the as-synthesised condition revealed a mean K concentration (*c*) of 20.4±7.0 at% corresponding to a stoichiometry of $K_{0.77\pm0.24}MoS_2$. Detailed analysis of the 1300-1700 individual pixels (pixels

size range between 20 nm -30 nm) comprising the spectrum image for each flake reveals significant local compositional variance in the K/Mo ratio, as shown in Fig. 5.1a. Fig.5.1b shows a representative HAADF STEM image of a typical K intercalated MoS_2 flake, and the corresponding SAED pattern viewed along [0001] (Fig. 5.1c) acquired from the area of the selected-area aperture indicated by the red circle in Fig. 5.1b. This flake has mean K/Mo ratio, $n = 0.84$, equivalent to 21.8 at% K as shown in Fig. 5.1c and the measured K/Mo ratio in the selected area aperture (red circle) is about 0.71(equivalent to 19.1 at% K). The electron diffraction pattern (Fig. 5.1d) shows superlattice spots along the $[11\bar{2}0]$ and $[10\bar{1}0]$ directions with two-fold periodicity, thus the superlattice spots closest to the directly transmitted beam are labelled $\frac{1}{2}11\bar{2}0$ and $\frac{1}{2}10\bar{1}0$ and Fig. 5.1e shows a corresponding simulated diffraction pattern. The origin of these superlattice reflections can be assigned either to intercalation-induced zigzag chains of Mo atoms as in the 1T' structure[34], or to ordering of the alkali ions between the layers[35]. To determine which of these is responsible we have performed atomic resolution high angle annular dark field (HAADF) STEM imaging of the crystal structure and compared this to image simulations (Fig. 5.1, S5.6, S5.7, S5.8). The zigzag chains of the 1T' phase make it readily distinguishable from the 1T or 2H phases in an atomic resolution image (Fig. 5.1f-h, S5.8). Although the coexistence of these three different MoS_2 polytypes is observed in different regions of the crystal, only one small region has the 1T' crystal structure and this is on the opposite edge to the SAED region (Fig. 5.1b, h). Thus, as majority of the crystalline flake appears to be either the 2H (trigonal prismatic) or 1T

(octahedral) phases (Fig. 5.1f, g), which do not produce superlattice reflections, this data suggests that the superlattice reflections form due to K atom ordering. Because of the measured K concentration in the selected area being 0.71 at%, an atomic model was produced for $K_{0.75}MoS_2$ where the intercalated K atoms periodically occupy 75% of the possible interstitial hexagonal sites in each layer, with pseudo-octahedral S atom coordination (see Fig. 5.1i, S5.12c-g). In this $K_{0.75}MoS_2$ model structure (Fig. 5.1e) the host MoS_2 lattice was included as the 1T phase since this was found to be the most abundant experimentally. This model is in line with theoretical predictions[36,37] and previous experimental observations for alkali metal intercalants in MoS_2,[38] and our simulations reproduce the superlattice positions present in the experimental SAED in Fig. 5.1d.

Closer inspection of the experimental electron diffraction pattern in Fig. 5.1d reveals a splitting of the host lattice $11\bar{2}0$ and $10\bar{1}0$ diffraction spots, with inner and outer positions highlighted by the dashed red and yellow hexagons respectively. The outer $11\bar{2}0$ spots correspond to the lattice constant a = 3.16 Å (d-spacing = 1.58 Å), which is the same as that of the pristine 2H MoS_2 crystal. The inner spots correspond to a 3% dilation of the hexagonal structure, a = 3.26 Å, close to the simulated structure predicted for $K_{0.75}MoS_2$ by Andersen et al. (a = 3.36 Å), where the lattice expansion is caused by the K intercalant[37]. In our experimental data the position of the superlattice reflections (marked by cyan arrows in Fig. 5.1d) shows that they are related to the expanded host lattice (indicated by the inner red dashed hexagons), which supports the conclusion that both host lattice expansion and superlattice formation are the result of the K

intercalation. It also confirms that the splitting of the diffraction spots is not related to local crystal bending/disorder at the nanoscale, which would be expected to produce streaking in all diffraction spots.

This splitting of the diffraction spots is evidence of the coexistence of different levels of intercalation within individual flakes and within the ~500 nm diameter region of the selected area aperture. Similar splitting has been observed previously in $LiMoS_2$ intercalated samples although the difference in the lattice constants for the intercalated and pristine phases was larger at ~6%[35]. The smaller expansion seen here maybe due to a difference in the composition of the intercalant between our work to the literature as no complementary EDS was available in the $LiMoS_2$ study.

The observations of the coexistence of two lattice constants and of different polytypes within a single flake suggests significant compositional variations. Earlier work has suggested that the trigonal prismatic (2H) coordination exists when $n < 0.4$ ($c < 11.8$ at% K), octahedral (1T) coordination for $0.4 < n < 1$ (11.8 at% $< c <$ 25.0 at% K) and the 1T' phase is present for $n > 1$ ($c > 25.0$ at%)[12,31] in the K_nMoS_2 crystal, although in the latter case the excess K is reported to cause disintegration of the MoS_2 layers[12]. The presence of all three phases (2H, 1T and 1T') therefore likely reflects local K content variations from $n<0.4$ to $n>1$. Previously it was not possible to directly compare structural and compositional variations, but our quantitative STEM-EDS elemental mapping of individual flakes does indeed reveal nanoscale K/Mo variations of this magnitude (Fig. 5.1a and c).

The analysis presented in Fig. 5.1 is broadly representative of the

mean composition for the majority of the 25 flakes studied in this work. However, it is interesting to note that one K_nMoS_2 flake with an unusually low $n = 0.27$ showed a superlattice arrangement not previously reported for this material (Fig. S5.10a). We assign this to a $2a \times \sqrt{3}a$ superstructure arrangement (Fig. S5.10c-g). Previously this structure has only been reported as an intermediate intercalation phase for $Na_{0.25}MoS_2$ produced via electrochemical intercalation but our measurements confirm it is similarly stable as part of the structural complexity in K_nMoS_2[29,39].

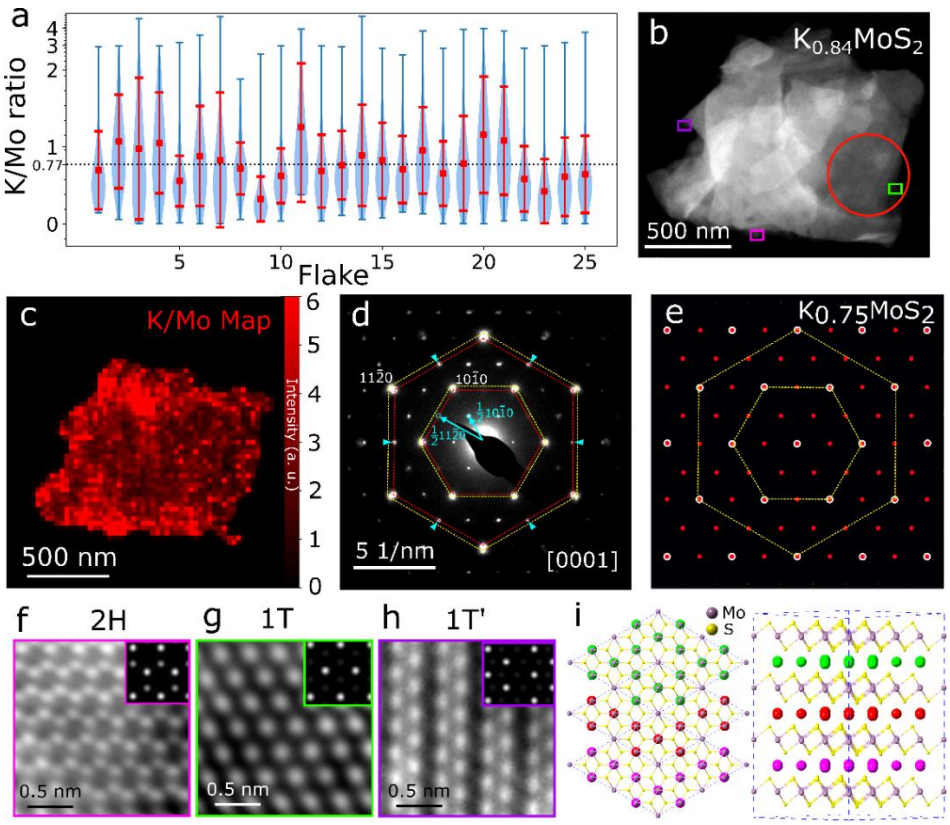

Figure 5.1 (S)TEM characterisation and atomic structure of K-doped MoS_2 flakes. (a) Violin plot of K/Mo ratio in 25 as-synthesised K-intercalated MoS_2 flakes. Red square in each subplot indicates the mean K/Mo ratio for the individual flake, with the standard deviation shown by the red error bars. Blue bars indicate the maximum and minimum measurements and the shadows illustrate the distribution and local variance in K/Mo ratio for individual flakes. (b) HAADF STEM image of a K intercalated MoS_2 flake with the average K concentration of 21.9 at% (corresponding to stoichiometry of $K_{0.84}MoS_2$). (c) EDS map of K/Mo distribution. (d) SAED pattern for the area indicated by the red circle in (b). Yellow and red dashed hexagons highlight reflections with different lattice constants corresponding to the pristine MoS_2 and the intercalated phase, respectively. Cyan arrow heads point to the extra superlattice spots seen only in the intercalated phase. (e) Simulated diffraction pattern of $K_{0.75}MoS_2$ (see panel (i) and SI Fig. S5.12 for structural model). The MoS_2 lattice reflections are depicted with white edges while the extra spots from the ordered K are shown as smaller red dots. (e) STEM-EDS K/Mo ratio map for the flake in (b). (f-h) Experimental HAADF STEM images of 2H (trigonal prismatic), 1T (octahedral) and 1T' (zigzag chains of Mo) phases acquired from the magenta, green and purple rectangles in (b). Simulated HAADF images are shown inset for reference. (i) Atomic model of $K_{0.75}MoS_2$ used for the diffraction simulation (d), where green, red and magenta balls indicate K atoms in different interlayers. In the plan view model (left) the different atomic layers are off-set for clarity.

5.3 Structural and Compositional Changes during Deintercalation

The large structural complexity demonstrated here and in the literature for intercalated materials[27,29], provides strong motivation for *in-situ* microscopy measurements where deintercalation of a K_nMoS_2 flake can be studied, thereby avoiding uncertainty regarding the starting material. In this work we study the changes in 20 K_nMoS_2 flakes during thermal deintercalation. Our *in-situ* studies employ fixed temperatures of 25, 150, 200 and 300 °C, a range which encompasses typical temperatures used in the fabrication of K-doped MoS_2 devices and their working conditions. Fig. 5.2g shows a schematic of the *in-situ* TEM experimental setup, where K-doped MoS_2 flakes are dispersed on a resistive heating membrane and holes in the membrane allow analysis of suspended 2D flakes.

Fig. 5.2a-d shows consecutive *in-situ* SAED patterns acquired from a $K_{0.65}MoS_2$ crystal at hourly increments at a temperature of 300 °C. This data reveals changes in the diffracted spot positions and intensities – suggesting compositional and structural changes occurring as the intercalated material is heated for 3 hours. Similar to Fig. 5.1d, splitting of the host lattice reflections is again visible in the starting material (representative $11\bar{2}0$ spot shown inset in Fig. 5.2a) with the inner (expanded) peak corresponding to the intercalated lattice having a higher intensity than the peak for the pristine lattice at $t = 0$. After 2 hours there is a notable increase in the intensity of the outer (pristine) spot, and after 3 hours the inner spot is no longer visible (insets in Fig. 5.2b-d). The loss of

the inner diffraction spots also corresponds to a loss of intensity of the superlattice reflections (Fig. 5.2e, f) with these being completely absent after 3 hours heating and only the expected diffraction spots from the pristine 2H phase remaining. This loss of superlattice spots after deintercalation is consistent with an earlier study from Chrissafis et al.[35], although this earlier work found that the lattice expansion was retained after heating. The difference is likely due to they may not achieve full deintercalation although superlattice reflections disappeared, since the higher temperature used here (300 °C vs 220 °C in the earlier work).

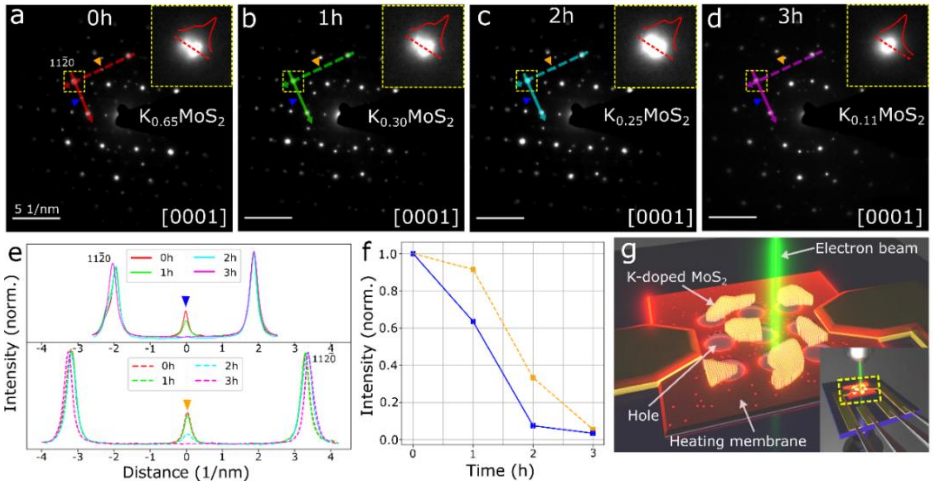

Figure 5.2 Phase transitions in K-doped MoS_2 observed by *in-situ* SAED. Selected area electron diffraction patterns of a single K-doped MoS_2 flake captured (a) before and (b) after 1 h, (c) 2 h and (d) 3 h heating at 300 °C, respectively. Insets in (a-d) show the splitting of the $11\bar{2}0$ diffraction spots, and how this evolves during heating. The relative peak intensities in the extracted $11\bar{2}0$ intensity profiles are further analysed in Fig. S5.9. The solid and dashed arrows indicate the positions of the extracted intensity profiles shown in (e). The orange and blue markers indicate the positions of two reciprocal superlattice spots further analysed by the intensity line profiles in (f). (e) Comparison of the intensity profiles from the *in-situ* SAED patterns for two crystallographic directions (marked by the solid and dashed lines in (a-d)). (f) Demonstration of the loss in superlattice spot intensity, measured from line profiles (e), as a function of heating time. (g) Schematic illustration of the K-doped MoS_2 flakes on the resistive heating E-chip membrane.

Previous studies of the intercalated 2D materials have combined electron microscopy with *ex-situ* elemental analysis via measuring the charge transferred during electrolysis[30], scanning electron microscope (SEM)-EDS[12], X-ray photoelectron spectroscopy (XPS)[40] or inductively coupled plasma optical emission spectrometry (ICP-OES)[2]. Here we combine *in-situ* SAED with *in-situ* STEM-EDS to correlate the observed structure and composition during deintercalation, by measuring the K concentration and electron diffraction for multiple flakes at hourly intervals over a range of heating temperatures. Compared to the *ex-situ* material characterisations, our *in-situ* technique avoids undesirable degradation of the specimen and monitors the changes in real time. In addition to this, STEM-EDS spectral imaging technique provides a flexible dataset for the post data processing. To prevent unwanted signals from the surrounding support film contributing to the elemental analysis and ensure a reliable K/Mo measurement, we employed binary masking, local averaging and the standardless Cliff Lorimer k-factor method as part of the elemental analysis processing workflow (see SI section 3 for post-processing steps and Fig. S5.14 for further details).

Fig. 5.3a,b shows an example of STEM-EDS elemental mapping for K in a single crystal K-doped MoS_2 flake, before and after *in-situ* heating at 300 °C for 1 hour. There are significant variations in K concentration across the flake before heating and strong EDS K signal are shown in the edge of the MoS_2 flake (Fig. 5.3a and Fig. S5.15) demonstrating high dopant concentrations particularly associated with edges and surface steps and thus suggesting K intercalation is accelerated at these low coordination

sites. This observation clarifies previous lower spatial resolution *in-situ* optical and Raman measurements where Zhang et al. suggested the K intercalation begins at edges[41]. The mean value of *n* (K/Mo) for this particular flake was found to decrease from 0.75 to 0.61 (K concentrations of 20.0 to 16.9 at%) after heating, with the standard deviation in the measurements also decreasing from 0.32 to 0.16, indicating that the K distribution of the flake becomes more uniform. Comparing the quantitative line-scans before and after heating (Fig. 5.3c and Fig. S5.16), the regions with the highest K concentration show the largest percentage decrease after heating. Together with the decrease in standard deviation of the measurements, this suggests that the annealing induced deintercalation acts to homogenise the composition of the crystal.

To determine the kinetics of deintercalation we then apply STEM-EDS to measure the change in *n* for individual flakes at temperatures of 25, 150, 200 and 300 °C annealed for up to 4 hours. To reduce the potential for anomalous data from a single measurement we have studied 5 separate flakes, each with 1300-1700 individual pixel measurements, at each temperature. To account for the initial variability in K concentration within the flakes, we employ the atomic ratio of K/Mo normalised to the flake's starting composition as a metric for measuring the changes in K concentration. The K/Mo ratio of the room temperature specimen decreases minimally over 4 hours (Fig. S5.17a), in agreement with previous reports of successful long-term storage at room temperature under inert gas or vacuum conditions[31]. This test also served to exclude any possible electron beam induced deintercalation effects, as the room temperature specimen

received the same electron fluence as the heated samples. Fig. S5.17f illustrates the normalised K, Mo and S counts detected by the EDS detector from a single intercalated flake, which fluctuate around ± 0.8% with a total cumulative electron fluence of 2.6×10^5 e^-/nm^2. This variation is minimal compared to the significant compositional change shown to occur with heating. MoS_2 is not expected to decompose over the studied temperature range (25 – 300 °C)[42] and indeed we find that Mo counts remain constant over time at all recorded temperatures, making it a suitable normalisation factor for these measurements. For each temperature, the average *n* was measured as a function of annealing time as shown in Fig. 5.3k. Consistent image processing steps were applied (masking, alignment, averaging, dose normalisation) to ensure comparability of the measurements. For temperatures 150 - 300°C, there is a decrease in *n* over time due to loss of K.

The *n vs t* plots in Fig. 5.3k exhibit an exponential decay in the K content during heating, to which can be fitted to the following function:

$$N(t) = N_0 e^{-kt},$$

where N(*t*) and N_0 represent the concentration at time *t* and time 0 respectively, *k* is the effective rate constant of K deintercalation in a MoS_2 crystal at a specific temperature and can be obtained via measuring the slope of each linear regression shown in Fig. S5.17e. This exponential relationship is indicative of first order kinetics to which the Arrhenius equation can be applied. Fitting the data to this model, a linear relationship between the reaction rate constant, *k*, and inverse temperature, 1/*T*, can be computed and plotted in Fig. 5.3m:

$$\ln(k) = -2414.76 \times \frac{1}{T} + 3.03$$

Based on this empirical model we can predict the rates of K deintercalation in K-doped MoS_2 for a given temperature and heating time. Knowledge of this relationship is important for applications where sample preparation requires annealing of K_xMoS_2 or where it is used at elevated temperatures. It should be noted that our experiments were done in vacuum and we expect that, for more oxidative environmental conditions, the rate constants would need adjustments. Importantly, these can be found using the above methodology for different experimental conditions and other intercalated or pillared nanomaterials.

The change in K concentration can also be tracked by the evolution of the intensities of the superlattice reflections measured via SAED (Fig. 5.3d-e), and this crystallographic data can also shed light on the deintercalation mechanism. The selected area aperture samples a circular region of the flake with a radius of 0.87±0.1 um, so the SAED pattern can be considered an average for the whole flake (maximum diameter ~ 2 μm). Before annealing the flake has a composition of n=0.75 and a diffraction pattern similar to the $K_{0.75}MoS_2$ atomic model presented in Fig, 5.1 and Fig. 5.3h. However, as the flake is annealed at 300˚C new superlattice spots are seen to emerge, representing a doubling of the lattice period along the $[1\bar{1}00]$ direction (example positions are marked by the blue triangles in Fig. 5.3e and g and magnified in the inset). Note that these new superlattice positions cannot be formed by chains of Mo (as in the 1T', 1T" or 1T"' polytypes)[43], suggesting that like in Fig. 5.1d, ordering of alkali ions is responsible for the superstructure. The pattern we observe can be

reproduced by hypothesising a new intermediate mixed phase which has formed during K deintercalation and combined $2a \times \sqrt{3}a$ and $2a \times 2a$ superstructures on different layers (Fig. 5.3i, S5.13d-e). Our proposed atomic model is thus built by a structure consisting of 4 MoS_2 layers, where three of the interlayer planes are 75% filled with ordered K and one with just 25% K (as illustrated in Fig. 5.3i, S5.13). The simulated SAED pattern reproduces the peak positions of the experimental SAED patterns, as demonstrated in line profiles taken along the same directions for each in Fig. 5.3j. The fitted model also has a mean composition of n = 0.625 (Fig. 5.3i, S5.13a) in close agreement with our experimental STEM-EDS measurement of n = 0.61 for this flake. This observation of a mixed phase crystal emerging during deintercalation is important as it sheds light on the mechanism of deintercalation, suggesting that reconfiguration of intercalated ions occurs through non-uniform deintercalation of individual K ion planes. Our data suggests there is a strong driving force for individual planes to release K preferentially so as to locally adopt one of the stable ordered n = 0.25, 0.5 or 0.75 values, rather than for individual planes to release K in a homogenous manner which would result in atomic planes with an intermediate n value. To our knowledge, this is the first observation of the creation of such an intermediate mixed phase superstructure in the alkali intercalated MoS_2 system.

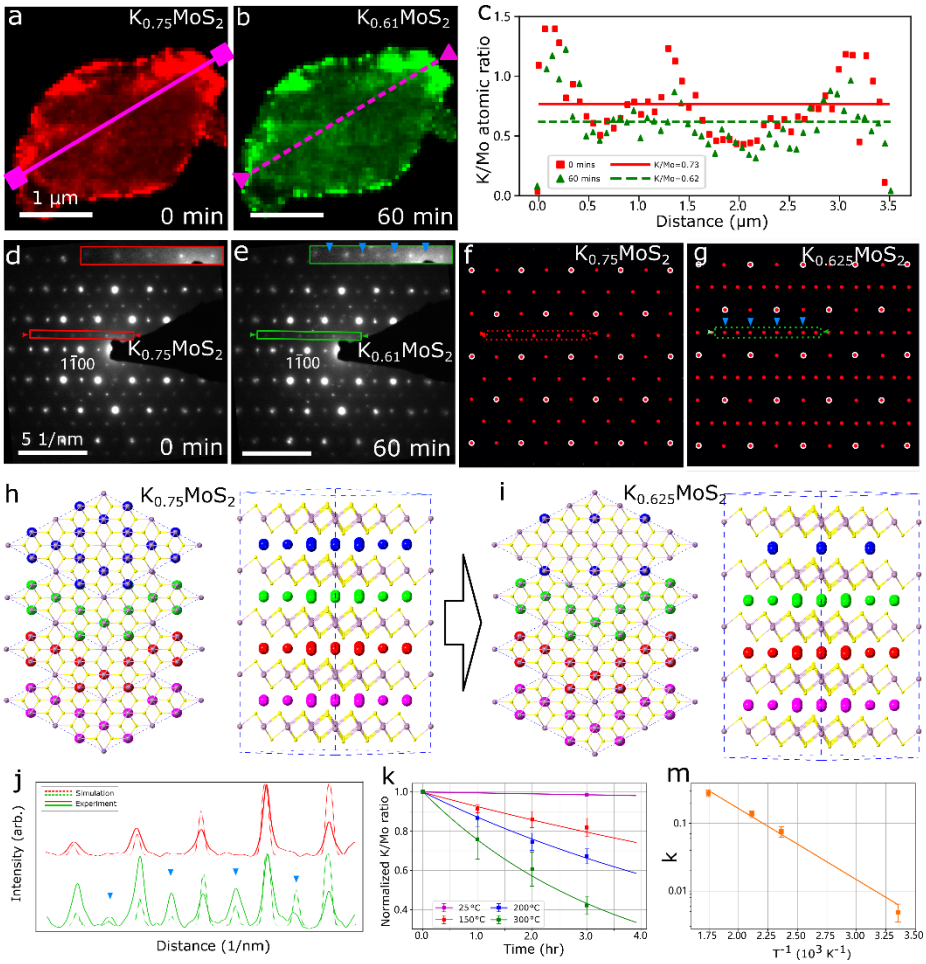

Figure 5.3 EDS mapping and TEM characterisation of the K deintercalation process. (a, b) K/Mo ratio STEM-EDS elemental maps of a same flake acquired before (a) and after 60 min heating at 300°C (b). Mean K concentrations measured for the entire flake are indicated top right. (c) Comparison of the atomic ratio of K/Mo along magenta lines shown in (a) and (b). Mean values are plotted as the solid red line for before annealing and the dashed green line after annealing. (d, e) Selected area diffraction patterns of the flakes shown in (a, b) respectively. The insets highlight the location of the extra reciprocal superlattice spots that appear in (e), indicated by blue triangles. (f, g) Simulated diffraction patterns obtained for atomic models with mean compositions of $K_{0.75}MoS_2$ and $K_{0.625}MoS_2$ respectively (crystal structures are shown in (h,i) with further details in SI Fig. S5.13). (j) Comparison of normalised experimental and simulated intensity across (c, d) electron diffraction and (f, g) the simulated patterns. The discrepancy between amplitude of measured and simulated may be due to slightly tilting of the specimen and the difference of the thickness. (k) Plot of the exponential decay for the normalised K/Mo ratio detected from the K-doped MoS_2 flakes at four different temperatures (25, 150, 200 and 300°C). (m) Arrhenius plot of the rate constant for K deintercalation against inverse temperature on a semi-ln scale.

As the presence, or absence, of K in the interlayer space is expected to change the interlayer separation, d_{0001}[23,44], as well as the basal plane lattice parameter, K (de)intercalation can also be probed using cross sectional S/TEM imaging. Fig. 5.4a shows a cross-sectional HAADF-STEM image at the edge of the as-prepared K-doped flake where individual MoS_2 atomic layers are clearly visible as bright lines, although K itself is not visible due to its relatively lower atomic number as compared to molybdenum (K:19, Mo:42). The cross-sectional images were acquired from the folded regions which often appear on edges of the layered materials[45]. These images show the atom layers as the bright lines in the HAADF STEM image and thus they can be used to count the number of layers and measure the interlayer spacings. Viewed locally at this resolution the atomic layer structure appears highly disordered with large variations in the interlayer spacing inducing considerable local curvature of the atomic planes. The expected values for d_{0001} in single layer intercalated MoS_2 range from 0.73 - 0.83 nm[37] yet, interestingly, we also observe local regions of much larger interlayer spacings (1.22 - 1.42 nm) (highlighted orange in Fig. 5.4a). It is possible that such large interlayer spacings are produced by nanoscale domains of three-dimensional intercalant trapped in the interlayer space and the formation of amorphous K or K_2S pockets may be produced by reaction of the intercalant with the parent material in K-rich MoS_2[43,46] as the bright regions near edges shown in Fig. 5.3a. The HAADF-STEM image also suggests the presence of dislocations in the structure, with such defects likely to act as fast transport routes for K diffusion[47]. and which may contribute to determining which

planes adopt the less dense ordering of K. When considering the changes in the interlayer spacings as a function of annealing time for this flake heated at 200 °C for 3 hours (Fig. 5.4a-d), we find that the mean interlayer separation decreases slightly during annealing from 0.91 ± 0.10 to 0.75 ± 0.05 nm (Fig. 5.4e,f and SI Fig. S5.19) corresponding to a decrease in K content from $n = 0.85$ to $n = 0.54$ (measured in the local region by STEM-EDS). Fig. S5.20 shows comparisons of variable d-spacings resulting from the different K intercalation degree in this work to the reported results based on XRD measurement and simulation, indicating sensible measurement in this work. Note that Andersen et al. demonstrated a small decrease of interlayer spacing with increasing K loading beyond $n>0.25$, and attributed to increased metallization of the intercalated K between host layers[37]. In addition, the number of expanded interlayer galleries decreases after annealing (Fig. 5.4e) and defects in individual MoS_2 layers appear to 'heal', as shown in the insets of Fig. 5.4a-d, consistent with the behaviour observed for annealing in undoped MoS_2[42] and which is encouraging for the potential annealing induced regeneration of degraded MoS_2-based electrodes.

The results presented in Fig. 5.4 demonstrate some local K domains and ultimate flexibility of the MoS_2 host to accommodate K ions into the lattice in the cross-sectional images, whilst maintaining a distinct long-range crystal order. The large variations in composition, polytype and interlayer spacing seen here at the nanoscale suggest that the structure of thin K intercalated MoS_2 flakes is poorly described by any average unit cell, even where this gives a good match to the mean experimental

composition and diffraction data. We propose that the actual crystal structure is likely to be less ordered than a simple unit cell suggests, and thus the deintercalated material in Fig. 5.3b,e may be better described by multiple $K_{0.25}MoS_2$ stacking faults in an $K_{0.75}MoS_2$ lattice or as an intercalated crystal structure containing both $K_{0.75}MoS_2$ and $K_{0.25}MoS_2$ atomic layers with a ~3:1 ratio. Interestingly, deintercalation appears to reduce local disorder, even when significant K content remains in the crystal. Consequently, excess intercalation followed by deintercalation to the required composition may be a viable route to achieve more homogeneous intercalated materials with more uniform performance.

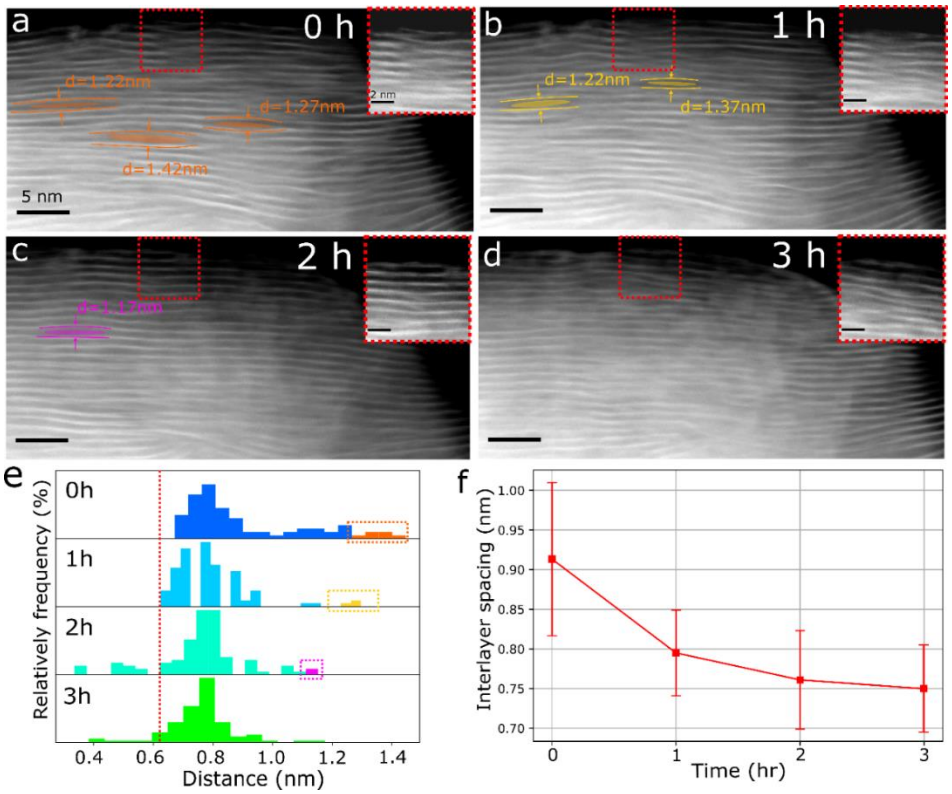

Figure 5.4 *In-situ* high-resolution STEM imaging of interlayer structures for K-doped MoS_2. (a - d) High-resolution HAADF STEM images from the edge of single flake over 3-hours of heating at 200 °C. Shaded areas represent the positions of large interlayer spacings suggested to consist of nanoscale K domains. The insets show enlarged views illustrating the healing of the defective atomic layer structure. (e) Measured distribution of interlayer distances as a function of annealing time with anomalously wide interlayer distances highlighted in orange, yellow and magenta (corresponding to regions annotated in (a - c)). Red dotted line illustrates the interlayer spacing of pristine the MoS_2. (f) Plot of the variation of the mean interlayer distance during annealing, with the standard deviation in measurements shown by the error bars.

In summary, the structure-composition relationships for K-intercalated MoS_2 few layer flakes were studied via correlated, atomic resolution imaging, electron diffraction and STEM-EDS elemental analysis. The starting material was found to be predominantly the 2H+1T polytype with small local regions of 1T'. A rich variety of superstructures produced by ordering of the K in the gallery spaces are observed, including the first observation of the $2a \times \sqrt{3}a$ superstructure in this system. *In-situ*

measurements of the thermal deintercalation process revealed the process is determined by first order kinetics and allowing empirical prediction of the mean composition as a function of time and temperature. During deintercalation a novel intermediate mixed phase was found to emerge, explained as a combination of the $2a \times \sqrt{3}a$ and $2a \times 2a$ superstructures, and demonstrating preferential loss of intercalant from individual planes in order to adopt one of the preferred superlattice orders for the intercalant species. Atomic resolution imaging and local elemental analysis reveal a rich structural variation at the nanoscale within individual host crystals. During deintercalation we observe a decrease in the variance of the local elemental compositions and in the interlayer spacings, suggesting a route to synthesis of more homogeneous intercalated materials. We propose that the combination of local *in-situ* crystallographic and compositional analysis demonstrated in this work is widely applicable to provide new insights in to other 2D materials systems that undergo dynamic structural and chemical changes.

5.4 Methods

The K-doped MoS_2 powder was prepared via the liquid ammonia method where the pristine 2H-MoS_2 powder (Aldrich 99%) and K metal (Aldrich 95%) were sealed in a quartz reactor tube in the inert atmosphere of a glovebox (oxygen < 0.5 ppm, moisture < 0.5 ppm). The tube was then evacuated to ~10^{-5} mbar and placed in a bath of dry ice/ethanol to keep it at a low temperature (~ −78 °C). The reactor was filled with high-purity ammonia gas (CK Gas 99.98%), which liquefies and dissolves the K metal

to form a deep blue solution of K in liquid ammonia. The residual volume left by liquification of the ammonia gas was filled by high-purity Ar gas to prevent the sample from oxidising. The reactor was kept in dry ice/ethanol bath for 24 h for the required degree of intercalation. Finally, ammonia was pumped out of the reactor and K-doped crystals were taken out, sealed in a closed container, and stored in the glovebox.

For *in-situ* S/TEM imaging the as-prepared powder for was dry-cast on the holey carbon coated ceramic resistive heating membrane of a Thermal E-chip from Protochips Inc. (Raleigh, NC) and the E-chip was mounted onto a double-tilt Protochips Aduro sample holder in the glovebox. The holder was then transferred to the TEM sealed in an Ar filled box and loaded quickly into the instrument to minimise exposure to air (~ a few seconds). Selected area electron diffraction (SAED) was performed in an FEI Tecnai G2 20 TEM operated at 200 kV with a 0.21±0.1 μm SAED aperture and an FEI Tecnai TF30 FEG-AEM operated at 300 kV with a 0.87±0.1 μm SAED aperture. High angle annular dark field (HAADF) STEM imaging was performed in an FEI Titan G2 80-200 "ChemiSTEM" operated at 200kV with a 21 mrad probe convergence angle, an aberration corrected probe and a HAADF inner angle of 64 mrad. STEM-EDS data was acquired using the Titan's Super-X EDS detector system (quad chip with a total collection solid angle ~ 0.7 srad) and on the TF30 TEM using a SDD X-ray detector from Oxford instrument. Hyperspy was used to process all STEM-EDS data.[48] To gain accurate compositional analysis for individual flakes from the STEM-EDS spectrum images, we employed binary masking, local averaging and standardless Cliff Lorimer k-factor

quantification (see SI and Fig. S5.14 for further details). HAADF simulations were performed with the QSTEM package[49] using the above experimental parameters with Cs = 0 mm and Cc = 1 mm. Electron diffraction patterns were simulated using the multislice method[50] implemented with the code developed by Kirkland[51].

Acknowledgements

The authors gratefully acknowledge support from the Engineering and Physical Sciences Research Council (EPSRC) Graphene NOWNANO Centre for Doctoral Training for a provision of a PhD studentship, EPSRC PhD plus award and EPSRC Doctoral Prize Fellowship. We acknowledge funding from EPSRC (EP/P009050/1) and from the European Research Council under the Horizon 2020 programme for the ERC Starter Grant EvoluTEM (715502). This work was supported by the Henry Royce Institute for Advanced Materials, funded through EPSRC grants EP/R00661X/1, EP/S019367/1, EP/P025021/1 and EP/P025498/1.

5.5 Supporting Information

Thermal Deintercalation of K-doped MoS_2 Analysed via *in-situ* TEM

Shouqi Shao[1,2], Daniel J. Kelly[1,2†], W. J. Kuang[3], Irina V. Grigorieva[2,3ϕ] and Sarah J. Haigh[1,2*]

[1] *Department of Materials, University of Manchester, Oxford Road, Manchester M13 9PL, United Kingdom*

[2] *National Graphene Institute, University of Manchester, Oxford Road, Manchester M13 9PL, United Kingdom*

[3] *Department of Physics and Astronomy, University of Manchester, Oxford Road, Manchester M13 9PL, United Kingdom*

Corresponding author email: *sarah.haigh@manchester.ac.uk; †dankel@dtu.dk; ϕirina.grigorieva@manchester.ac.uk;

5.5.1 Characterisation of Intercalated K_nMoS_2 Material

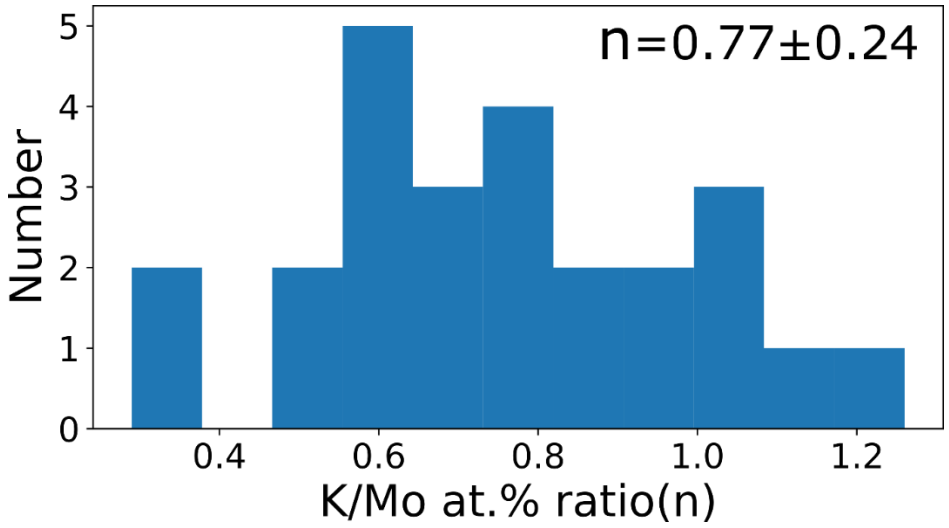

Figure S5.5 Distribution of the elemental composition (atomic percent ratio of K to Mo) for 25 individual as produced K-intercalated flakes characterised by STEM-EDS.

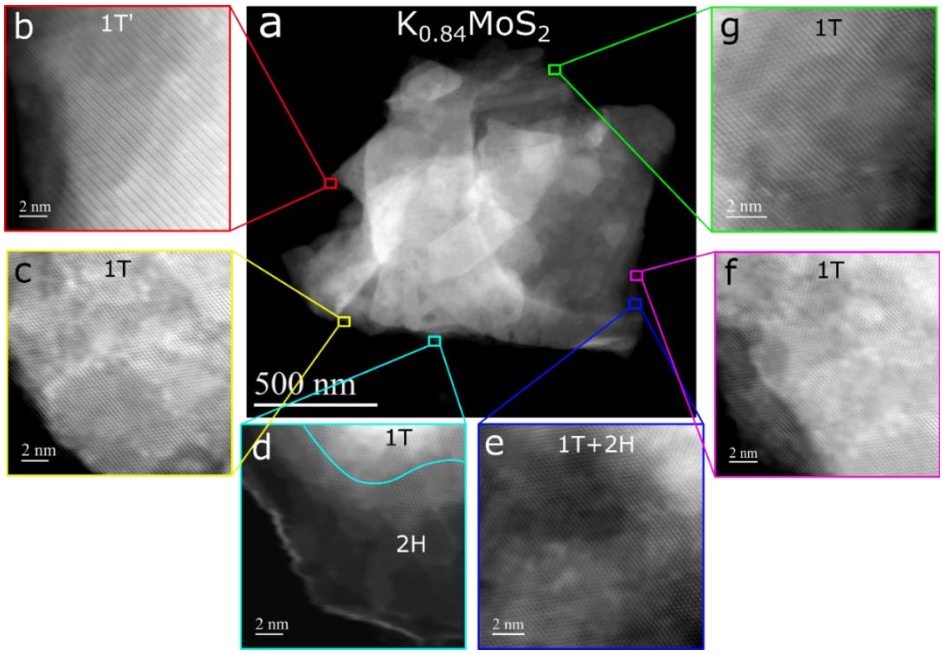

Figure S5.6 HAADF-STEM images of polymorphism within a K intercalated MoS_2 flake. (a) Low magnification HAADF image of a typical K intercalated flake with the mean atomic ratio of K/Mo= 0.84 (corresponding to K concentration of 21.9 at %). Different phases of MoS_2 identified: (b) 1T' (zigzag chains of Mo); (c,d,f,g) 1T; (e) 1T and 2H.

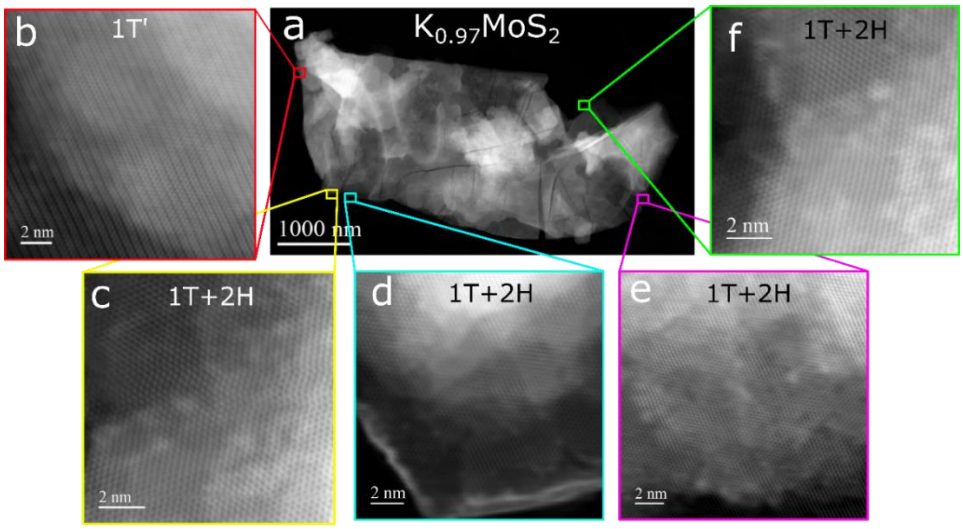

Figure S5.7 HAADF-STEM images of polymorphism within a K intercalated MoS_2 flake. (a) Low magnification HAADF image of a typical K intercalated flake with the mean atomic ratio of K/Mo= 0.97 (corresponding to a K concentration of 24.4 at %). Three different phases are found to be present: (b) 1T' (zigzag Mo chains); (c-f) 1T+2H.

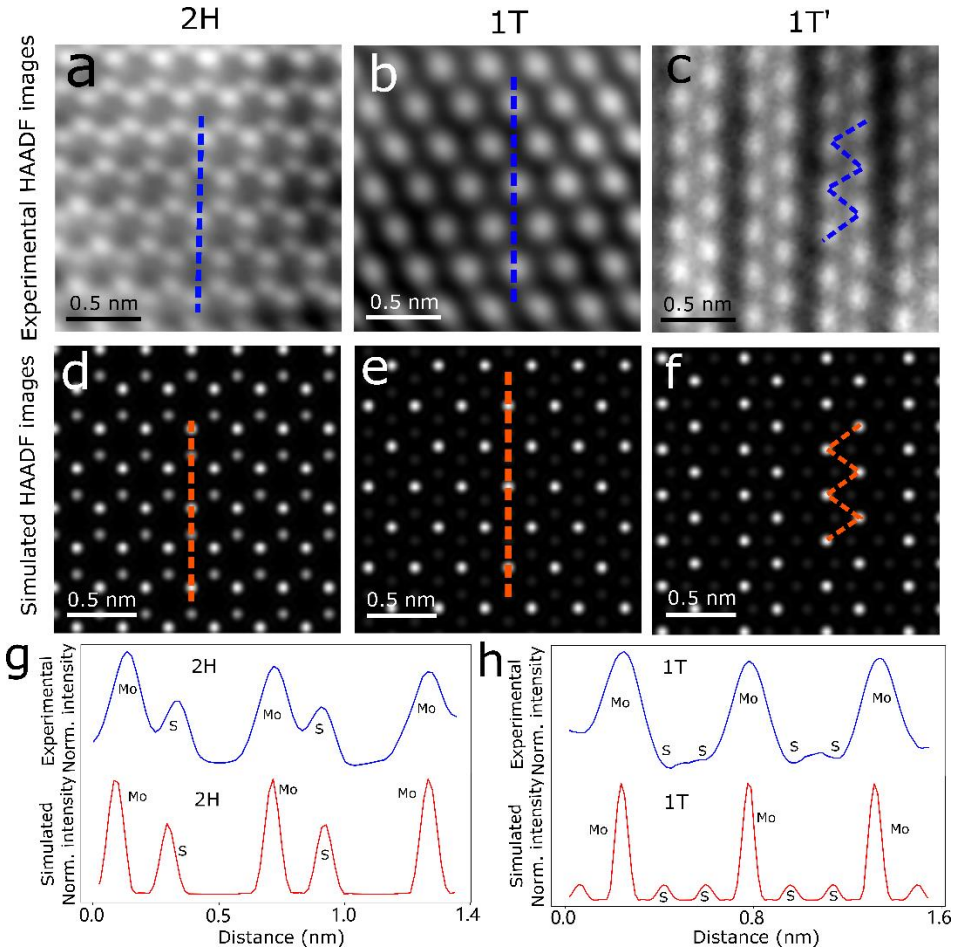

Figure S5.8 High resolution STEM images of MoS_2 polytypes and their corresponding simulated images. (a-c) Experimental and (d-f) simulated HAADF-STEM images of 2H (trigonal prismatic), 1T (octahedral) and 1T' (zigzag chains of Mo) phases. (g, h) Comparisons between 2H and 1T by using line scanning across the experimental and simulated images in (a, b, d, e). The broader experimental peaks shown in the (g, f) can be attributed to the slight probe aberration which was not considered in the STEM image simulation.

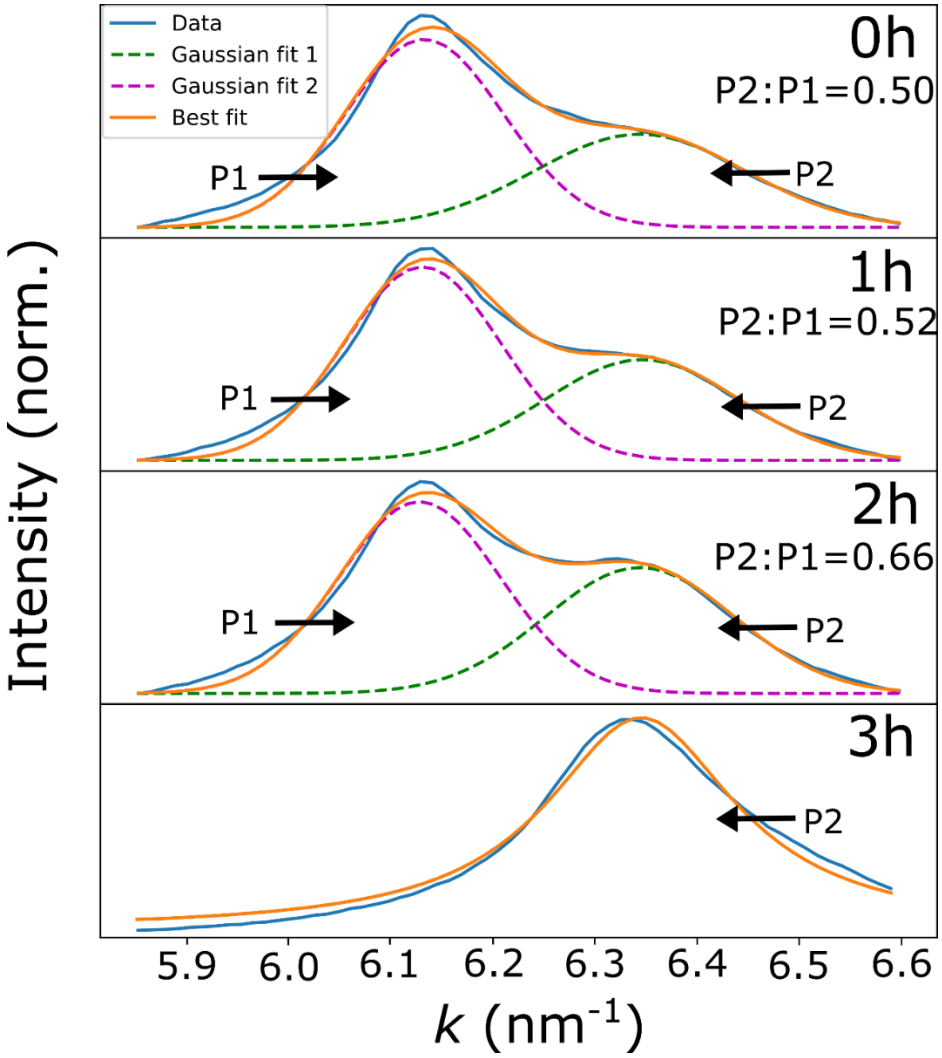

Figure S5.9 The relative peak intensities measured from a Gaussian fit in the extracted $11\bar{2}0$ intensity profiles from the line scanning shown in Fig. 5.2a-d insets. There is only one peak in the bottom subplot due to disappearance of splitting spots.

5.5.2 Comparison of Atomic Models with Experimental Electron Diffraction Patterns

Atomic models of 2H and 1T MoS_2 as the host lattice and ordered K atoms in the galleries between layers are shown alongside experimental ED patterns with similar K/Mo ratios for a range of compositions in Fig. S5.10-S5.13 and demonstrates how the ordering alkali ions can give rise to the observed superstructure reflections. Furthermore, for the lower concentration crystals: $K_{0.25}MoS_2$ (Fig. S5.10) and $K_{0.5}MoS_2$ (Fig. S5.11), partial filling and ordering occurs in individual layers and thus atomic planes of K atoms with identical ordering and occupancy arrangements can have three equivalent orientational relationships with the host MoS_2 lattice. This results in significant variability in the local crystal structure[27] which can be analysed by SAED[27,44]. According to the mathematical relationship[29] between the orthogonal (K lattice) and hexagonal systems (MoS_2 lattice) we can refer to the superstructures shown in Fig. S5.10 and S5.11 as $2a \times \sqrt{3}a$ and $a \times \sqrt{3}a$ respectively[15,29], where a refers to the lattice parameter of pristine 2H-MoS_2. The $a \times \sqrt{3}a$ pattern (Fig. S5.11) has been widely observed in Li, Na and K-intercalated MoS_2 compounds, although without confirmation from complementary quantitative elemental analysis[15,27,29,39]. The $2a \times \sqrt{3}a$ superstructure pattern (Fig. S5.10), has only previously been reported as an intermediate intercalation phase for sodiated MoS_2 produced via electrochemical intercalation but SAED measurements presented here confirm it is similarly stable for K-MoS_2[29,39]. Based on this, we attribute the generation of the superstructure to the ordering foreign K ions in this K-doped MoS_2 crystal.

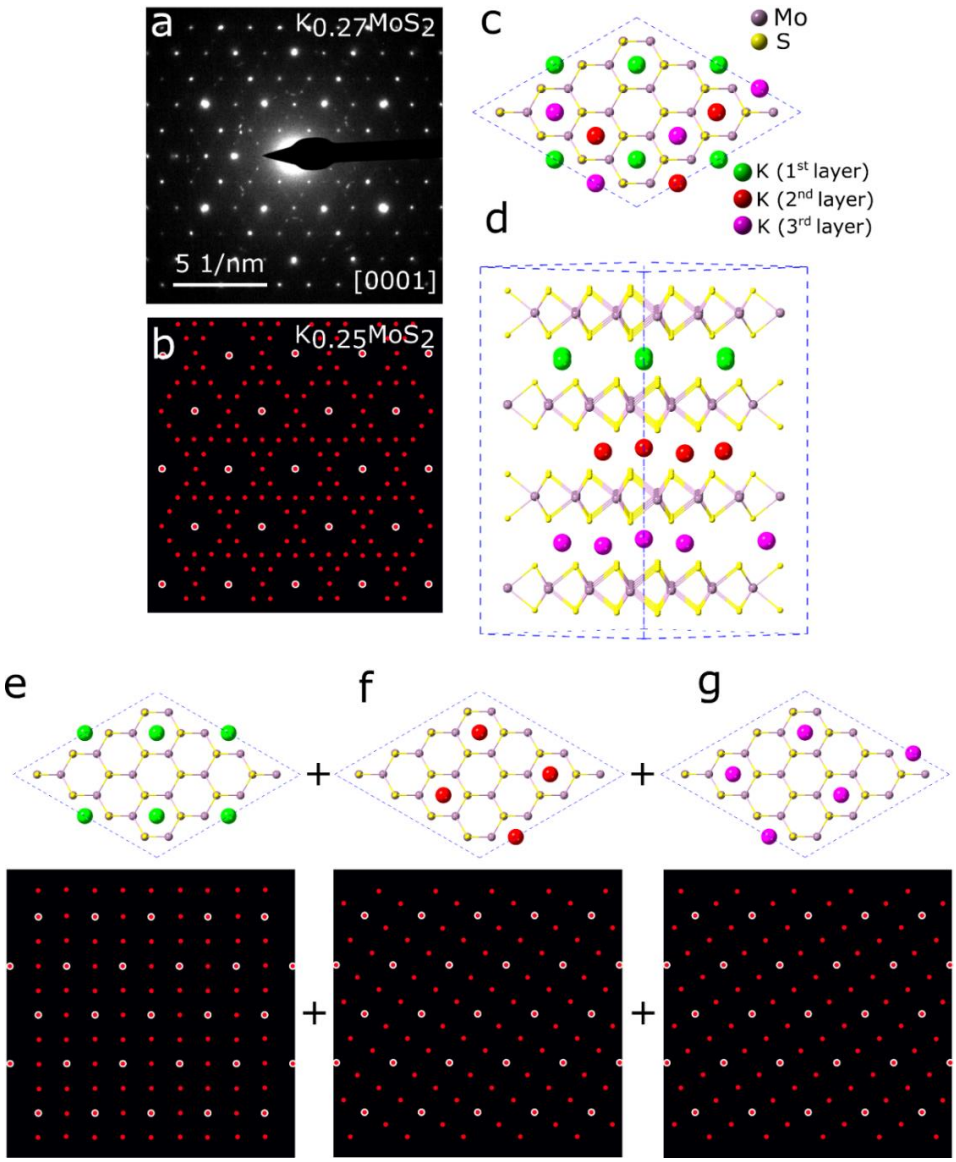

Figure S5.10 Electron diffraction TEM characterisation and atomic structure of K-doped MoS_2 flakes ($K_{0.25}MoS_2$). (a) SAED pattern of $K_{0.27}MoS_2$ flakes viewed along the [0001] zone-axis (elemental composition measured by STEM-EDS). (b) Simulated diffraction pattern of $K_{0.25}MoS_2$. (c, d) Atomic models of one $4 \times 4 \times 4$ supercell of the proposed superstructure of $K_{0.25}MoS_2$, projected along [0001] (c) and $[11\bar{2}0]$ (d). (e-g) The three separate atomic layers that make up the $K_{0.25}MoS_2$ superlattice shown in (c-d) and their corresponding diffraction patterns that combine to give the simulated diffraction pattern shown in (b).

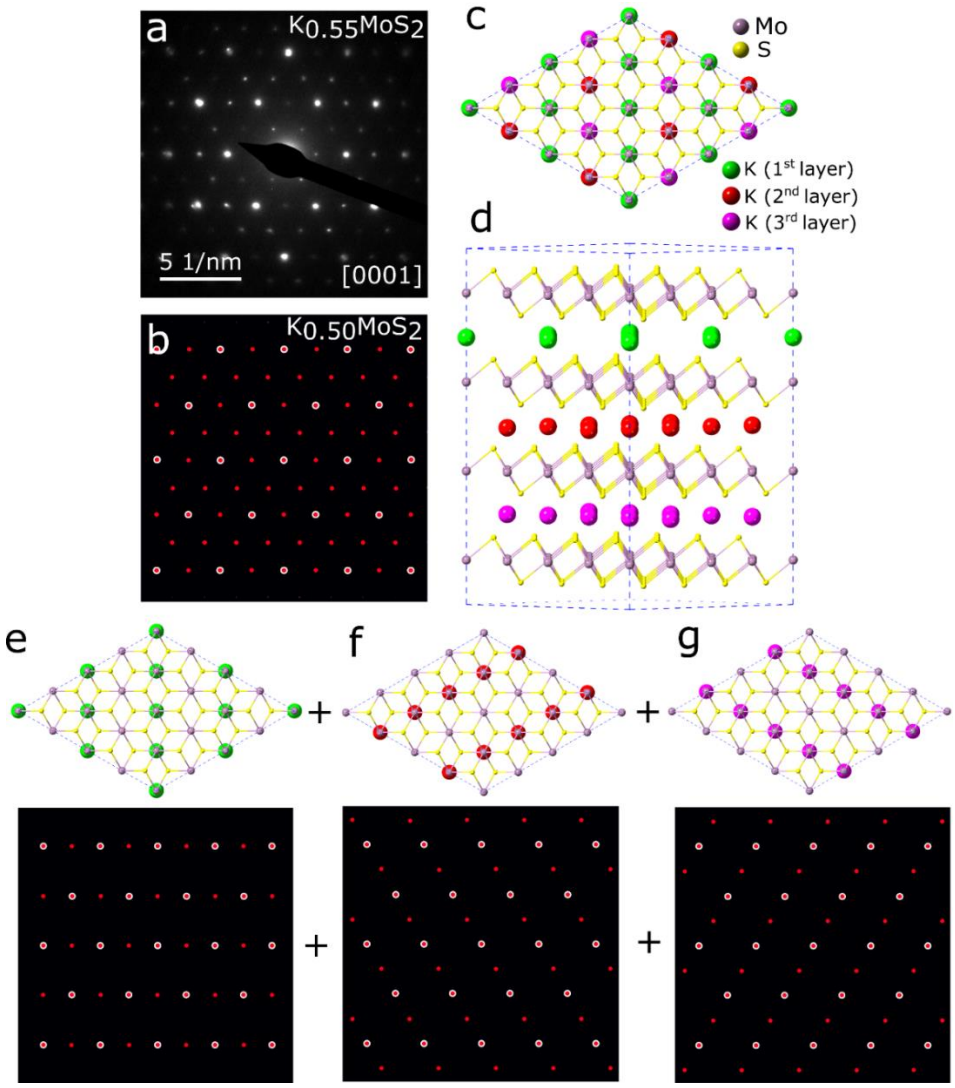

Figure S5.11 Electron diffraction TEM characterisation and atomic structure of K-doped MoS_2 flakes ($K_{0.5}MoS_2$). (a) SAED pattern of $K_{0.55}MoS_2$ flakes viewed along the [0001] zone-axis (elemental composition measured by STEM-EDS). (b) Simulated diffraction pattern of $K_{0.5}MoS_2$. (c, d) Atomic models of one $4 \times 4 \times 4$ supercell for the proposed superstructure of $K_{0.5}MoS_2$ (c, d), projected along [0001] (c) and $[11\bar{2}0]$ (d). (e-f) The three separate atomic layers that make up the $K_{0.5}MoS_2$ superlattice in (c-d) and their corresponding diffraction patterns that make up the simulated diffraction pattern in (b).

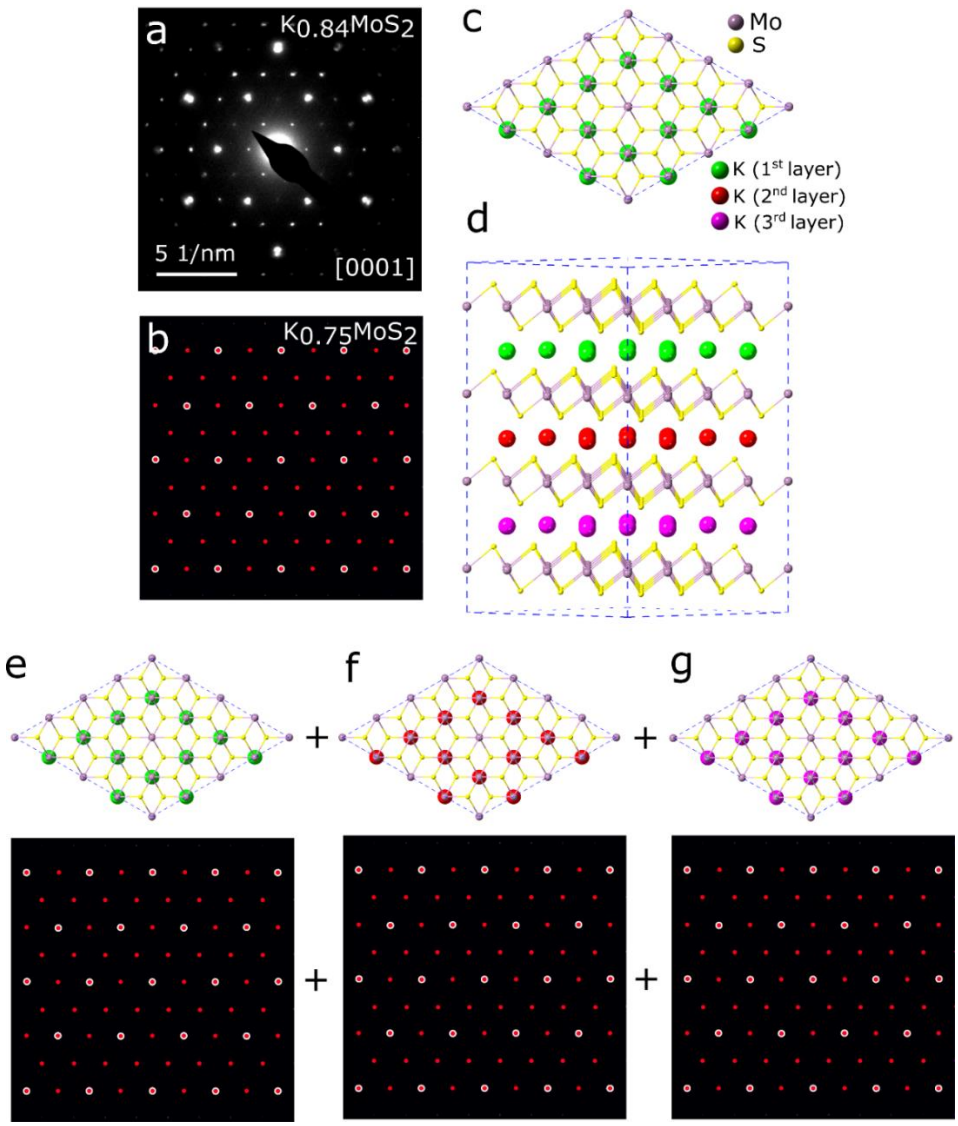

Figure S5.12 Electron diffraction TEM characterisation and atomic structure of K-doped MoS_2 flakes ($K_{0.75}MoS_2$). (a) SAED pattern of a $K_{0.84}MoS_2$ flake viewed along the [0001] zone-axis (elemental composition measured by STEM-EDS). (b) Simulated diffraction pattern of $K_{0.75}MoS_2$. (c, d) Atomic models of one $4 \times 4 \times 4$ supercell for the superstructure of $K_{0.75}MoS_2$, projected along [0001] (c) and $[11\bar{2}0]$ (d). (e-g) The three separate atomic layers that make up the $K_{0.75}MoS_2$ superlattice model in (c-d) and their corresponding diffraction patterns that combine to produce the simulated diffraction pattern in (b).

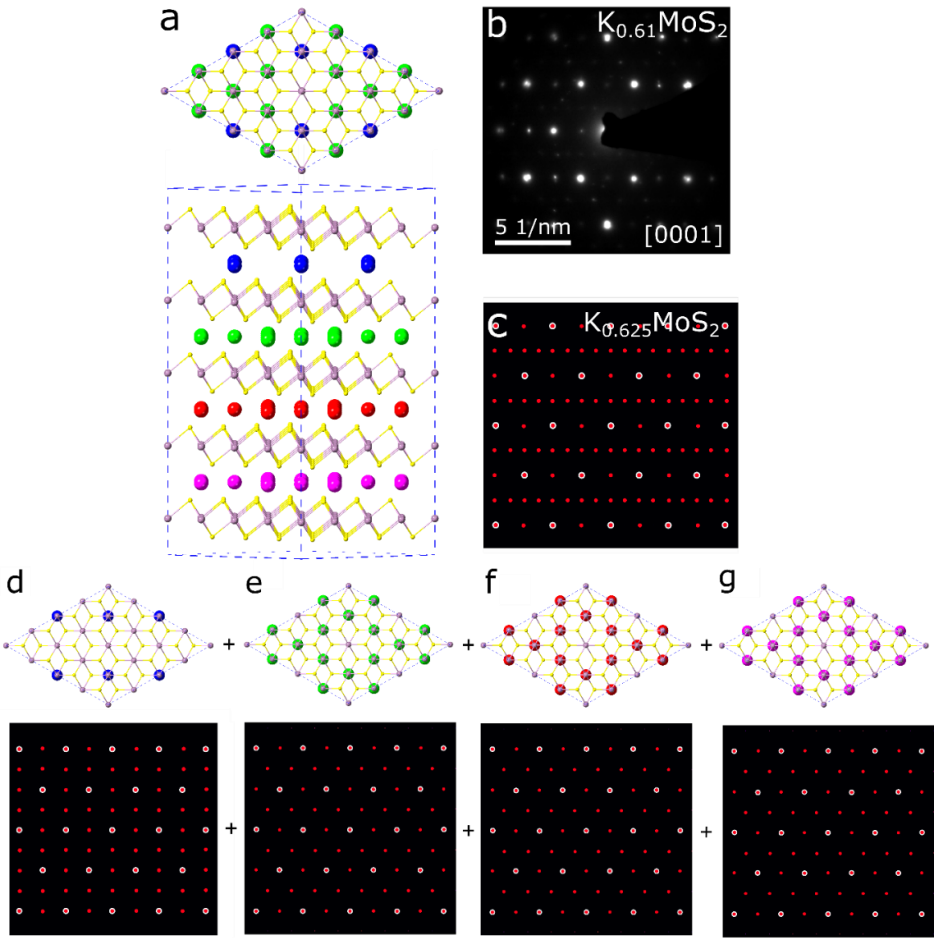

Figure S5.13 TEM characterisation and atomic structure of K-doped MoS_2 flakes ($K_{0.625}MoS_2$, elemental composition measured by STEM-EDS). (a) Plan-view and side view of the atomic model for $K_{0.625}MoS_2$. (b) SAED pattern of the flake shown in Fig. 5.3b. (c) Simulated diffraction pattern of $K_{0.625}MoS_2$. (d-g) The four separate atomic layers that make up the $K_{0.625}MoS_2$ superlattice model. The layer in d equates to a composition of $K_{0.25}MoS_2$ while layers in (e-g) have a local composition of $K_{0.75}MoS_2$. Below each layer are their corresponding diffraction patterns which together constitute the simulated diffraction pattern shown in (c).

5.5.3 Quantification of STEM-EDS Spectral Images

In order to precisely acquire the K content from the specimen, we performed image processing of the scanning transmission electron microscope (STEM) energy dispersive X-ray spectroscopy (EDS) spectral images using Python with the Hyperspy, Numpy, Matplotlib and Scikit-image packages[52-55]. Raw high angle annular dark field STEM images and EDS maps (size 800 × 800 pixels) were acquired for multiple flakes at hourly increments for a given heating temperature, with an example shown in Fig. S5.14a-c. The spectrum images were initially binned 15 times down to the size of 53 pixel × 53 pixels in order to increase signal-to-noise ratio for further quantification. The STEM images and maps were aligned using a rigid-registration algorithm and cropped to a consistent area. After that, we defined a mask (Fig. S5.14d) to remove contribution K associated with the surrounding carbon support film. EDS signals in the masked area of the spectrum image (white area) are considered and areas outside the masked (black area) are neglected, and the size of the mask is determined by the Mo distribution of the specimen as this defines the location of the MoS_2 (Fig. S5.14f). This allows generation of masked and binned STEM images and EDS elemental maps (Fig. S5.14e-g). The acquired EDS counts of different elements were normalised by total electron beam dose to compensate for differences in the acquisition time. Final quantification of the atomic ratio of K to Mo was performed on the processed EDS spectral maps via the Cliff-Lorimer method with standardless k-factors.

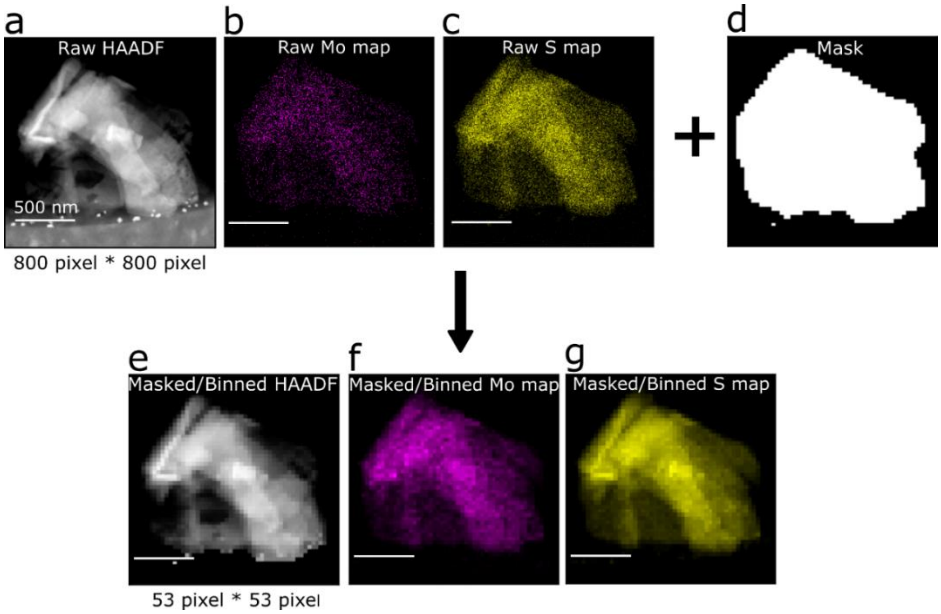

Figure S5.14 Workflow of processing a STEM-EDS spectral image. (a) Raw HAADF-STEM image of an example K-doped MoS_2 flake, (b) raw EDS Mo elemental map and (c) raw EDS S elemental map from a MoS_2 flake. (d) The mask applied to filter out the background and keep only the X-ray counts coming from the area of the flake in the spectral image. (e-f) Masked and binned (e) HAADF-STEM image, (f) Mo map and (g) S map resulting from processing of (a), (b) and (c) respectively.

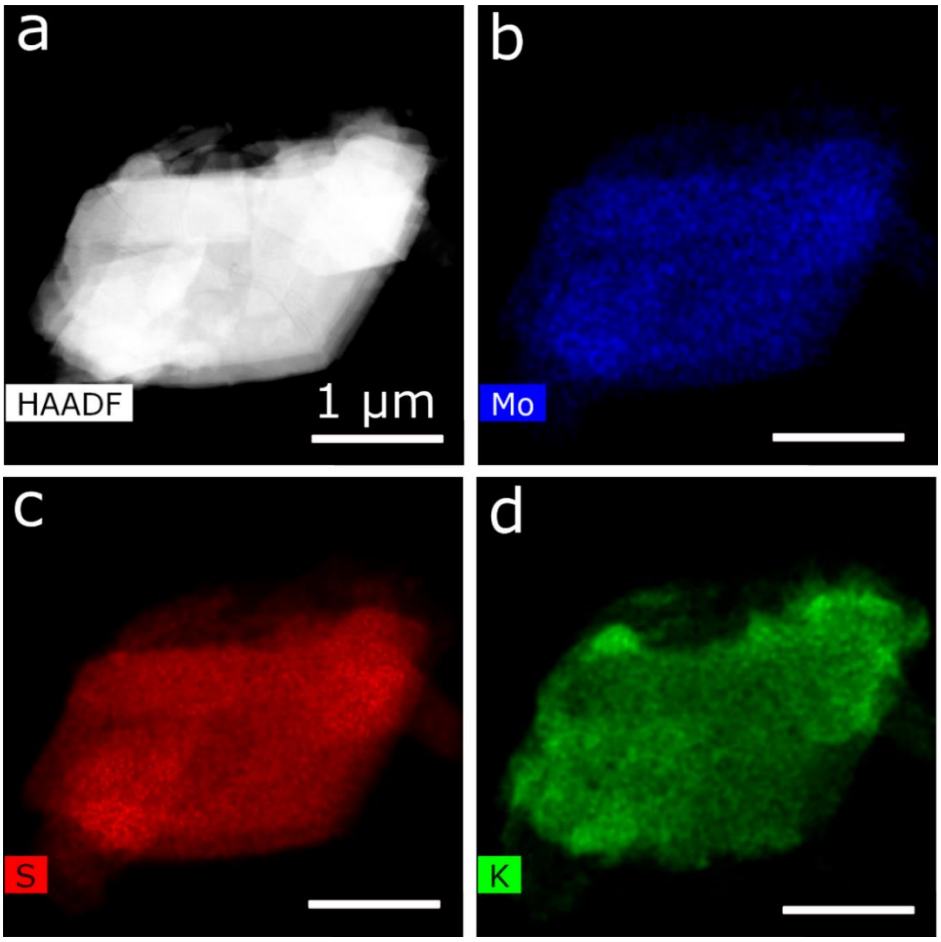

Figure S5.15 STEM-EDS maps of $K_{0.75}MoS_2$. (a) HAADF-STEM image of $K_{0.75}MoS_2$ flake and (b-d) STEM-EDS maps of Mo, S and K, respectively.

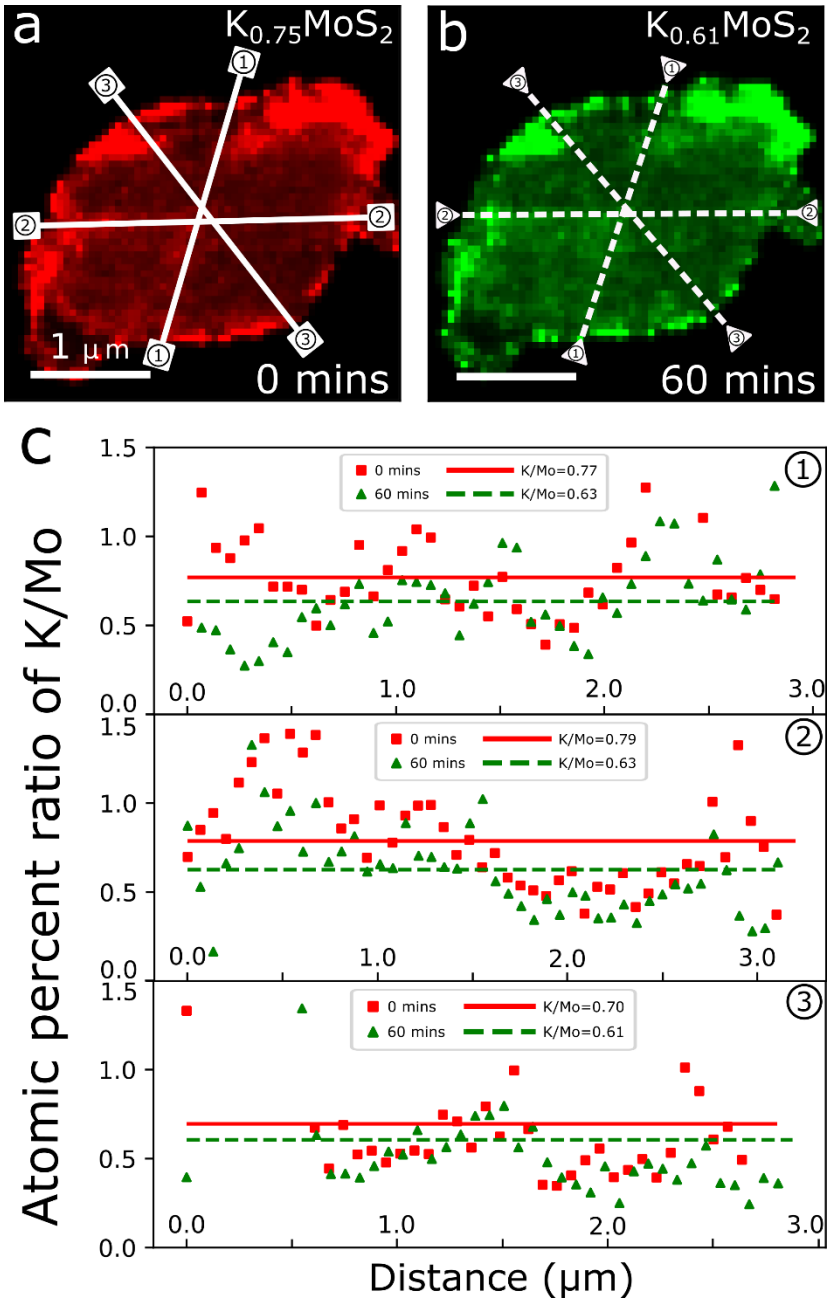

Figure S5.16 STEM EDS mapping of K-doped MoS_2 flakes. K/Mo ratio STEM EDS maps of the identical flake before (a) and after (b) 300 °C heating for 60 mins with three white lines across the flake labelled by number 1, 2, 3 in the circles which indicate the line intensity shown in (c). Red solid and green dashed lines indicate the mean values of the K/Mo ratio for that line scan. The width of each line scan is one binned pixel (approximately 65.6 nm).

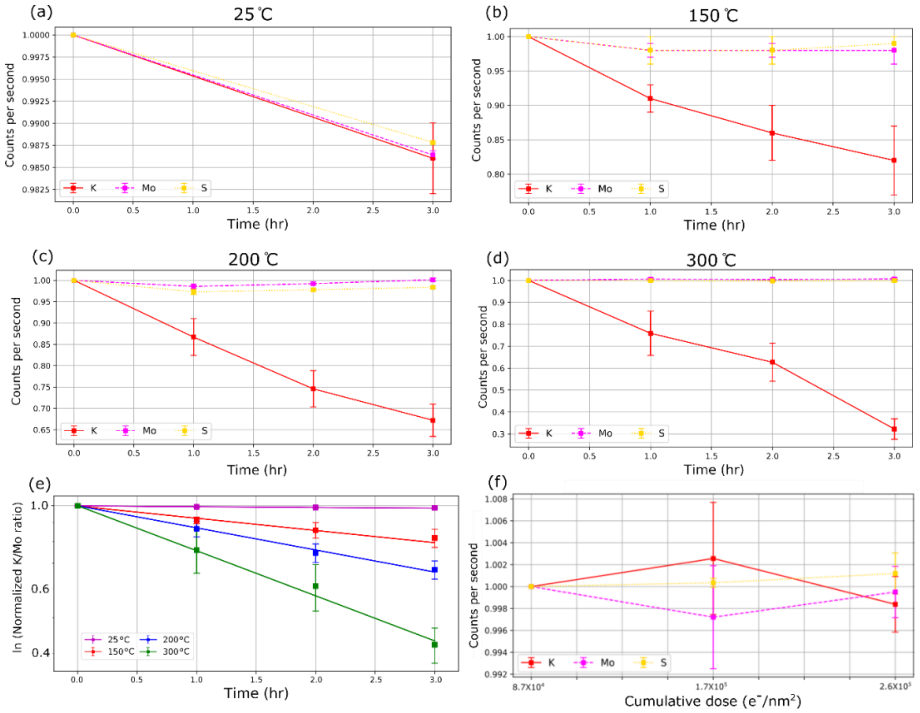

Figure S5.17 Normalised K, Mo and S EDS signal (counts detected per second) at hourly increments whilst continuously heating different flakes at different temperatures. (a) 25 °C, (b) 150 °C, (c) 200 °C and (d) 300 °C. (e) Normalised K_{Ka} counts detected per second from the flakes heated at 25 °C, 150 °C, 200 °C and 300 °C plotted on a semi-ln scale. Solid lines are linear fits to extract the rate constant of K deintercalation. (f) Quantification of the effect of electron beam irradiation on the K-doped MoS_2 flakes. Normalised average counts detected per second of K, Mo and S against the cumulative dose at room temperature. Error bars represent the standard deviation from three repeat measurements and four different flakes.

5.5.4 Measurement of Interlayer Spacing

To measure the interlayer spacing between adjacent MoS_2 planes, we converted the raw cross-sectional HAADF-STEM images (Fig. S5.18a) to fast Fourier transform (FFs) and then applied a bandpass (0.319-1.662 nm^{-1}) filter (Fig. S5.18b) to remove high frequency noise and information not associated with the MoS_2 basal planes. The inverse FFTs (Fig. S5.18c) were then analysed to obtain the interlayer spacing. For further image processing and analysis, we used Numpy, Matplotlib and Scikit-image packages to obtain the intensity along the dashed lines normal to the basal planes (Fig. S5.19a-d) and plot the intensity profiles as shown in the insets of the subplots (Fig. S5.19e-h). The interlayer spacing can also be calculated through the measurement of distance between two adjacent peaks in line scans extracted from the HAADF STEM images producing the distribution of interlayer distances illustrated in Fig. S5.19e-h for each line-scan in Fig. S5.19a-d.

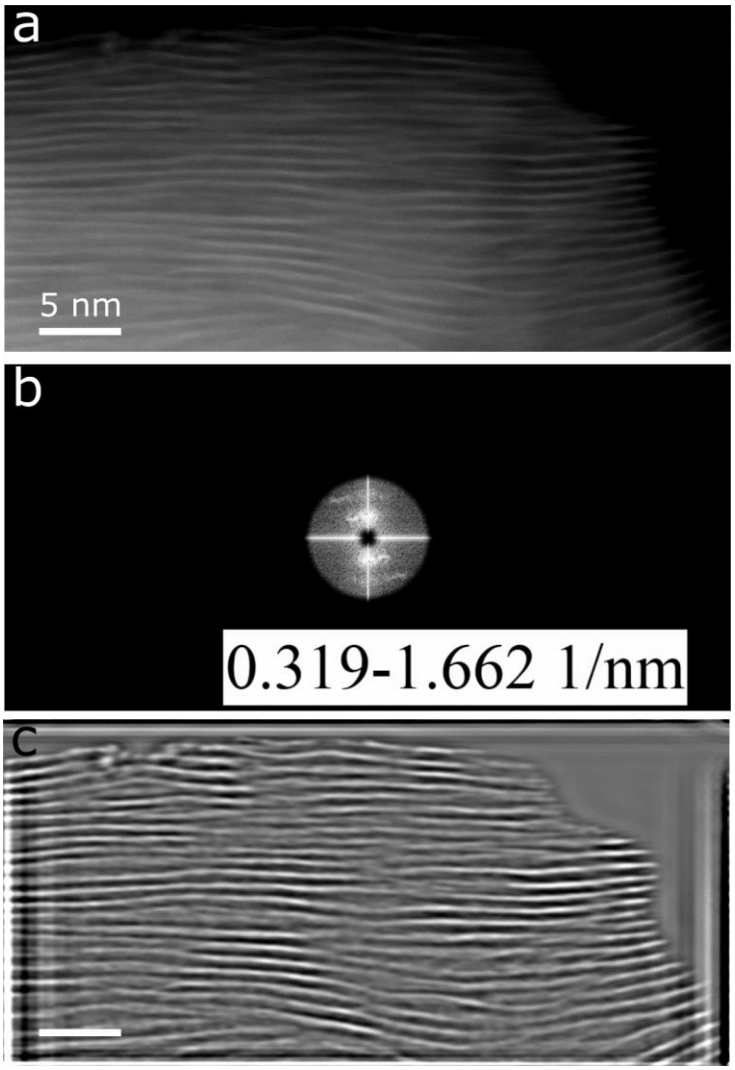

Figure S5.18 FFT processing for measurement of interlayer spacing from cross-sectional images. (a) The original high-resolution HAADF STEM cross-sectional image. (b) Bandpass filter with the range of 0.319-1.662 nm^{-1} selects the relevant area on the Fast Fourier Transform. (c) Filtered cross-sectional HAADF STEM image.

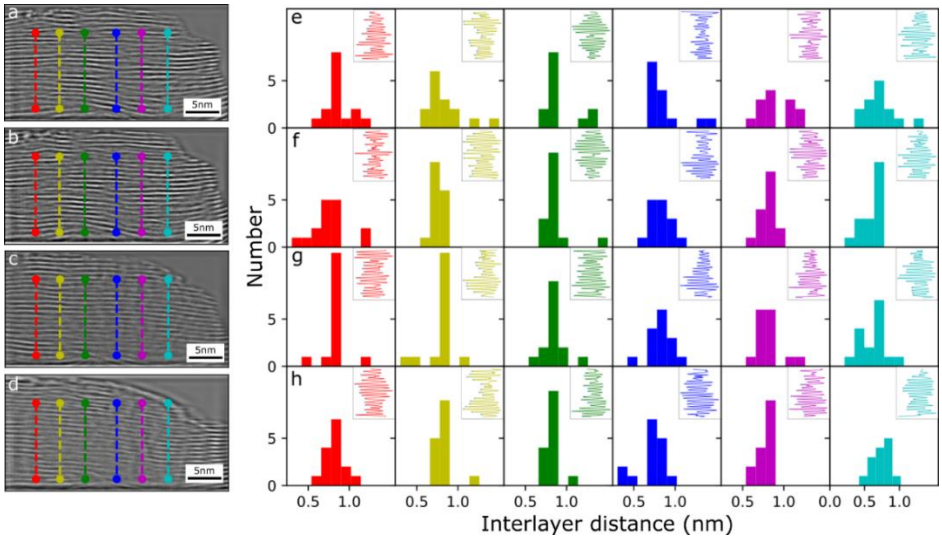

Figure S5.19 Interlayer distance measurements from filtered HAADF STEM images. (a - d) Filtered high-resolution STEM cross-sectional images acquired as a function of heating at 1 h intervals. (e - h) Distribution of the interlayer distances along the line scan in (a - d). The insets show the intensity profiles of the line scans.

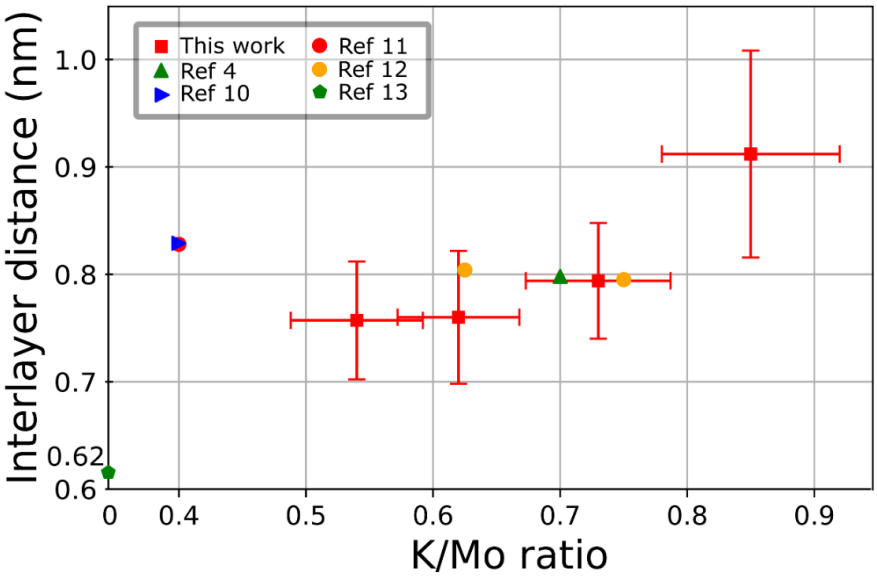

Figure S5.20 Various interlayer distances of K-intercalated MoS_2 with different intercalation degrees. Red squares show the mean interlayer distance and K/Mo ratio with the standard deviation shown by vertical and horizontal red error bars, respectively. The values of d-spacing represented by green and blue triangles and red spheres were measured by Wypych et al.[15], Somoano et al.[31] and Du et al.[56] using X-ray diffraction, respectively. Orange spheres show simulated results performed by Andersen et al.[37] Green pentagon shows the d-spacing of pristine MoS_2 (0.62 nm)[57].

Bibliography

1 Zhao, L., Zhang, R., Deng, C., Peng, Y. & Jiang, T. Tunable infrared emissivity in multilayer graphene by ionic liquid intercalation. *Nanomaterials* **9**, 1096 (2019).

2 Zeng, F. *et al.* Synthesis of mixed alcohols with enhanced C3+ alcohol production by CO hydrogenation over potassium promoted molybdenum sulfide. *Applied Catalysis B: Environmental* **246**, 232-241 (2019).

3 Salihoglu, O. *et al.* Graphene-based adaptive thermal camouflage. *Nano letters* **18**, 4541-4548 (2018).

4 Hart, J. L. *et al.* Control of MXenes' electronic properties through termination and intercalation. *Nature communications* **10**, 1-10 (2019).

5 Soon, J. M. & Loh, K. P. Electrochemical double-layer capacitance of MoS2 nanowall films. *Electrochemical and Solid State Letters* **10**, A250 (2007).

6 Kappera, R. *et al.* Phase-engineered low-resistance contacts for ultrathin MoS 2 transistors. *Nature materials* **13**, 1128-1134 (2014).

7 Nishitani, R., Uno, Y. & Suematsu, H. In situ observation of staging in potassium-graphite intercalation compounds. *Physical Review B* **27**, 6572 (1983).

8 Friend, R. & Yoffe, A. Electronic properties of intercalation complexes of the transition metal dichalcogenides. *Advances in Physics* **36**, 1-94 (1987).

9 Xiong, F. *et al.* Li intercalation in MoS2: in situ observation of its dynamics and tuning optical and electrical properties. *Nano letters* **15**, 6777-6784 (2015).

10 Yu, Y. *et al.* High phase-purity 1T′-MoS 2-and 1T′-MoSe 2-layered crystals. *Nature chemistry* **10**, 638-643 (2018).

11 Peng, J. *et al.* High Phase Purity of Large-Sized 1T′-MoS2 Monolayers with 2D Superconductivity. *Advanced Materials* **31**, 1900568 (2019).

12 Zhang, R. *et al.* Superconductivity in potassium-doped metallic polymorphs of MoS2. *Nano letters* **16**, 629-636 (2016).

13 Yang, D., Sandoval, S. J., Divigalpitiya, W., Irwin, J. & Frindt, R. Structure of single-molecular-layer MoS 2. *Physical Review B* **43**, 12053 (1991).

14 Wypych, F. & Schöllhorn, R. 1T-MoS 2, a new metallic modification of molybdenum disulfide. *Journal of the Chemical Society, Chemical Communications*, 1386-1388 (1992).

15 Wypych, F., Solenthaler, C., Prins, R. & Weber, T. Electron diffraction study of intercalation compounds derived from 1T-MoS2.

Journal of Solid State Chemistry **144**, 430-436 (1999).

16 Lin, Y.-C., Dumcenco, D. O., Huang, Y.-S. & Suenaga, K. Atomic mechanism of the semiconducting-to-metallic phase transition in single-layered MoS 2. *Nature nanotechnology* **9**, 391-396 (2014).

17 Chou, S. S. *et al.* Understanding catalysis in a multiphasic two-dimensional transition metal dichalcogenide. *Nature communications* **6**, 1-8 (2015).

18 Fang, Y. *et al.* Structural determination and nonlinear optical properties of new 1T‴-type MoS2 compound. *Journal of the American Chemical Society* **141**, 790-793 (2019).

19 Pal, B. *et al.* Chemically exfoliated Mo S 2 layers: Spectroscopic evidence for the semiconducting nature of the dominant trigonal metastable phase. *Physical Review B* **96**, 195426 (2017).

20 Eda, G. *et al.* Coherent atomic and electronic heterostructures of single-layer MoS2. *ACS nano* **6**, 7311-7317 (2012).

21 Eda, G. *et al.* Photoluminescence from chemically exfoliated MoS2. *Nano letters* **11**, 5111-5116 (2011).

22 Voiry, D. *et al.* Conducting MoS2 nanosheets as catalysts for hydrogen evolution reaction. *Nano letters* **13**, 6222-6227 (2013).

23 Ophus, C., Ercius, P., Sarahan, M., Czarnik, C. & Ciston, J. Recording and using 4D-STEM datasets in materials science. *Microscopy and Microanalysis* **20**, 62-63 (2014).

24 Acerce, M., Voiry, D. & Chhowalla, M. Metallic 1T phase MoS 2 nanosheets as supercapacitor electrode materials. *Nature nanotechnology* **10**, 313-318 (2015).

25 Xie, K. *et al.* Superior potassium ion storage via vertical MoS2 "Nano-Rose" with expanded interlayers on graphene. *Small* **13**, 1701471 (2017).

26 Ren, X., Zhao, Q., McCulloch, W. D. & Wu, Y. MoS 2 as a long-life host material for potassium ion intercalation. *Nano Research* **10**, 1313-1321 (2017).

27 Wang, L., Xu, Z., Wang, W. & Bai, X. Atomic mechanism of dynamic electrochemical lithiation processes of MoS2 nanosheets. *Journal of the American Chemical Society* **136**, 6693-6697 (2014).

28 Gao, P., Wang, L., Zhang, Y., Huang, Y. & Liu, K. Atomic-scale probing of the dynamics of sodium transport and intercalation-induced phase transformations in MoS2. *ACS nano* **9**, 11296-11301 (2015).

29 Huang, Q. *et al.* The Mechanistic Insights into the 2H-1T Phase Transition of MoS2 upon Alkali Metal Intercalation: From the Study of Dynamic Sodiation Processes of MoS2 Nanosheets. *Advanced Materials Interfaces* **4**, 1700171 (2017).

30 Santa-Ana, M. A., Sanchez, V. & Gonzalez, G. Temperature effects on the diffusion of lithium in MoS2. *Electrochimica acta* **40**, 1773-

1775 (1995).
31 Somoano, R., Hadek, V. & Rembaum, A. Alkali metal intercalates of molybdenum disulfide. *The Journal of Chemical Physics* **58**, 697-701 (1973).
32 Rudorff, W. Inclusion of base metals in graphite and in metallic chalcogenides of the type MeX 2. *Chimia* **19**, 489-499 (1965).
33 Catterall, R. & Mott, N. Metal-ammonia solutions. *Advances in Physics* **18**, 665-680 (1969).
34 Heising, J. & Kanatzidis, M. G. Structure of restacked MoS2 and WS2 elucidated by electron crystallography. *Journal of the American Chemical Society* **121**, 638-643 (1999).
35 Chrissafis, K. *et al.* Structural studies of MoS2 intercalated by lithium. *Materials Science and Engineering: B* **3**, 145-151 (1989).
36 Enyashin, A. N. & Seifert, G. Density-functional study of LixMoS2 intercalates ($0 \leqslant x \leqslant 1$). *Computational and Theoretical Chemistry* **999**, 13-20 (2012).
37 Andersen, A. *et al.* First-principles characterization of potassium intercalation in hexagonal 2H-MoS2. *The Journal of Physical Chemistry C* **116**, 1826-1832 (2012).
38 Zak, A. *et al.* Alkali metal intercalated fullerene-like MS2 (M= W, Mo) nanoparticles and their properties. *Journal of the American Chemical Society* **124**, 4747-4758 (2002).
39 Huang, Q., Wang, L., Xu, Z., Wang, W. & Bai, X. In-situ TEM investigation of MoS 2 upon alkali metal intercalation. *Science China Chemistry* **61**, 222-227 (2018).
40 Zhou, M., Li, X., Yang, L. & Dong, C. Synthesis, crystal structure and superconducting properties of calcium intercalates of MoS2. *Journal of Solid State Chemistry* **258**, 131-137 (2018).
41 Zhang, J. *et al.* Reversible and selective ion intercalation through the top surface of few-layer MoS 2. *Nature communications* **9**, 1-9 (2018).
42 Zink, N. *et al.* In situ heating TEM study of onion-like WS2 and MoS2 nanostructures obtained via MOCVD. *Chemistry of Materials* **20**, 65-71 (2008).
43 Habenicht, C., Lubk, A., Schuster, R., Knupfer, M. & Büchner, B. Investigation of potassium-intercalated bulk MoS 2 using transmission electron energy-loss spectroscopy. *Physical Review B* **101**, 155429 (2020).
44 Li, Q. *et al.* Intermediate phases in sodium intercalation into MoS2 nanosheets and their implications for sodium-ion batteries. *Nano Energy* **38**, 342-349 (2017).
45 Meyer, J. C. *et al.* The structure of suspended graphene sheets. *Nature* **446**, 60-63 (2007).
46 Du, X. *et al.* Preserved layered structure enables stable cyclic

performance of MoS2 upon potassium insertion. *Chemistry of Materials* **31**, 8801-8809 (2019).

47 Xu, Y. *et al.* Enhancing potassium-ion battery performance by defect and interlayer engineering. *Nanoscale Horizons* **4**, 202-207 (2019).

48 de la Peña, F. *et al.* (Zenodo, 2017).

49 Koch, C. T. *Determination of core structure periodicity and point defect density along dislocations*. (Arizona State University, 2002).

50 Cowley, J. M. & Moodie, A. F. The scattering of electrons by atoms and crystals. I. A new theoretical approach. *Acta Crystallographica* **10**, 609-619 (1957).

51 Kirkland, E. J. *Advanced computing in electron microscopy*. (Springer, 1998).

52 de la Peña, F. *et al.* Electron microscopy (big and small) data analysis with the open source software package HyperSpy. *Microscopy and Microanalysis* **23**, 214-215 (2017).

53 Walt, S. v. d., Colbert, S. C. & Varoquaux, G. The NumPy array: a structure for efficient numerical computation. *Computing in science & engineering* **13**, 22-30 (2011).

54 Hunter, J. D. Matplotlib: A 2D graphics environment. *Computing in science & engineering* **9**, 90-95 (2007).

55 Van der Walt, S. *et al.* scikit-image: image processing in Python. *PeerJ* **2**, e453 (2014).

56 Du, X. *et al.* Exploring the structure evolution of MoS 2 upon Li/Na/K ion insertion and the origin of the unusual stability in potassium ion batteries. *Nanoscale Horizons* **5**, 1618-1627 (2020).

57 Yu, X. *et al.* A material of hierarchical interlayer-expanded MoS 2 nanosheets/hollow N-doped carbon nanofibers as a promising Li+/Mg 2+ co-intercalation host. *Journal of Materials Chemistry A* **9**, 11545-11552 (2021).

Chapter 6

4D-STEM Imaging Local Nano-structures of K-doped MoS_2

This chapter consists of a detailed introduction of the new four-dimensional scanning transmission electron microscopy (4DSTEM) technique and characterisation of nanostructures in the K-intercalated MoS_2 van der Waals crystal using 4DSTEM. This technique has generated significant research interests since the development of the fast pixelated camera, advanced data processing and analysis algorithms in the past few years. One of the key applications of 4DSTEM is to obtain local structural information such as new phases, lattice strains and crystal orientations at the nanoscale. Such information is challenging to obtain via the conventional TEM and STEM. The 4DSTEM presented in this chapter discusses optimal conditions for achieving the goal of revealing the superstructures merging in the K-intercalated MoS_2 flakes.

Firstly, we demonstrate the theory and principle of the 4DSTEM dataset acquisition and data processing method. Then, we present results where we perform 4DSTEM on the similiar K-intercalated specimen which has been detailed discussed in Chapter 5, with the aim of understanding the potential of 4DSTEM to complement the conventional TEM and STEM techniques. Taking advantage of the flexibility of the 4DSTEM dataset we manipulate and reconstruct the stack of diffraction patterns by employing a virtual objective aperture and virtual selected area aperture to map

distributions of the superstructures in different orientations and combinations found in the specimen. Note that a complex superstructure such as the structure shown in Chapter 5 Fig. S5.10c is composed of three superlattices in different orientations shown in Chapter 5 Fig. S5.10e-g. This is the first document reporting the tracking of basic superstructures in the intercalated van der Waals crystal by 4DSTEM and having the potential to advance the investigation of intercalated structures for further application in nanoelectronics, high energy storage devices, catalysis and superconductivities.

Author Contributions

S. Shao performed all S/TEM and 4DSTEM imaging, STEM-EDS data collection, STEM image analysis and EDS data process. W. J. Kuang prepared the K intercalation MoS_2 sample. This manuscript was written by S. Shao, with contributions from S. J. Haigh, and it has not yet been submitted.

4D-STEM Imaging Local Nanostructures of K-intercalated MoS_2

Shouqi Shao[1,2], W. J. Kuang,[3] Irina V. Grigorieva[2,3], Sarah J. Haigh[1,2]

[1] *Department of Materials, University of Manchester, Oxford Road, Manchester M13 9PL, United Kingdom*

[2] *National Graphene Institute, University of Manchester, Oxford Road, Manchester M13 9PL, United Kingdom*

[3] *Department of Physics and Astronomy, University of Manchester, Oxford Road, Manchester M13 9PL, United Kingdom*

6.1 Four-dimensional Scanning Transmission Electron Microscopy

Transmission electron microscope (TEM) is a powerful tool for structural characterisation for a wide range of materials. Electron diffraction and diffraction contrast imaging are two important techniques routinely performed in the structural analysis of materials at the nanoscale in the conventional transmission electron microscopy (CTEM) mode. In CTEM the sample is illuminated by an electron beam parallel to the optical axis and crystal structural information is carried by the diffracted electrons. This pattern demonstrates crystallinity, the type of crystal lattice, lattice parameters and the crystal orientation of a single- or multi-phase material. In the most CTEM diffraction experiments a selected area (SA) aperture is used to select a region of interest in the image plane of the objective lens

to study local structural characteristics. Diffraction contrast imaging can be performed by choosing either the transmitted or a specific diffracted reflection with a small objective aperture, so as to form bright or dark field images, respectively. This approach allows more details of crystal features to visualize such as defects, and changes in the lattice orientation or phase in the selected region.

Diffraction information can also be acquired in the scanning transmission electron microscopy (STEM) mode in which the condenser lenses converge the electron beam to a fine spot scanning over the sample pixel by pixel. Elastically and inelastically scattered electrons produced by interaction between the sample and the electron beam are detected by the segmentation of STEM detectors, allowing to simultaneously acquire a variety of signals, including the bright and annular dark field (BF and ADF) images. For high angle annular dark field (HAADF) STEM, Rutherford scattered electrons with high scattering angles (usually more than three times the convergence semi-angle) contribute to form an image known as Z-contrast imaging due to its sensitivity to atomic number[1]. Annular dark field (ADF) STEM provides an opportunity for imaging diffraction contrast as the Bragg diffracted electrons predominate the image intensity, making this as one of the best ways to show the defects of a crystalline material, such as dislocations, with the reduction of the dynamic scattering effect compared to CTEM[2,3]. However, STEM records the integrated detector intensity in each probe position but does not record the whole diffraction pattern since the positions where the diffracted electrons landing on the detectors is not recorded.

Recently the availability of improved computing and high-speed electron detectors has enabled the widespread application of the four-dimensional STEM (4DSTEM) where electron diffraction patterns acquired by the converged beam are recorded for each probe position. This large 4DSTEM dataset contains rich diffraction information which can be analysed and processed by multiple methods using open source codes[4]. Fig. 6.1 demonstrates the experimental process of acquiring a 4DSTEM dataset where the electron probe with a small convergence angle scans over a sample divided into an n × m pixels grid (Fig. 6.1a). For each pixel where the probe dwells one electron diffraction pattern is captured (Fig. 6.1b). One 128 × 128 pixels 4DSTEM data is about 8 GB and contains 16384 diffraction patterns. These diffraction data can be processed to produce virtual images – for example taking the integrated intensity of each diffraction pattern contributes to the intensity of the corresponding pixel in the virtual image with size n × m pixels shown in Fig. 6.1c. Therefore, the 4DSTEM dataset contains rich structural information of the material, including the characteristics of local structure[5], crystal orientation in polycrystalline[6], and local deformation of the strained crystal lattice[7].

Studying the structural evolution and phase transition in alkali-ion intercalated molybdenum disulphide (MoS_2) is significance of understanding the intercalation mechanism in 2D crystals and further to promote possible applications of MoS_2 in the high energy storage, superconductivity and catalysis. Alkali ions, such as lithium (Li), sodium (Na) and potassium (K) occupying in the gallery between the adjacent MoS_2 layers prefer to occupy the sulphide octahedral sites, resulting in the

ordering superstructures with the formula X_yMoS_2 (X is the alkali ion and y depends on the degree of intercalation). These superstructures have been widely studied using selected area electron diffraction (SAED) by which researchers have found different electron diffraction patterns formed by the superlattices in the X_yMoS_2 flakes in various different levels of intercalation[8,9]. However, the size of the intercalated domains is thought to be only 3-5 nm[10] so many domains will be averaged within the ~ 100 nm radius of the SA aperture and some diffraction patterns may be the results of superimposing several different patterns[9], which is also discussed in Chapter 5. The useful size of the SA aperture is limited by the lens aberration which causes an error in selecting the area if an extremely small SA aperture is inserted, so it is not possible to use SAED to study individual intercalated domains. High resolution (HR) TEM images can be used to study individual superlattice domains although interpretation is challenging[10,11]. 4DSTEM has the advantage of a spatial resolution much better than the domain size and can also be combined with energy dispersive X-ray spectroscopy to achieve correlation of superstructure to local composition, in order to reveal the relation between the intercalation structure and alkali ion content.

Hence, this paper reveals the local superlattices of the K-intercalated MoS_2 characterized using 4DSTEM to complement the structural analysis and hypothesis provided by SAED patterns in Chapter 5. We revealed the different combinations of the ordering K superlattice in the intercalated material by virtual SAED patterns and performed the structural classification to exhibit the regimes of the different superlattices in the

intercalated MoS_2 flake by using virtual objective apertures, which cannot be achieved using conventional CTEM and STEM approaches.

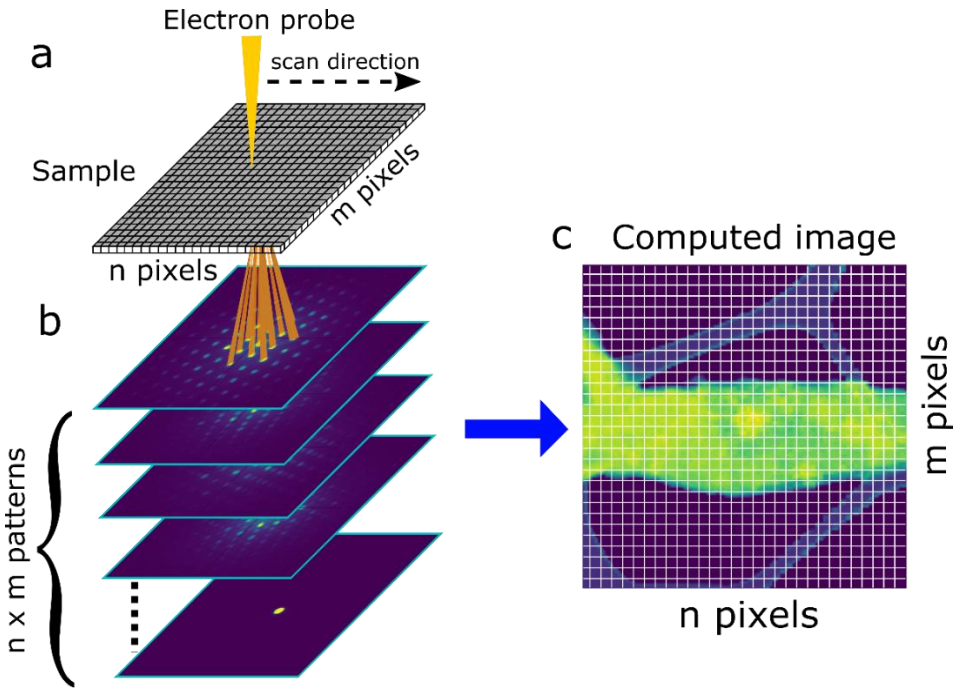

Figure 6.1 Experimental process of acquiring four-dimensional STEM data. (a) demonstrates convergent electron probe being scanned over a sample, and (b) a series of diffraction patterns acquired for every probe position. (c) shows a computed virtual image of the mean intensity obtained for the sample in (a). Higher signal is seen where there is more material to produce scattering.

6.2 Methods

The K-doped MoS_2 samples were also prepared via the liquid ammonia method as introduced in Chapter 5 (see Chapter 5 Methods for details).

CTEM and STEM imaging were performed in a Talos F200X S/TEM equipped with a FEG operated at 200 kV and the sample was oriented along a [001] zone-axis for both CTEM and STEM imaging. CTEM images (2048 × 2048 pixels) were captured using a Thermo Scientific Ceta 16M camera with an exposure time of 2 s and 4 s for bright and dark field TEM images, respectively. For STEM images (1024 × 1024 pixels), the BF,

ADF and HAADF images were acquired at scattering semi-angles of <10 mrad, 10-26 mrad and 28-170 mrad, respectively. The semi-convergence angle of the electron probe is 1.52 mrad and the dwell time is 50 μs in STEM imaging. The semi-angle (α) was calculated by the equation[12]:

$$\alpha = \theta \frac{a}{2b} \tag{6.1}$$

where θ is the Bragg angle of the $(10\bar{1}0)$ plane in MoS_2 lattice (4.58 mrad in this work), a is the diameter (34.21 pixels in this work) of the transmission reflection, b is the distance (51.54 pixels in this work) between the centres of the transmission spot (0000) and the diffraction spot $(10\bar{1}0)$ in the pattern as shown in Fig. 6.2. Note that by opening up the semi-convergence angle, the electron beam size will be decreased in the real space leading to improve the spatial resolution of the measurement and form the larger diffraction disks in the BFP. In this work, however, the large diffraction disks are unexpected because the analysis of the superstructures' disks from the ordering K will be deteriorated due to the overlapped disks. Therefore, the smallest semi-angle was chosen in this work.

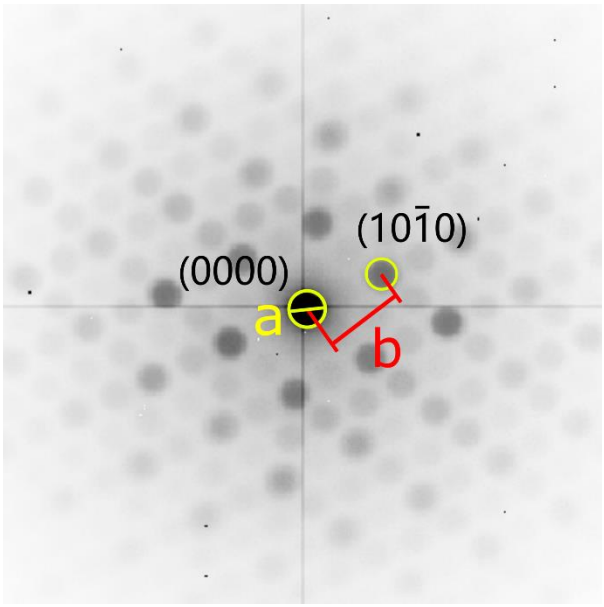

Figure 6.2 Representative diffraction patterns acquired by 4DSTEM. a and b are the diameter of the transmission disk and the distance between the centres of two disks, respectively.

The 4DSTEM datasets were acquired using the MerlinEM direct electron detector placed at the bottom of the Talos. Every 4DSTEM dataset consists of 16,384 single diffraction patterns recorded from a region (128 × 128 pixels). The semi-convergence angle (1.52 mrad) of the electron probe employed in 4DSTEM acquisition was same as STEM imaging in order to compare their results under the same imaging condition, and the camera length of 205 mm was chosen in order to detect clearly separated diffracted disks. To optimise the signal-to-noise ratio without introducing significant beam damages to the sample, the probe current was ~56 pA and the dwell time 50 ms resulting in a total dose of 2.3×10^5 e^-nm^{-2} which is in a safe range (determined as < 2.6×10^5 e^-nm^{-2} as shown in the supporting information of Chapter 5) to prevent the sample being degraded by the electron beam. The evaluation of the 4DSTEM datasets was performed by python packages: Hyperspy[13], py4DSTEM[14], and pyxem[15].

6.3 Results

Fig. 6.3 compares the 4DSTEM reconstructed virtual images and conventional STEM images produced by the conventional BF and ADF detectors. The studied MoS_2 multi-layer flake is intercalated by ordering K ions, forming a complex superstructure in the SAED pattern acquired along [001] orientation as shown in Fig. 6.3b (acquired from a flake region indicated by the red circle in Fig. 6.3a). The BF-STEM image (Fig. 6.3d) produced by the transmitted wave and the HAADF-STEM image (Fig. 6.3f) shows the flake contains several individual crystals with terraces suggesting each crystal consists of multiple layers, and that the edges of the flake are thinner than the central region. In addition, cracks can be seen in the HAADF-STEM image. The ADF-STEM image (Fig. 6.3e) shows a number of bright spot features particularly near the edges of the flake, which may be related to K domains causing the local curvature of the MoS_2 layers (as suggested in Chapter 5 Fig. 5.4). The similar features were also observed in the other intercalated sample as shown in the DF-TEM images (Fig. 6.4a-b). In contrast DF-TEM images of a pristine MoS_2 (Fig. 6.4c-d) do not contain these features but show uniform intensity indicating the MoS_2 layers are relatively flat.

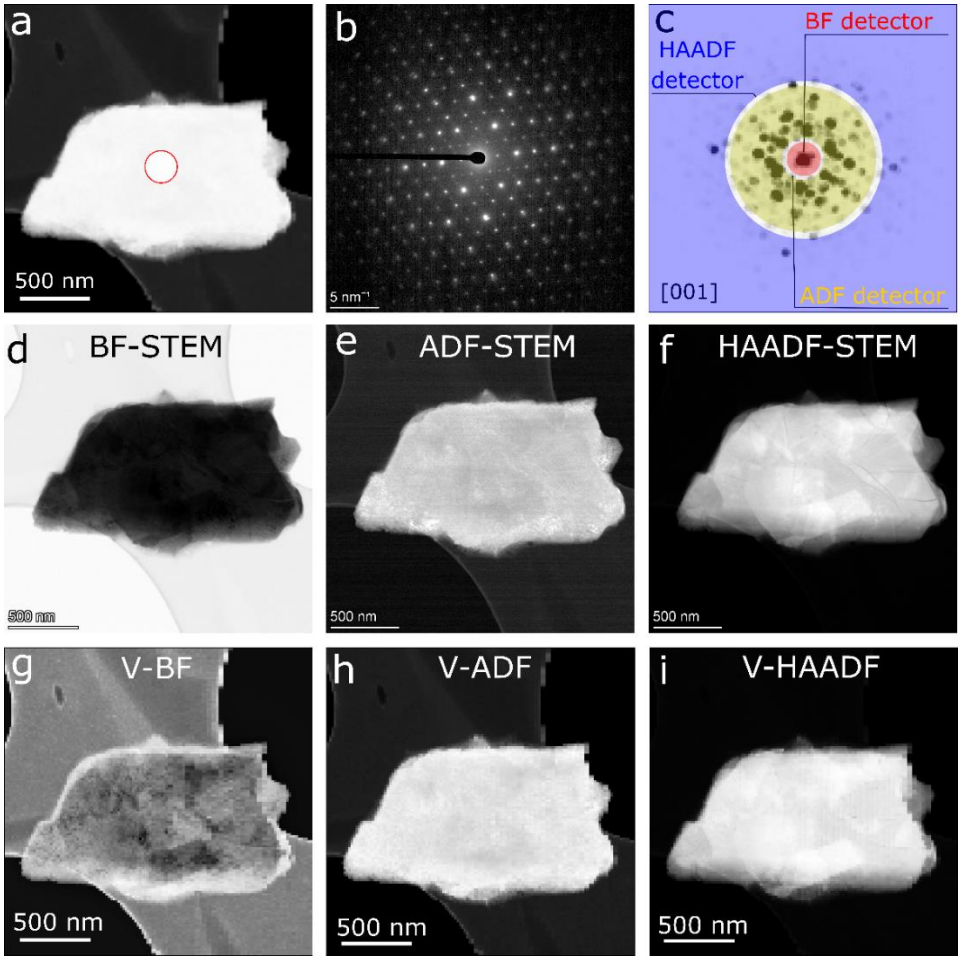

Figure 6.3 Comparisons between the computed virtual images from 4DSTEM dataset and STEM images from real detectors. (a) shows reconstructed 4DSTEM image of a K intercalated MoS_2 flake. (b) is a SAED pattern of the enclosed areas in (a) by a red circle. (c) is a summed 4DSTEM diffraction pattern with the regimes of virtual BF, ADF and HAADF detectors shown as red, yellow and blue, respectively. (d-f) are BF, ADF and HAADF-STEM images of the specimen. (g-i) shows the reconstructed virtual BF, ADF and HAADF images by integrating pixels in the corresponding virtual detectors in (c).

The 4DSTEM virtual image and summed diffraction stack for the same flake are shown in Fig. 6.3a and Fig. 6.3c, respectively. The schematic locations used for the detectors to form the virtual images are shown as the overlays in Fig. 6.3c. The summed diffraction stack viewed along [001] clearly shows that the specimen is composed of a few crystals with small twist angles. A qualitive comparison of the same area (2187 × 2187 nm) between the real detector data in Fig. 6.3e-f and the virtual

images in Fig. 6.3h-i shows that the DF images are similar, although the virtual images carry less spatially resolved detail of the specimen such as cracks and spots due to the poorer image pixel resolution (128 × 128 pixels) in 4DSTEM acquisition compared to STEM images (1024 × 1024 pixels). It is possible to acquire 4DSTEM data with the spatial resolution down to 0.39Å at 80kV[16], but here we chose to sacrifice the spatial resolution to reduce the data size. The contrast reversal seen for the vacuum and carbon support film in the virtual BF (Fig. 6.3d, g) is attributed to the fill the information storage of the counting detector in the 16-bit mode. This means that for the pixelated detector the central spot is saturated (intensity value: 65520) regardless of whether the electron probe is on the specimen or in the vacuum, and the differences in intensity are therefore determined by the amount of scattering just outside the central diffraction spot which is greater when a specimen is present (as illustrated in Fig 6.5).

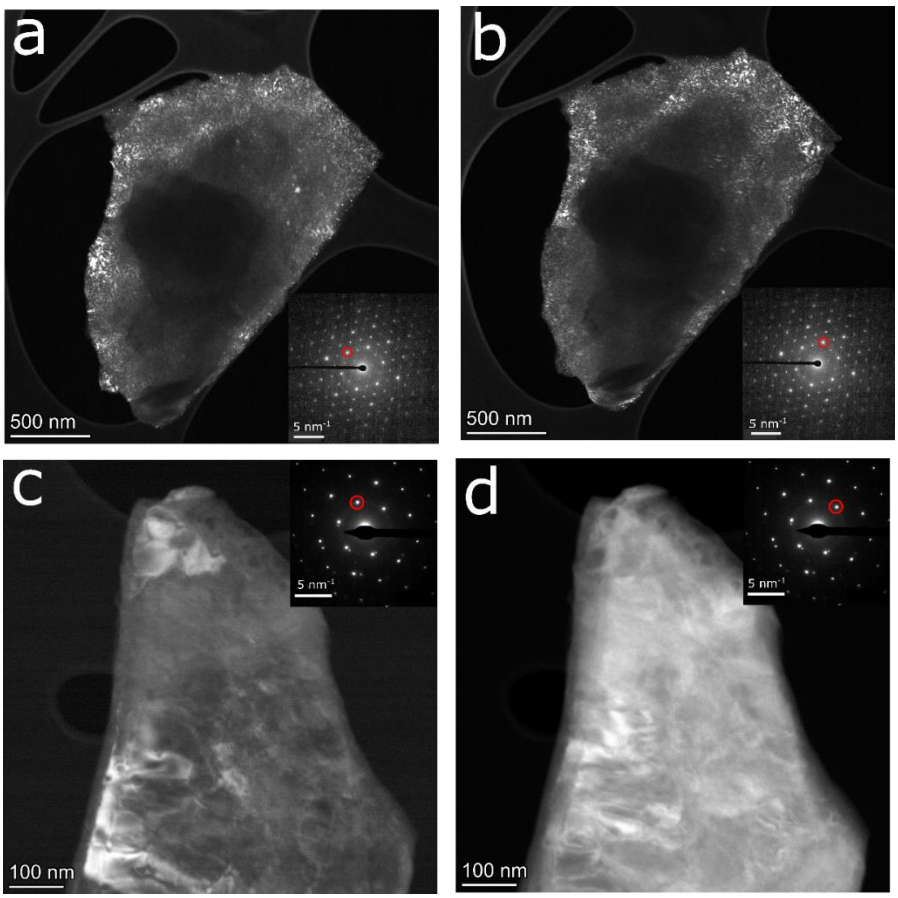

Figure 6.4 DF-TEM images of K intercalated MoS_2 and pristine MoS_2 flake. (a-b) show DF-TEM images of a K intercalated MoS_2 with bright dotted features distributed near the edge of the flake, and their corresponding diffraction reflections selected by the objective aperture indicate by the red circles in insets. (c-d) show DF-TEM images of a pristine MoS_2 flake exhibiting a continuous diffraction contrast different to the features in the K intercalation flake.

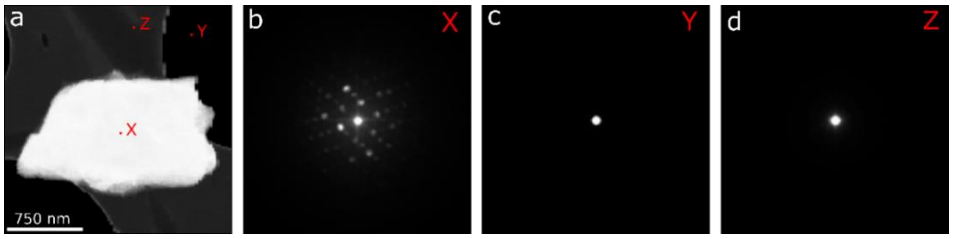

Figure 6.5 Virtual DF image and three 4DSTEM diffraction patterns acquired at different probe positions for the intercalated K-MoS_2. (a) virtual dark field and (b), (c), and (d) are patterns from regions of the image X, Y and Z indicated in (a), where the probe is incident on the sample, vacuum and supporting carbon film, respectively. (b) shows an example of a crystalline diffraction pattern from the specimen. (c) shows a sharp and uniform central spot representing the electron probe, but the probe in (d) has a blurred edge due to the carbon film causing scattering of the electron beam.

Virtual DF images produced by placing the specific objective apertures at desired locations can be calculated from the 4DSTEM datasets to understand scattering from the particular diffraction reflections. This approach can be used to interrogate the spatial distribution of the differently orientated superstructures and the distinct combination of superstructures in the K-intercalated MoS_2 flake (see Chapter 5). According to the report of the sodiated MoS_2 flake, the domain size of the superstructure is approximately 3-5 nm[10], thus SAED is useless to resolve this feature (SA aperture with the radius of hundreds of nanometres in TEM). Fig. 6.6 shows the analysis of the superstructure distribution in a single crystal region of a $K_{0.57}MoS_2$ specimen. The colour overlays on the summed electron diffraction pattern in Fig. 6.6d is used to highlight the MoS_2 reflections (orange) as well as the different superlattice reflections (red, green and blue) that contribute to the overall scattering intensity. The composite reconstructed DF image of the superlattices in Fig. 6.6e shows that the different ordering superstructures is spatially uncorrelated. The single colour pixels show the domains with dimensions of 10s nm to 100s nm composed by one orientated superstructure and the areas of colour pixel overlapping. These overlay regions are due to different superlattice orientations collocating in a single van der Waals gallery space or given their uncorrelated nature, may be the result of single direction intercalation at different depth in the flake. There are also two distinct domains with order 100s nm that show no significant superlattice reflections. The separate distribution maps of individual superlattice are shown in Fig. 6.7 with the corresponding diffraction reflections highlighted. Another

example of the structural classification of the superlattices and the host is given in Fig. 6.8, which also shows that the different superlattices are not collocated.

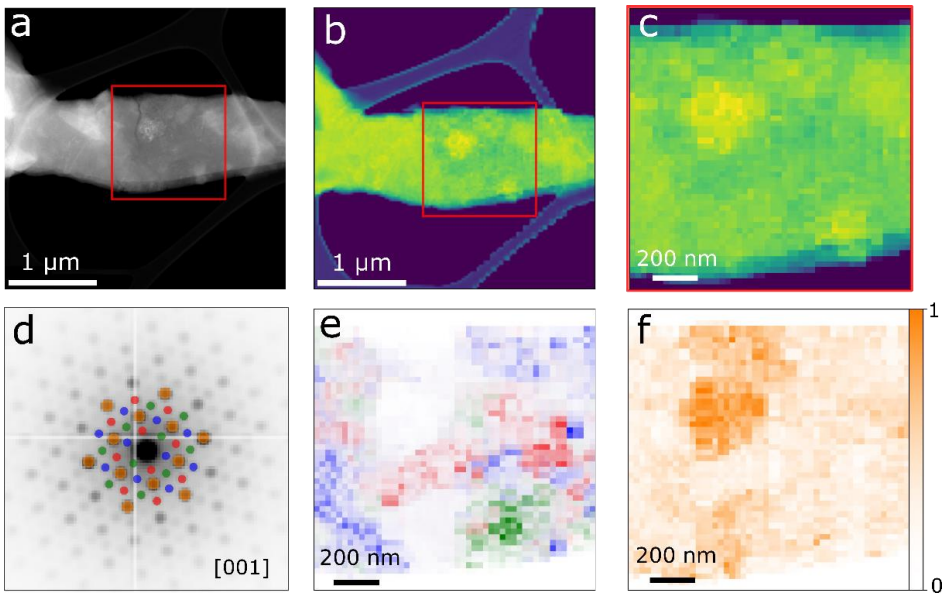

Figure 6.6 Spatial distribution of the scattering from different diffraction spots revealed by virtual DF apertures in 4DSTEM. (a) is a HAADF-STEM image of a K intercalated MoS_2 flake (1024 x 1024 pixels) and (b) is the virtual 4DSTEM summed intensity image of the same region (128 x 128 pixels). The red square (50 x 50 pixels) selects a single crystal area that is shown magnified in the virtual summed intensity image in (c). (d) illustrates the summed electron diffraction data for the selected area shown in (c) where the superlattice reflections for different scattering orientations are highlighted by red, green and blue virtual objective apertures and the MoS_2 host lattice reflections are marked by the orange virtual objective apertures. The computed DF images of three superlattices and of the underlying MoS_2 are shown in (e) and (f), respectively. The colours in the composite image in (e) correspond to those used in the diffraction overlay in (d).

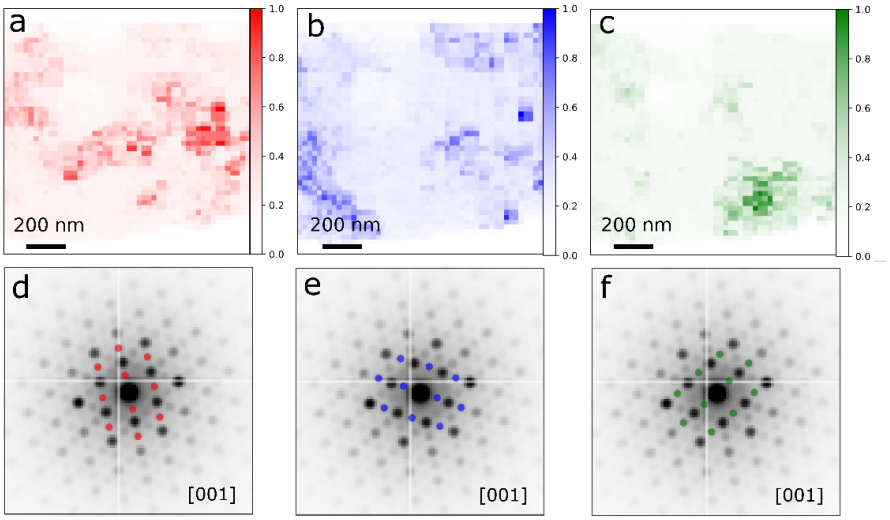

Figure 6.7 (a-c) Structural classification maps and (d-f) electron diffraction patterns of the superlattices for different crystallographic orientations. (Composite map shown in Fig. 6.6e).

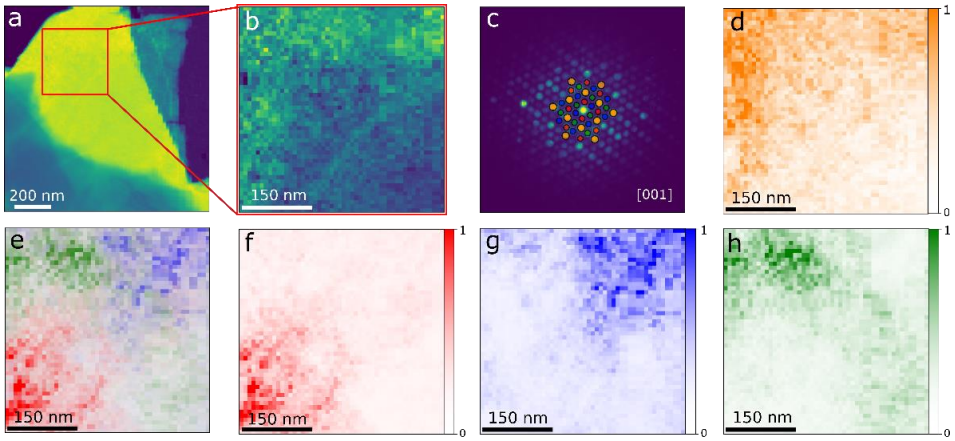

Figure 6.8 Spatial distribution of the scattering from different diffraction spots revealed by virtual DF apertures in 4DSTEM. Structural classification maps of a K intercalated MoS_2. (a) shows a computed 4DSTEM image of the specimen where the red square selects a single crystal region that is magnified and shown in (b). (c) is the summed electron diffraction pattern of the selected region in (a), and red, blue and green disks represent the virtual objective apertures selecting superlattice reflections while the orange disks select the host lattice reflections of MoS_2 crystal. (d) is a distribution map of MoS_2. (e) illustrates a combination of three distribution maps of the individual superlattices in (f-h).

Fig. 6.9a shows a summed diffraction data for a 50 x 50 pixels 4DSTEM image with pixel size of 20.5 nm as shown in Fig. 6.9b. In this work we selected the virtual SAED aperture with the size of 5 x 5 pixels to characterise the local structure to reduce the data processing time. Eight representative virtual SAED apertures have been illustrated in Fig. 6.9b as the regimes of the colour squares with circled numbers inside. Eight corresponding virtual SAED patterns (Fig. 6.9c-j), which are summed diffraction data for the virtual SAED apertures, demonstrate different structural characteristics of domains (regions shown in Fig. 6.9b) in the region of interest. Fig 6.9d shows the expected hexagonal diffraction pattern of MoS_2 without any superlattice spots (area 2 in Fig. 6.9b). However, the comparison to the EDS map in Fig. 6.10 shows that the absence of superlattice reflections does not indicate the disappearance of K ions, but only to the loss of K ordering. As this loss of ordering is positioned in the centre of the image where the electron beam park position is located by default, it is possible that the loss of ordering of the K seen here is the result of local electron beam induced degradation. The calculated summed SAED patterns in Fig. 6.9c, e and f display superlattice arrangements with ordering along only one orientation as the atomic models shown in Fig. S5.11e-g, supporting our hypothesis that the single orientated superlattices exist independent of each other in the K intercalated MoS_2 flake. Regions where two or even all three superlattices overlap are also observed within the particular ~100 nm regions (Fig. 6.9g-j) and the combination of superstructure are even present within the diffraction patterns extracted for the single pixels (20.5 nm spatial

resolution) as shown in Fig. 6.11c,d. A complete data set of 100 diffraction patterns (each 5x5 pixel summation from this 50 × 50 pixels image) are shown in Fig. 6.12.

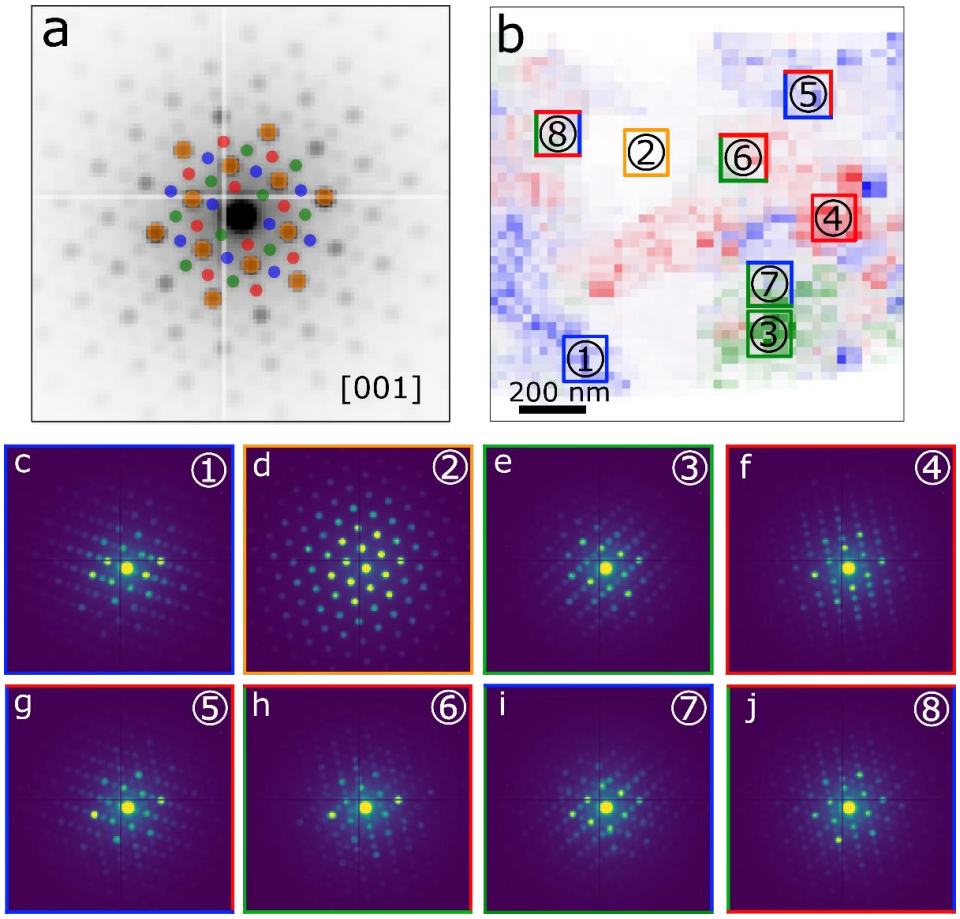

Figure 6.9 Virtual selected area aperture positions and the corresponding summed 4DSTEM selected area diffraction patterns. (a) shows summed electron diffraction of the selected area (identical to Fig. 6.6d). (b) is the composite computed DF image showing the superlative ordering in the three superlattice orientations with 8 selected regions of interest (5 × 5 pixels) used to produce the computed SAED patterns shown in (c-j). (c, e-f) show single superlattice patterns. (d) illustrates a hexagonal MoS_2 pattern (without K ordering). (g-i) display mixed patterns including ordering for two of the three superlattices. (j) shows all three superlattices superimposed within one pattern.

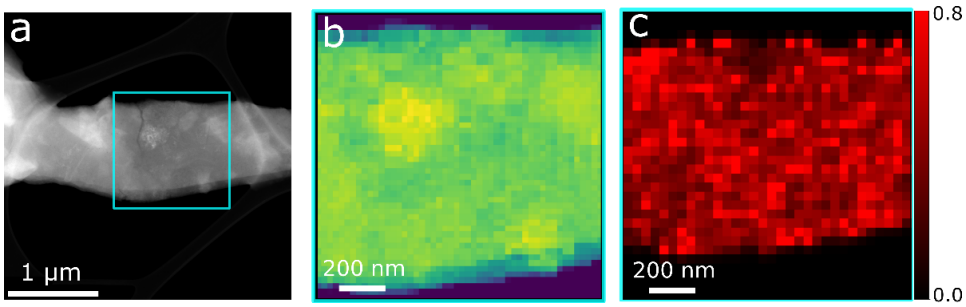

Figure 6.10 Comparison between 4DSTEM image to the EDS map. (a) is a HAADF-STEM image of K intercalated MoS_2 flake. (b) shows 4DSETM computed image of a selected area in (a) enclosed by cyan square. (c) illustrates the EDS map of K/Mo ratio in the same selected area.

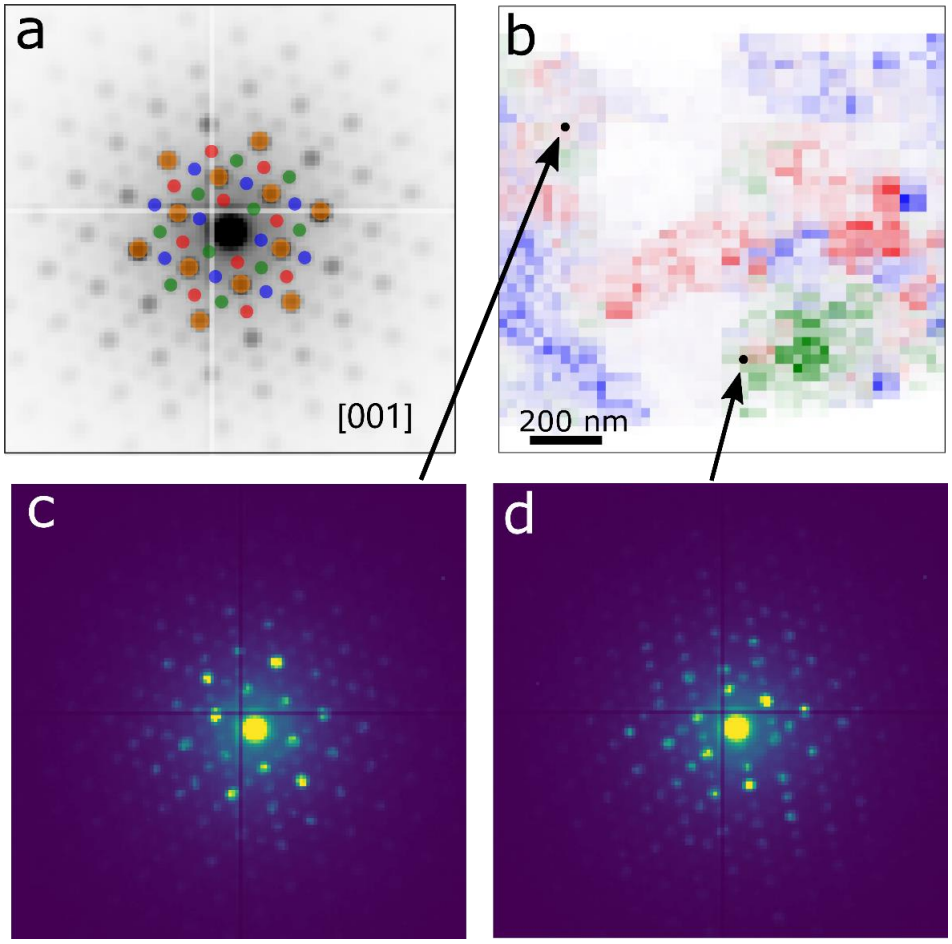

Figure 6.11 4DSTEM electron diffraction data for the single pixels. (a) is summed diffraction pattern of the image (50 x 50 pixel) shown in (b). (c) and (d) are electron diffraction patterns acquired from two individual pixels in (b) highlighted by the black dots, demonstrating three and two superlattice overlapping, respectively.

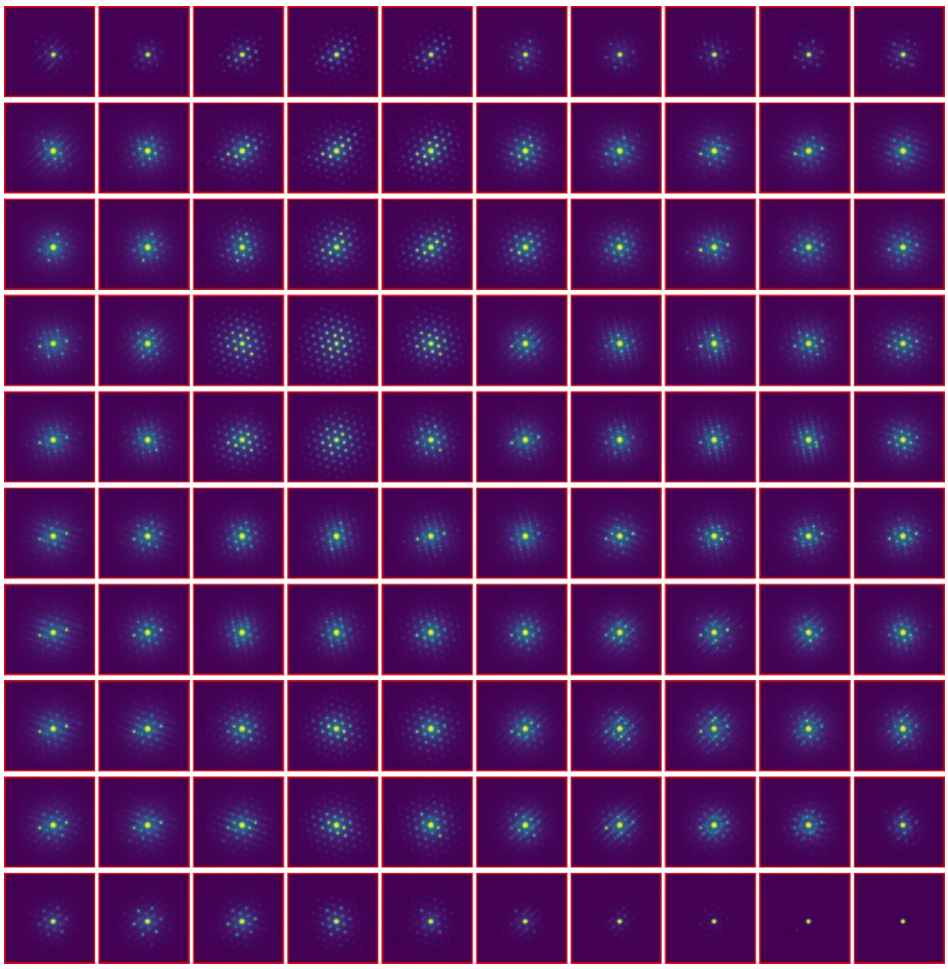

Figure 6.12 100 (5 x 5 pixel) summed SAED patterns are derived from 4DSTEM dataset represented in Fig. 6.6. The crosses shown in Fig. 6.11c-d are not showing very clearly in these 100 images, since the images are zoomed out.

6.4 Conclusions

This manuscript introduces the 4DSTEM technique by which large datasets containing wealthy structural information are acquired. The advanced data processing methods can provide highly flexible analytical potential to retrieve nano-structural information. They have been implemented into the investigation of K-intercalated MoS_2. The results of 4DSTEM, STEM-EDS, CTEM and conventional STEM were compared. Although the image spatial resolution is reduced in the 4DSTEM dataset compared to the traditional CTEM/STEM, it has the advantage of the greater spatial resolution in diffraction space. This enables our 4DSTEM results to show unambiguously that the ordering K superlattices are distributed independently and the lateral dimensions of domain sizes is 10-100 nm, which are not correlated to the local potassium concentration. The presence of K ordering for several lattice orientations to form a coherent unit cell cannot be ruled out in this data but given the spatial independence that is observed within the basal plane, we hypothesise that the ordering regions are also spatially separated along the electron beam direction. This novel data set provides additional structural understanding of this complex intercalated nanostructure, which can be used further develop intercalated materials for a range of applications.

Bibliography

1 Jesson, D. & Pennycook, S. J. Incoherent imaging of crystals using thermally scattered electrons. *Proceedings of the Royal Society of London. Series A: Mathematical and Physical Sciences* **449**, 273-293 (1995).

2 Phillips, P., Brandes, M., Mills, M. & De Graef, M. Diffraction contrast STEM of dislocations: Imaging and simulations. *Ultramicroscopy* **111**, 1483-1487 (2011).

3 Jácome, L. A., Eggeler, G. & Dlouhý, A. Advanced scanning transmission stereo electron microscopy of structural and functional engineering materials. *Ultramicroscopy* **122**, 48-59 (2012).

4 Ophus, C. Four-dimensional scanning transmission electron microscopy (4D-STEM): From scanning nanodiffraction to ptychography and beyond. *Microscopy and Microanalysis* **25**, 563-582 (2019).

5 Tao, J. *et al.* Direct imaging of nanoscale phase separation in La 0.55 Ca 0.45 MnO 3: relationship to colossal magnetoresistance. *Physical Review Letters* **103**, 097202 (2009).

6 Kobler, A., Kashiwar, A., Hahn, H. & Kübel, C. Combination of in situ straining and ACOM TEM: A novel method for analysis of plastic deformation of nanocrystalline metals. *Ultramicroscopy* **128**, 68-81 (2013).

7 Rottmann, P. F. & Hemker, K. J. Nanoscale elastic strain mapping of polycrystalline materials. *Materials Research Letters* **6**, 249-254 (2018).

8 Wang, L., Xu, Z., Wang, W. & Bai, X. Atomic mechanism of dynamic electrochemical lithiation processes of MoS2 nanosheets. *Journal of the American Chemical Society* **136**, 6693-6697 (2014).

9 Huang, Q. *et al.* The mechanistic insights into the 2H-1T phase transition of MoS2 upon alkali metal intercalation: from the study of dynamic sodiation processes of MoS2 nanosheets. *Advanced Materials Interfaces* **4**, 1700171 (2017).

10 Gao, P., Wang, L., Zhang, Y., Huang, Y. & Liu, K. Atomic-scale probing of the dynamics of sodium transport and intercalation-induced phase transformations in MoS2. *ACS nano* **9**, 11296-11301 (2015).

11 Huang, Q., Wang, L., Xu, Z., Wang, W. & Bai, X. In-situ TEM investigation of MoS 2 upon alkali metal intercalation. *Science China Chemistry* **61**, 222-227 (2018).

12 Weyland, M. & Muller, D. A. Tuning the convergence angle for optimum STEM performance. *arXiv preprint arXiv:2008.12870* (2020).

13 de la Peña, F. *et al.* hyperspy/hyperspy: HyperSpy v1. 5.2. *Zenodo* (2019).
14 Savitzky, B. H. *et al.* py4DSTEM: A software package for multimodal analysis of four-dimensional scanning transmission electron microscopy datasets. *arXiv preprint arXiv:2003.09523* (2020).
15 Johnstone, D. N. *et al.* (Zenodo, 2019).
16 Nishitani, R., Uno, Y. & Suematsu, H. In situ observation of staging in potassium-graphite intercalation compounds. *Physical Review B* **27**, 6572 (1983).

Chapter 7

Imaging Eu Intercalation in Bilayer Graphene via TEM *In-situ* Biasing

This chapter presents the results of *in-situ* TEM experiments towards europium (Eu) intercalation in bilayer graphene. We demonstrate a novel workflow for manufacturing an electrochemical nanodevice based on a commercial *in-situ* biasing TEM chip, including mechanical exfoliation of bilayer graphene, dry transfer of the flake and preparation of the solid-state ionic liquid electrolyte on the TEM chip. The intercalation process is imaged by STEM in real time and we observe the morphologic changes of the suspended bilayer graphene membrane induced by intercalation. Both intercalation of Eu and ionic liquid cations are suggested to have been achieved at low applied bias (-4V) and high applied bias (-8V), respectively evidenced by SAED and STEM-EDS.

Author Contributions

S. Shao performed all *in-situ* S/TEM imaging and STEM-EDS data collection, Raman spectrum collection, SAED and S/TEM image analysis, STEM-EDS elemental and Raman spectrum analysis, and partial *ex-situ* S/TEM imaging. M. Feng prepared bilayer graphene and Eu electrolyte. R. Cai performed partial *ex-situ* S/TEM imaging. The manuscript was drafted by S. Shao with input and discussions with R. Cai, M. Feng, A. Mishchenko and S. J. Haigh, and it has not yet been submitted.

Imaging Eu Intercalation in Bilayer Graphene via TEM *In-situ* Biasing

Shouqi Shao[1,2], Mengjie Feng[2,3], Rongsheng Cai[1], Artem Mishchenko[2,3], Sarah J. Haigh[1,2]

[1] *Department of Materials, University of Manchester, Oxford Road, Manchester M13 9PL, United Kingdom*

[2] *National Graphene Institute, University of Manchester, Oxford Road, Manchester M13 9PL, United Kingdom*

[3] *Department of Physics and Astronomy, University of Manchester, Oxford Road, Manchester M13 9PL, United Kingdom*

7.1 Introduction

Metallic ion intercalation in van der Waals materials (e.g. graphite and MoS_2) and the resulting physiochemical properties and intercalation structures have been widely studied in the 1970s and 1980s[1-4]. More recently, intercalation of the exfoliated van der Waals materials down to a few-layer thickness, have been observed to exhibit different intercalation behaviours compared to their bulk counterparts[5,6]. In addition, many open questions still remain regarding intercalation mechanisms, phase transition and superstructure formation, in both bulk and few-layer van der Waals materials.

Ex-situ has been widely applied to the study of intercalated materials

and it provides a key method to study local superstructures, intercalation inhomogeneity and crystal defects. However, the snapshot TEM approach, where separate materials are studied at different time points during the intercalation processes is very labor intensive, time consuming and even missing crucial intermediary steps[7], and may be impossible to employ for air sensitive intercalation processes. In the last decades, *in-situ* scanning/transmission electron microscopy (S/TEM) methods have become increasingly popular, possible due to technical developments in the environmental TEM (ETEM)[8] and *in-situ* sample holders[9,10]. *In-situ* TEM allows researchers to dynamically observe physical and chemical variations of the specimen under external stimuli, for instance high temperature[9], voltage biasing[10] or applied mechanical strain[11]. A wide variety of material studies have benefited from *in-situ* TEM including imaging of the electrochemical reaction process[12], elucidating chemical synthesis routes[13] and recording mechanical failure mechanisms at the nanoscale[14].

In-situ TEM has been used to image the intercalant diffusing in the 2D flake in real time[5,15], to observe the development of the intercalated superstructures[16] and to characterise the evolution of new phases[5,17].

Eu intercalated few-layer graphene (FLG) is of interest as a straightforward approach to produce a van der Waals 2D ferromagnet[18]. Intercalated Eu ions prefer to occupy the hollow sites of the graphene lattice to form a $\left(\sqrt{3}\times\sqrt{3}\right)R30°$ superstructure with the EuC_6 stoichiometry according to reflection high-energy electron diffraction pattern[18,19]. Additionally, by employing encapsulation the EuC_6 is

prevented from being oxidized in the air and ensures the material's ferromagnetism is retained[18]. Even before intercalation in FLG was demonstrated in 2021, a great number of studies have been devoted to investigating Eu intercalation between a graphene layer and an iridium (Ir) or aluminum (Al) metal prepared by the heating method to produce magnetic properties[19-22], however this system has not yet been investigated by *in-situ* TEM to reveal intercalation dynamics and structural evolution in real time under biasing.

In this chapter we introduce a homemade electrochemical nanodevice based on a commercial *in-situ* TEM chip manufactured by Protochips (Fusion Protochips nc.). Fabrication is achieved via conventional dry transfer steps[23] with modifications (adding some heating steps detailed in section 7.2) to suit the commercial chip for the flake transfer. Compared to the conventional heating and liquid ammonia approaches to intercalation[24,25] the electrochemical method is better suited to *in-situ* TEM studies, requiring shorter intercalation times and having fewer safety concerns. The choice of Eu as the metallic intercalating cations is beneficial for TEM studies since Eu has a much higher atomic number than carbon so should be clearly visible by using HAADF-STEM, exhibiting significantly greater contrast than the alkali metals such as lithium, sodium and potassium. The Eu ions are in a solid state electrolyte, which has a low vapour pressure than conventional liquid electrolytes thus preventing it being lost in the TEM vacuum[26].

7.2 Fabrication of Nanodevice for TEM *In-situ* Biasing

7.2.1 Bilayer Graphene Flake Exfoliation

To prepare polymer coated silicon wafers a piece of the wafer was cleaned in deionised water (DI water), acetone and isopropyl alcohol (IPA) for 5 minutes in a sonication bath and dried in a stream of nitrogen to remove potential surface contamination. Then the cleaned wafer was coated with a layer of water-soluble polyvinyl alcohol (PVA) followed by a layer of poly methyl methacrylate (PMMA). The PVA was spin coated on the wafer with a spin speed of 4000 rpm at an acceleration of 1000 rpm/s, and cured at 100 °C for 5 minutes. Then, the PMMA layer was spin coated on top of the PVA layer with the same spin-coating conditions, and the wafer was baked at 130 °C for 5 minutes to cure the polymer.

The mechanical cleavage technique was applied to exfoliate bilayer graphene from the highly oriented pyrolytic graphite (HOPG) supplied by NatureGraphite GmbH[27]. Bilayer graphene can be peeled off from the bulk graphite by repeatedly folding the adhesive tape (BT-150E-KL) several times to thin the graphite until the flake is not easy to be exfoliated by the tape. Bilayer graphene on the adhesive tape was then stuck onto the polymer coated silicon wafer, and the tape was removed after waiting a few hours to increase the adhesion between bilayer graphene and the PMMA layer (Fig. 7.2a). Bilayer graphene can be identified based on its relatively weaker optical contrast compared to graphite (Fig. 7.1a). Although the

number of few-layer graphene cannot be precisely determined by optical microscopy unless the reflectance conditions are precisely controlled[28,29], Raman spectroscopy is frequently used to identify the number of layers[30,31].

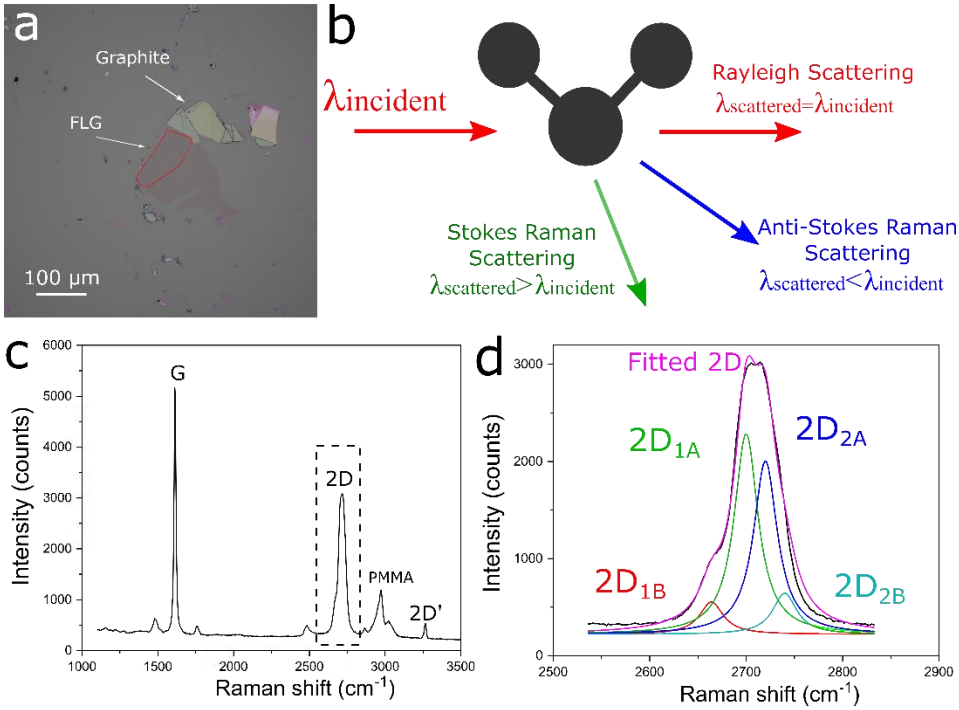

Figure 7.1 Optical image of the bilayer graphene enclosed by the red lines and the graphite (silver color) shown in (a). (b) illustrates the interaction between the photon and molecule, resulting in the Raman scatters. (c) is a Raman spectrum of the selected bilayer in (a). The magnified 2D peak in (c) presents in (d).

7.2.2 Raman Spectroscopy

Raman spectroscopy is a non-destructive structural analysis technique which provides detailed information of graphene about intrinsic defects, lattice strain, doping and atomic arrangement of the edges.[32-35] It also enables to identify the layer number of few-layer graphene as the main purpose of employing Raman spectroscopy in this work.[36] This section briefly introduces the theory of this technique.

Raman spectroscopy is based on the intercalation between the photon

from a laser source and the molecule in the materials. The oscillating electromagnetic field of a photon induces a polarization of the molecular electron cloud that causes the molecule excited into a virtual state with higher energy. The energy difference between the ground and the virtual state is equal to the energy transferred from the incident photon. However, this virtual state is not stable and the photon is re-emitted almost immediately as the scattered signal. There are two possible results of this scattering events (Fig. 7.1b): 1. in the vast majority events, the energy of the molecule is unchanged after phone-molecule interaction, called elastic or Rayleigh scattering; 2. in the much rarer event, Raman scattering occurs with energy transfer between the photon and the molecule. If the energy of the incident photon increases ($\lambda_{scattered}>\lambda_{incident}$), i.e. the molecule loses energy, it is known as Stokes Raman scattering. Inversely, if the energy of the incident photon decreases ($\lambda_{scattered}<\lambda_{incident}$), it is called Anti-Stokes Raman scattering. Statistically, the Stokes Raman scatter is the more probably process, resulting in higher intensity compared to the Anti-Stokes scatter, and thus the Stokes scatter is measured in Raman spectroscopy. Note that the wavelength of the scattered photon highly depends on the incident energy of the light. Therefore, in order to compare the Raman spectra acquired by different laser sources, the wavenumber Raman shift ($\Delta \boldsymbol{v}$) is introduced as demonstrated in the equation (7.1):

$$\Delta v(cm^{-1}) = \left(\frac{1}{\lambda_{\text{incident}}(nm)} - \frac{1}{\lambda_{\text{Stokes}}(nm)}\right) \times \frac{(10^7\, nm)}{(cm)} \qquad (7.1)$$

where λ_{Stokes} is the wavelength of the Raman scatter in nm.

The characteristic Raman peaks for monolayer graphene include the G peak at ~1580 cm^{-1} and 2D peak at ~ 2700 cm^{-1} [36]. The intensity of 2D

peak is roughly four times more intense than the G peak, but the shape and height of 2D peak changes as a function of the number of graphene layers. For the bilayer graphene, 2D peak is comprised by 4 components[36]: $2D_{1B}$, $2D_{1A}$, $2D_{2A}$, $2D_{2B}$, and two of which, $2D_{1A}$, $2D_{2A}$, have relatively higher intensity. Fig, 6.1c-d illustrates the exfoliated flake that has bilayer nature. Additionally, the absence of the D peak at ~1350 cm^{-1} in the Raman spectrum indicates the integrity of the flake without a great number of defects. Refer to Ref [34,36-38] for more details about graphene or few-layer graphene characterised by Raman spectroscopy.

7.2.3 Dry Transfer of Bilayer Graphene

Once the desired bilayer graphene is identified it is transferred onto the cleaned *in-situ* TEM chip using a series of steps illustrated in Fig. 7.2. The approach is based on the previously reported dry transfer method[23] with some improvements to increase the adhesion between the flake and the commercial TEM chip. First a circle is scratched around the flake using a scriber to define a region to be peeled off from the Si wafer (diameter ~ 3.5 mm, Fig. 7.2b). A few drops of DI water were then pipetted onto the outside border of the circular scratch and infiltrates along the polymer interface (Fig. 7.2c). After a few minutes the DI water had dissolved the PVA layer, releasing the PMMA membrane from the Si wafer (Fig. 7.2d). Then the wafer was gently dipped into a beaker filled with DI water, enabling the detached PMMA membrane with bilayer graphene to float on the surface of the DI water (Fig. 7.2e). Next a plectrum coated with PMMA is used to pick up the membrane from the bottom while avoiding letting the upper

surface of the PMMA with the flake attached to make contact with the DI water in the beaker (Fig. 7.2f). Next the flake was attached to the pre-cleaned *in-situ* TEM chip while it was being heated at 120 °C. Heating is used to increase the adhesion between the flake to the chip and also evaporate the residual water ensuring the flake is fully attached to the chip without any bubbles at the interface (Fig. 7.2g). Finally, the PMMA membrane is removed by soaking the chip in hot acetone (~ 70 °C) for 10 minutes. This step is repeated 3 times to ensure that the PMMA film was entirely washed off the chip (Fig. 7.2h). Note that the adhesion between the flake and chip is still weak in the washing-off step so stirring and sonicating should be avoided.

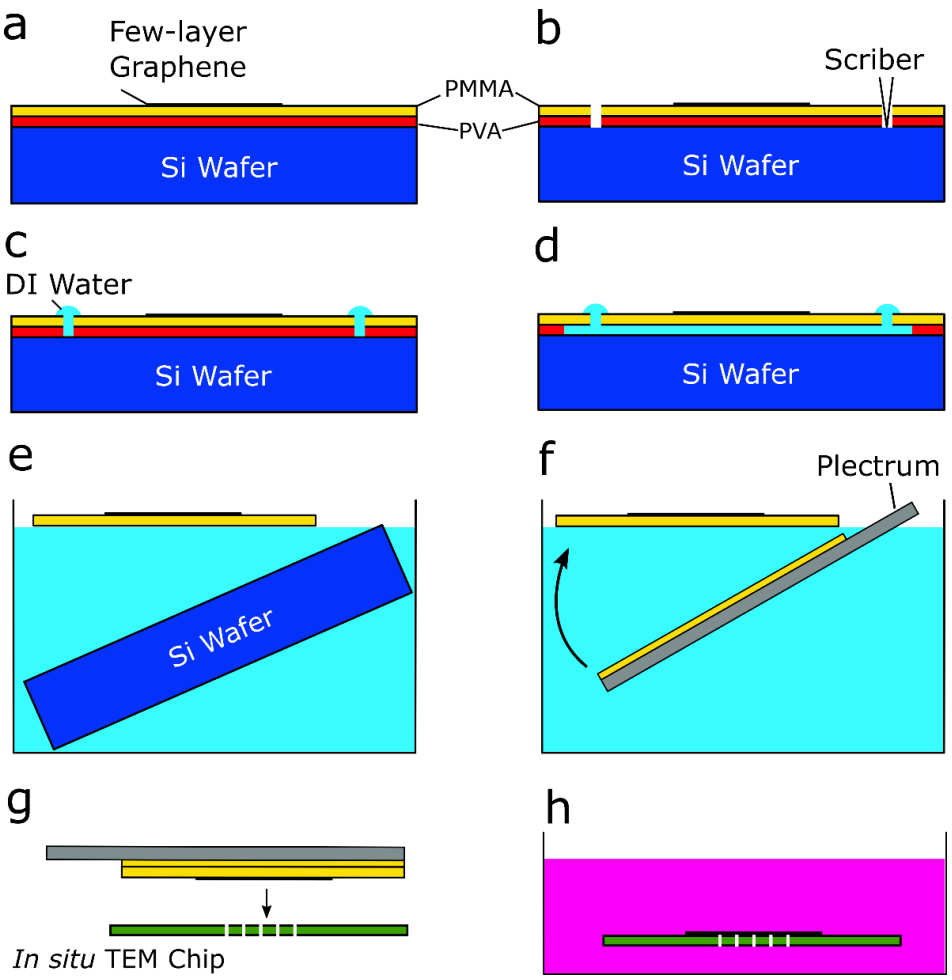

Figure 7.2 A schematic of the modified dry transfer process used to obtain bilayer graphene on the *in-situ* TEM chip. (a) shows a Si wafer coated by a PVA and a PMMA layer, and bilayer graphene transferred on top. The polymer layers were then circular scratched by a scriber shown in (b). (c) DI water is introduced into the scratch. (d) shows the PVA layer being dissolved by the DI water. (e) shows the PMMA membrane with bilayer graphene released from the Si wafer and floating on the DI water. (f) illustrates picking up the PMMA membrane using a plectrum. (g) shows transfer of bilayer graphene onto an *in-situ* TEM chip which was then washed in the acetone and IPA to remove the polymer transfer layer as shown in (h).

7.2.4 Preparation of Solid-state Electrolyte

In this work, a solid-state electrolyte was prepared in an Ar filled glovebox. The polymer matrix of the electrolyte was prepared by mixing of bisphenol A ethoxylate dimethacrylate (BEMA, average M_n=1700, Sigma Aldrich, Fig. 7.3a) and poly(ethylene glycol) methyl ether methacrylate (PEGMA, average M_n=500, Sigma Aldrich, Fig. 7.3d) in 7:3 weight ratio adapted from previous work[26]. 3 wt% of radical photo-infitiator: 2-Hydroxy-2-methylpropiophenone (Da-rocur 1173, Fig. 7.3c) was added to accelerate the solidification of the electrolyte matrix under an UV exposure.[5] 3 wt% Eu salt (europium trifluoromethanesulfonate, Sigma Aldrich, Fig. 7.3e)[39] was mixed with 15 wt% ionic liquid (1-Butyl-1-methylpyrrolidinium bis (trifluoromethylsulfonyl) imide, Sigma Aldrich, Fig. 7.3b) which ensure the high ion conductivity of the electrolyte at room temperature.[40] The mixture of polymer matrix and ionic liquid with Eu salt was stirred for 2 hours for complete mixing, followed by drop casting onto the *in-situ* TEM chip. The drop is then exposed to ultraviolet radiation for 2 minutes to cure the polymer matrix. This solid-state electrolyte is ideal for *in-situ* TEM experiments due to its stability and non-volatility in the vacuum chamber.[26] Fig. 7.4 shows optical images of the *in-situ* chip before and after drop casting the electrolyte and the region of bilayer graphene.

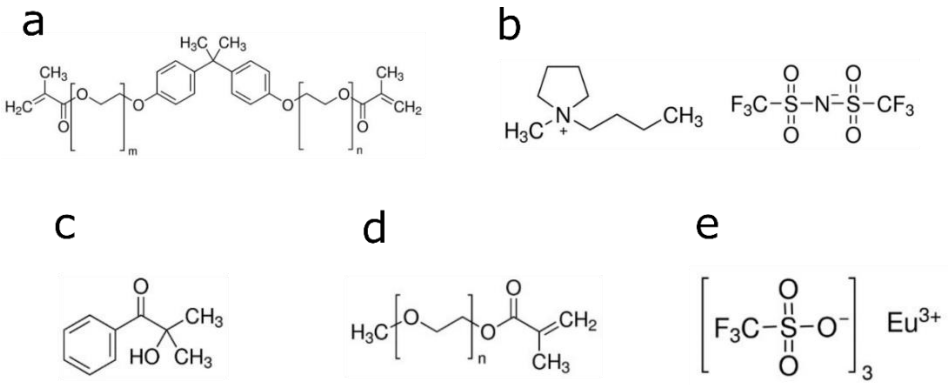

Figure 7.3 Chemical substances used in the preparation of the solid-state electrolyte. (a) BEMA, (b) ionic liquid, (c) photo-initiator, (d) PEGMA and (e) Eu salt.

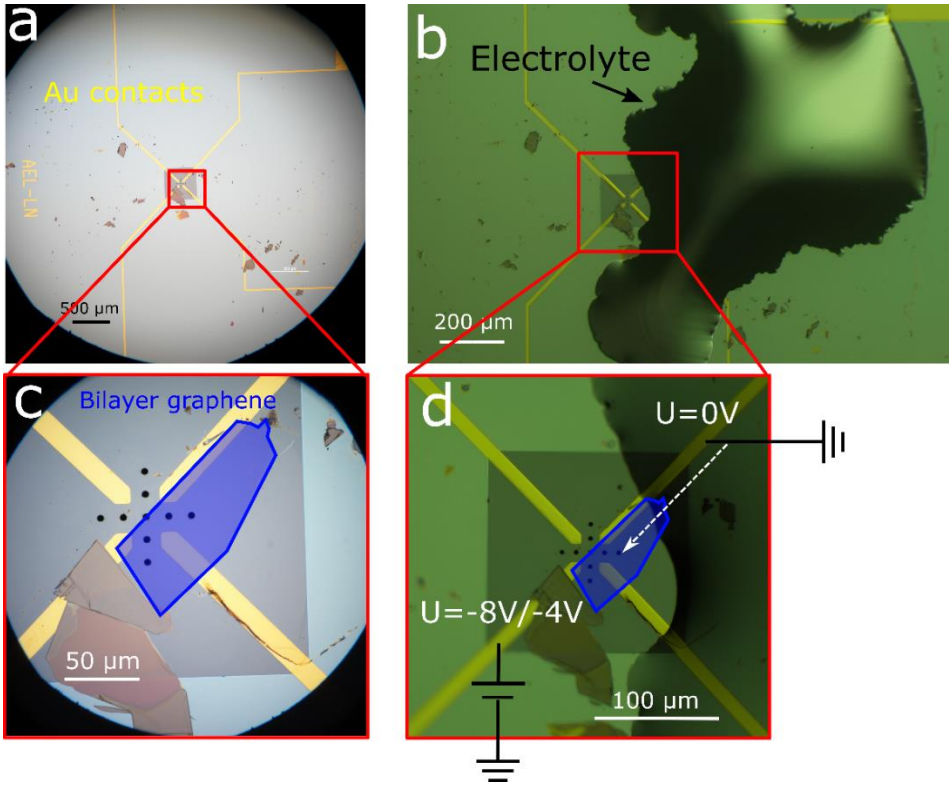

Figure 7.4 Device configuration for the *in-situ* TEM intercalation experiment. (a) shows the *in-situ* TEM chip where the flake has been transferred (flake region magnified in (c)). The blue shadow overlay highlights the region of the transferred bilayer graphene. (b) shows the same area after the solid-state electrolyte is deposited on the chip (flake region magnified in (d)). The white arrow indicates the intercalation direction of the cations

7.2.5 *In-situ* TEM characterisation

For *in-situ* S/TEM imaging the nanodevice was mounted onto a double-tilt Protochips Aduro sample holder in the glovebox. The holder was then transported to the TEM in a sealed Ar filled box and loaded into the TEM column in a few seconds to minimise the electrolyte decomposition in air. TEM selected area electron diffraction (SAED), STEM imaging and EDS mapping were performed in an FEI Talos F200X and FEI Titan G2 80-200 "ChemiSTEM" operated at 80 kV to minimise knock-on damage of bilayer graphene by the electron beam. For the *in-situ* biasing experiments we applied -8V or -4V to the bottom left Au electrode and grounded the top right Au electrode (0V) to create a potential difference as shown in Fig. 7.4d, thus allowing the cations to intercalate into the flake along the direction of the white dashed arrow.

7.3 Results

7.3.1 Pre-intercalation S/TEM Characterisation

Fig. 7.5 shows S/TEM characterisation of bilayer graphene before *in-situ* biasing. In the bright field (BF) TEM image the bilayer graphene membrane is seen to completely cover a hole in the TEM chip (Fig. 7.5a). Black dots and vague small shadows are believed to be organic residue contamination left after washing off the PMMA transfer layer. Fig. 7.5b displays a SAED pattern of the bilayer graphene membrane in Fig. 7.5a, demonstrating the expected hexagonal lattice of graphene (red dotted hexagons). A line profile along a yellow dotted line crosses four primary

lattice reflections showing higher intensities of the high order spots {1210} compared to that of the lower order spots {0110} and the normalised intensity ratio of {0110}/{1210} is around 0.41, close to the expected simulated ratio for AB stacked bilayer graphene of 0.44[6], in agreement with the bilayer conclusion taken from the Raman spectroscopy. Diffraction contrast in a ADF-STEM image of the bilayer graphene membrane illustrates periodic ripples in the transferred membrane (Fig. 7.5c), likely produced during mechanical transfer[41]. STEM-EDS spectral imaging indicates only the four commonly expected elements appearing in the EDS spectrum (Fig. 7.5d); silicon (Si), nitrogen (N) and oxygen (O) primarily due to the SiN in the TEM chip, and carbon (C) is mainly from contaminants and bilayer graphene. The HAADF-STEM images and EDS maps are oval rather than round due to poor scan coil setup, but this will not affect the qualitative EDS elemental analysis.

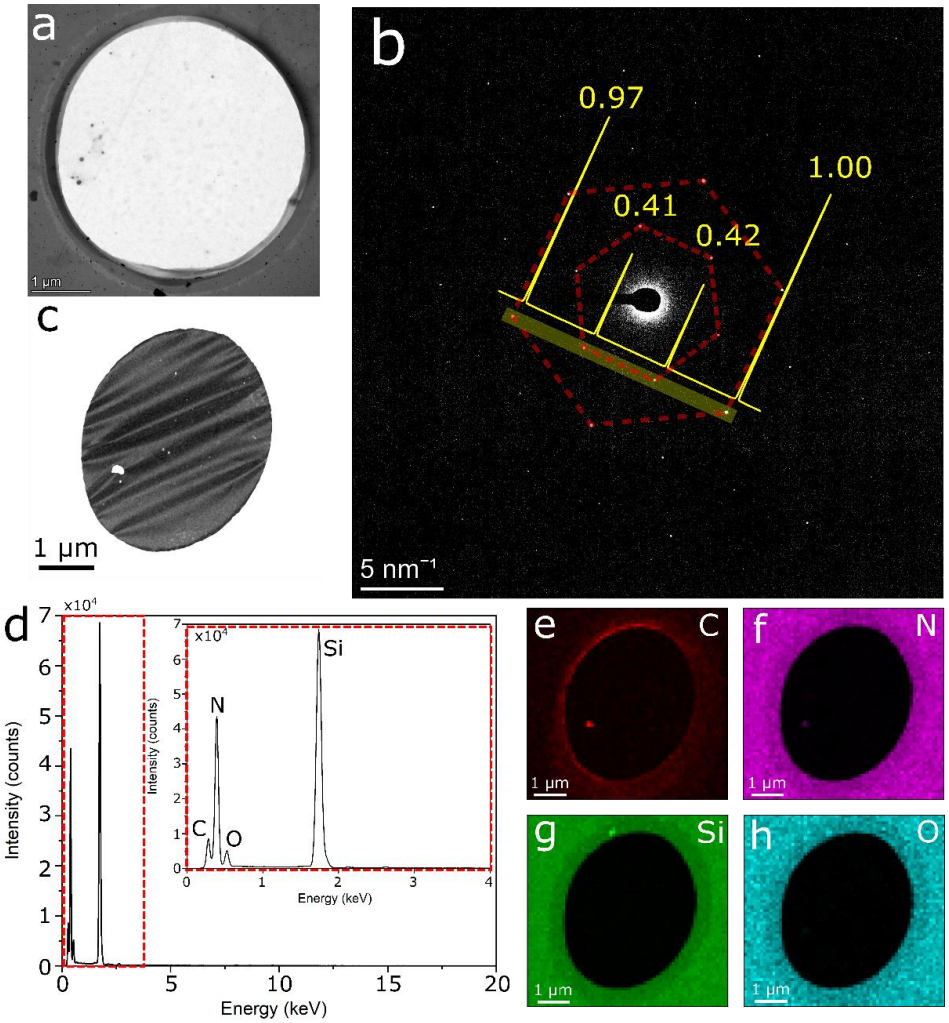

Figure 7.5 S/TEM characterisation of the suspended bilayer graphene membrane before intercalation. (a) BF-TEM image of the bilayer graphene membrane entirely covering a hole in the *in-situ* chip and (b) corresponding SAED pattern with the numbers refer to the normalised brightness values of peak ({0110} and {1210}) intensities. (c) Enhanced contrast ADF-STEM image showing the ripples of bilayer graphene membrane. (d) EDS spectrum of the same area in (c) with part the spectrum (energy 0 – 4 keV) magnified in the inset to illustrate C, N, O and Si peaks. (e-h) are EDS maps of C, N, Si and O distribution in the region of interest.

7.3.2 *In-situ* Biasing TEM Imaging Intercalation

Stacks of real time ADF-STEM images were acquired while the *in-situ* nanodevice was biased (-8V) in the TEM. Each image was acquired with a 3.1 s frame time. Fig 7.6a-h show time resolved images for the same area in Fig. 7.5c. There is no morphologic change of the bilayer graphene

membrane observed in the first 213.9 s (corresponding to the 69th frame). However, at 217.0 s (70th frame) two needle-shape features emerge highlighted by the red ovals on the left side of membrane (Fig. 7.6b). These two needle features extended their length and also became wider, forming short 'rods' as the intercalation proceeded, with a third 'needle' feature appearing at 220.1 s (71st frame) visible in Fig. 7.6c. A further time series from 300 s to 600 s (Fig. 7.6e-f) reveals that the needle features continue to enlarge, while others continuously formed and grew. Increasing the brightness reveals the features are also present in the supported areas of bilayer graphene (on top of the SiN support). These features show higher ADF contrast suggesting they contain additional material. The morphology is also similar to the bubble features often observed in TEM of stacked graphene heterostructures[42,43], suggesting that the additional material induced as a result of the applied bias is between the graphene layers rather than simply surface contaminants.

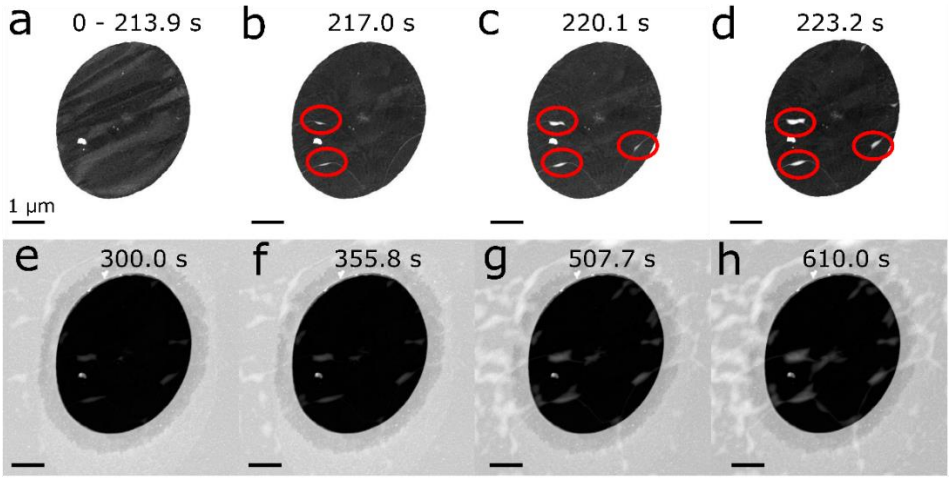

Figure 7.6 *In-situ* STEM imaging of the intercalation process with a -8V applied bias. (a-h) show a series of real time STEM images of the intercalation process. Red circles highlight the appearance of the features shown in the suspended bilayer graphene membrane. Note that (a-d) are enhanced contrast STEM images of the bilayer graphene membrane to exhibit the bubbles.

7.3.3 Post-intercalation S/TEM Characterisation

Intercalation induced structural and chemical changes were characterised by SAED and STEM-EDS. Fig. 7.7a shows the morphology of the intercalated bilayer graphene membrane biased at -8V for 20 minutes where the additional contrast features produced during intercalation are clearly visible. SAED patterns from the regions without the intercalant (indicated by the green circle) is similar to the pattern for the original bilayer graphene as shown in Fig. 7.7b. The SAED patterns from the intercalant features enclosed by red and cyan circles (Fig. 7.7c-d) exhibit broad amorphous rings suggesting the intercalant observed here is composed of disordered structures.

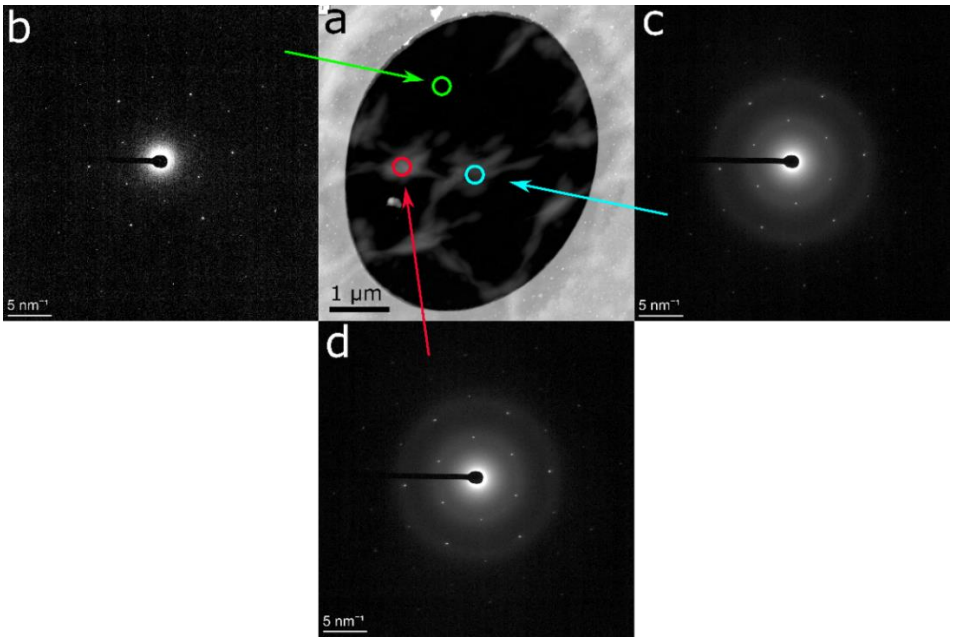

Figure 7.7 Structural analysis of the intercalant formed at -8V using SAED. (a) is the ADF-STEM image of the intercalated bilayer graphene membrane where three representative areas were selected to acquire the corresponding SAED patterns shown in (b-d).

STEM-EDS characterisation was used to identify the chemical composition of the intercalant. Fig. 7.8a-e show EDS spectral images of the intercalated membrane and Fig. 7.8f is an EDS spectrum of the Area 1 selected by a blue dashed square in Fig. 7.8a. The intercalant features are found to contain C and a small amount of N with very little Si and O. No Eu-L (5.845 keV) peak is found suggesting the likely intercalant is the ionic liquid electrolyte cation (1-Butyl-1-methylpyrrolidinium, shown in Fig. 7.3b). Note that the Eu signal was not detected in this specimen after *in-situ* intercalation by using EDS, however the detection limit of EDS is about 0.2 wt%, therefore it is possible that Eu concentration is below this threshold.

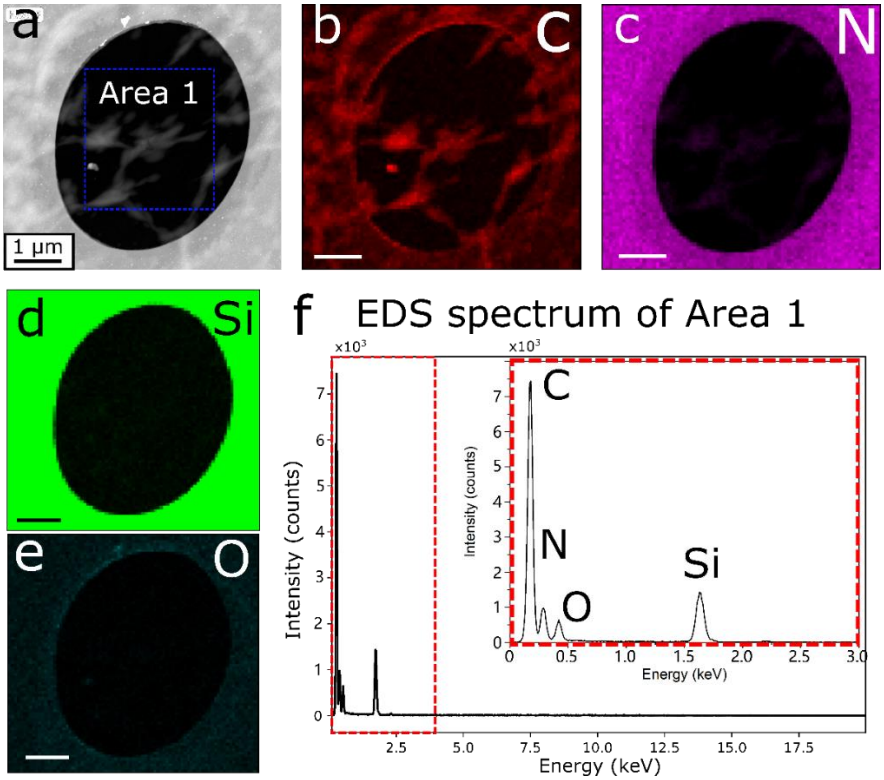

Figure 7.8 STEM-EDS spectral imaging the suspended bilayer graphene membrane after intercalation at -8V. (a) shows the ADF-STEM image of the bilayer graphene membrane covering the hole in the SiN substrate. (b-e) EDS maps of C, N, Si and O distributions in the examined region. (f) summed EDS spectrum of the Area 1 highlighted in (a) with the energy range of 0-3 keV magnified in the inset.

A further set of electrochemical experiments of intercalation into bilayer graphene were performed at a lower applied voltage bias of -4 V as shown in Fig. 7.9 and Fig. 7.10. Fig. 7.9a shows a TEM image of the bilayer graphene membrane before intercalation. The SAED pattern (Fig. 7.9b) corresponding to the area in the membrane indicated by the magenta circle in Fig. 7.9a shows an intensity ratio for {0110}/{1210} spots of 0.48 proving the bilayer nature of the flake. In contrast, the SAED pattern acquired at the same position after intercalation demonstrates an intensity ratio of {0110}/{1210} = 1.09, close to the simulation results of 1.17 for Li-saturated bilayer graphene (LiC_6) with A*R*A stacking (*R* stands for the Li layer between the bilayer graphene)[6], which indicates the stacking order change in bilayer graphene from AB to AA after Eu intercalation. Previous literature has reported the formation of Eu superstructure in the bilayer graphene prepared by the heating method[18,19], however, no superlattice spots were found in this work. Higher magnification HAADF-STEM images (Fig. 7.9e and Fig. 7.10c) show that after intercalation at -4V the bilayer graphene is covered in many small clusters with high atomic number. These are found to be more beam stable than organic surface contaminants, but no atomic resolution information could be obtained even using low current. EDS spectrum imaging (Fig. 7.9f,h) shows the intercalant features formed at -4V contain weak Eu_L and Eu_M peaks uniformly distributed over the examined area. The bilayer also showed features containing oxygen and a small amount of N, similar to the features formed with higher intercalation bias (Fig. 7.9i-k).

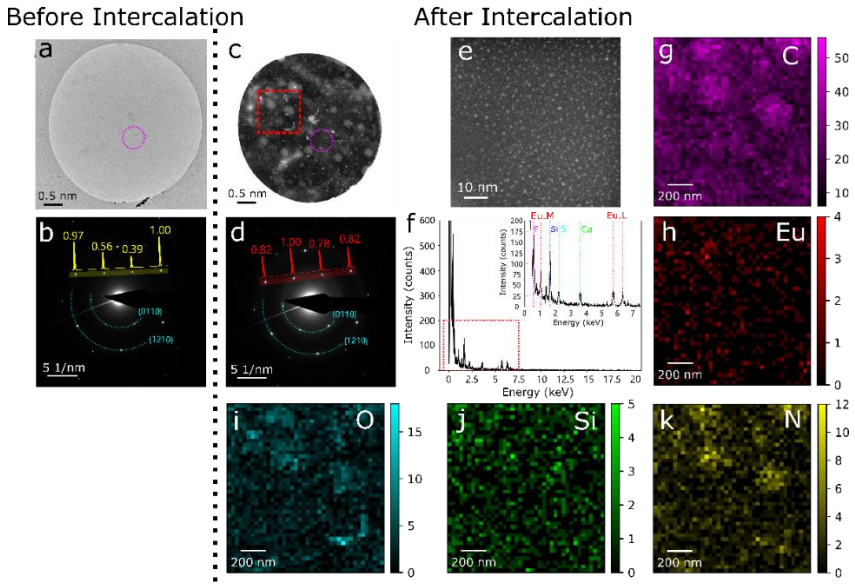

Figure 7.9 S/TEM results of Eu intercalation at -4V in bilayer graphene. (a) and (b) show the TEM image and SAED pattern of bilayer graphene before intercalation. The selected area is highlighted by the magenta dotted circle in (a). The solid yellow line in (b) demonstrates the intensity profile of the {0110} and {1210} spots and the numbers refer to the normalised brightness values. (c-h) demonstrate the structural and compositional variations of the specimen after Eu intercalation at -4V. (c) is an enhanced contrast ADF-STEM image of the bilayer membrane and (d) presents the SAED pattern of the magenta circle area in (c). The red line shows the intensity profile of the {0110} and {1210} spots in (d). (e) exhibits the high resolution HAADF-STEM image of the Eu clusters that appeared after intercalation for the bilayer graphene membrane. (f) and (g-h) illustrate the EDS spectra and C, Eu, O, Si and N maps of the selected regime shown in the red dashed square in (c).

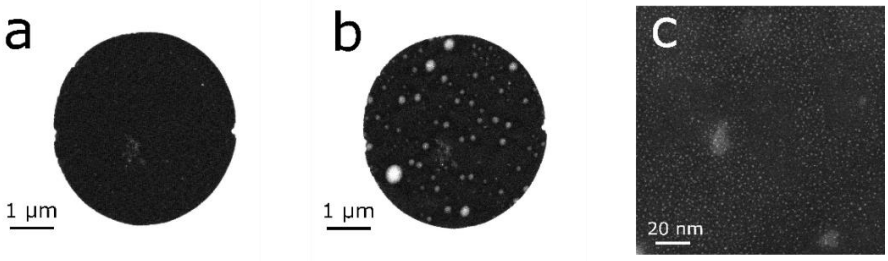

Figure 7.10 STEM images of the specimen after intercalation at -4V. (a) and (b) show enhance contrast ADF-STEM images of the bilayer graphene membrane before and after Eu intercalation, respectively. (c) is high resolution HAADF-STEM image of the intercalated Eu clusters in the membrane. However, there is no atomic resolution imaging to see bilayer graphene or the Eu clusters due to the contaminations which may developed in sample preparation and intercalation process, affecting HAADF-STEM imaging. The origin of the contaminations is unknown at present, but it will be further investigated in the future work.

7.4 Conclusions

In summary, electrochemical *in-situ* TEM intercalation using solid state polymeric electrolytes was demonstrated on a commercial *in-situ* biasing TEM chip manufactured by Protochips. Using an electrolyte containing Eu ions and ionic liquid, morphological and structural changes were monitored in the suspended bilayer graphene membranes during *in-situ* bias in real time. For -8V applied bias, the bubbles were originated from intercalation of amorphous species inferred as the ionic liquid cations in the bilayer graphene according to the EDS evidence. When the applied bias was reduced to -4V, 1-3 nm diameter Eu clusters were observed to be associated with the graphene after biasing. These are suggested to be between the bilayer graphene sheets as evidenced by a clear disruption to the Bernal stacking in the bilayer graphene after biassing. Clusters appear to be a new intercalation phenomenon, which may have been missed in previous works as their size is below what could be detected by low magnification TEM imaging, electron diffraction or X-ray diffraction.

Bibliography

1 Somoano, R., Hadek, V. & Rembaum, A. Alkali metal intercalates of molybdenum disulfide. *The Journal of Chemical Physics* **58**, 697-701 (1973).

2 Nishitani, R., Uno, Y. & Suematsu, H. In situ observation of staging in potassium-graphite intercalation compounds. *Physical Review B* **27**, 6572 (1983).

3 Axdal, S. A. & Chung, D. A theory for the kinetics of intercalation of graphite. *Carbon* **25**, 377-389 (1987).

4 Chrissafis, K. *et al.* Structural studies of MoS2 intercalated by lithium. *Materials Science and Engineering: B* **3**, 145-151 (1989).

5 Kühne, M. *et al.* Reversible superdense ordering of lithium between two graphene sheets. *Nature* **564**, 234-239 (2018).

6 Ji, K. *et al.* Lithium intercalation into bilayer graphene. *Nature communications* **10**, 1-10 (2019).

7 Zou, Y.-C. *et al.* Ion exchange in atomically thin clays and micas. *Nature materials* **20**, 1677-1682 (2021).

8 Boyes, E. & Gai, P. Environmental high resolution electron microscopy and applications to chemical science. *Ultramicroscopy* **67**, 219-232 (1997).

9 Mecklenburg, M. *et al.* in *Microscopy Society of America conference.*

10 Hsueh, Y.-H., Ranjan, A., Lyu, L.-M., Hsiao, K.-Y. & Lu, M.-Y. In situ TEM observations of void movement in Ag nanowires affecting the electrical properties under biasing. *Chemical Communications* (2021).

11 Kiener, D. & Minor, A. M. Source truncation and exhaustion: insights from quantitative in situ TEM tensile testing. *Nano letters* **11**, 3816-3820 (2011).

12 Liu, X. H. *et al.* In situ TEM experiments of electrochemical lithiation and delithiation of individual nanostructures. *Advanced Energy Materials* **2**, 722-741 (2012).

13 Kelly, D. J. *et al.* In Situ TEM Imaging of Solution-Phase Chemical Reactions Using 2D-Heterostructure Mixing Cells. *Advanced Materials*, 2100668 (2021).

14 Kiener, D., Kaufmann, P. & Minor, A. M. Strength, hardening, and failure observed by in situ tem tensile testing. *Advanced engineering materials* **14**, 960-967 (2012).

15 Wang, X., Shen, X., Wang, Z., Yu, R. & Chen, L. Atomic-scale clarification of structural transition of MoS2 upon sodium intercalation. *ACS nano* **8**, 11394-11400 (2014).

16 Gao, P., Wang, L., Zhang, Y., Huang, Y. & Liu, K. Atomic-scale probing of the dynamics of sodium transport and intercalation-

induced phase transformations in MoS2. *ACS nano* **9**, 11296-11301 (2015).

17 Huang, Q. *et al.* The Mechanistic Insights into the 2H-1T Phase Transition of MoS2 upon Alkali Metal Intercalation: From the Study of Dynamic Sodiation Processes of MoS2 Nanosheets. *Advanced Materials Interfaces* **4**, 1700171 (2017).

18 Sokolov, I. S. *et al.* Two-dimensional ferromagnetism in Eu-intercalated few-layer graphene. *Journal of Alloys and Compounds* **884**, 161078 (2021).

19 Sokolov, I. S. *et al.* 2D ferromagnetism in europium/graphene bilayers. *Materials Horizons* **7**, 1372-1378 (2020).

20 Schumacher, S. *et al.* Europium underneath graphene on Ir (111): Intercalation mechanism, magnetism, and band structure. *Physical Review B* **90**, 235437 (2014).

21 Liu, X. *et al.* Adsorption and growth morphology of rare-earth metals on graphene studied by ab initio calculations and scanning tunneling microscopy. *Physical Review B* **82**, 245408 (2010).

22 Huttmann, F. *et al.* Magnetism in a graphene-4 f− 3 d hybrid system. *Physical Review B* **95**, 075427 (2017).

23 Tien, D. H. *et al.* Study of graphene-based 2D-heterostructure device fabricated by all-dry transfer process. *ACS applied materials & interfaces* **8**, 3072-3078 (2016).

24 Zhang, R. *et al.* Superconductivity in potassium-doped metallic polymorphs of MoS2. *Nano letters* **16**, 629-636 (2016).

25 Ebert, L. B. Intercalation compounds of graphite. *Annual Review of Materials Science* **6**, 181-211 (1976).

26 Nair, J. R., Gerbaldi, C., Destro, M., Bongiovanni, R. & Penazzi, N. Methacrylic-based solid polymer electrolyte membranes for lithium-based batteries by a rapid UV-curing process. *Reactive and Functional Polymers* **71**, 409-416 (2011).

27 Novoselov, K. S. *et al.* Electric field effect in atomically thin carbon films. *science* **306**, 666-669 (2004).

28 Gaskell, P., Skulason, H., Rodenchuk, C. & Szkopek, T. Counting graphene layers on glass via optical reflection microscopy. *Applied physics letters* **94**, 143101 (2009).

29 Obelenis, F. & Champi, A. Determination of the Number of Graphene Layers on Different Substrates by Optical Microscopy Technique. *Brazilian Journal of Physics* **44**, 682-686 (2014).

30 Wang, Y. Y. *et al.* Raman studies of monolayer graphene: the substrate effect. *The Journal of Physical Chemistry C* **112**, 10637-10640 (2008).

31 Das, A., Chakraborty, B. & Sood, A. Raman spectroscopy of graphene on different substrates and influence of defects. *Bulletin of Materials Science* **31**, 579-584 (2008).

32 Ferrari, A. C. Raman spectroscopy of graphene and graphite: Disorder, electron–phonon coupling, doping and nonadiabatic effects. *Solid state communications* **143**, 47-57 (2007).
33 Ferrari, A. C. *et al.* Raman spectrum of graphene and graphene layers. *Physical review letters* **97**, 187401 (2006).
34 Casiraghi, C. *et al.* Raman spectroscopy of graphene edges. *Nano letters* **9**, 1433-1441 (2009).
35 Casiraghi, C., Pisana, S., Novoselov, K., Geim, A. K. & Ferrari, A. Raman fingerprint of charged impurities in graphene. *Applied physics letters* **91**, 233108 (2007).
36 Ferrari, A. C. *et al.* Raman spectrum of graphene and graphene layers. *Phys Rev Lett* **97**, 187401, doi:10.1103/PhysRevLett.97.187401 (2006).
37 Malard, L., Pimenta, M. A., Dresselhaus, G. & Dresselhaus, M. Raman spectroscopy in graphene. *Physics reports* **473**, 51-87 (2009).
38 Eckmann, A. *et al.* Probing the nature of defects in graphene by Raman spectroscopy. *Nano letters* **12**, 3925-3930 (2012).
39 Smith, M. J. & Silva, C. J. Conductivity studies of a polymer electrolyte based on europium trifluoromethanesulphonate. *Solid state ionics* **58**, 269-273 (1992).
40 Rao, C. J., Venkatesan, K., Nagarajan, K., Srinivasan, T. & Rao, P. V. Electrochemical behavior of europium (III) in N-butyl-N-methylpyrrolidinium bis (trifluoromethylsulfonyl) imide. *Electrochimica Acta* **54**, 4718-4725 (2009).
41 Bao, W. *et al.* Controlled ripple texturing of suspended graphene and ultrathin graphite membranes. *Nature nanotechnology* **4**, 562-566 (2009).
42 Pan, W. *et al.* Biaxial compressive strain engineering in graphene/boron nitride heterostructures. *Scientific reports* **2**, 1-6 (2012).
43 Vincent, T. *et al.* Probing the nanoscale origin of strain and doping in graphene-hBN heterostructures. *2D Materials* **6**, 015022 (2018).

Chapter 8

Summary and Future Work

8.1 Summary of Thesis

This doctoral thesis has investigated the structural evolution and chemical variation of the van der Waals materials as a result of alkali ion intercalation using *in-situ* S/TEM and related analytical techniques.

Chapter 5 demonstrates the structure-composition relationships for the K-intercalated MoS_2 flakes being studied via atomic resolution imaging, electron diffraction and STEM-EDS elemental analysis. The freshly prepared intercalated MoS_2 flake was found to be predominated by 2H and 1T polytypes with a few regions of 1T'. Ordering K in the interlayer spaces of the MoS_2 contributed to the formation of various superstructures including the $2a \times \sqrt{3}a$ superstructure first observed in the K-doped MoS_2 system. *In-situ* measurements of the thermal deintercalation process revealed that this process is ruled by first order kinetics, and the result allows empirical prediction of the mean composition as a function of time and temperature. During deintercalation a novel intermediate mixed phase emerged and was illustrated as a combination of the $2a \times \sqrt{3}a$ and $2a \times 2a$ superstructures. This phenomenon demonstrated the preferential loss of intercalant from individual planes so as to adopt one of the preferred superlattice orders for the intercalant species. Atomic resolution imaging and local elemental analysis revealed a rich structural variation at the

nanoscale within individual host crystals. During deintercalation we observed a decrease in the variance of the local elemental compositions and in the interlayer spacings, suggesting a route to synthesis of more homogeneous intercalated materials. We proposed that the combination of local *in-situ* crystallographic and compositional analysis demonstrated in this work is widely applicable to provide new insights in to other 2D materials systems that undergo dynamic structural and chemical changes.

Chapter 6 presents structural characterisation of K-doped MoS_2 by using the cutting-edge 4DSTEM imaging technique, and the principles of 4DSTEM were introduced in this chapter including the data acquisition and the data processing method. The results of 4DSTEM and conventional S/TEM were compared to demonstrate the superior capability of 4DSTEM in structural characterisation at the nanoscale. In the case of 4DSTEM, the data availability of associating a series of diffraction patterns with pixels in a 4DSTEM image allows us to reconstruct the virtual BF, DF images and virtual SAED patterns for structural characterisation of the materials. Additionally, the 4DSTEM technique enabled development of the structural classification map to illustrate the distribution of the superstructures. We pioneered the finding that superstructures can independently exist in the specimen or coexist to form complex superstructures, agreeing with the atomic models proposed to obtain the simulated diffraction patterns shown in Chapter 5 and revealing the structural changes appearing during the deintercalation process. This work is expected to promote deeper understanding of this novel material system for its exploitation in potential applications such as nanoelectronics,

catalysis and superconducting materials.

Chapter 7 presents the new results of *in-situ* intercalation of ionic liquid and Eu nanoclusters in bilayer graphene achieved via the fabrication of an electrochemical nanodevice on a commercial TEM chip. *In-situ* STEM was used to observe the formation of intercalant bubbles in real time in the suspended bilayer graphene membrane under -8V biasing. SAED demonstrates the amorphous characteristic of the bubbles and STEM-EDS suggest the same chemical compositions to the ionic liquid. For the electrochemical intercalation biased at -4V, the Eu clusters were imaged by HAADF-STEM, and EDS elemental mapping revealed a uniform distribution of Eu clusters in the bilayer membrane. The intensity ratio of {0110}/{1210} planes in the SAED patterns demonstrated stacking changes in bilayer graphene from AB to AA suggesting Eu intercalation between the layers.

8.2 Future Work

The structural and chemical variations of the K-doped MoS_2 flake have been discussed in Chapter 5 and 6. However, as the average thickness of the imaged individual flakes was over 50 layers, the atomic structures of the central region of the flake were invisible in high resolution S/TEM imaging, and only the atomic structures near edges of the flakes were explicitly imaged. Additionally, a crystal with over 50 layers cannot be strictly defined as a 2D material. The study was limited to thicker liquid exfoliated materials as we could find no viable method to fabricate and transfer few-layer K-doped MoS_2 flakes to the TEM while retaining the

intercalant. Nonetheless, it would be of particular interest to study *in-situ* the K intercalation/deintercalation behaviour in few-layer MoS_2 under heating, which may be expected to show the distinct deintercalation dynamics and kinetics found in other few-layer crystals in the 2D limit[1,2]. The new knowledge of nanodevice fabrication demonstrated in Chapter 6 suggests that a new *in-situ* sample preparation workflow might be possible in order to study the deintercalation behaviour of few-layer MoS_2. The few-layer MoS_2 will be mechanical exfoliated and transferred onto the *in-situ* TEM heating chip, followed by K intercalation via the liquid ammonia intercalation method. To reduce electron beam damage of the few-layer intercalation compound, S/TEM, EDS and EELS characterisations will be performed at 80 keV accelerating voltage. The intercalation will initially be imaged by annular bright field (ABF-STEM) which is likely to define the position of the K in the material lattice, since it has been previously employed to image Na and Li in MoS_2[3,4]. *In-situ* structural and chemical characterisation will be performed to investigate structural changes in the few-layer MoS_2. Like the experiments introduced in Chapter 5, the temperatures of *in-situ* heating TEM will be varied from room temperature to 300 ˚C to investigate the kinetics of K deintercalation from 2D MoS_2 and this will be compared to those already recorded for bulk (50L) crystals. The phase transition of MoS_2 from 1T (or distorted 1T) to 2H and the superstructure variations of ordering K are expected to be imaged readily for the whole flake during *in-situ* heating. Furthermore, we can prepare a series of samples with distinct intercalation degrees by manipulating the intercalation time. Intercalation compounds with higher degrees of

intercalation are expected to be acquired for longer intercalation times, facilitating understanding of the relationship between the intercalation time and the K concentration varying in a large range (K/Mo = 0 ~ 1.5) for 2D MoS_2 flakes. The role of edges and creases will also be more readily elucidated in highly controlled 2D crystals compared to studying disordered liquid exfoliated flakes.

The investigation of K-doped MoS_2 using 4DSTEM (Chapter 6) also has the potential to be greatly expanded in future work. The strain in the host lattice of the intercalation compound is generated due to the foreign ions, which also can be measured at the nanoscale by 4DSTEM[5]. One potential approach is to measure the d-spacing difference between the different samples or the regions of the sample by measuring distances between the origin to the centre of mass of the diffracted reflections. Repeating this process in all 4DSTEM patterns and compare the calculated d-spacings to the data from a standard MoS_2 species would enable to map the strain for the K-intercalated MoS_2 flakes with simultaneous mapping of K concentration in order to correlate the strain and the chemical composition. For maximum clarity, both structural classification and strain mapping should ideally be carried on the few-layer materials.

The study of imaging intercalation via *in-situ* biasing TEM showcases in Chapter 7 can be extended to find more unexpected intercalation behaviours differing from those seen in the more widely studied alkali ion cations. Eu is a heavy element with atomic number of 63 so that its atomic arrangement in the interlayer spacing of bilayer graphene should be possible to be tracked by STEM easier than Li, Na and K.

According to the literatures, Eu can form EuC_6 compound in the bilayer or few-layer graphene[6,7]. Therefore, it should be an excellent intercalation compound to study the formation of superstructures and intercalation dynamics at the high spatial resolution. The formation of Eu clusters and their mobility demonstrated in Chapter 7 as a new intercalation phenomenon may be the result of the use of a solid-state electrolyte containing the ionic liquid. It is worth further study to determine if this may be the new intercalation mechanism or a strategy for the dense charge storage. Further works also contain the study of the 2D ferromagnet behaviour of the intercalated material and build the relationship between structures and the properties so as to tune the physical properties. Furthermore, once the fabrication barriers are overcome, *in-situ* TEM provides the only viable means to study intercalation dynamics in small area of the 2D heterostructures, particularly in twisted heterostructures of graphene and TMDCs.

Bibliography

1 Li, G. *et al.* Enhanced Reversible Sodium-Ion Intercalation by Synergistic Coupling of Few-Layered MoS2 and S-Doped Graphene. *Advanced Functional Materials* **27**, 1702562 (2017).

2 Hui, J., Burgess, M., Zhang, J. & Rodríguez-López, J. Layer number dependence of Li+ intercalation on few-layer graphene and electrochemical imaging of its solid–electrolyte interphase evolution. *ACS nano* **10**, 4248-4257 (2016).

3 Wang, X., Shen, X., Wang, Z., Yu, R. & Chen, L. Atomic-scale clarification of structural transition of MoS2 upon sodium intercalation. *ACS nano* **8**, 11394-11400 (2014).

4 Gu, L. *et al.* Direct observation of lithium staging in partially delithiated LiFePO4 at atomic resolution. *Journal of the American Chemical Society* **133**, 4661-4663 (2011).

5 Rottmann, P. F. & Hemker, K. J. Nanoscale elastic strain mapping of polycrystalline materials. *Materials Research Letters* **6**, 249-254 (2018).

6 Sokolov, I. S. *et al.* 2D ferromagnetism in europium/graphene bilayers. *Materials Horizons* **7**, 1372-1378 (2020).

7 Sokolov, I. S. *et al.* Two-dimensional ferromagnetism in Eu-intercalated few-layer graphene. *Journal of Alloys and Compounds* **884**, 161078 (2021).